PACIFIC EARTHQUAKE ENGINEERING RESEARCH CENTER

NGA-East Regionalization Report: Comparison of Four Crustal Regions within Central and Eastern North America using Waveform Modeling and 5%-Damped Pseudo-Spectral Acceleration Response

Jennifer Dreiling
Marius P. Isken
Walter D. Mooney

U.S. Geological Survey
Menlo Park, California

Martin C. Chapman
Richard W. Godbee

Department of Geosciences
Virginia Polytechnic Institute and State University
Blacksburg, Virginia

PEER 2014/15
OCTOBER 2014

NGA-East Regionalization Report: Comparison of Four Crustal Regions within Central and Eastern North America using Waveform Modeling and 5%-Damped Pseudo-Spectral Acceleration Response

Jennifer Dreiling
Marius P. Isken
Walter D. Mooney

U.S. Geological Survey
Menlo Park, California

Martin C. Chapman
Richard W. Godbee

Department of Geosciences
Virginia Polytechnic Institute and State University
Blacksburg, Virginia

PEER Report 2014/15
Pacific Earthquake Engineering Research Center
Headquarters at the University of California, Berkeley

October 2014

ABSTRACT

An important aspect of the Next Generation Attenuation for Central and Eastern North America (NGA-East) project led by the Pacific Earthquake Engineering Research Center (PEER) entails assigning seismic wave attenuation values to major crustal regions. In this study, Central and Eastern North America (CENA) is subdivided into four regions based on the geologic and tectonic setting. The regions are the Central North America (CNA), the Appalachian Province (APP), the Atlantic Coastal Plain (ACP), and the Mississippi Embayment/Gulf Coast region (MEM). Each region is described by a statistically representative crustal seismic velocity-depth structure and *Q*-factor model. The crustal structure models are for very hard rock conditions and do not include any sediments. The four regions are shown in the figure below. The largest region is Central North America (CNA) and the others are, following a clockwise order, the Appalachian Province (APP), the Atlantic Coastal Plain (ACP), and the Mississippi Embayment/Gulf Coast region (MEM).

The purpose of this study was to evaluate similarities and differences in attenuation for these regions and to assess whether regions needed to remain separate or if they could be grouped based on their attenuation properties. This was achieved through a series of ground motion simulations. Seismic wave propagation was simulated for earthquakes at focal depths of 5, 10, 20, and 30 km, using two different ground motion simulation codes. Synthetic time series and the 5% damped pseudo-absolute response spectral acceleration (PSA) provide insight into the attenuation of ground motions that are typical for each region. The calculated PSA covers a hypocentral distance range of 7.5–500 km and oscillator frequencies ranging from 0.5 to 20 Hz. Spectral accelerations were compared both within and between regions.

The CNA is the biggest region geographically and offers the largest variety of crustal seismic velocity-depth structures associated with the unique geologic evolution of its sub-regions. We define CNA as our base region and use it for both comparisons and to estimate a reference range of within-region variability. After generalizing the 417 profiles available for CNA into one representative profile (CNA_{Rep}), ground motions were calculated for the four aforementioned focal depths. The within-region variability was also assessed using ground motion simulations for a selected set of 18 alternative velocity models developed for the region (CNA_{Alt}). We compared the PSA calculated for CNA_{Rep} to the PSA values for the 18 alternative crustal structures, CNA_{Alt}. We find that the representative crustal structure for CNA is reasonable based on the observation that the PSA matrix for CNA_{Rep} and the mean PSA matrix of CNA_{Alt} are almost identical. The range of uncertainties of ground motions for CNA may be estimated using the standard deviations of CNA_{Alt}, which are dependent on the frequency and distance to the source as well on the focal depth of the event. While the standard deviations are relatively small for closer hypocentral distances, they increase at a distance of 45–85 km, which is an effect due to the time and space variations in arrival of strong Moho reflections.

To determine which of the four regions should be assigned to a common attenuation group, we compared the ACP, APP, and MEM regions to the CNA base region. Statistical distributions (histograms) of the PSAs for specific distance and frequency bands were used to show if there were significant differences between the regions. Additional analysis tools, such as moving window average of PSA versus distance for specific frequency bands, were also used in these comparisons.

This analysis demonstrates that there are two distinct attenuation groups:

- GROUP 1: Central North America, Appalachians, Atlantic Coastal Plain
- GROUP 2: Mississippi Embayment/Gulf Coast

We found that the seismic velocity structure of the crust, rather than the Q-factor, has the largest effect on the attenuation of ground motions for the earthquake-to-source distances considered here. The PSA values for the CNA and APP regions look very similar for all four focal depths. Their representative PSAs are highly comparable and only at larger distances from the epicenter do the values show significant differences. However, these differences are well within the range found in the CNA base region itself (i.e., within the range of possible ground motions for CNA). Thus, a clear majority of the PSAs for the APP region fits CNA's ground motions or fall within its range of variability.

The PSA values for the ACP region are also very similar to the PSA values of the CNA representative model. This applies to all focal depths except the 20 km source depth, which was excluded because a layer boundary at 20.5 km produces unrealistically strong reflections for this source depth. Thus, the ACP region belongs to the same attenuation group as the CNA region, but with a statistical agreement that is somewhat lower than for the APP region.

The MEM region was found to clearly belong to a separate attenuation group. This result is in agreement with previous analyses that have found that the MEM region has unique attenuation characteristics.

ACKNOWLEDGMENTS

This work was supported primarily by the Nuclear Regulatory Commission and the Pacific Earthquake Engineering Research Center (PEER) as part of the NGA-East Research Project funded by the Nuclear Regulatory Commission, Department of Energy and Electric Power Research Institute. Support from the National Earthquake Hazards Program of the U.S. Geological Survey is also gratefully acknowledged. Discussions with Christine Goulet, Norm Abrahamson, David Boore, and Yousef Bozorgnia have clarified many technical issues. Remaining errors are solely the responsibility of the authors.

Any opinions, findings, and conclusions or recommendations expressed in this material are those of the authors and do not necessarily reflect those of the sponsoring agencies.

CONTENTS

LIST OF TABLES

LIST OF FIGURES

1 Introduction

In 1993 the Electric Power Research Institute (EPRI) investigated earthquake ground motions in North America. The quantification of crustal path effects on ground motions was one part of the investigation. As is well known, the attenuation of ground motion can vary greatly due to differences in crustal properties. North America has a diversity of geologic settings, each influencing the propagation of seismic waves through the crust.

The EPRI investigation [1993] subdivided North America into 16 crustal regions, each with a different crustal seismic velocity-depth structure (i.e., layer thicknesses and velocities) and seismic attenuation (Quality-factor). The Quality-factor (*Q*-factor or *Q*) accounts for intrinsic seismic damping by internal friction within rocks [Stein and Wysession 2003]. The attenuation of each of the 16 regions was estimated. It was then determined that it was possible to group these regions into three major *Q*-factor groups.

The study presented herein is an extension the 1993 EPRI's investigation that also builds on a recently compiled database of crustal structural models [Mooney 2013]. The objectives are to assign PSA attenuation values for major regions for Central and Eastern North America (CENA). As such, CENA has been subdivided into four regions based on the geologic and tectonic setting. The crustal structure in each region directly influences the attenuation of seismic waves traveling through the region. Following standard practice, the observed decrease in pseudo-absolute response spectral acceleration (PSA) with distance is referred to as the PSA attenuation. It is dominated by geometrical wave spreading effects, which in turn are determined by the specific seismic velocity-depth structure of the crust and earthquake focal depth. These are sometimes referred to as crustal path effects. The intrinsic seismic damping, or Quality-factor, *Q*, also contributes to the measured decrease in PSA with distance.

The four regions with CENA are: the Atlantic Coastal Plain (APC), the Appalachians (APP), Central North America (CNA), and the Mississippi Embayment/Gulf Coast (MEM). Each region is described by a statistically representative crustal velocity structure and *Q*-factor. To evaluate the differences in attenuation between the four regions, earthquakes were simulated for focal depths of 5, 10, 20, and 30 km. Synthetic time series and the 5%-damped PSA provide insight into ground motions that are typical for each of the four regions.

The aim of this study was to analyze the attenuation of PSA for each of the four regions and evaluate the differences between them. The attenuation of PSA for all regions was compared and the significance of these differences documented statistically. Depending on the quantification of these differences, we evaluated whether it is reasonable to combine any of the regions into a common attenuation group.

1.1 REPORT OUTLINE

This report contains seven chapters. Chapter 1 consists of a short introduction and description of this study's objectives. Chapter 2 summarizes some key background information and the study approach. The first part of Chapter 2 is based on the EPRI Technical Report [1993], while the second part explains the method used to determine the geophysical differences between the four crustal regions examined here. As mentioned, the key measure used is the attenuation of PSA.

The third chapter describes the parameters needed for the computation of acceleration time series and response spectral acceleration. It explains the subdivision of our study region, CENA, and defines the relevant seismic properties for each of the four sub-regions. These properties include a representative seismic crustal structure and the Quality-factor, Q. Based on statistical analyses published by other researchers, earthquake source properties like focal mechanism, depths, and magnitude are discussed. A discussion of computational parameters is also included.

Chapter 4 gives a short summary of the analysis procedure, starting with the computation of time series and 5%-damped PSA. To estimate the uncertainty of the representative velocity structure for each region, a description for a layer boundary and velocity sensitivity test is provided. Chapter 4 introduces the various analysis tools generated as part of the project to evaluate differences in regional attenuation.

Chapters 5 and 6 summarize the results in terms of time series and record sections and PSA for all the regions. These chapters also include the final comparison of attenuation for the four regions. Chapter 5 provides a summary of results based on simulations conducted for frequency-independent Q models. Chapter 6 provides a summary of results from frequency-dependent Q simulations. In addition, simulations conducted for Chapters 5 and 6 are based on different simulations codes, providing a redundancy and ensuring that results are consistent for different simulation methodologies. Chapter 7 summarizes the findings and provides a recommendation for regionalization of ground motions in CENA.

2 Background and Scope

2.1 PREVIOUS RESEARCH

This study was preceded by the 1993 EPRI technical report entitled, "Guidelines for Determining Design Basis Ground Motions. Volume 1: Method and Guidelines for Estimating Earthquake Ground Motion in Eastern North America" [1993]. Within that volume, Chapter 5, "Quantification of Crustal Path Effects," is of particular relevance to this report, and its key concepts are summarized below.

2.1.1 Importance of Consideration of Crustal Velocity Structure and *Q*

The EPRI report [1993] considered ground motions from ten earthquakes within the Grenville Province and ten earthquakes in eastern North America. The ground motions analysis included the modeling of the observed data and the calculation of synthetic (theoretical) ground motions. Attenuation was modeled at four frequencies: 1, 2, 5, and 10 Hz. Figures 2.1 and 2.2 show examples of the analyses presented in the EPRI report [1993], which highlights several key results:

- The largest variation in the attenuation among these earthquakes is due to differences in focal depth, with crustal structure of secondary importance.
- The influence of Q (intrinsic seismic damping) on the attenuation of ground motion grows as the path length increases Q is frequency dependent.
- The effect of the crustal seismic velocity structure can become significant when the reflected waves reach the critical angle and are completely reflected back to the surface at the critical distance R_{crit}. The primary reflector is at the base of the crust—the Moho—but locally intra-crustal seismic velocity boundaries can also generate strong critical angle reflections. In the critical distance range, these strong seismic reflections lead to distance-dependent variations in the rate of attenuation.

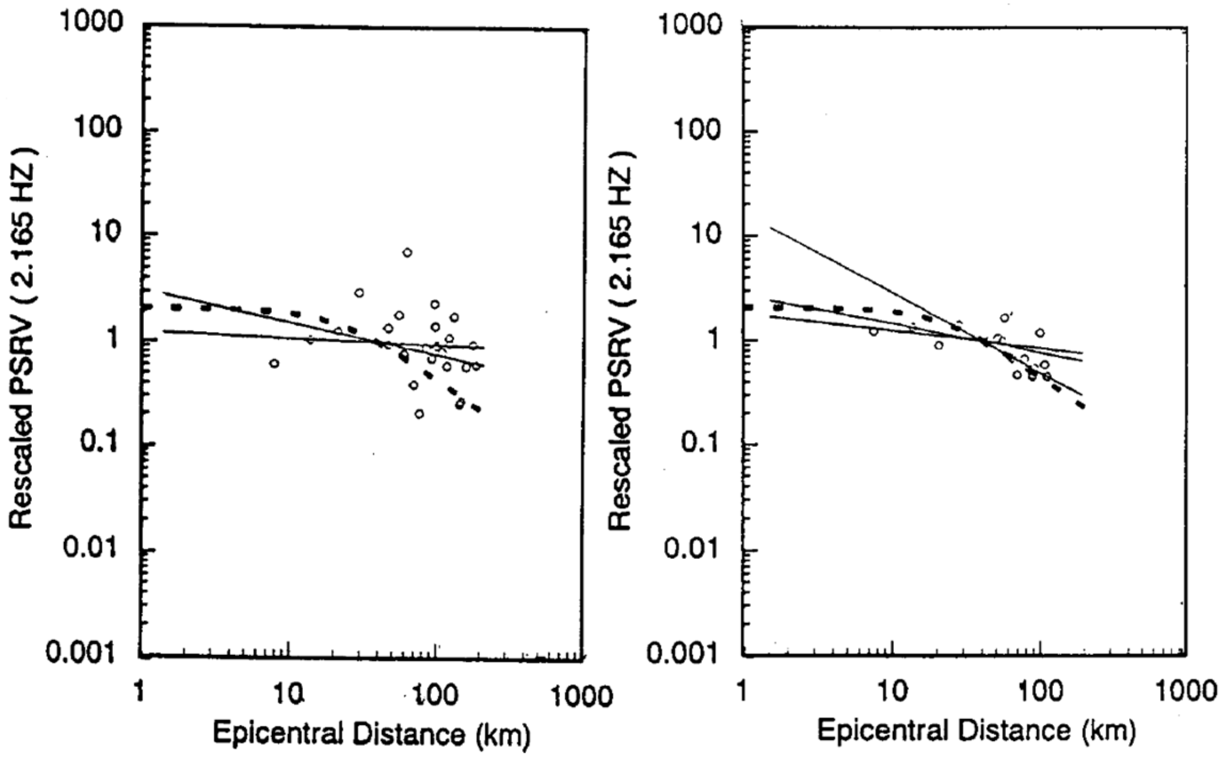

Figure 2.1 **Comparison of recorded and synthetic peak acceleration as a function of distance for Grenville Province earthquakes. Recorded PSRV at 5% damping at 2 Hz is shown on the left, synthetic values on the right. Illustration is for three deep events. Straight lines are normalized least-square fits to each event; dashed lines correspond to the 1/*R* attenuation [EPRI 1993].**

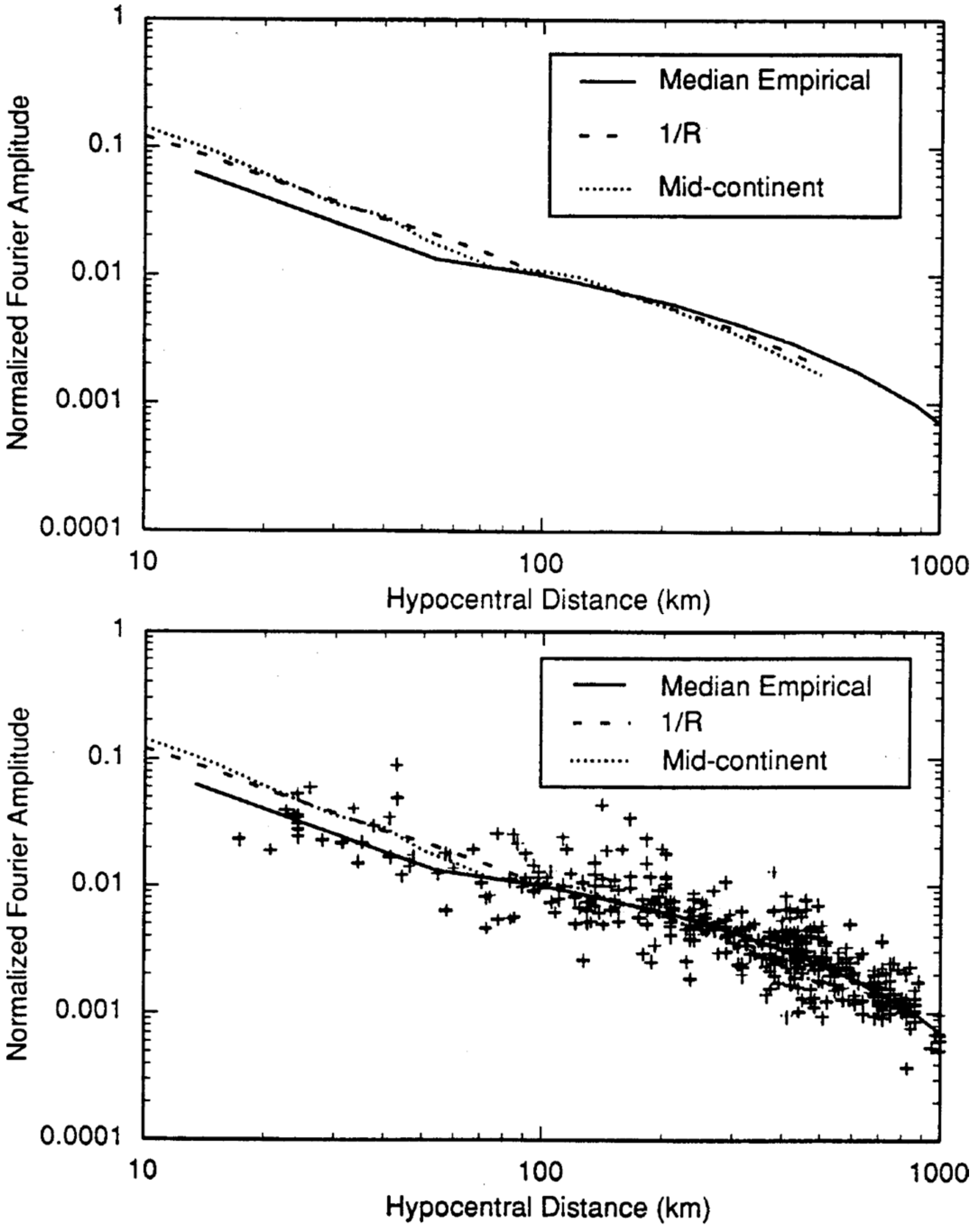

Figure 2.2 **Empirical attenuation in southeastern Canada for Fourier amplitude of acceleration at 2 Hz. The solid curve is the regression fit to these data. The dashed and dotted lines are based on a stochastic model [EPRI 1993].**

2.1.2 Regionalization of Crustal Seismic Velocity Structure, *Q,* and Focal Depth

The EPRI report [1993] subdivided the U.S. and southern Canada into 16 regions (Figure 2.3, top panel) based on the local velocity structure and eight regions based on the intrinsic seismic *Q*-values (Figure 2.3, bottom panel). These subdivisions were guided by the results presented in the book, "Geophysical Framework of the Continental United States" [Pakiser and Mooney 1989] and other publications.

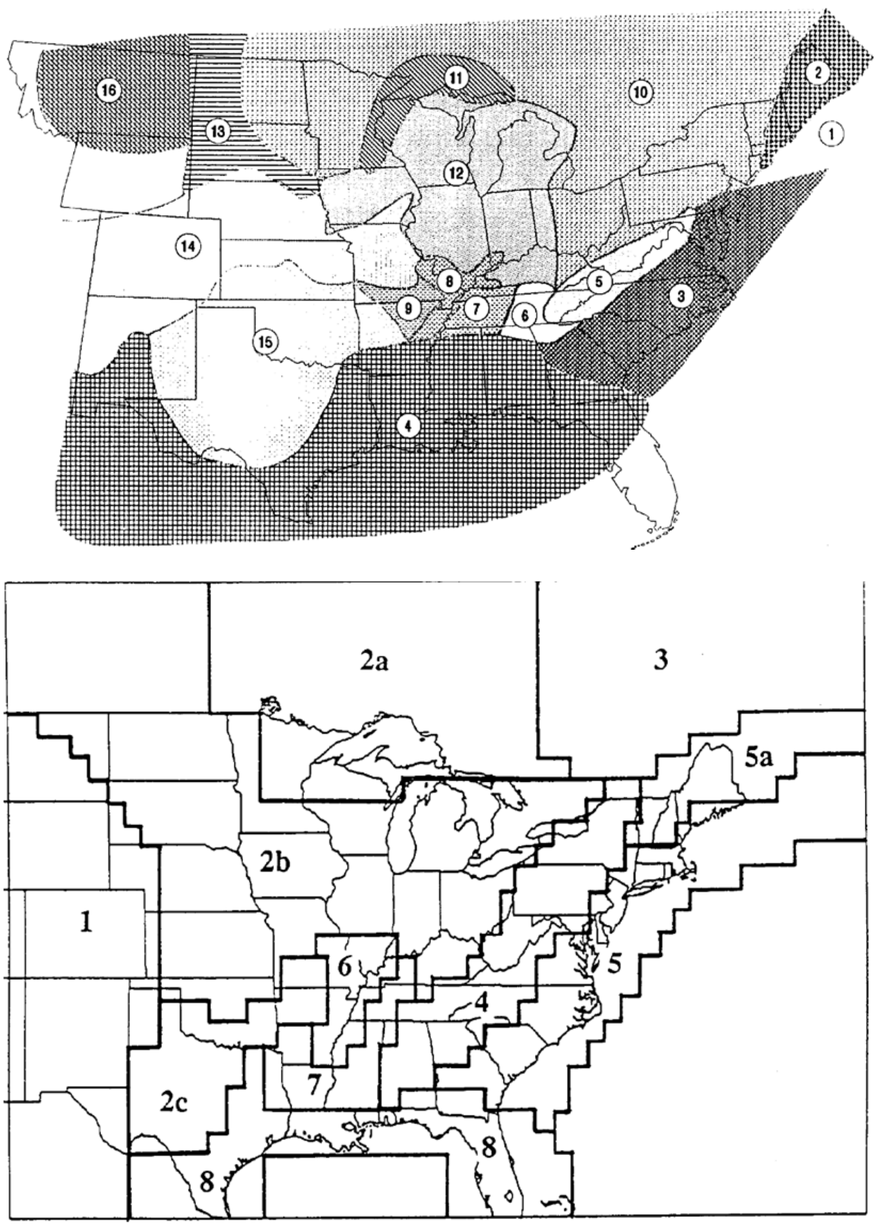

Figure 2.3 **Regionalization of southern Canada and U.S. [EPRI 1993]. Top: regionalization of crustal seismic velocity structure into 16 regions. Bottom: Intrinsic seismic damping *Q*-value regionalization into eight regions.**

The EPRI report [1993] also noted that there are systematic regional variations of focal depths (Table 2.1). These variations are correlated with the tectonic setting of each region. The identification of these regional variations is significant, because the focal depth has a strong effect on earthquake ground motions. Focal depth distributions were developed using the EPRI Stable Continental Regions (SCR) earthquake catalog of Johnston [1993]. All of the events in the EPRI [1993] database with a magnitude >5 and having an assigned tectonic setting were considered (Figure 2.4).

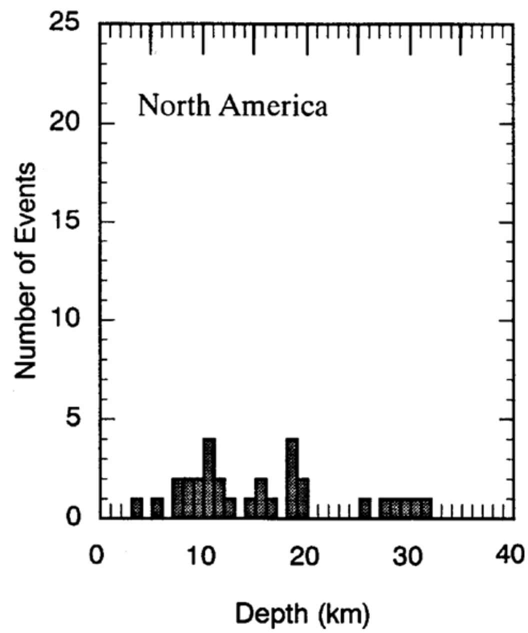

Figure 2.4 Focal depth distributions for eastern North America from the EPRI stable continental regions catalog [EPRI 1993].

Table 2.1 Summary of typical focal depths for earthquakes with M >5 for different regions.

Region	Range of focal depths (km)	Earthquake depths concentrated at (km)
Eastern North America	3–32	-
Central Craton	3–18	5
New Madrid	5–12	7
Appalachian	5–8	7
Proterozoic Margin	> 25	-

2.1.3 Effects of Crustal Velocity Structure and *Q* on Ground Motions

The EPRI study [1993] considered intra-regional variations in seismic crustal structure for fixed *Q*. For the Grenville Province—one of the sixteen regions—four velocity models were used to represent the variability of the seismic velocity-depth structure within the region. Using these four seismic velocity models, the standard error of spectral acceleration versus distance was considered for three frequencies: 1, 5, and 15 Hz. It was found that ground motions from shallow focal depths are more sensitive to the seismic velocity structure than ground motions from deep (greater than 15 km) focal depths.

Intrinsic seismic attenuation, *Q*, was found to be correlated to the seismic velocity structure, but the regional *Q* boundaries did not correspond to the boundaries that defined the seismic velocity structure regionalization. It was found that the effect of *Q* becomes significant for distances greater than 100 km.

Ground Motion Regionalization

The EPRI report [1993] considered spectral ground accelerations for 10 km distance intervals and at the frequencies of 1, 1.5, 2.5, 3.45, 5, 7.5, 10, 15, 25, and 34 Hz. Figure 2.5 presents an example of the median spectral acceleration at 5 Hz for each of the sixteen regions. Based on a comparison of these regions, it was found to be reasonable to reduce the number of attenuation groups for the U.S. to three.

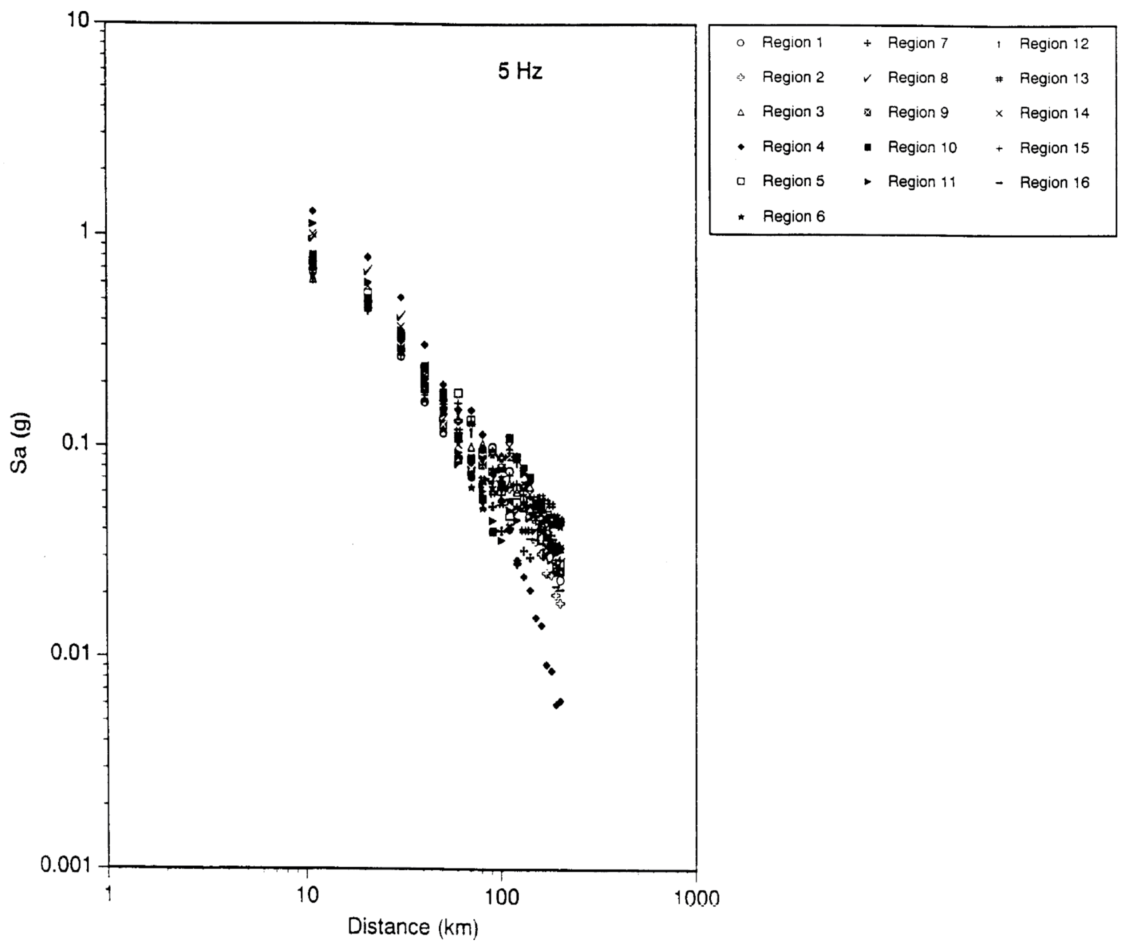

Figure 2.5 **Comparison of median ground motion attenuation of spectral acceleration at 5 Hz for the sixteen regions [EPRI 1993].**

2.2 CURRENT APPROACH

The current study follows the essential attributes on the EPRI [1993] approach and builds on the latest crustal information available [Mooney 2013]. The study was conducted as a supporting task for the NGA-East project, the goal of which is to develop a new ground motion characterization (GMC) model for the vast region of CENA. The NGA-East project's end products are to consist of a series of ground motion prediction Equations (GMPEs) that characterize the median and standard deviation of ground motion organized in a logic tree structure. The GMPEs were developed for peak ground acceleration (PGA) and for 5%-damped pseudo-spectral acceleration (PSA) for a period range of 0.01 sec to 10 sec (frequencies ranging 0.1 to 100 Hz). Therefore, the current study focused on evaluating the impact of the different regions on these ground motion measures, regardless of the specific geologic or tectonic differences the geophysical data may suggest. Chapters 3 and 4 describe the project methodology and computational products, and Chapters 5 and 6 present the results for two complementary simulation approaches, leading to a global conclusion in Chapter 7.

As was done in the EPRI [1993] study, ground motion simulations were conducted to estimate the differences between different parts of the CENA territory. There are several codes available for the calculation of synthetic seismograms using an assumed seismic velocity structure as the input. One interesting aspect of the current study was the use of alternate computational codes and assumptions for completing the simulations. Two computer codes were considered: *FK* developed by Zhu [2012], which assumes a frequency-independent Q, and *hspec96* developed by Herrmann [2013a; 2013b], which allows a frequency-dependent Q formulation. Chapter 3 provides the background for the attenuation models used in each region, lists the simulation parameters, and describes the project scope in terms of frequency, hypocentral depths, and distance ranges covered.

The PSA was then computed from the various time series for a range of oscillator frequencies. Differences in PSA as a function of hypocentral depth, distance from the epicenter, and frequency dependency were examined, both within a given region and between different regions.

The extracted "typical" velocity structure (representative profile) for each crustal region cannot be assumed without considering the uncertainty of layer boundary depths and layer velocities. Therefore, an important task was to evaluate the profile relative to the existing variability for the region. This was performed based on the statistics of the available profiles and ground motion analyses from simulations using these profiles. The CNA region was selected to assess the sensitivity of ground motions to changes in layer depths and velocities. Because the CNA region has a variety of crustal seismic velocity structures, it can be used to quantify the impact of profile variability on ground motion variability within a region.

The representative model of CNA, also referred to as the "base model," was compared with eighteen modifications (i.e., 18 alternative crustal velocity structures with respect to the base region). The calculation of the standard deviation of PSA for all eighteen alternatives was used to gain a first impression of the range of differences of the ground motions for CNA; this minimized the output to less than a handful of illustrations. To produce comparisons more detailed, this study focused on the statistical distribution of PSA values within specific frequency and distance bands.

Finally, differences in ground motions for each region were quantified and used to combine the regions into different attenuation groups with specific attenuation properties.

3 Selection of Input Parameters for Ground Motion Simulations

Synthetic acceleration time series and 5%-damped PSA were calculated at periods between 0.05 sec and 2 sec using waveform modeling. This chapter provides the documentation of the selected input parameters for those simulations. Sections 3.1–3.3 describe the general propagation input parameters for the different regions. Sections 3.4–3.8 explain modeling choices made to (1) address global differences in ground motions and to (2) accommodate the two different simulation codes used in the study: Zhu [2012] (assumes a frequency independent *Q*) and *hspec96* [Herrmann 2013a; 2013b], which allows a frequency-dependent *Q* formulation.

The following offers a summary of the selected parameters and provides the organization of the chapter (Sections 3.1–3.10):

Regionalization (crustal seismic parameters)		
(3.1)	Regions	Atlantic Coastal Plain, Appalachians, Central North America, Mississippi Embayment
(3.2)	Velocity depth structure	
(3.3)	*Q*-factor model	
Earthquake Parameters		
(3.4)	Focal depths	5, 10, 20, and 30 km
(3.5)	Focal mechanism	pure reverse fault strike / dip / rake = 180° / 45° / 90°
(3.6)	Source time function/ magnitude	shape: triangle, duration: 4 sec/6
Computation Parameters		
(3.7)	Distances to EQ source	1−500 km in log10 spaced steps (number 60)
(3.8)	Azimuth of stations	90°
(3.9)	Frequencies of interest	0.5–1 Hz, 5–10 Hz
(3.10)	Additional parameters	
	components	vertical, radial, transverse (z, r, t)
	no. of samples	$nt = 8192$
	sampling interval of time	$dt = 0.02$ sec
	sampling interval of wave number	$dk = 0.2$

3.1 REGIONALIZATION

3.1.1 Initial Selection of Regions

The study area is the Central and Eastern part of the North American continent (CENA), which has been subdivided into four regions on the basis of their unique geologic and tectonic settings; see Figure 3.1. The four sub-regions are:

1. Atlantic Coastal Plain (ACP)
2. Appalachians (APP)
3. Central North America (CNA)
4. Gulf Coastal Region/ Mississippi Embayment (MEM)

The western boundary of the ACP region is defined by an increase in elevation and the exposure of the rocks associated with the Appalachian Mountains. The western boundary of the Appalachians is defined in Canada by the exposure of older Grenville Province rocks, and in the U.S. by the flat topography of the continental interior. The western boundary of the CNA region is defined by the high topography of the Rocky Mountains. The northern boundary of the MEM region is defined by limit of surficial Quaternary and Tertiary sediments.

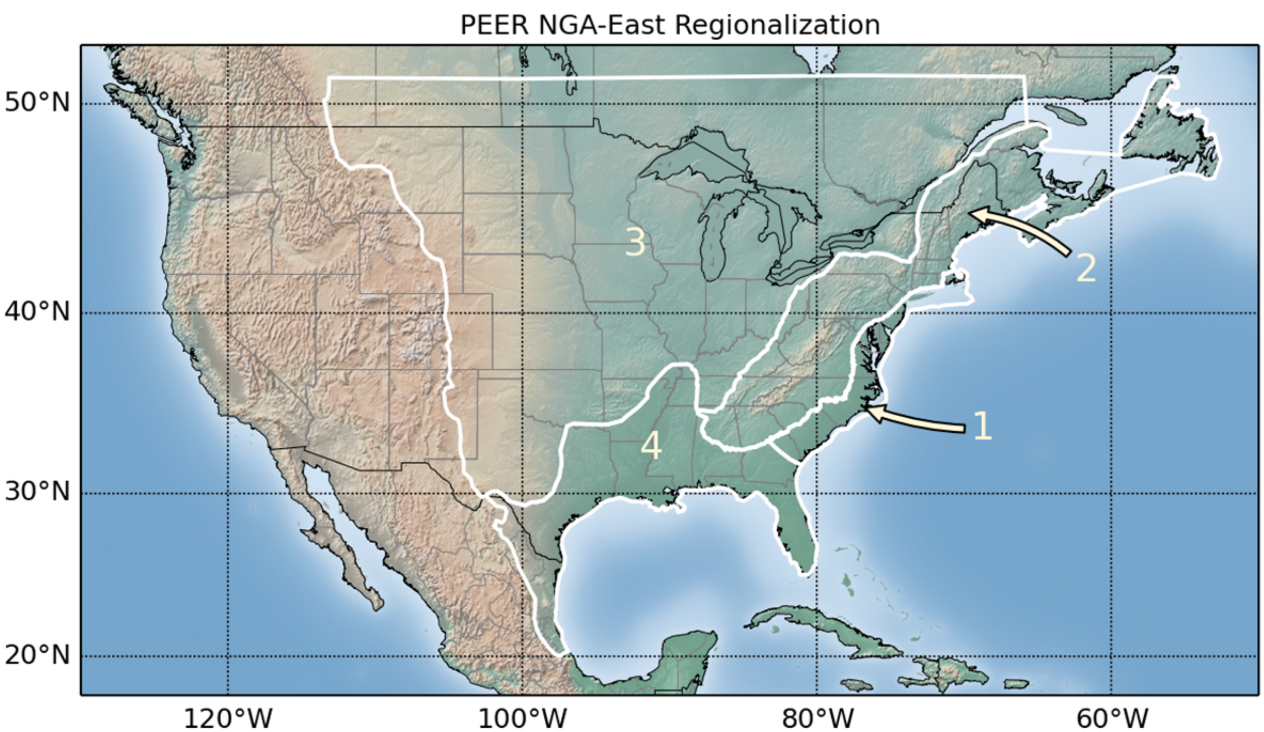

Figure 3.1 **Regionalization of four crustal provinces used in this study for the NGA-East project: the Atlantic Coastal Plain, the Appalachians, Central North America, and the Mississippi Embayment/Gulf Coast Province.**

A concise characterization of the North American continent was made by Baqer and Mitchell [1998], who summarized the region between the Atlantic Coast and the Rocky Mountains as being a large, relatively stable, province consisting of several units, including the Appalachian Mountains, the Central Lowlands, the Great Plains, and the Atlantic and Gulf Coastal Plains. Most of the sediments that cover this region are of Paleozoic and Mesozoic age, while younger sediments are mainly restricted to river valleys and glacial deposits. Precambrian basement crops out in a few places, including the central and southern Appalachians. Most of this large region has been stable since the Paleozoic, but the Atlantic and Gulf coastal regions underwent extensional deformation when the North American plate separated from the African plate during Jurassic time. The Appalachian is an orogen that developed along the eastern and southern continental margins of North America during the Paleozoic era [Baqer and Mitchell 1998].

3.1.2 Justification for Selection of Regions

The Gulf Coast is comprised of vast amounts of Mesozoic and younger sediments that overlay early Mesozoic to Middle Paleozoic units. The Gulf is the depository of the sediments coming from a wide region bounded by the eastern Rocky Mountains on the west and the Appalachian Mountains on the east. As more and more sediments are deposited along the Gulf Coast, the crust continues to subside, resulting in a particularly thick accumulation of sediments. Onshore the basin has a maximum fill of 7 km of sediment; the thickness is even greater (14–16 km) offshore [Buffler and Thomas 1994]. All of these sediments are relatively young and loosely cemented and, consequently, are distinct from crystalline rocks in term of their lower density, seismic *P*- and *S*-wave velocities, and *Q*-factor. Within the sedimentary deposits there is a layer of Jurassic salts, which are rheologically soft, and readily deform as the stress field changes. The Gulf Coast salt domes are the results of the inherent plasticity of these salts and other evaporite minerals, which causes them to intrude into overlying layers in the form of diapirs.

The Gulf Coast, as defined here, includes the Mississippi Embayment, an area that extends north from the Gulf Coast into the interior of North America along the Mississippi river. It is included because, like the rest of the Gulf Coast, it is an area dominated by the deposition of young sediments, particularly coming from the Mississippi River. This region, referred to as MEM in the current report, has experienced at least three episodes of significant tectonic activity [Buffler and Thomas 1994]. The first recorded evidence of tectonic activity was crustal rifting at ca. 550 Ma associated with the breakup of an ancient super-continent called Rodinia. The next tectonic event took place during the late Paleozoic formation of a younger super-continent, Pangaea. This resulted in North-South compression in southern North America, including the Mississippi Embayment and the Ouachita Mountains, and Northwest–Southeast compression in the east along the Appalachian orogeny. Finally, eastern and southern North America experienced rifting during the Mesozoic associated with the breakup of Pangaea and the formation of the Atlantic Ocean [Buffler and Thomas 1994]. The New Madrid Seismic Zone is presently active within the Mississippi Embayment. The zone trends approximately northeast-southwest and is located along the border of Tennessee and Arkansas. This is one of the main regions in central and eastern North America that has seen significant seismic activity in historical times. Due to the thick sedimentary strata, the Gulf Coast is expected to have a very high rate of attenuation of seismic waves traveling through the province.

The ACP region is characterized by relatively young (Mesozoic and younger) sediment that has been shed from the Blue Ridge and Appalachian Mountains and has been deposited on the passive continental margin. The basement of the APC shows evidence of rifting. However, this deformation does not extend into the sediments that make up much of the upper crust. The coastal plain overlies predominantly Paleozoic rocks similar to those exposed farther west in the Appalachian Province. The ACP region contains failed rift basins in places that are remnants of regional-scale extension during the early Mesozoic. These rift basins were formed during the breakup of Pangaea that led to the formation of the modern Atlantic Ocean. Like the Gulf Coast, the ACP is composed of relatively young sediments that exhibit relatively low seismic velocities as compared to the crystalline crust. However, since the rate of deposition is lower owing to the smaller source area, the sediment cover is not nearly as thick as on the Gulf Coast. Also, the Atlantic Coastal plain does not have salt diapirs, which are found throughout the Gulf Coast. All of these factors suggest that while the Atlantic Coastal Plain will have relatively high attenuation, it will be lower than that of the Gulf Coast.

The Continental Interior is the region between the Rocky Mountains to the west and the Appalachian Plateau to the east. It extends from the northern boundary of the Gulf Coast into Canada. Like the rest of eastern North America, the Continental Interior has been stable and tectonically inactive since the middle-to-late Paleozoic—in some areas even longer. However, there are local regions of seismic activity within the Continental Interior. Unlike the two coastal provinces discussed earlier, there is no thick young sediment overlying much of the Continental Interior. The province is dominated by Paleozoic age sediments that in some areas have been eroded away to expose older underlying Proterozoic age strata. The Continental Interior is dominated by large regional scale structural domes and basins but is otherwise relatively un-deformed. Because of the cold and competent nature of the crust in this region the North American interior province has a low seismic attenuation.

The APP region consists of predominately Paleozoic strata located between the ACP and the Continental Interior. The border between the ACP and the APP region in the east is marked by what is known as the fall line. Historically, this is a geographic boundary that marked the farthest up river boats could travel from the coast before reaching waterfalls and impassible water. This geographic boundary, which is the result of an underlying geologic boundary, forms the basis for the boundary between provinces. At the contact between the two provinces, there is a transition from the young coastal plain sediment to the underlying Paleozoic and Proterozoic sediment. The older Appalachian sediments are harder and much more resistant, resulting in very hilly topography.

The Appalachian Province includes the Piedmont, Blue Ridge, Valley and Ridge, and Appalachian Plateau physiographic provinces along the central east coast of North America. This province and the geologic structures within it are characterized by a consistent northeast-southeast trend and extend from the eastern coast of Canada to Alabama in the southwest. Its history is one of repeated Wilson Cycles. Parts of the Piedmont exhibit evidence for the formation and subsequent rifting of Rodinia in the Early Paleozoic, followed by the Appalachian Orogeny in the Late Paleozoic, which formed Pangaea [Hatcher 1989]. Perpendicular to the long axis mentioned earlier, deformation decreases from east to west as the distance from the collisional centers is increased. Some areas of the Piedmont contain failed rift basins, providing evidence of the rifting of Pangaea during the early Mesozoic [Swanson 1986]. The Appalachian Province has been relatively stable since this rifting. However, there are prominent zones of seismic activity such as the Eastern Tennessee Seismic Zone and the Central Virginia Seismic zone. The preferred explanation is that these areas are zones of stress concentration due to forces transmitted from plate boundaries. Aside from these and several other zones, the Appalachians have been inactive since the Mesozoic and are composed of cold, competent crust. The Appalachian Province therefore has a low attenuation rate, similar to the Continental Interior Province.

3.2 REPRESENTATIVE VELOCITY-DEPTH STRUCTURE

This section provides the documentation for the development of a representative velocity-depth structure for each of the four regions. Because of their large geographic size, it is not a simple task to find one crustal model that is typical for each crustal region. To determine the best representative velocity-depth structure for a region, we rely on the Global Crustal Database (GCD) from the U.S. Geological Survey (USGS). The database contains ~14,000 entries [Mooney 2013]. Each entry refers to a geographical location and a one-dimensional (1D) velocity profile (see following subsection).

3.2.1 Aims and Conditions

- Definition of a representative crustal profile for each crustal region: the crustal velocity profile consists of homogeneous layers, each defined through layer thickness, V_s and V_p. Each model extends from Earth's surface to the Moho.
- Simple "average" models are not used as they tend to smooth out variations with depth and do not represent plausible profiles.
- The top of the seismic velocity structure for shear waves is constrained to a value near V_s = 3 km/sec in order to be consistent with the reference rock condition selected for CENA. This means that only the crystalline crust was considered to the exclusion of overlying sedimentary layers.

3.2.2 Global Crustal Database

As part of the NGA-East Project, the USGS has compiled crustal velocity information from the published literature. The USGS crustal structure database contains information for both *P*- and *S*-waves [Mooney 2013].

Figure 3.2(a) shows the locations of available information in the USGS crustal structure database. Each point signifies a 1D seismic velocity-depth function. Large amounts of continental data are available within North America, Europe, the eastern regions of Asia (e.g., Japan and China), and the western regions of South America. The majority of offshore data are located on the East Coast of North America (the greater North Atlantic region, including the Gulf of Mexico and the Caribbean Sea), the East Coast of South America (i.e., the South Atlantic), the region north of Europe (the Norwegian Sea and Barents Sea) and east and south of Asia (Sea of Japan, North Pacific Ocean, East China Sea, Bay of Bengal, and Java Sea). A special effort was made to compile a large amount of data in North America as part of the NGA-project, and our results focus on the data for CENA.

The crustal seismic velocity structure within the entire crust is documented by 7943 (or 57%) of the available profiles, whereas 5896 profiles or 43% provide only the crustal seismic velocities within the upper crust. The latter profiles reach maximum depths of 10 km. There are 13,112 (95%) entries that provide a 1D *P*-wave seismic velocity structure and 2316 (17%) entries that contain a 1D *S*-wave seismic velocity structure. The total number of entries is 13,839.

Figure 3.2(b) shows the North American continent and the locations of crustal seismic velocity-depth profiles. A total of 3350 profiles are located in the area shown; 3164 (94%) provide *P*-wave velocities and 596 (18%) provide *S*-wave velocities. One thousand nine hundred and thirty-five (or 58%) of all profiles document a whole crustal structure; and 1415 profiles (or 42%) define only the shallow (maximum depth, 10 km) crustal structure. Shallow crustal profiles can be found offshore (representing oceanic crustal structure) or close to or within coast regions (representing continental shelves). Onshore shallow crustal models are mostly associated with rivers or lakes (sedimentary basins). There are 1447 profiles within the outlines of our four regions within CENA.

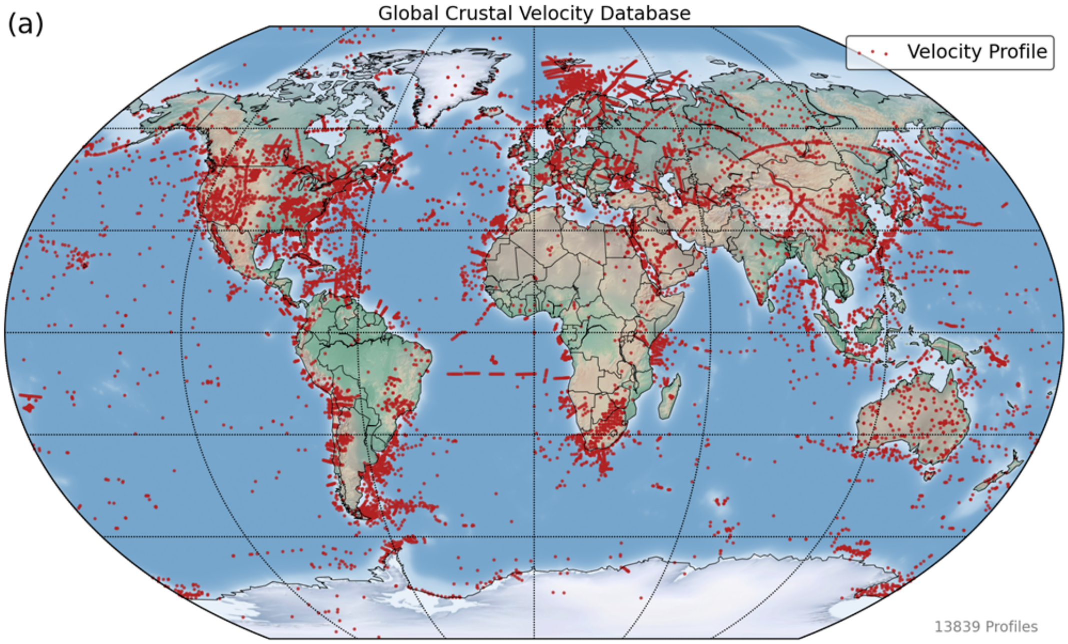

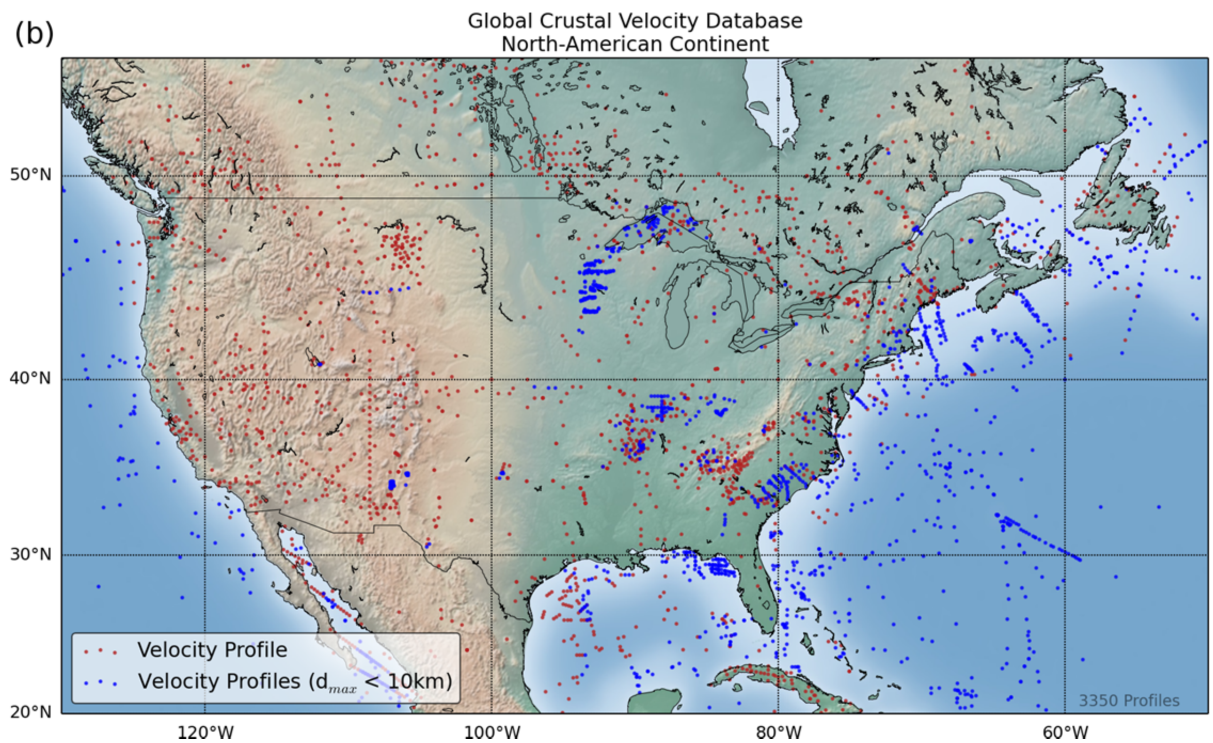

Figure 3.2 **Locations of compiled 1D seismic velocity-depth profiles with the USGS database: (a) Global data and (b) North American data. Locations are sub-divided into whole crustal models (red) versus shallow (≤ 10 km) crustal profiles (blue).**

3.2.3 The Database Entries

Each seismic velocity-depth function is specified by its unique latitude and longitude, and consists of the measured subsurface Earth layers at that location, identified by compressional wave velocity, optional shear wave velocity, thickness, and depth (see example in box above). Each entry also includes other information, such as elevation, geologic province, age of last significant thermo-tectonic activity, and the principal seismic methodology that determined the velocity-depth function. For a complete description, see the example given in Appendix B.

1	23.70N	3.00	.00	.80	.00	s	39.15	2.20	.00	NAC–ME	5 U
	103.95W	4.95	.00	3.40	.80	s	43.35	MCz	142.00	61M.1	ORO
		6.01	.00	28.46	4.20						
		7.63	.00	10.69	32.66						
		8.38	.00	.00	43.35	m					
2	29.76N	2.30	.00	2.00	.00	s	25.70	.10	.00	NAC–CO	5 U
	96.31W	3.94	.00	5.30	2.00	s	33.00	MCz	39.00	61C.3	EXC
		5.38	.00	12.50	7.30	c					
		6.92	.00	13.20	19.80	c					
		8.18	.00	.00	33.00	m					
3	34.35N	3.00	.00	3.00	.00	s	35.00	1.60	.00	NAC–BR	4 R
	117.83W	6.30	.00	16.50	3.00		38.00	MCz	55.00	63R.1	ORO
		7.00	.00	18.50	19.50						
		7.80	.00	.00	38.00	m					
4	33.75N	5.68	.00	11.30	.00		43.90	.70	.00	NAC–PB	3 U
	117.00W	7.18	.00	32.60	11.30		43.90	MCz	115.00	61S.1	ORO
		8.10	.00	.00	43.90	m					

The database is an ASCII-formatted computer file that can: (1) be manipulated to extract specific seismic information (e.g., the crustal thickness at a particular location in CENA); (2) be used to calculate other specific seismic properties (e.g., the average crustal compressional wave velocity at a particular location in CENA); or (3) be used to construct maps and perform statistical analysis of such information and properties.

The compilation covers the region between about 20° and 55° N and about 60° and 115° W and contained 1491 entries by the end of 2011. An additional 1112 entries were added during the course of this NGA-East project during 2012 [Mooney 2013]. This represents a 75% increase in the number of velocity-depth functions for the CENA region.

The data sources for the compilation consist mainly of peer-reviewed articles dating from 1938 through 2012. The entries are derived from all types of methods for determining seismic crustal structure, including refraction surveys, reflection surveys, surface wave dispersion, seismic tomography, and receiver functions. Of these, the majority are from active-source seismic refraction surveys. Entry selection criteria are described in Chulick [1997]. To identify the data to be included, a very extensive literature search was undertaken to track down as many seismic survey publications as possible. A large number of these publications have been carefully scrutinized, with the appropriate data for the CENA database having been extracted.

The map of the thickness of the crust under CENA and the adjacent ocean basins (Figure 3.3) was constructed from the 1570 Moho depth points. The resultant map illustrates the following crustal features: (1) the definition of the continental margins at the edge of the continental slope along the Atlantic and Gulf Coasts; (2) the thick continental crust under the southern Appalachian Mountains, under the Rocky Mountains, the Mid-Continental Rift under Lake Superior, and under portions of the Great Plains; and (3) the thin crust underneath the Rio Grande Rift, the MEM region, and portions of the ACP.

The accuracy of contour maps is directly related to the uncertainties in the published interpretations of crustal structure. Useful reviews of the methods used (and uncertainties) to determine the structure of the crust and sub-crustal lithosphere are provided by Mooney [1989] and Bostock [1999]. The uncertainties in crustal models arise from factors such as the survey method, the analysis technique, and the spatial resolution of the survey (i.e., the spacing of shot points and recording stations). Typically, the uncertainty in the calculated depth to the Moho is approximately 5–10%. Thus, a reported crustal thickness of 40 km has an uncertainty of ± 2–4 km. Seismic velocities determined from refracted first-arrivals (e.g., P_n) are typically accurate to within a few hundredths of km/sec [Mooney 1989; Chulick 1997].

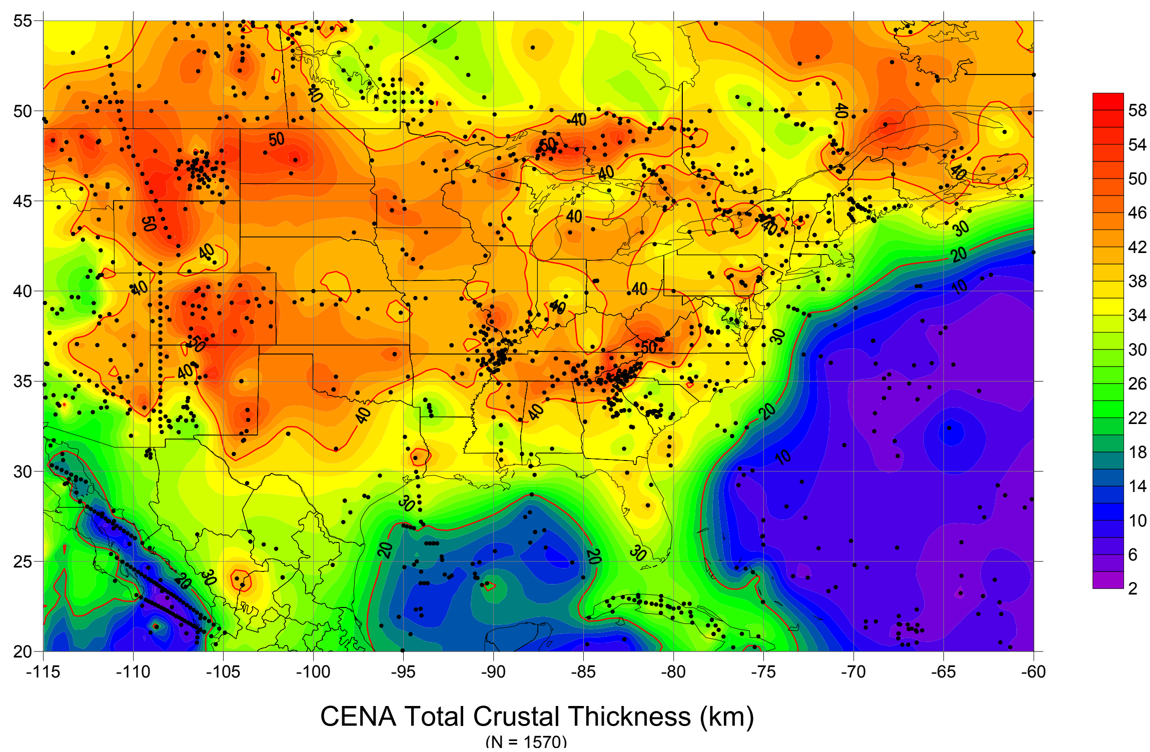

Figure 3.3 **Crustal thickness for the Central and Eastern North American region extracted from 1570 crustal velocity-depth profiles (data compilation as of January 2013).**

3.2.4 Data Evaluation for Extracting a Representative Velocity Structure

To define a representative velocity structure, additional constraints on data quality are necessary. Each region contains between about 130 and 900 crustal seismic velocity-depth profiles. However, not every profile is suited to our needs, either because it consists of a single crustal layer, or it does not provide deep crustal information. The statistical analyses used to find a representative velocity structure for each region are based on the compressional-wave seismic velocity (V_p) because more than 90% of the database entries provide the compressional wave velocity, while only 18% offer a shear wave velocity. To obtain V_s, we assumed a V_p/V_s of 1.73. Our final model's depths and seismic velocities have one decimal place; to give more than one decimal place would imply a higher resolution than can be extracted.

To obtain a representative profile for each of the four distinct regions, the selected crustal velocity profiles were evaluated using the cumulative occurrence of V_p and the *P*-wave velocity two-dimensional (2D) histograms. Additional literature (e.g., Pakiser and Mooney [1989]) were consulted as needed. Table 3.1 summarizes the number of profiles with and without sufficient information.

Minimum of two layers: One-layer seismic structures that provide just a Moho depth and not the crustal seismic velocity-depth structure were excluded. A one-layer crustal model is not a realistic representation of the Earth's crust.

Minimum depth of 20 km: Studies that investigated oceanic crust or only the shallow structure of continental sedimentary basins were excluded. The seismic velocity-depth profile should extend to a depth of at least 20 km.

Table 3.1 Summary of crustal velocity-profiles for each of the four regions, indicating all available profiles and those profiles selected for further analyses).

Region	Number of profiles (all)	Number of profiles selected for further analysis
Atlantic Coastal Plain	138	32
Appalachians	348	194
Central North America	857	417
Gulf Coastal Region/ Mississippi Embayment	104	86

The cumulative occurrence of V_p (e.g., Figure 3.6) gives information about how often *P*-wave velocities occur, regardless of their depth. Each velocity profile originally consists of a number of velocity values congruent with the number of layers. Instead of weighting a layer velocity with its layer thickness, the profile was re-sampled to get a sample of velocity every 100 m. A profile with a length of 30 km therefore has 301 samples. The thicker a crustal layer is, the more samples of its velocity are available. The absolute cumulative occurrences of a velocity were extracted analyzing the span of velocities with a 0.1 km/sec interval. Most of the *P*-wave velocities lie between 5.5 and 8.5 km/sec. Peaks at specific velocity ranges (e.g., 6.0–6.1 km/sec) imply that these velocities occur often throughout all of the analyzed profiles or that they form thick layers in the crust at less profiles (probably a combination of both). In the analyses of cumulative V_p occurrences; the lower interval boundary of the velocity is provided (e.g., 6.0 km/sec) instead of the velocity range (e.g., 6.0–6.1 km/sec).

3.2.5 Atlantic Coastal Plain

The ACP covers the smallest area of the four regions and has the fewest seismic velocity models that fulfill our requirements. Of the 32 profiles shown in Figure 3.4, most of them are located in the southern part of the region.

The thirty-two selected *P*-wave velocity profiles are depicted in Figure 3.5(a), displaying velocity versus depth (black lines). The red line indicates the representative profile obtained from the analysis of the cumulative occurrences of V_p (Figure 3.6) and the *P*-wave velocity 2D histogram [Figure 3.5(b)]. Two-dimensional *P*-wave velocity histograms show how often *P*-wave velocities occur as a function of depth. The crustal velocity structures were binned every 2 km of depth and every 0.1 km/sec of velocity. The color bar represents the number of profiles occurring within a bin, whereby blue colored fields mean no or low occurrence and red mean high occurrence. Two lines are displayed: the continuous white line represents the mode or the maximum occurrence of *P*-wave seismic velocities, and the dashed white line shows the extracted representative model for the region, based on the mode and the cumulative occurrence of V_p values.

Relatively high cumulative occurrences of *P*-wave velocities are at evident at 6.0, 6.1, and 6.7 km/sec. The upper mantle velocity peak is at 8.1 km/sec. The *P*-wave velocity 2D histogram reveals our approximation of the representative crustal structure of the ACP, which is a two-layer velocity structure with an upper crustal thickness of 20.5 km and V_p of 6.0 km/sec, and a lower crustal thickness of 15.5 km and V_p of 6.7 km/sec. The representative model places the Moho at 36 km depth and indicates upper mantle velocity of 8.1 km/sec.

There have been relatively few crustal seismic investigations within the ACP; only 32 profiles were appropriate after applying our quality-control constraints. Nevertheless, we decided not to loosen the constraints for this region. An upper crustal velocity of 6.0 km/sec is evident: the histogram (Figure 3.6) shows a slightly higher peak at a velocity of 6.0 km/sec, and, most importantly, we avoid a reversal of velocity at depths between 12 and 21 km.

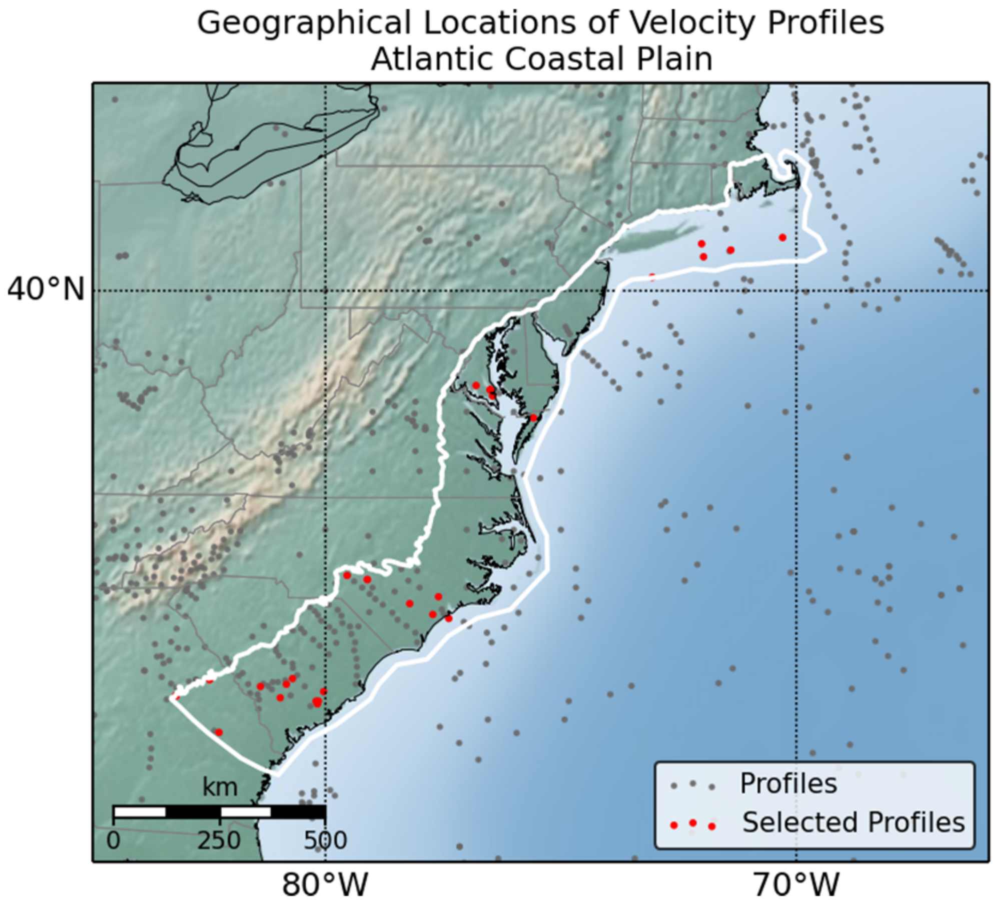

Figure 3.4 **Location map of selected 1D seismic velocity-depth profiles within the ACP. Red dots mark the available profiles that satisfy data requirements.**

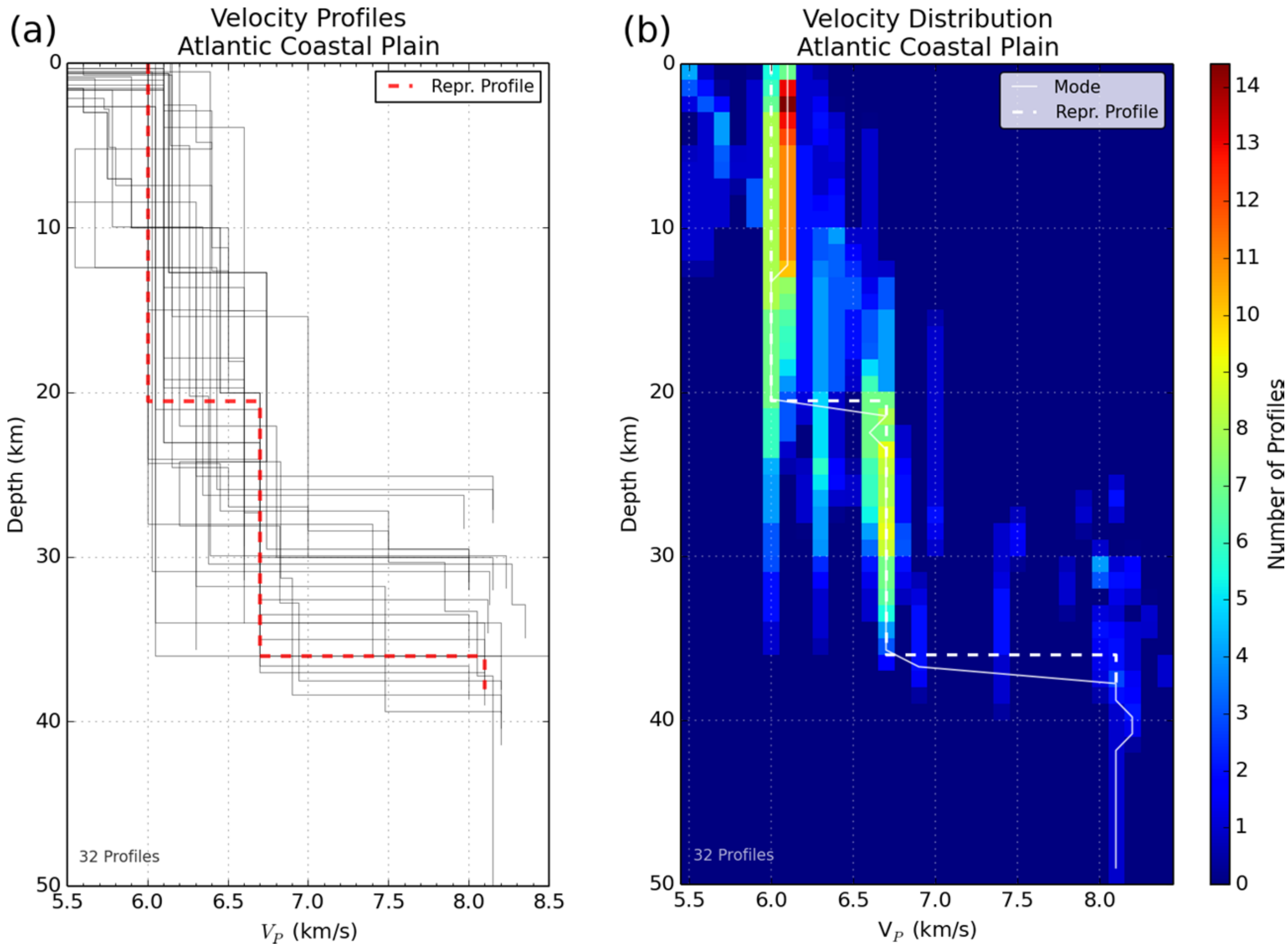

Figure 3.5 Crustal velocity structure within the ACP. These 32 profiles satisfy quality-control requirements: (a) ***P***-wave velocity profiles as black lines and their representative model as red line; and (b) ***P***-wave velocity 2D histogram. Data are binned within a 2 km depth step and 0.1 V_p step. The color bar shows the number of profiles that lie within a bin. The continuous line represents the mode and the dashed line the representative profile.

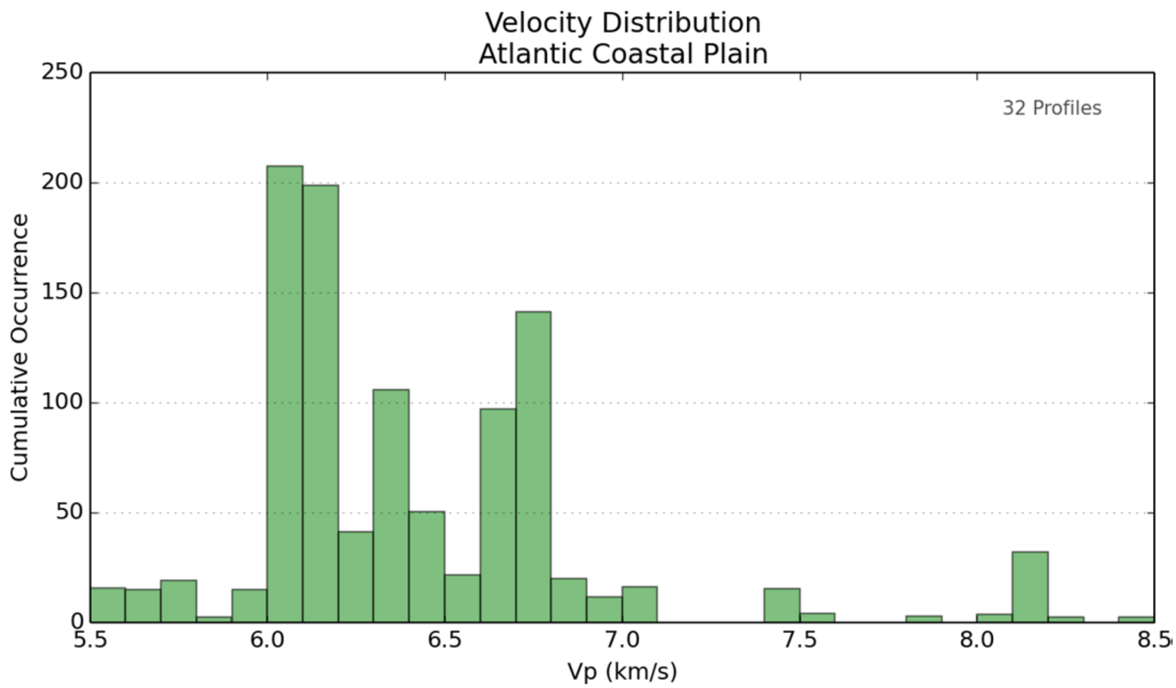

Figure 3.6 **Cumulative occurrence of V_p for the ACP. Data are binned every 0.1 km/sec. Peaks can be seen at velocities of 6.0, 6.1, 6.3, and 6.7 km/sec, and Moho velocity peak is at 8.1 km/sec.**

3.2.6 Appalachians

The APP region is represented by 194 profiles (Figure 3.7) that fulfill the data quality-control requirements described above. The many of the profiles are located in the southern part of the orogen.

The selected *P*-wave velocity-depth profiles are illustrated in Figure 3.8(a), displaying velocity versus depth (black lines). The red line indicates the representative profile, which was concluded analyzing the cumulative occurrences of V_p (Figure 3.9) and the *P*-wave velocity 2D histogram [Figure 3.8(b)]. High cumulative occurrences of *P*-wave velocities are at 6.0, 6.1, 6.3, 6.5, and 6.7 km/sec. The upper mantle velocity peak is at 8.1 km/sec. The *P*-wave velocity histogram indicates that the Appalachian crustal structure consists of three layers with seismic velocities of 6.1, 6.4, and 6.7 km/sec. The Moho is at 37 km depth, and the upper mantle velocity is 8.1 km/sec.

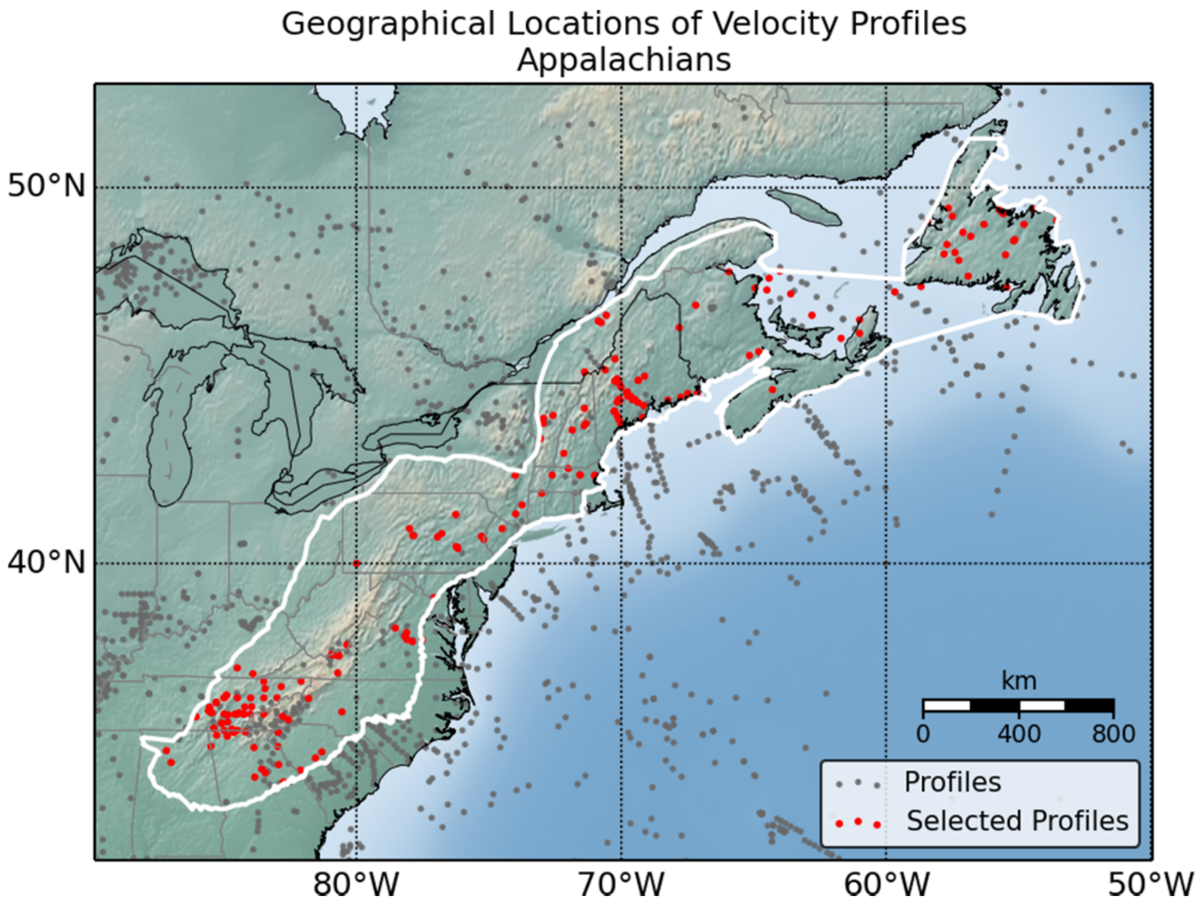

Figure 3.7 **Location map of selected 1D-velocity profiles within the APP region. Red dots mark the available profiles that match the constraints.**

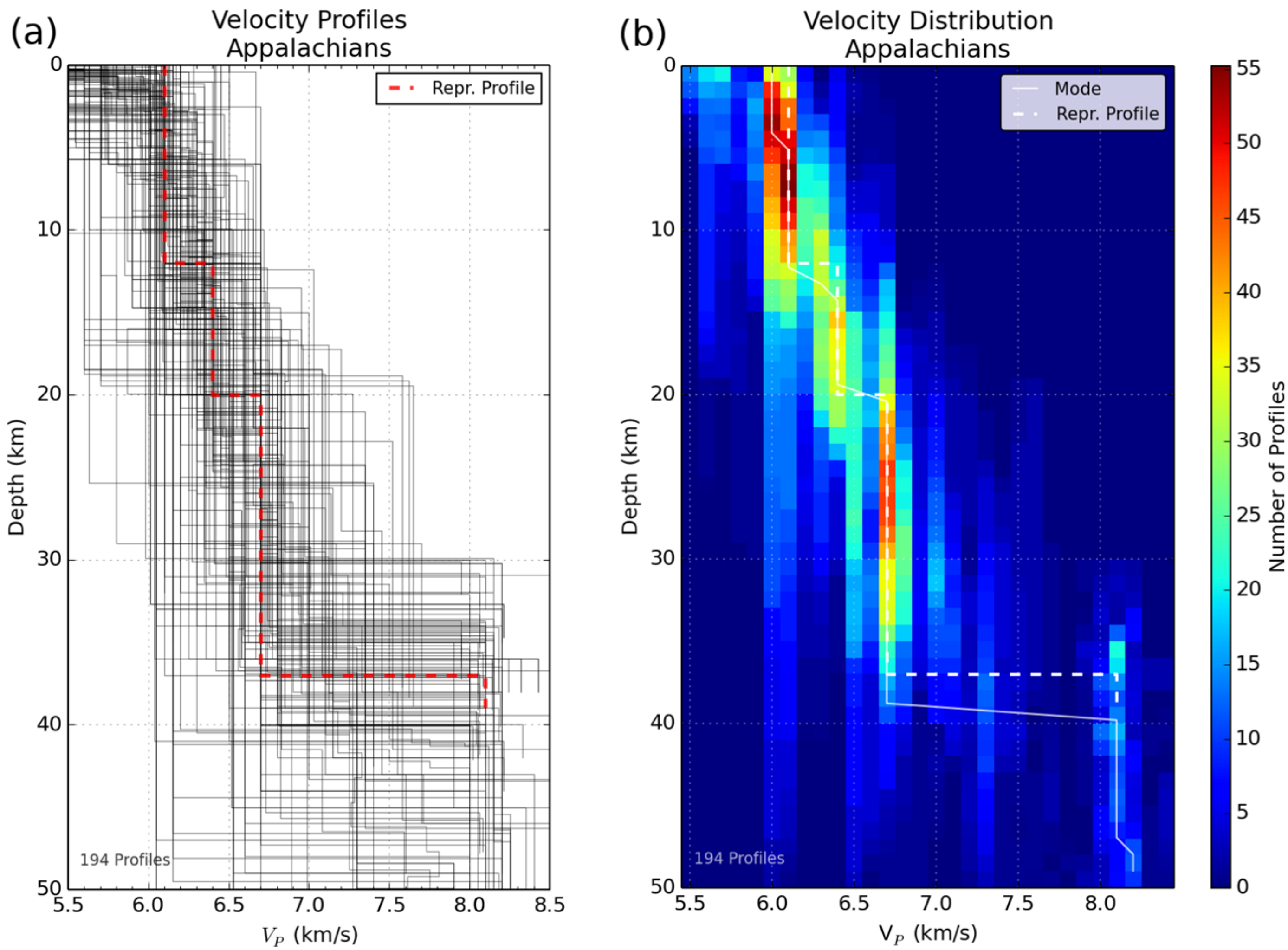

Figure 3.8 **Crustal velocity structure within the APP region. These 194 profiles satisfy quality-control requirements: (a) Illustrated are *P*-wave velocity profiles as black lines and their representative model as red line. (b) *P*-wave velocity 2D histogram. Data are binned within a 2 km depth step and 0.1 V_p step. The color bar shows the number of profiles that lie within a bin. The continuous line represents the mode and the dashed line the representative profile.**

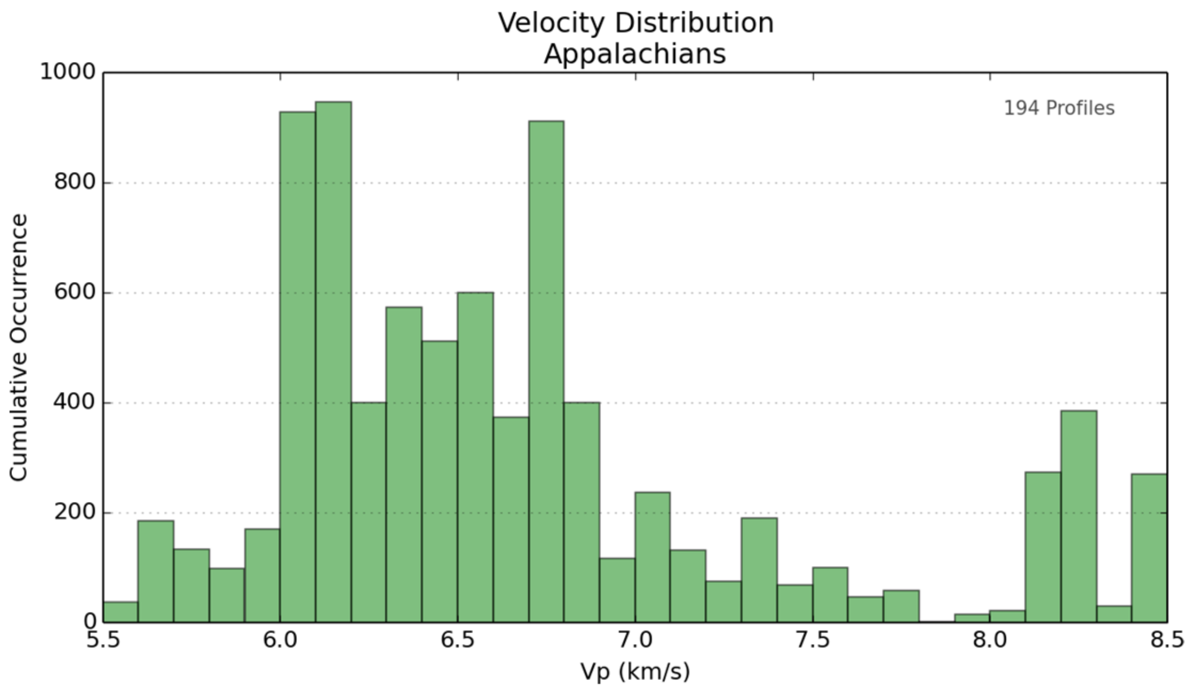

Figure 3.9 **Cumulative occurrence of V_p for the APP region. Data are binned every 0.1 km/sec. Peaks can be seen at velocities of 6.0, 6.1, 6.3, 6.5, and 6.7 km/sec, and Moho velocity peak is at 8.2 km/sec.**

3.2.7 Central North America

The CNA region Central North America covers the largest area and has the largest number of available seismic velocity models. The locations of the 417 1D seismic velocity-depth profiles that satisfy quality-control requirements are shown in Figure 3.10.

The selected *P*-wave seismic velocity-depth profiles are illustrated in Figure 3.11(a), displaying velocity versus depth (black lines). The red line indicates the representative velocity-depth profile, which was determined by analyzing the cumulative occurrences of V_p (Figure 3.12) and the *P*-wave velocity 2D histogram (Figure 3.11(b)]. The velocities between 6.0 and 7.0 km/sec have, in general, a higher occurrence, compared to both the ACP and APP region. High cumulative occurrences of *P*-wave seismic velocities are less obvious for these data. Nevertheless, peaks can be found at velocities of 6.1, 6.5, and 6.7 km/sec. The upper mantle seismic velocity peak is at 8.2 km/sec.

The selected approximation is a four-layer velocity structure with an upper crustal thickness of 12 km and V_p of 6.1 km/sec, a middle crustal thickness of 8 km and V_p of 6.5 km/sec, a medium lower crustal thickness of 14 km and V_p of 6.7 km/sec, and a basal lower crustal thickness of 6 km and V_p of 6.8 km/sec. The Moho is placed at 40 km depth, and the upper mantle velocity is 8.2 km/sec.

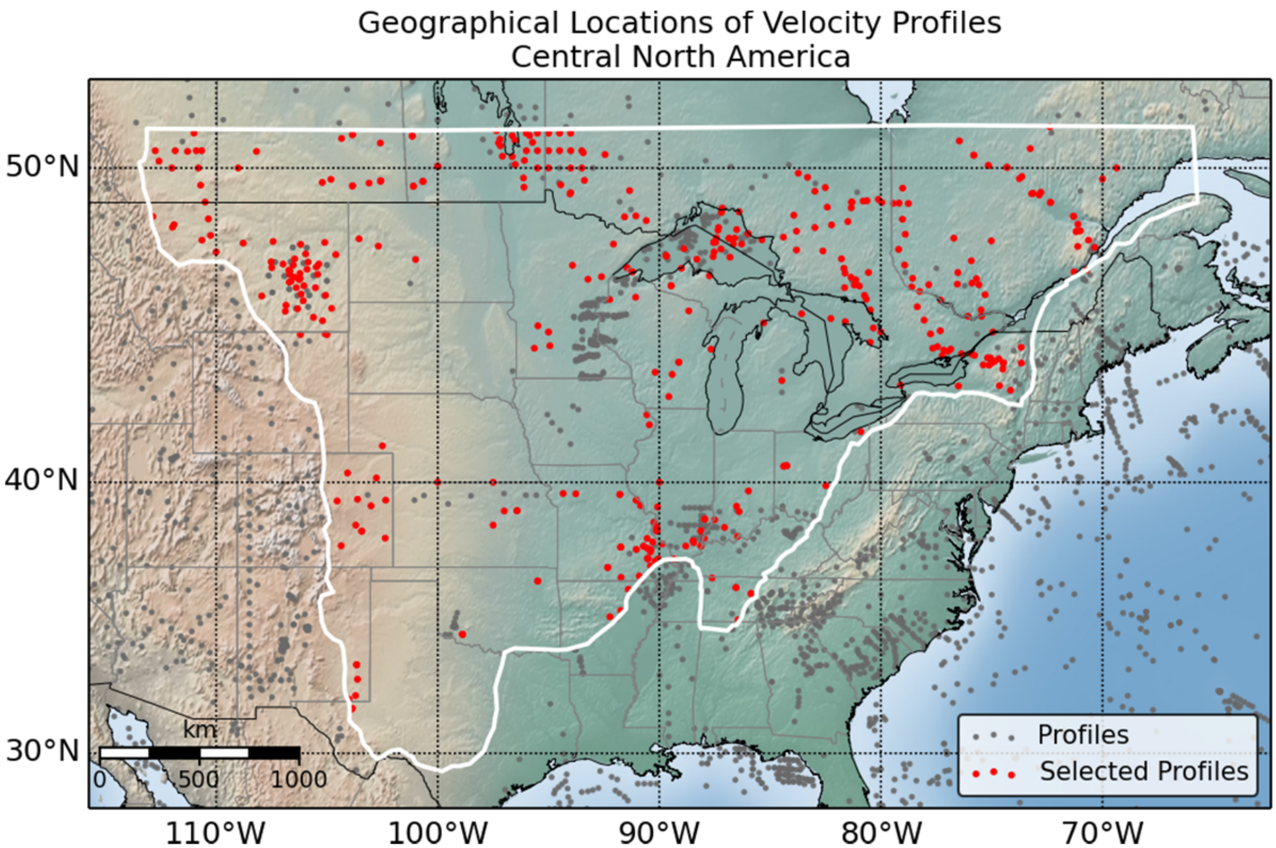

Figure 3.10 **Location map of selected 1D velocity profiles within Central North America. Red dots mark the available profiles that satisfy quality-control requirements.**

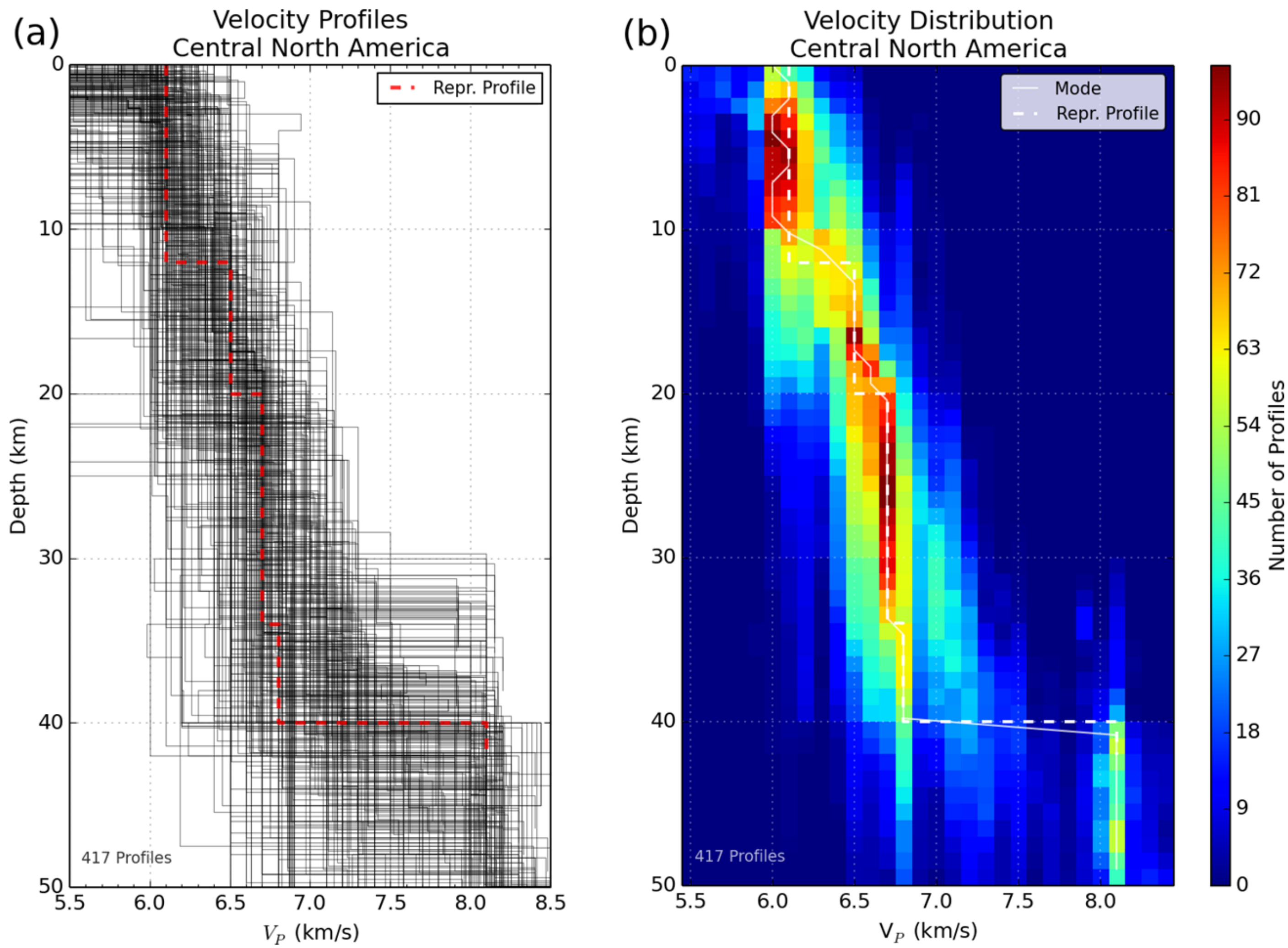

Figure 3.11 **Crustal velocity structure within the CNA region. These 417 profiles satisfy quality-control constraints: (a) Illustrated are *P*-wave velocity profiles as black lines and their representative model as red line; and (b) *P*-wave velocity 2D histogram. Data are binned within a 2 km depth step and 0.1 V_p step. The color bar shows the number of profiles that lie within a bin. The continuous line represents the mode and the dashed line the representative profile.**

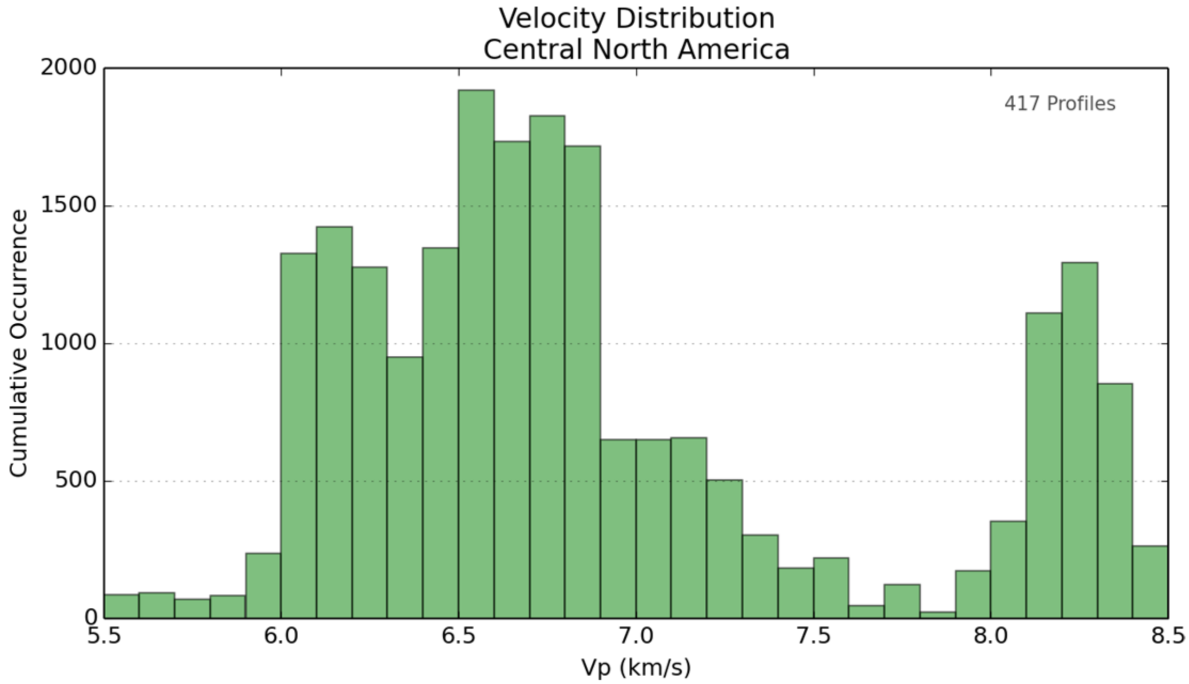

Figure 3.12 Cumulative occurrence of V_p for the CNA region. Data are binned every 0.1 km/sec. Peaks, but not outstanding, can be seen at velocities of 6.1, 6.5, 6.7 km/sec, and Moho velocity peak is at 8.2 km/sec.

3.2.8 Mississippi Embayment/Gulf Coastal Region

The Gulf Coastal Region is represented by 86 profiles that fulfill the quality-control requirements; see Figure 3.13. Many profiles are located within the MEM region and close to the southern border of our CNA region.

The selected *P*-wave seismic velocity profiles are illustrated in Figure 3.14(a), displaying velocity versus depth (as black lines). The red line indicates the representative profile. Figure 3.15 shows the occurrence of V_p for the 86 selected profiles. High cumulative occurrences of *P*-wave velocities appear at velocities of 6.2, 6.6, 6.9, and 7.3 km/sec. The upper mantle velocity peak is at 8.0 km/sec.

The selected approximation is a four-layer velocity structure with an upper crustal thickness and V_p of 4 km and 5.9 km/sec, a medium upper crustal thickness and V_p of 12.5 km and 6.2 km/sec, a middle crustal thickness and V_p of 13.5 km and 6.6 km/sec, and a lower crustal thickness and V_p of 11 km and 7.3 km/sec. The base of the crust is placed at 41 km depth, and the upper mantle velocity is 8.0 km/sec.

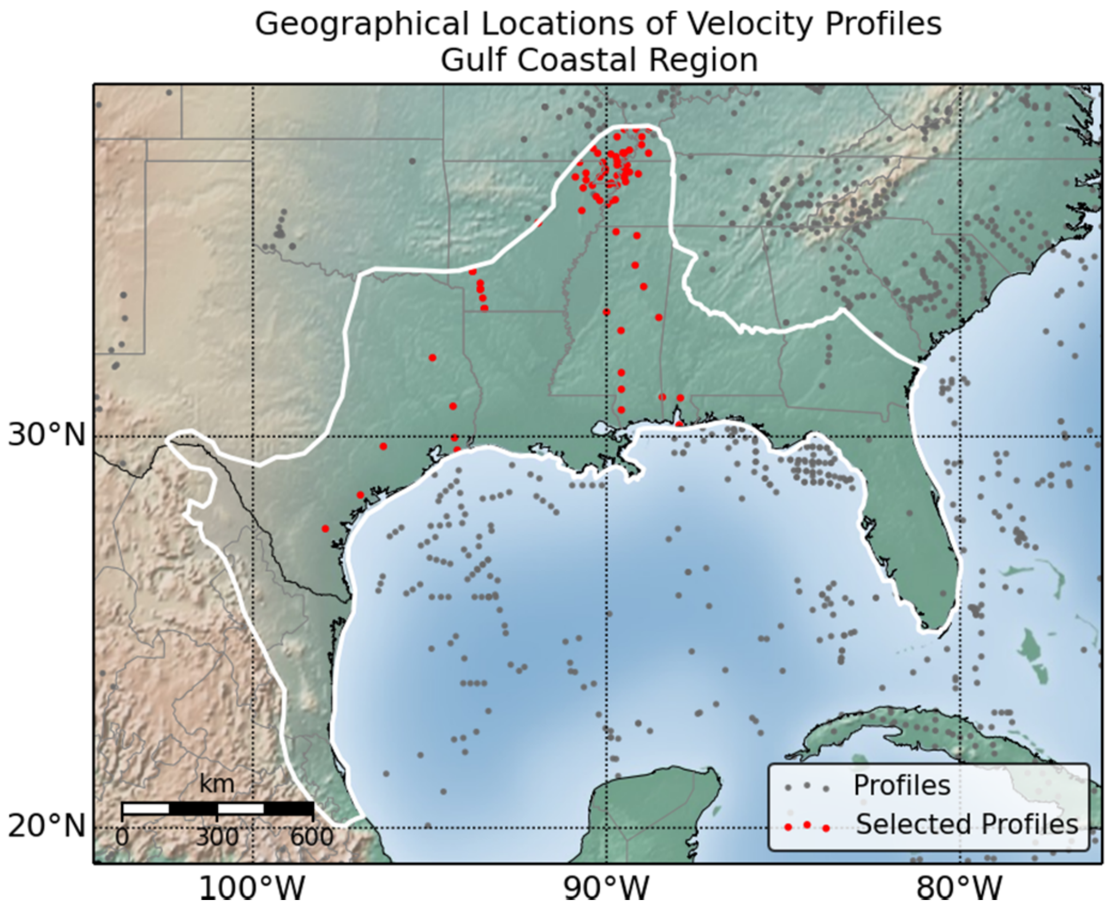

Figure 3.13 **Location map of selected 1D seismic velocity profiles within the Gulf region, which are concentrated within the Mississippi Embayment. Red dots mark the available profiles that satisfy the data requirements**

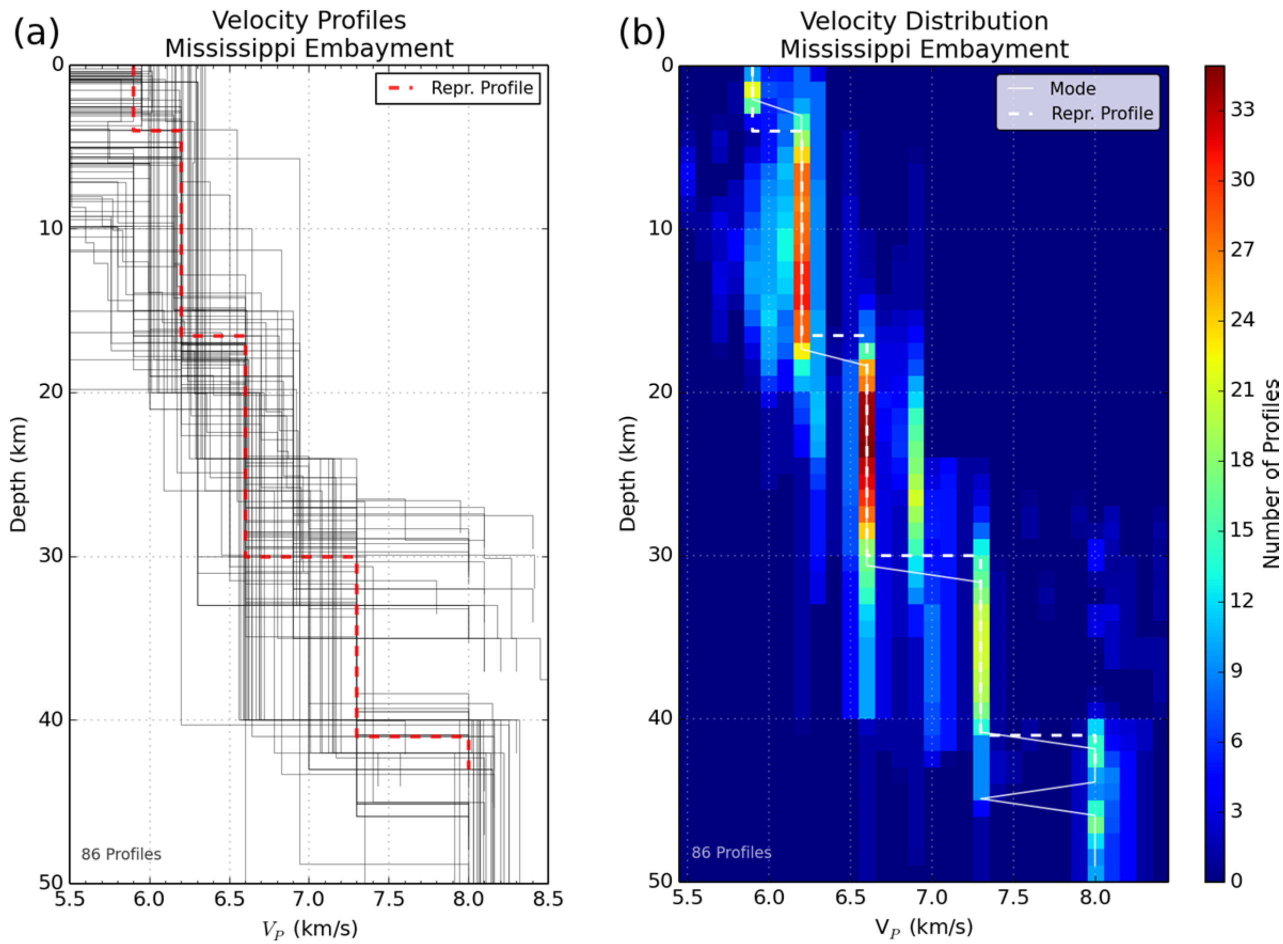

Figure 3.14 **Crustal velocity structure within the MEM region. Most of the 86 available profiles were obtained within the Mississippi Embayment: (a) illustrated are *P*-wave velocity profiles as black lines and the representative velocity model for the MEM region as a red line; and (b) *P*-wave velocity 2D histogram. Data are binned within a 2 km depth step and 0.1 V_p step. The color bar shows the number of profiles that lie within a bin. The continuous line represents the mode and the dashed line the representative profile.**

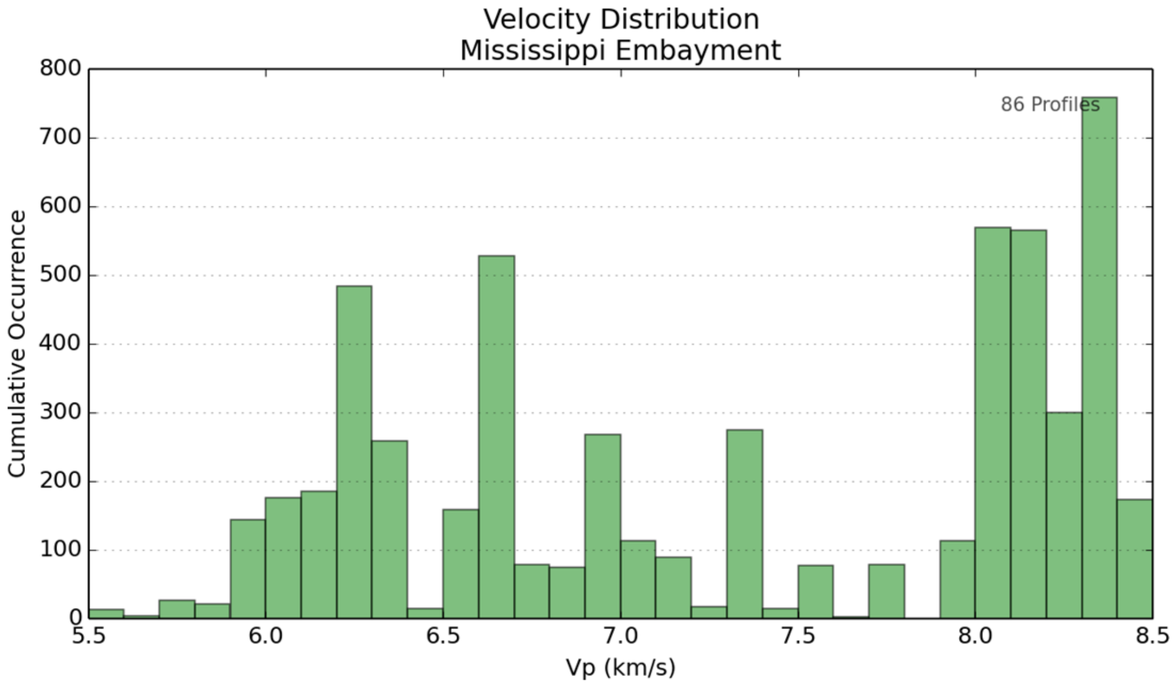

Figure 3.15 Cumulative occurrence of V_p for the Gulf Coastal Region. Data are binned every 0.1 km/sec. Peaks can be seen at velocities of 6.2, 6.6, 6.9, and 7.3 km/sec, and Moho velocity peak is at 8.0 km/sec.

3.3 SUMMARY

3.3.1 Representative Seismic Velocity-Depth Profiles.

The representative seismic velocity-depth profiles for each of the four regions are summarized in Table 3.2, and their shear-wave velocities are illustrated in Figure 3.16. Comparing the representative seismic velocity-depth structures from each of the four regions, a great similarity is apparent between the APP and CNA representative velocity profiles. These velocity profiles have the same layer boundaries at 12 and 20 km, and a very similar seismic velocities in the upper (6.4–6.5 km/sec) and middle (6.7 km/sec) crust. The CNA lower crust consists of two layers with a Moho depth just 3 km deeper than the APP Moho depth.

The ACP and the APP regions also have similar seismic velocity structures. Both show an upper crust with a *P*-wave velocity of 6.0–6.1 km/sec, and the lower crust occupies the depth from 20 km to 36 km with a *P*-wave velocity of 6.7 m/sec. However, the Appalachian orogen region contains a distinct mid-crustal layer with an intermediate (6.4 km/sec) velocity.

The Mississippi Embayment/Gulf Coast representative profile is distinct from that of other regions. It is the only region that contains a high-velocity lower crust (7.3 km/sec). The middle and upper crust velocities for this region are 5.9 km/sec and 6.6 km/sec.

Table 3.2 **Representative seismic velocity-depth profiles of the four regions of interest. V_s was calculated using a V_p/V_s ratio of 1.73.**

Atlantic Coastal Plain			Appalachians			Central North America			Mississippi Embayment		
Depth (km)	V_p (km/sec)	V_s (km/sec)	Depth (km)	V_p (km/sec)	V_s (km/sec)	Depth (km)	V_p (km/sec)	V_s (km/sec)	Depth (km)	V_p (km/sec)	V_s (km/sec)
0.0	6.0	3.46	0.0	6.1	3.52	0.0	6.1	3.52	0.0	5.9	3.41
20.5	6.7	3.87	12	6.4	3.70	12	6.5	3.75	4	6.2	3.58
36	8.1	4.68	20	6.7	3.87	20	6.7	3.87	16.5	6.6	3.81
			37	8.1	4.68	34	6.8	3.93	30	7.3	4.21
						40	8.1	4.68	41	8.0	4.62

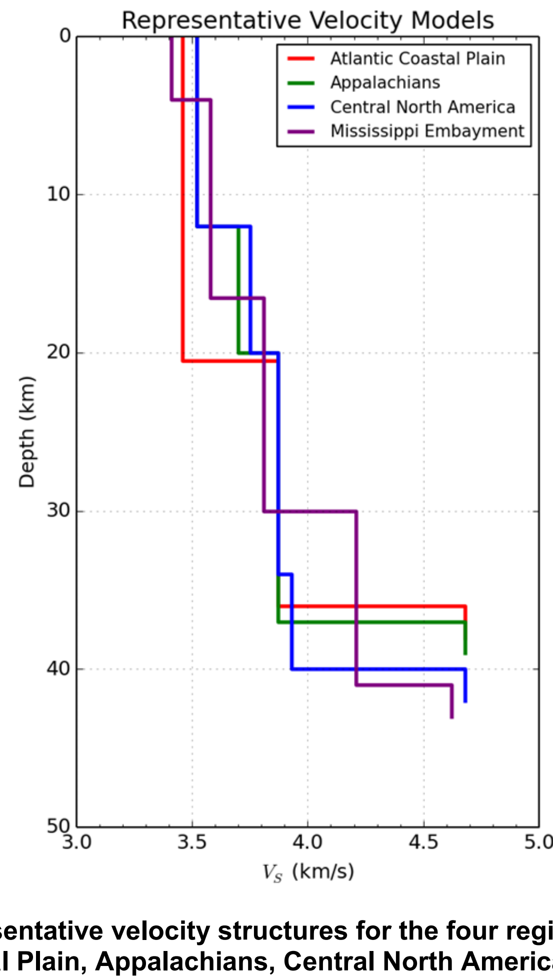

Figure 3.16 **Representative velocity structures for the four regions of interest: Atlantic Coastal Plain, Appalachians, Central North America, and the Mississippi Embayment/Gulf Coastal Region. Illustrated are seismic shear-wave velocities (V_s).**

3.3.2 Uncertainty of Representative Models

Figures 3.5, 3.8, 3.11 and 3.14 show clear variations in crustal structure within each region. To quantify this variability, a sensitivity study was performed (see Section 4.3). Being the largest, the CNA region has the most obvious variability of crustal seismic velocity structure, so its representative structure was chosen as the base model for the sensitivity test. The aim is to make an estimate of how sensitive the ground motions are to variations in layer thicknesses or velocities.

Figure 3.17 offers an overview of the selected crustal profiles for each region underlain in conjunction with all CENA profiles. The CNA and APP regions have the highest number of profiles; the ACP has the lowest. The CNA and APP regions have a similar coverage and wide spread of velocity ranges for the upper, middle, and lower crust. The crustal-velocity structure of the MEM region seems to be more defined. The ACP is too under-sampled to make specific statements, but the 32 profiles available spread over the same wide range as do the CNA and APP profiles.

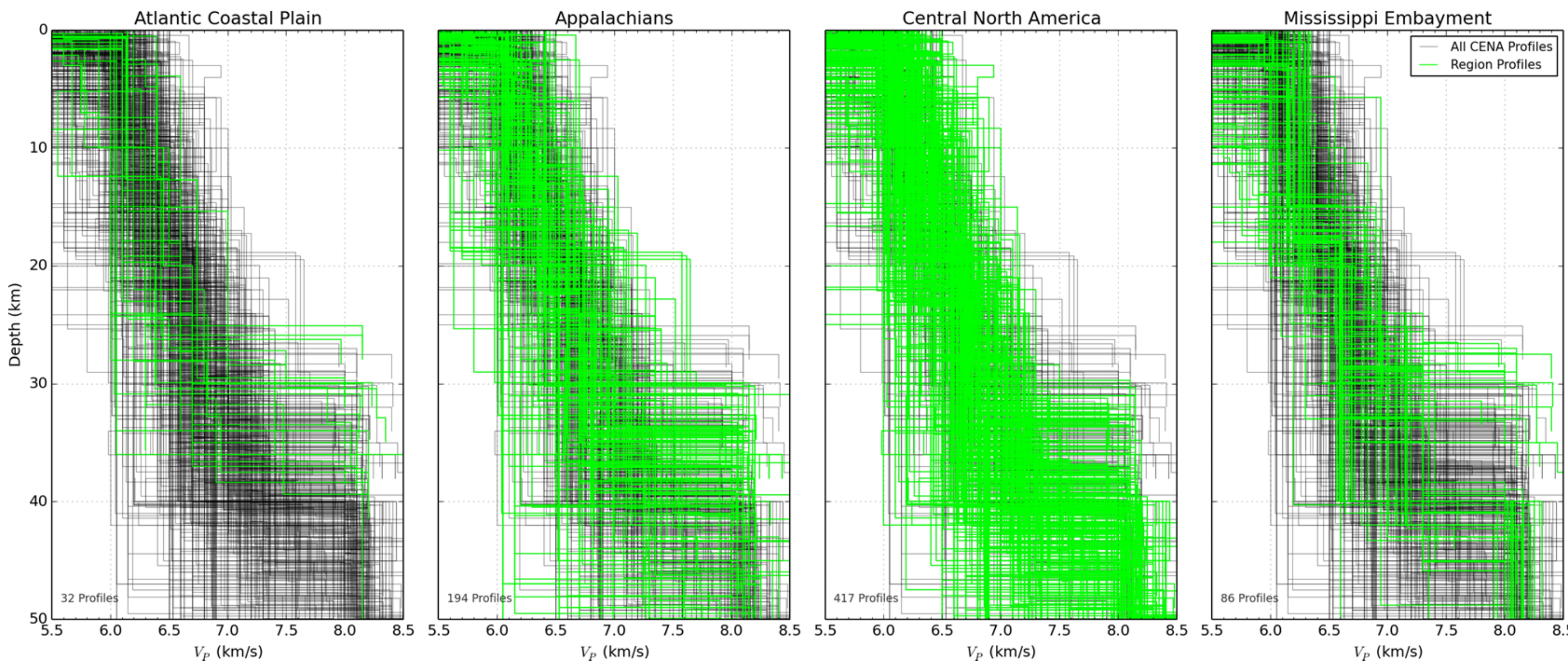

Figure 3.17 **Comparison of seismic velocity-depth profiles for each of the four regions in comparison with the seismic velocity-depth profiles for CENA. All profiles for CENA are illustrated in black, whereas each region's quality-controlled profiles are overlain in green.**

3.4 *Q*-FACTOR MODEL

The quality factor (Q) provides information about the damping (intrinsic seismic attenuation and dispersive effects) of the seismic waves, and is dependent on rock type, wave type, and wave frequency. The quantification of Q is defined as the number of wavelengths a wave can propagate through a medium before its amplitude has decreased by $e^{-\pi}$ [Blanch et al. 1995].

3.4.1 Definition Q_0 and η

To extract Q from real data, surface waves (e.g., Love waves, Lg) are often used. These are captured shear waves, reflecting both through the surface and the whole crust, with high periods. This is why Q_{Lg}^{C} can be used as an average Q value for shear waves for the whole crust thickness (Q_s). The relationship between Q and frequency f is defined as:

$$Q(f) = Q_0 f^{\eta} \tag{3.1}$$

where Q_0 is the value of Q_{Lg}^{C} calculated from the codas of Lg waves with a specific reference frequency. This is valid for every frequency f in the given range. The formula also contains η, the frequency coefficient, which, like Q_0, is region dependent.

3.4.2 Empirical Values for Q_0 and η

To find the best parameters for the frequency-dependent $Q(f)$ formula for each of the four regions, published estimates were compared. The following list shows the Q-regions and EPRI definitions [1993]. Figure 3.18 shows the subdivision into the Q-regions, as shown in Chapter 2. Table 3.3 assigns the EPRI-regions to the four crustal regions considered this study. The latitudes and longitude of boundaries for these four crustal regions are available in Appendix E, which is an electronic file. Three of the crustal regions fall within two of the EPRI [1993] Q-regions.

***Q*-region**	**Model**
1	$Q(f) = 600 f^{0.50}$
2	$Q(f) = 610 f^{0.65}$
4	$Q(f) = 850 f^{0.50}$
6	$Q(f) = 600 f^{0.60}$
8	$Q(f) = 180 f^{0.80}$

Table 3.3 Assignment of *Q*-region to each of the four crustal regions of interest through the subdivision after EPRI report [1993].

Crustal region (this study)	*Q*-region	General
Atlantic Coastal Plain	5	medium Q_0
Appalachians	4, 5	high Q_0
Central North America	2, 6	medium Q_0
Gulf Coastal Region	7, 8	low Q_0

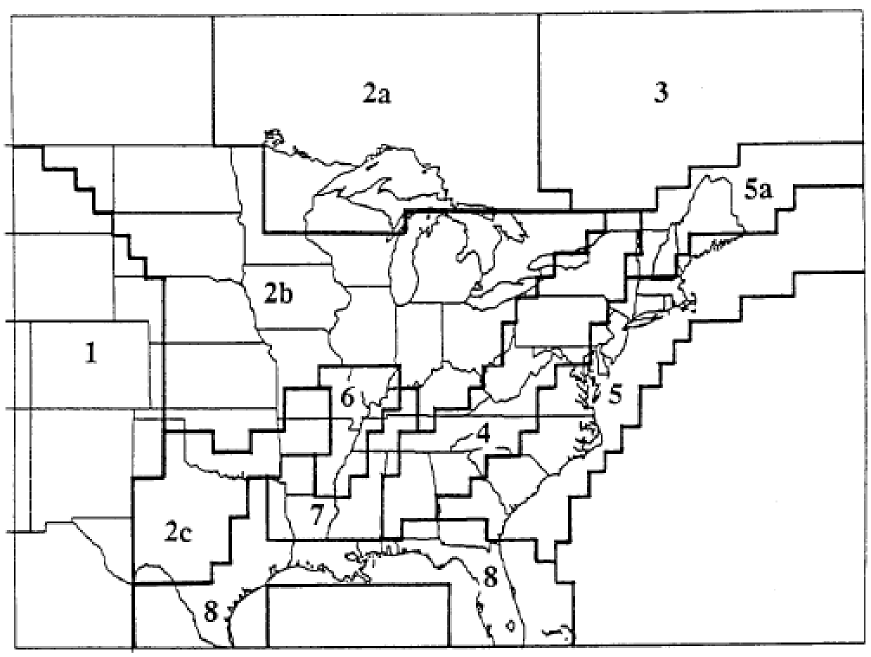

Figure 3.18 Subdivision of the North America in different *Q*(*f*) regions (see Section 2.1) [EPRI 1993].

Baqer and Mitchell [1998] provide a good overview of Q_0 and η for the U.S.; see Table 3.4, and Figures 3.19 and 3.20. They used records from broadband digital stations to illustrate regional variations of Q_0 across almost the entire U.S. Over 218 event–station pairs were analyzed to obtain estimates for Q_0 (*Lg* coda *Q* at 1 Hz) and its frequency dependence, η. Using a back-projection method, Baqer and Mitchell [1998] inverted these sets of estimates to obtain tomographic images of Q_0 and η. The interested reader is referred to Baqer and Mitchell [1998] for a more in-depth discussion of the method of analysis used by these authors.

Simplifying the results shown in Figure 3.19 results in a gradient of Q_0 with low values in the westernmost U.S. and increasing values towards the east coast. Focusing on the four crustal regions in this study, the highest Q_0 can be found within eastern North America (North), Central North America (Central, East), and the northern Appalachians. Medium values are found in the Atlantic Coastal Plain (South), Central North America (North, West) and the Appalachians (South). The lowest values can be found in the Gulf Coast region. In general terms, this corresponds to the subdivision of Q-regions reported by EPRI [1993]. EPRI [1993] provided η values within the range of 0.5 and 0.8; Baqer and Mitchell reported η values within the range of 0.4 and 0.8 (Figure 3.20). The values are comparable between these two studies for the APC and the APP regions, and for CNA, but are not consistent for the MEM region. (e.g., EPRI had an η of 0.8, while Baqer and Mitchell [1998] show an average for η of about 0.55).

Table 3.4 Assignment of Q_0 to each of the four geographical regions of interest after the results of Baqer and Mitchell [1998].

Crustal Region (this study)	Q_0–range	General
Atlantic Coastal Plain	500–650	medium Q_0
Appalachians	450–750	medium–high Q_0
Central North America	420–750	medium Q_0
Gulf Coast	350–600	low Q_0

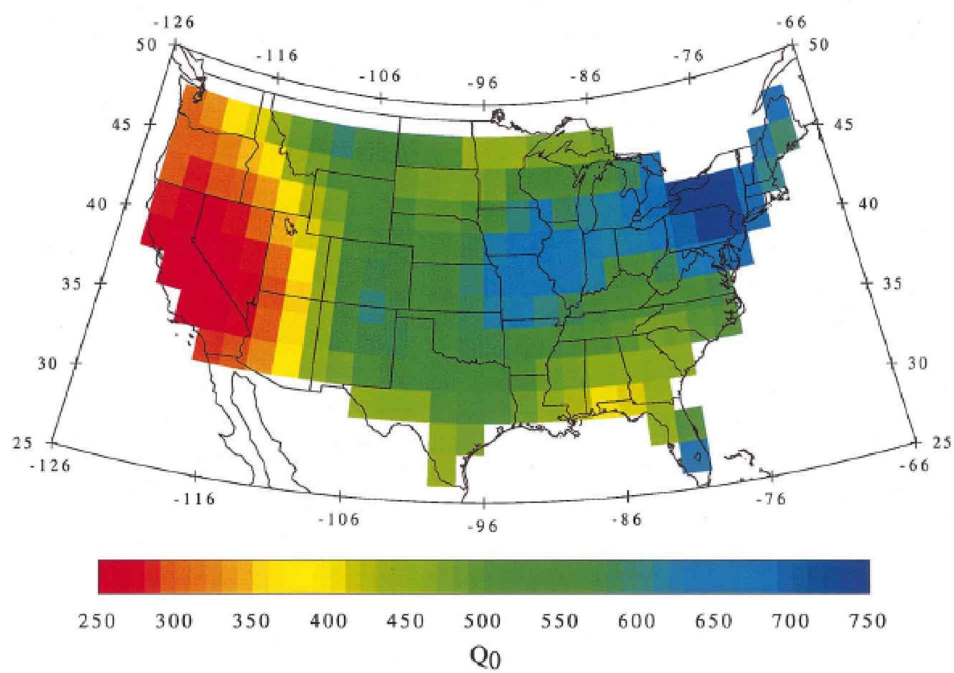

Figure 3.19 Q_0 map of the U.S. [Baqer and Mitchell 1998].

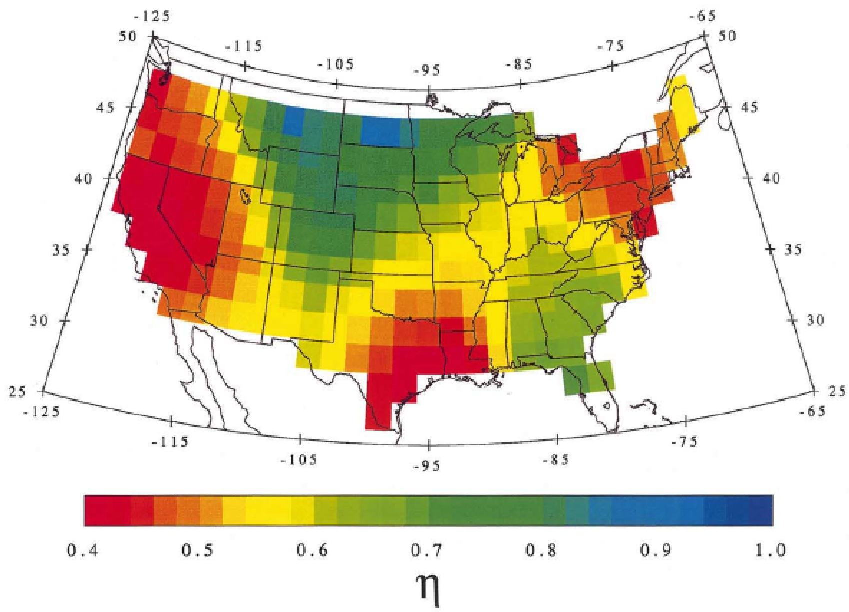

Figure 3.20 η **[defined in Equation (3.1)] map of the U.S. from 1998 [Baqer and Mitchell 1998].**

Baqer and Mitchell [1998] subdivided the U.S. into just two large Q-regions: one province spans the area from the Rocky Mountains to the Atlantic coast, is tectonically stable, and exhibits relatively high Q_0; the other extends westward from the approximate western margin of the Rocky Mountains to the Pacific coast, is tectonically active, and exhibits low Q_0.

According to Mitchell [1995], tectonically stable regions are usually characterized by high values of Q and a weak frequency dependence. Lower Q and stronger frequency dependence characterize tectonically active regions such as western North America [Mitchell 1995]. According to Baqer and Mitchell [1998], the difference in Q_0 between the western and eastern U.S. can be attributed to a greater amount of interstitial crustal fluids in the west. Regions of moderately reduced Q within the stable platform often occur where there are accumulations of Mesozoic and younger sediments. Reduced Q_0 in the southeastern U.S. may not be due to anelasticity but may be a gradational velocity increase at the crust-mantle boundary that causes shear energy to leak into the mantle [Baqer and Mitchell 1998].

3.4.3 Empirical Values for Q_0 and η for Four Regions of Interest

About twenty-four published studies covering fifty study areas were examined to find Q_0 and η values (see Appendix A). Publications used but were not limited to the authors listed below. Additional references are available in Appendix A:

- Atkinson, G.M. (1989)
- Woodgold, C.R.T. (1990)
- Liu, Z. et al. (1994)
- Shi, J. et al. (1996)

- Benz, H.M. et al. (1997)
- Erickson, D. et al. (2004)
- McNamara, D.E. et al. (2004)
- Chapman, M. and Catchings, R.D.(2008)
- Boatwright, J. and Seekins, L. (2011)

Almost all of these studies are based on the analysis of *Lg*-waves. A few investigated both *S*- and *P*-waves, and in some cases active studies (explosive sources) were used. Also, most of the studies using *Lg*-waves assume a geometrical spreading r of 0.5 (surface waves). To stay consistent within a region and make comparisons between regions, studies were selected that fulfilled the following constraints:

- investigation was conducted using *Lg*-waves
- earthquake sources were used rather than active source
- $r = 0.5$ is assumed
- frequency-dependent Q, $\eta \neq 0$

Two widely used synthetic seismogram computation programs were used in this study: *FK* from Zhu [2012] (assumes a frequency independent Q) and *hspec96* [Herrmann 2013a; 2013b], which allows a frequency-dependent Q formulation. Q-studies using *Lg*-waves were used to get a representative value for Q_s. Q_p was calculated as equal to $2Q_s$. Because this study was most interested in frequencies between 5 and 10 Hz, a reference frequency f of 5 Hz was used. Equation (3.2) is a modification of Equation (3.1):

$$\begin{aligned} Q_s &= Q(5\ Hz) = Q_0 5^{\eta} \\ Q_p &= 2Q_s \end{aligned} \tag{3.2}$$

3.4.4 Atlantic Coastal Plain

Figure 3.21 shows the linear relation between Q-values and frequency [see Equation (3.1)] for four studies [Pulli 1984; Gupta and McLaughlin 1987; Atkinson and Boore 1995; Shi et al. 1996] within the ACP Estimated Q-values for specific frequencies are plotted, when available (crosses). The dashed line represents the median of all Q-f relations. Instead of favoring a specific study, the median was used for the purpose of this investigation. The median represents the typical Q-f relation of the ACP's Q-studies: $Q(f) = 628 f^{0.38}$.

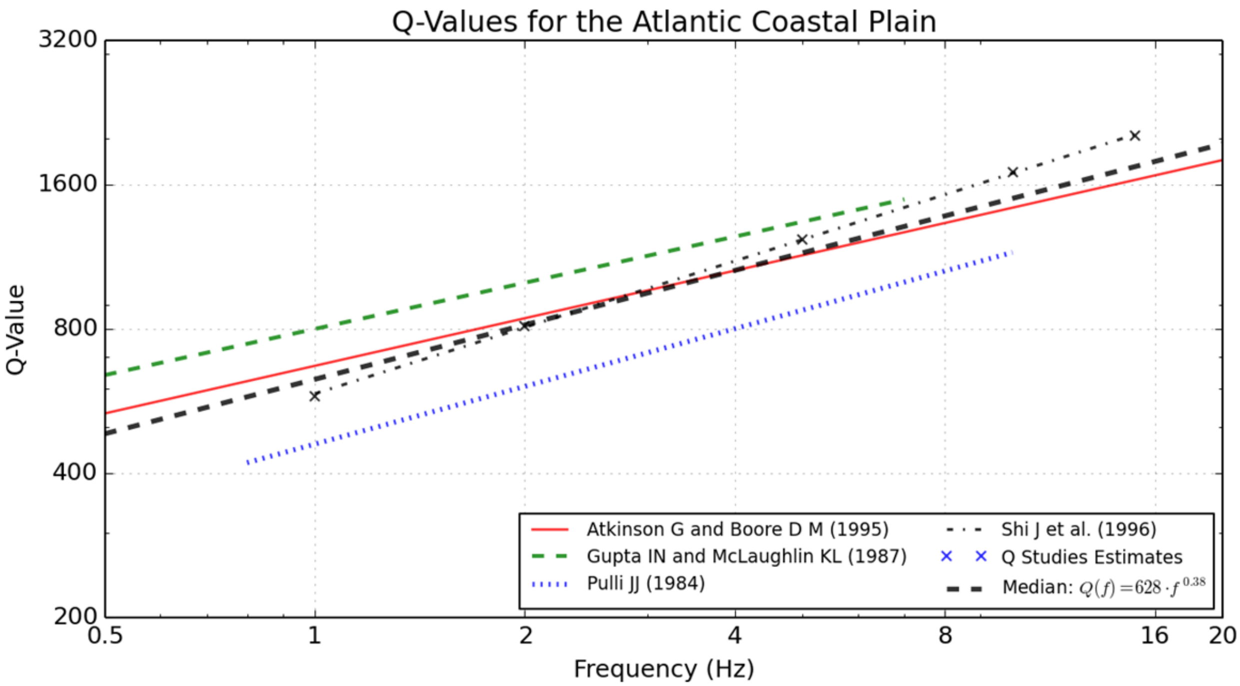

Figure 3.21 Comparison of *Q*(*f*) within the ACP. Illustrated are four studies (continuous lines) and their *Q-f* estimates, if available (crosses). The dashed line shows the median of all *Q-f* relations.

3.4.5 Appalachians

Figure 3.22 shows the linear relationship between Q-values and frequency [see Equation (3.1)]) for five studies [Shi et al. 1996; Benz et al. 1997; Erickson et al. 2004; Atkinson 2004; and Boatwright and Seekins 2011] within the APP region, although these studies partially include an investigation area within the defined CNA region. Estimated Q-values for specific frequencies were plotted when available (crosses). The dashed line represents the median of all Q-f relations. Instead of using a specific study, the median was used. The median should represent the variety of the APP region's Q-studies: $Q(f) = 713 f^{0.39}$.

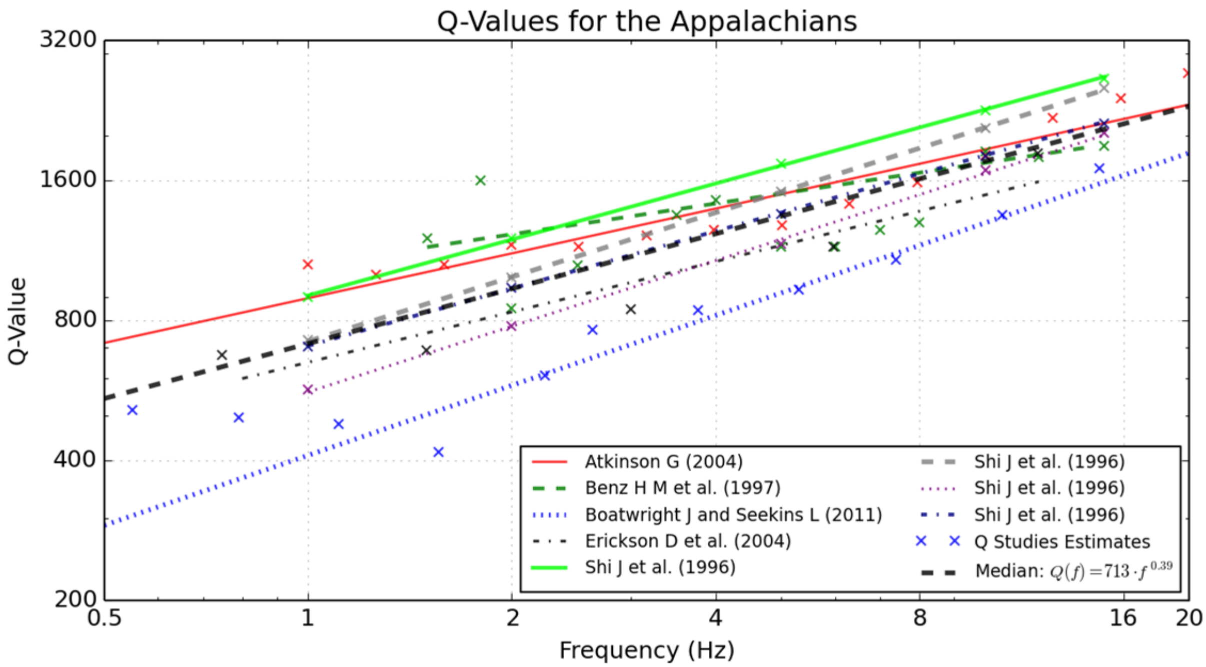

Figure 3.22 Comparison of *Q*(*f*) within the APP region. Illustrated are eight studies (continuous lines) and their *Q-f* estimates, if available (crosses). The dashed line shows the median of all *Q-f* relations.

3.4.6 Central North America

Figure 3.23 shows the extracted relation between *Q*-values and frequency [regressed after Equation (3.1)] for seven studies (continuous lines) within CNA [Hasegawa 1985; Chun et al. 1987; Shin and Hermann 1987; Atkinson 1989; Woodgold 1990; Atkinson and Mereu 1992; and Erickson et al. 2004). These studies partly include an investigation area within the APP region. Estimated *Q*-values for specific frequencies are plotted when available (crosses). The dashed line represents the median of all *Q-f* relations. Instead of using a specific study, the median was used. The median should represent the variety of CNA region's *Q*-studies: $Q(f) = 630 f^{0.40}$.

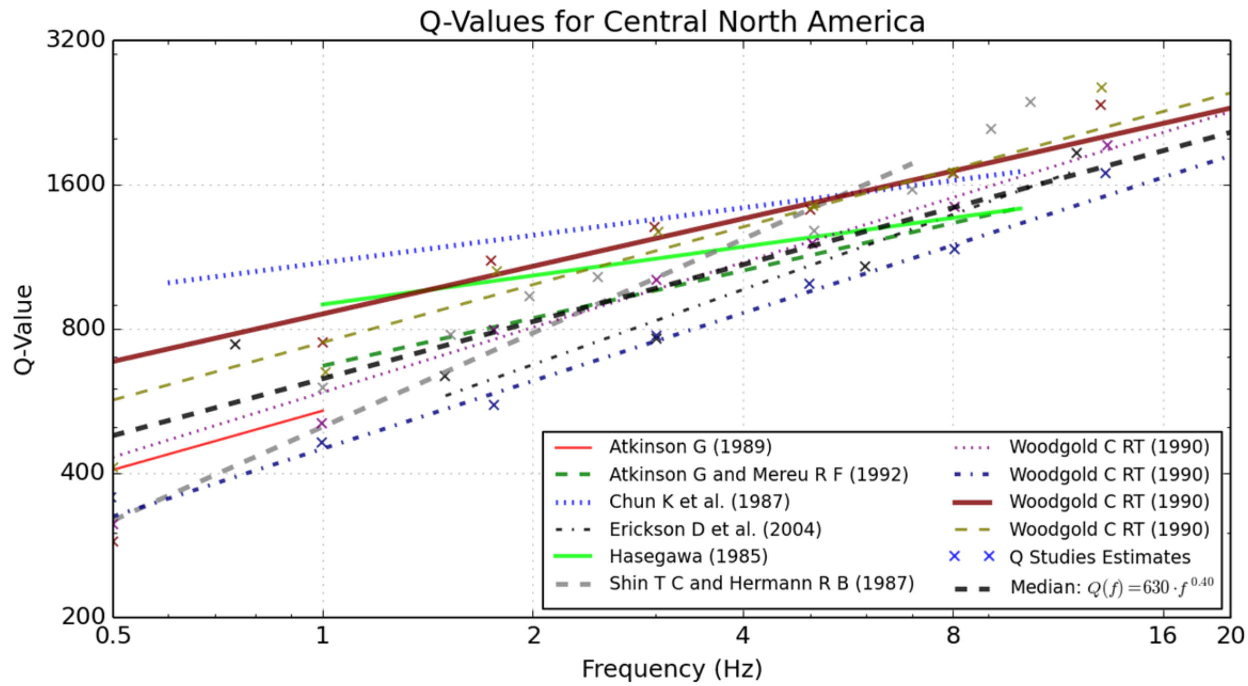

Figure 3.23 Comparison of *Q*(*f*) within the CAN region Illustrated are ten studies (continuous lines) and their *Q-f* estimates if available (crosses). The dashed line shows the median of all *Q-f* relations.

3.4.7 Mississippi Embayment/ Gulf Coastal Region

Figure 3.24 shows the extracted relation between *Q*-values and frequencies [regressed after Equation (3.1)] available for the MEM region [Zandieh and Pezeshk 2010]. Most of the studies for this region are active source or *P*-wave studies. Zandieh and Pezeshk [2010] "NMSZ and Mississippi Embayment" derived the *Q*-factor model specifically for the Mississippi Embayment: $Q(f) = 614 f^{0.32}$.

When comparing the extracted *Q-f* dependencies, the ACP, CNA, and the MEM regions offer a very similar model; see Table 3.5. The *Q*-factor models used for our computations will have relatively small effect on the ground motions in comparison with the effect of the crustal seismic velocity models. See Appendix C.

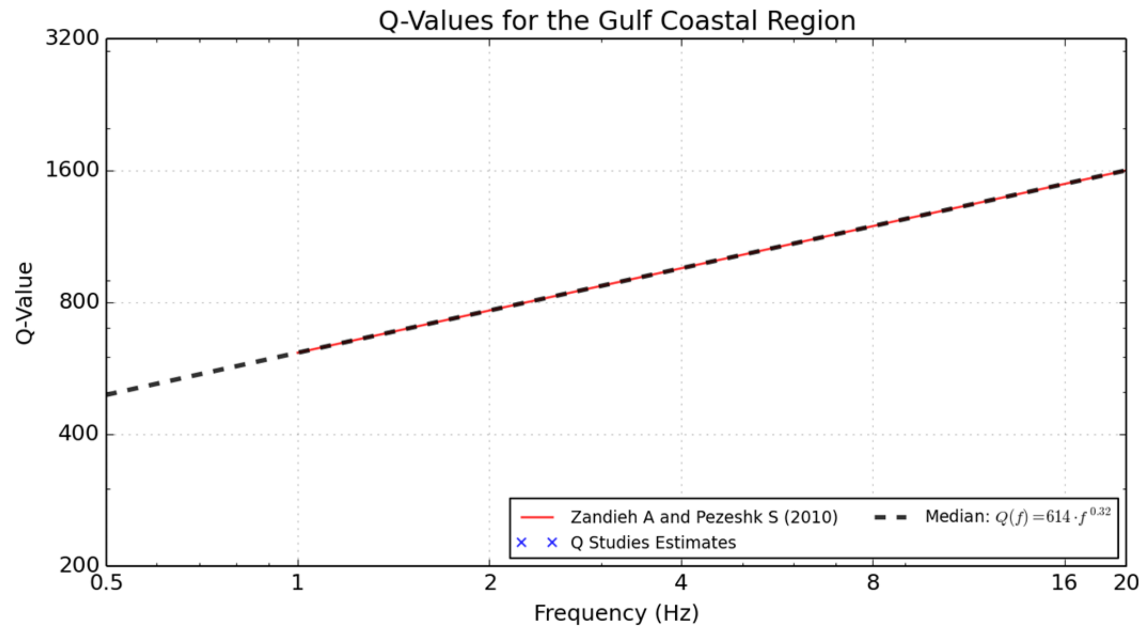

Figure 3.24 **Available *Q-f* studies within the MEM region, which satisfy the requirements defined earlier. Illustrated is the study of Zandieh and Pezeshk [2010], which offers a *Q*-factor model for the Mississippi Embayment.**

Table 3.5 **Quality-factors (Q_s and Q_p) of the four regions of interest, extracted from the previous analyses (a reference frequency of 5 Hz was used).**

Quality-Factor	Atlantic Coastal Plain	Appalachians	Central North America	Mississippi Embayment
$Q(f)$	$628\ f^{0.38}$	$713\ f^{0.39}$	$630\ f^{0.40}$	$614\ f^{0.32}$
Q_s	1157	1335	1200	1027
Q_p	2314	2670	2400	2054

3.5 FOCAL DEPTHS

Data from events and their focal depths within CENA were downloaded from the Central and Eastern U.S. from the Seismic Source Characterization (CEUS-SSC) catalog [EPRI/USDOE/USNRC 2012] and the Saint Louis University (SLU) catalog [SLU 2013]. Both catalogs provide information about the event's magnitude and focal depth. The CEUS-SSC catalog contains data for thousands of events; the SLU catalog offers more precise data for well recorded but fewer events. Figure 3.25 shows a comparison of the two catalogs.

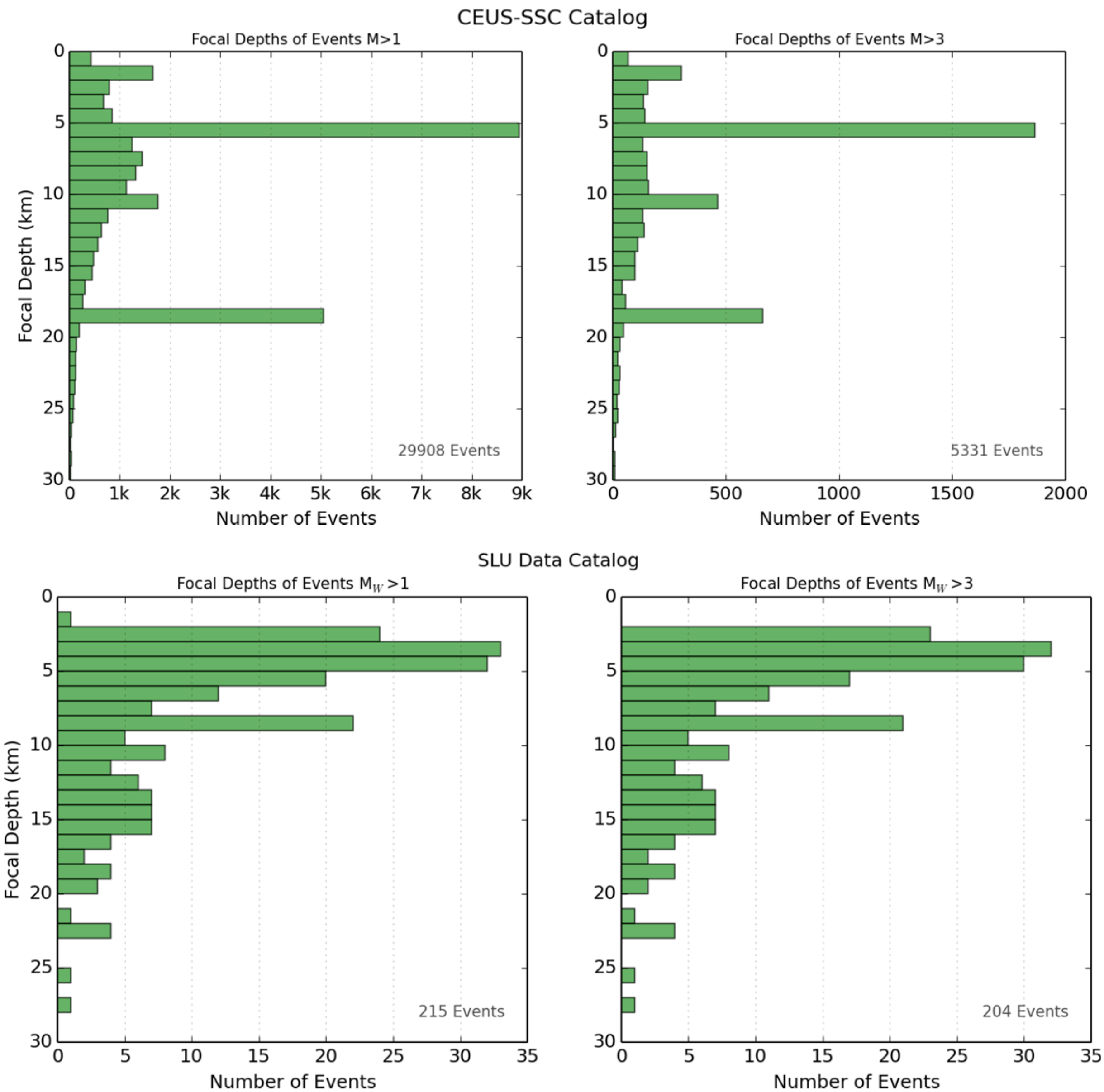

Figure 3.25 Comparison of focal depths within CENA, from (top) the CEUS-SSC and (bottom) the SLU catalog.

The CEUS-SSC catalog contains almost 30,000 Ml >1 events, and 5000 Ml >3 events. There are peaks at focal depths of about 5, 10, and 18 km. The SLU catalog contains about 200 Ml >1 events, with the majority being Ml >3 events. There is a peak in the number of events at about 3–4 and 8 km depth, and to a lesser degree at 22 km. In general, there are accumulations of events at 5, 10, and 20 km of depth. The number of events becomes less as focal depth increases. To achieve a general overview of the ground motion and to account for possible deeper crustal events, a wide range of focal depths was considered. The following focal depths were used for the computations: 5, 10, 20, and 30 km.

3.6 FOCAL MECHANISM AND AZIMUTH

Figure 3.26 shows an overview of typical focal mechanisms for North America and synthesizes these results by color: normal, thrust, and strike-slip faulting are represented by red, blue, and green, respectively. There are dominant regimes for each region: for Eastern North America, most faults rupture in a reverse or thrust sense; the APP region is dominating by reverse faults (north) and strike-slip faults (south); the CNA region shows all three faults mechanisms in nearly equal proportion. There are few events within the MEM region, although the dominant slip mechanism appears to be normal faulting.

Although our four defined regions show varying regimes of faulting, we elected to use a reverse mechanism for all the simulations to facilitate comparisons between regions. The catalog provides, among others, the faulting regime of 657 events within North America. Limiting the area to CENA and extracting events with magnitudes $M_w > 5$, only ten events are left; see Table 3.6. There are six events that ruptured on thrust faults (TF) and four on strike slip (SS) faults. The chosen standard fault mechanism represents a pure reverse fault, striking North-South. To get full radiation pattern and maximum amplitude within synthetic seismograms, the azimuth was set to 90°, with movement of the hanging wall towards the east. A statistical analysis of the fault plane's dips of past events is shown in Figure 3.27. The 215 events illustrated in Figure 3.25 (bottom) were used. There is defined peak at 45° dip.

- strike = 180° , dip = 45° , rake = 90°
- azimuth = 90°
- double couple source

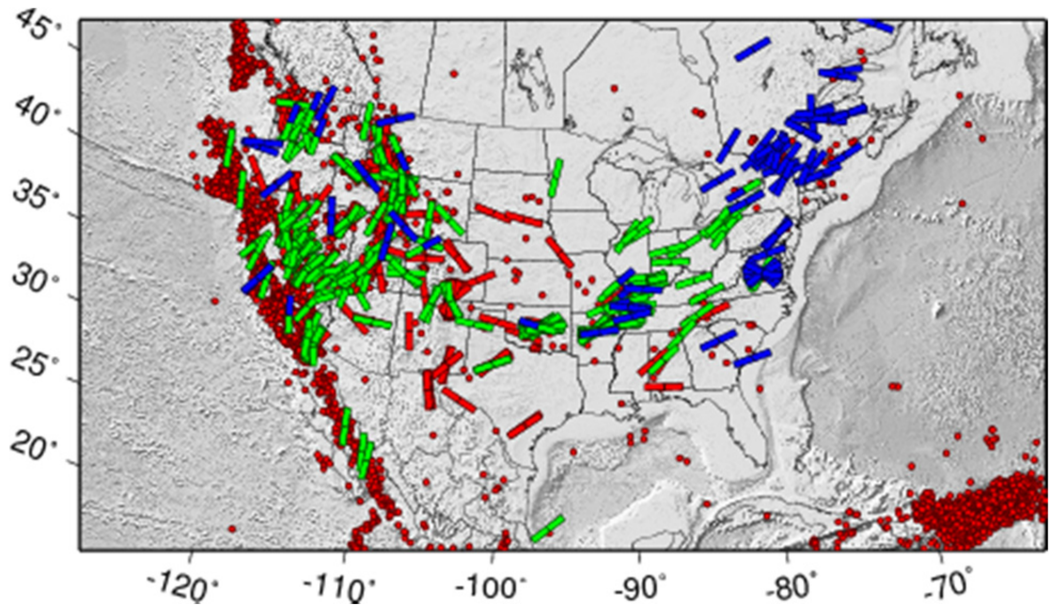

Figure 3.26 Orientation of maximum horizontal compressive stress following the convention of Zoback [1992]. Red indicates normal faulting, blue thrust faulting and green strike-slip faulting [SLU 2013].

Table 3.6 Extracted events within CENA with magnitudes M_w > 5.0. TF= thrust fault, SS= strike slip.

Year	Mon	Day	Hour	Min	Sec	Lat	Lon	Dep	M_W	Regime
1968	11	09	17	01	42	37.91	-88.37	22	5.29	TF
1980	07	27	18	52	21	38.17	-83.91	12	5.04	SS
1982	01	09	12	53	51	46.98	-66.66	10	5.47	TF
1982	01	11	21	41	07	46.98	-66.65	8	5.14	TF
1997	12	06	08	06	47	64.84	-88.19	9	5.07	TF
2007	05	23	19	09	15	22.02	-96.27	11	5.60	SS
2008	04	18	09	37	00	38.45	-87.89	14	5.23	SS
2010	06	23	17	41	42	45.86	-75.46	22	5.04	TF
2011	08	23	17	51	05	37.94	-77.93	6	5.65	TF
2011	11	06	03	53	10	35.54	-96.75	8	5.59	SS

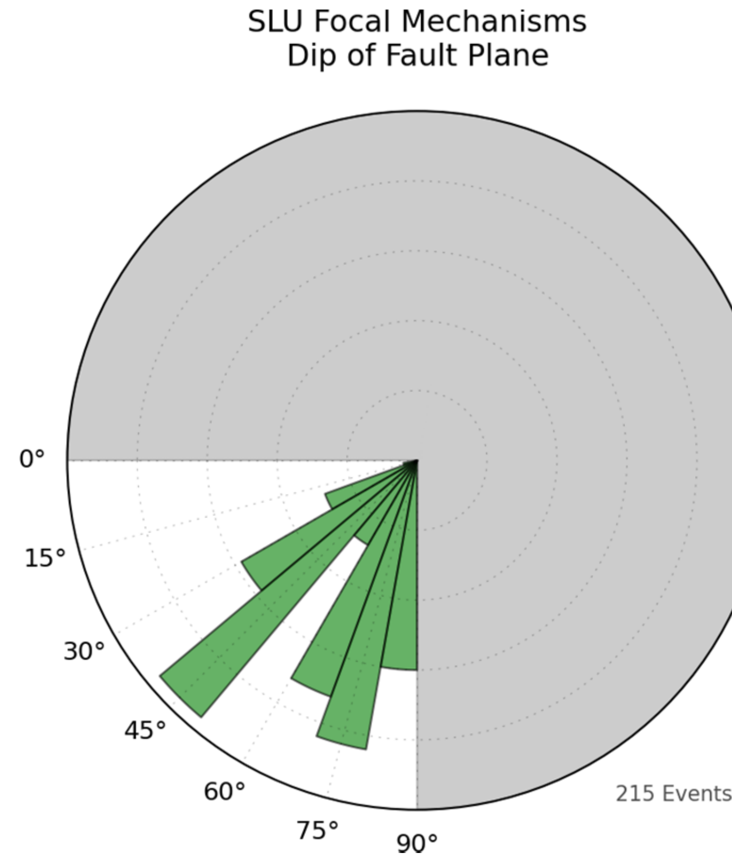

Figure 3.27 **Fault plane dips of the SLU catalog events, illustrated in Figure 3.25 (bottom).**

3.7 SOURCE TIME FUNCTION AND MAGNITUDE

The earthquake source signal is called the "source time function." Stein and Wysession [2003] write: "In the simplest case of a short fault that slips instantaneously, the seismic moment function is a step function, whose derivative (a Δ function) is the source time function. This example is easy, but not very likely to occur in this way. The total radiated signal is not impulsive because the finite fault does not all break at the same time. Instead, waves arrive first from the initial point of rupture and later from points further along the fault. So the rupture propagates at a rupture velocity (V_R) along a fault of a specific length (L). The time, which can be described by L/V_R, is the rupture time T_R. The time pulse due to the finite fault length can be described as a "boxcar" of duration T_R."

$$T_R = L/V_R \tag{3.3}$$

Because V_R is typically assumed to be about 0.7–0.8 times the shear velocity V_s, the rupture time T_R can also be estimated by:

$$T_R \approx L/V_s \tag{3.4}$$

A second effect lengthens the time function so that even at a single location on the fault, slip does not occur instantaneously. The slip history is often modeled as a ramp function, which begins at time zero and ends at the rise time T_D (see Figure 3.28, top). For the ramp, the derivative is a boxcar.

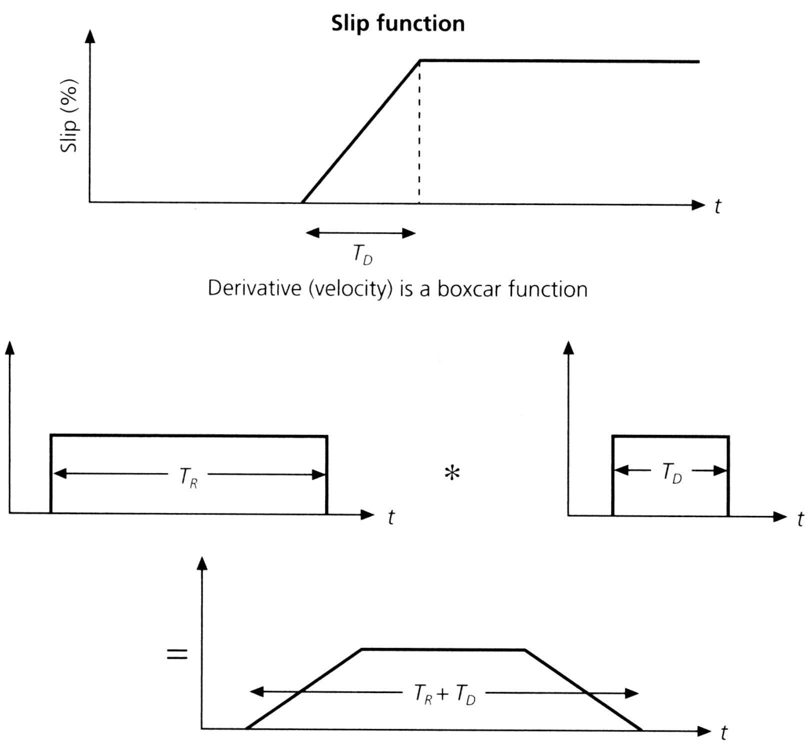

Figure 3.28 **Source time function depends on the derivative of the history of slip on the fault. A ramp time history (top) with duration T_D has a "boxcar" time derivative. When convolved with the "boxcar" time function due to rupture propagation (center), a trapezoidal source time function results (bottom) [Stein and Wysession 2003].**

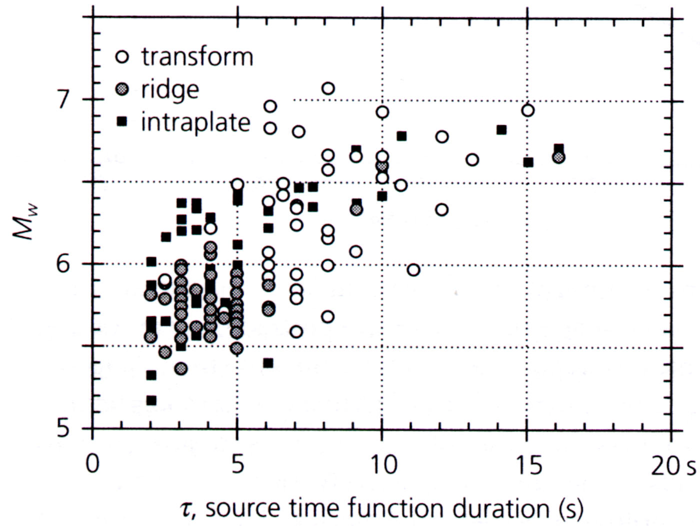

Figure 3.29 Empirical relation between source time function duration ($T_{Duration}$) and moment magnitude of earthquakes for different tectonic regions [Stein and Wysession 2003].

Convolving the finiteness and rise time effects (Figure 3.28, center) yields a trapezoid (Figure 3.28, bottom), whose length is equal to the sum of the two boxcar lengths (sum of rise and rupture time, [Equation (3.5)], and whose rise and fall is equal to the duration of the shortest boxcar.

$$T_{Duration} = T_{Rupture} + T_{Rise} \tag{3.5}$$

The *FK* synthetic seismogram code [Zhu 2012] accepts a limited number of source function shapes: triangle, rectangle or a trapezoid. This study used a traditional triangle to represent an earthquake source time function. To define a duration time and rise time, empirical relations were considered as detailed below.

We considered $M_w = 6$ for the calculations. Looking at the source time function duration for the intraplate regions, the duration for this magnitude had a range of roughly 2 to 5 sec (Figure 3.29). A duration time of 4 sec was considered. A value of 0.5 was used for the rise time, which is the portion of the duration time considered for rising and falling. A value of 0.5 means 50% of the duration time, which means 2 sec of rising and falling. This results in a triangle source time function.

The earthquake magnitude was another important parameter to consider. The same moment magnitude was used for the computations for each of the four regions in order to stay comparable between the regions. The chosen magnitude was $M_w = 6$; it is high enough to recognize clear and significant pattern of PSA and yet is still a realistic and possible source magnitude for an event within CENA. The computations were done for just one magnitude to minimize the amount of output data and were found to be entirely sufficient for the relative comparison of PSA between the regions and to define to crustal attenuation groups.

3.8 DISTANCE TO THE EARTHQUAKE SOURCE

Ground motions were computed for a distance ranging from 1 km to 500 km from the source by using a logarithmic spaced sampling rate with 60 samples. The dense sampling is important to extract detailed information and to minimize the effects of interpolation.

3.9 FREQUENCIES

The computations were conducted for a wide range of output frequencies (0.1–20 Hz). After looking at and evaluating results for all frequencies, a decision was made to focus the analysis over two key frequency bands: 5−10 Hz and 0.5–1 Hz. This simplification of results into two main bands allows the interpretation of global trends in attenuation for relatively high and low frequencies respectively.

3.10 ADDITIONAL PARAMETERS

3.10.1 Computation of Acceleration Time Series

Sampling Interval of Time (*dt*)

The highest frequency of interest for PSA was 20 Hz; however, the maximum frequency calculated was extended to 25 Hz for computational accuracy at 20 Hz. A Nyquist frequency of 25 Hz requires a sampling rate of 50 Hz. That implies a sampling interval of (1/50 Hz), or a time step *dt* of 0.02 sec.

Number of Samples (*nt*)

The synthetic seismogram program requires an input number of samples (*nt*) that is equal to the shape of:

$$nt = 2^x \tag{3.6}$$

The number of samples is important because it defines the length of the time series (*L*), which is:

$$L = dt \cdot nt \tag{3.7}$$

Direct waves propagate 500 km from the hypocenter to the farthest station (500 km epicentral distance). Taking an average travel velocity of $V_p = 6.19$ and $V_s = 3.57\ \mathrm{km/sec}$, the direct *P*-wave should be visible on the time series at 81 sec, and the *S*-wave is visible at 140 sec. The first Moho-reflection should arrive a few seconds later. To get a sufficient length of the acceleration time series (that includes all reflection and refraction signals), *nt* was set to 8192, which makes an observation time of:

$$nt \cdot dt = 8192 \cdot 0.02 = 164\ \mathrm{sec} \tag{3.8}$$

Sampling Interval of Wavenumber (*dk*)

In the program readme files, *dk* is described as:

$$dk = \pi / \max(X_{\max}, source\_depth) \tag{3.9}$$

which would be π/500 km = 0.0062 km. This value is too small, because the suitable range for *dk* is 0.1–0.5. The default value is in the middle of this range (default $dk = 0.3$). After empirical testing, the most appropriate output is a sampling interval with a wavenumber of 0.2/km.

$$dk = 0.2/\text{km}$$

Components (vertical, radial and transverse)

The output of the synthetic seismogram program is the ground motion time series for the three components of motion: vertical (*z*), radial (*r*), and transverse (*t*). Because of the particular focal mechanism that was chosen and its associated radiation pattern, the majority of the ground motion appears on the radial component. This can be seen in the high (maximal) amplitudes on the radial component, and on very small amplitudes (close to zero) on the transverse component. Building the arithmetic mean (am) of the horizontal components would lead to a radial component-dominated output. This report provides an overview of all components, but places emphasis on the radial component.

Default Parameters

Several parameters are assigned default values in the program:

```
$smth = 1;            # densify the output samples by a factor of smth.
$src = 2;             # source type, 2=double couple; 1=single force; 0=explosion.
$sigma = 2;           # small imaginary frequency, in 1/T, 2-3.
$kmax = 15.;          # max wavenumber at w=0, in 1/h, 10-30.
$pmin = 0.;           # max. phase velocity, in 1/vs, 0 the best.
$pmax = 1.;           # min. phase velocity, in 1/vs.
$taper = 0;           # for low-pass filter, to suppress high frequencies, 0-1, 0=off.
($f1,$f2) = (0,0);    # for high-pass filter transition band, in Hz.
$tb=50;               # number of samples before the first arrival.
$flat=0;              # Earth flattening transformation.
$r_depth = 0.;        # receiver depth.
$updn = 0;            # 1=down-going wave only; -1=up-going wave only.
```

For more explanations of these default parameters, see Section 5.1.

3.10.2 Computation of PSA

The PSA was computed for 5 % damping using a publicly available FORTAN routine [Boore 2012]. The code accepts input in terms of periods rather than frequencies. The frequency range therefore has to be converted to the period range. The PSA was calculated up to the Nyquist frequency of the time series (25 Hz). The range for PSA calculation was set to periods from 0.04–10 sec (frequencies: 25–0.1 Hz).

The sampling rate was not linear, but logarithmic. For each logarithmic range of periods (0.01–0.1, 0.1–1, and 1–10 sec), there were the same amount of samples. The sample amount in general should be high, so that the resolution is also high and no interpolation is necessary. The number of samples used herein was 300. More details on the code and computations are presented in Section 5.2.

3.11 DESCRIPTION OF CRITERIA

The criteria used to define what were considered to be significant differences in ground motion are listed below, as adopted from EPRI [1993].

1. The differences in the medians must be significant at the 95% confidence level.
2. The difference in the medians must be greater than 20%.
3. Criteria 1 and 2 must be met for three consecutive distances and frequencies, and the polarity of the difference in the medians must also be consistent over this distance and frequency range. (For this analysis, the distance criterion corresponds to a 30-km range.)

4 Calculation and Analysis Method

This chapter summarizes the computation procedures used to develop PSA distributions from ground motion simulations. For clarity, the current chapter only refers to simulations completed with the *FK* code [Zhu 2012], but the same post-processing tools were used in conjunction with the simulations from *hspec96* [Herrmann 2013a; 2013b]. An extensive software package was developed in PYTHON to streamline the computations and to generate a series of analysis products including statistics summarized in tables and plots. This chapter describes the key parts of the computation process, including a summary of the PYTHON code output. The different analysis products are then introduced to facilitate the interpretation of results, which are presented in Chapters 5 and 6 for each of the simulation methods.

4.1 ACCELERATION TIME SERIES

4.1.1 Simulations Code

In simple terms, there are three steps in the computation of synthetic seismograms (see Figure 4.1):

1. Definition of seismic parameters for the input model (crustal seismic velocity structure).
2. Calculation of Green's functions (including reflection coefficients,/reflectivity) using acoustic impedance (i.e., density times velocity).
3. Convolution of reflectivity and source signal to obtain the synthetic seismogram.

The first step was accomplished by the regionalization study (Sections 3.1–3.3). The second and third steps were executed using the computer code *FK* developed by Zhu [2012], as described below.

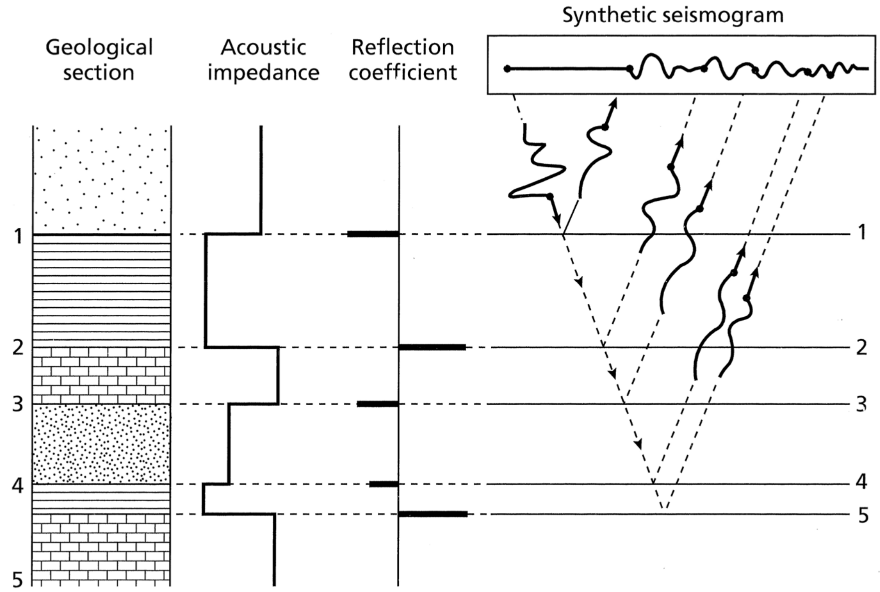

Figure 4.1 Steps used in the computation of a synthetic seismogram [Kearey et al. 2002].

Calculating Green's Function using "*Fk.pl*" [Zhu, 2012]

fk.pl -Mmodel/depth[/f] [-D] [-Hf1/f2] [-Nnt/dt/smth/dk/taper] [-Ppmin/pmax[/kmax]] [-Rrdep] [-SsrcType] [-Uupdn] [-Xcmd] distances

- M: model name and source depth in km.

f invokes Earth flattening (off).

The model has the following format (in units of km, km/sec, *g*/cm3): thickness, Vs, Vp, rho, Q_0, η

rho=0.77 + 0.32*Vp if not specified.

If the first layer thickness is zero, it represents the top elastic half-space. Otherwise, the top half-space is assumed to be a vacuum and does not need to be specified. The last layer (i.e. the bottom half space) thickness should always be zero.

-D: use degrees instead of km (off).

-H: apply a high-pass filter with a cosine transition zone between freq. f1 and f2 in Hz ($f1/$f2).

-N: nt is the number of points in the seismogram, must be 2N ($nft). Note that nt=1 will compute static displacements (require st_fk compiled). nt=2 will compute static displacements using the dynamic solution.

dt is the sampling interval ($dt sec).

smth makes the final sampling interval to be dt/smth, must be 2^N ($smth).

dk is the non-dimensional sampling interval of wavenumber ($dk).

taper applies a low-pass cosine filter at fc=(1-taper)*f_Niquest ($taper).

-P: specify the min. and max. slownesses in term of 1/vs_at_the_source ($pmin/$pmax) and optionally kmax at zero frequency in term of 1/hs ($kmax).

-R: receiver depth ($r_depth). -S: 0=explosion; 1=single force; 2=double couple ($src).

-U: 1=down-going wave only; -1=up-going wave only ($updn).

-X: write the input to cmd for debugging ($fk).

The output is the surface displacement (in SAC format for the dynamic case and ASCII file for the static case), in the components in the following order: vertical (UP), radial, and tangential (counterclockwise) for n=0, 1, 2 (i.e. Z0, R0, T0, Z1, etc.). Assuming V in km/s, rho in g/cm^3, and thickness in km, the units are10^{-20} cm/(dyne cm) for double couple source and explosion;

Calculating Synthetic Seismograms from Green's Function using "*Syn*"

syn -Mmag([[/Strike/Dip]/Rake]|/Mxx/Mxy/Mxz/Myy/Myz/Mzz) –Aazimuth ([-SsrcFunctionName | -Ddura[/rise]] [-Ff1/f2[/n]] [-I | -J] -OoutName.z -GFirstCompOfGreen | -P)

-M: Specify source magnitude and orientation or the moment-tensor

For double-couple, mag is Mw, strike/dip/rake are in A&R convention

For explosion; mag is in dyne-cm, and no strike, dip, and rake are needed

For single-force source; mag is in dyne, only strike and dip are needed

For moment-tensor; mag in dyne-cm, x=N,y=E,z=Down

-A: Set station azimuth in degree measured from the North

-D: Specify the source time function as a trapezoid

give the total duration and rise-time (0-0.5, default 0.5=triangle)

-F: apply n-th order Butterworth band-pass filter, SAC lib required (off, n=4, must be < 10)

-G: Give the name of the first component of the FK Green function

-I: Integration once

-J: Differentiate the synthetics

-O: Output SAC file name

-P: Compute static displacement, input Green functions from stdin in the form distance Z45 R45 T45 ZDD RDD TDD ZSS RSS TSS [distance ZEX REX TEX]

The displacements will be output to stdout in the form of distance azimuth z r t

-Q: Convolve a Futterman Q operator of tstar (no)

-S: Specify the SAC file name of the source time function (its sum. must be 1)

As before, the output is the surface displacement (in SAC format for the dynamic case and ASCII file for the static case), produced by different seismic sources in the following order:

vertical (UP), radial, and tangential (counterclockwise) for n=0, 1, 2 (i.e. Z0, R0, T0, Z1, etc.). Their units are (assume v in km/s, rho in g/cm^3, thickness in km):

- cm — for displacement
- cm/s — for velocity
- cm/s^2 — for acceleration

4.1.2 Using the Simulations Code

Calculating Green's Function using "*Fk.pl*"

fk.pl -M$model/$dep/f -N$nt/$dt/1/$dk 1.000 1.111 1.234 1.371 …

The parameters are:

$model	= V(z), Q(f) input model	EAST_CST, APPALACH, CENTRALS, GULF_TRC
$dep	= source depth	5, 10, 20, 30 km
f	= triggers earth flattening	
nt	= number of samples	8192
dt	= sampling interval of time	0.02 (50 Hz–$f_{Nyquist}$ = 25 Hz)
dk	= sampling interval of wavenumber	0.2
1 … 500	= log-spaced distances in km	

Calculating Synthetic Seismograms from Green's Function using "*Syn*"

syn -M$mw/$str/$dip/$rake -A$azi -D$dur -J -G$gf

-O$dir/$model'_dep'$dep'_'dist$current_dist'_'z

The parameters are:

$mw	= focal magnitude	6
$str	= strike	180°
$dip	= dip	45°
$rake	= rake	90°
$azi	= station azimuth in degrees measured from the North	90°
$dur	= total duration and rise-time	4 s
-J	= option to differentiate the synthetics, from velocity to acceleration time series	
-G	= name of the first component of the FK Green function	
-O	= Output SAC file name	*$model'_dep'$dep'_'dist$current_dist'_'z*

The output of the synthetic seismogram computation contains 60 files, one for each of the 60 distances calculated for each earthquake source. This study computed four different source depths, each with three components (vertical, radial, and transverse), thus obtaining 720 files for each crustal seismic velocity-depth model.

4.2 5%-DAMPED PSA

Boore's FORTRAN programs [2012] were used to calculate PSA. This collection provides comprehensive options for converting formats, data processing, and other time series subroutines. The acceleration time series had to be converted into a file format suitable for Boore's software programs. This data format is called the SMC-format, which is a useful format for saving strong-motion time series. It uses ASCII character codes and provides text, integer, and real headers, followed by a block of comments, and then the data is written in binary SAC format [Boore 2012].

- **sac2smc** (the program to reformat the SAC files into the SMC-format)

Used control file:

```
! Control file for SAC2SMC      ! first line
! Name of summary file:
sum.sac2smc
! Xfactr
! 1.0e-7   ! convert nanometers to cm (assume SAC data is in nanometers)
!Input file name ("stop" in any column to quit):
APPALACH_dep05_dist1.000_r
APPALACH_dep05_dist1.000_t
APPALACH_dep05_dist1.000_z
APPALACH_dep05_dist1.111_r
...
STOP
```

The output unit from *FK* is displacement (cm). Hence there is no need to convert the unit (line 5 of the code), and there is no problem in processing all multiple files at once.

- **smc2rs** (a program to calculate spectral ground motion from time series)

Used control file:

```
! Control file for program SMC2RS
! Use smc2rs2 for RS computed at a fixed set of periods up to 15 s
! Revision of program involving a change in the control file on this date:
03/06/10
! Summary file name:
sum.smc2rs
```

! Use PEER NGA periods? (y/n)

n

!Use tabulated periods? (y/n)

n

! If "y" above: Number of periods, followed by the periods:

! If "n" above: Periods for response spectra (nperiods log spaced from per_low to per_high):

! Note: need two lines as placeholders if the PEER NGA periods are used.

300

0.04 10.0

! Damping values (ndamp, damp(1), damp(2), ..., damp(ndamp)):

1 0.05

! t4mean (removes a mean from the whole record, where the mean is determined from t = 0 to t = t4mean. If t4mean = 0.0 the mean of the whole record is used, and if t4mean < 0, no mean is removed. NOTE: need entries even if the parameter is not used (because read info use list- directed (unformatted) input). Note that if working with a processed record that includes the complete time series produced by the processing (e.g., the padded time series for acausal filtering or the post-processing baseline corrected time series produced from pad-stripped or pass-through data in the first NGA project), it is inadvisable to remove the mean as this may produce unintended distortions at long periods; in this case set t4mean < 0.0. If the record is pad-stripped, however, as provided by most data centers, without post-processing to remove drifts in displacement, a mean determined from the overall record probably should be removed. But in this case the displacement will probably be inaccurate (compared to the displacement derived from the padded, filtered acceleration time series), it may be that a better approach is to specify the initial Velocity and displacement of the record - I am working on that (11/26/10):

-10.0

! Xfactr, used to lengthen time series to max(tend_in, xfactr per_high) Note that this is a relic from a time when I thought that this would be an important parameter. In fact, adding zeros to the input acceleration trace usually leads to an effective step in baseline and consequently a disastrous increase in long period response. In almost all cases xfactr should be set to 0.0. Because the oscillator response for a long period is close to the ground displacement, extending the time series is not needed unless the displacement has unbounded growth, in which case the long-period oscillator response is meaningless

0.0

! character string to append to filename to make the output filename:

.psa

!tskip tlength

0.0 400.0

!accel_file names

```
! ("STOP" in any column, any case, to quit)
APPALACH_dep05_dist1.000_r.smc
APPALACH_dep05_dist1.000_t.smc
APPALACH_dep05_dist1.000_z.smc
APPALACH_dep05_dist1.111_r.smc
        ...
STOP
```

The periods used for this work were sampled between 0.04−10 sec, with a total number of 300 discrete periods (see Section 3.9.2). One damping value of 5% was used. It was not necessary to remove the mean because the data is synthetic and had already been demeaned.

The result for each acceleration time series (file name listed in the control file) was an eight-column output file in ASCII format, containing 300 periods (per), frequencies (freq) and response spectra: relative displacement response spectrum (sd), pseudo-absolute response spectral velocity (pv), pseudo-absolute response spectral acceleration (pa), relative velocity response spectrum (rv), absolute response spectral acceleration (aa) and peak ground acceleration (ag). Important to this study is (pa), the 5%-damped PSA.

4.3 ARRANGING, ILLUSTRATING, AND COMPARING DATA USING PYTHON

PYTHON is an object-oriented programming language for which a wide variety of open-source libraries are available. As such, PYTHON consists in a versatile tool for data processing, computations and plot generation. A PYTHON script was used to reorganize and format the large amount of data into a more manageable set of files.

```
### ARRANGING RESPONSE SPECTRA DATA

Amount of PSA files: 2880
Arranging ...
Saving ...

Amount of new files: 960
```

In object-oriented programming terms, a *class* is defined by its *parameters* (akin to variables or "data") and by its *methods* (i.e., functions or sub-routines used to modify the "data"). The PSA *class* contains the following *parameters* and *methods*:

- Parameters:

○ Region	e.g., Appalachians	string
○ Region abbreviation	e.g., APP, CNA	string
○ Focal depth	e.g., 5, 10, 20	integer
○ Frequencies,	[…]	list

- Distances [...] list
- Psa_data .r, .t, .z, .am [...] list

- Methods of illustration:
  - Attenuation plot, plotVsDistance() 1D
  - Scatter plot, plotScatter() 2D
  - Contour plot, plotContour() 2D
- Methods of comparison:
  - Statistical distribution, plotHistogram()
  - Moving average, 1D
  - Mean difference, 2D

The *methods* listed above form the conceptual basis used in the analyses. Results for both simulations codes summarized in Chapters 5 and 6 refer to these methods. In order to avoid unnecessary repetitions in each chapter, the methods are described in the following sections.

4.4 METHODS OF ILLUSTRATION

The ground motions were initially computed for epicentral distances to the source (as specified for *FK* [Zhu 2012]). For illustration and data analysis, it is common to use hypocentral distances. A limit was placed on events at a hypocentral distance of 1.5 * focal depth to avoid using data strongly influenced by the source radiation pattern; this reduces the number of seismogram distances used from 60 to 43 distances or less (depending on the focal depth). In addition, the number of frequencies was reduced from the original set of 300 frequencies (within the range of 0.1 to 25 Hz) to 200 frequencies. Table 4.1 summarizes the number of PSA values (for each region) as a function of the focal depth. The methods of illustration summarized below were used to visualize the PSA values coming out of the simulation results.

Table 4.1 PSA-matrix dimensions dependent on focal depth (distance × frequency).

Focal depth	5 km	10 km	20 km	30 km
PSA-matrix dimensions (distance × frequency)	43 x 200	37 x 200	30 x 200	26 x 200

Attenuation Plot

An illustration of PSA attenuation with distance is shown in Figure 4.2. This specific case is for an event with a focal depth of 5 km and shows the attenuation of PSA for frequencies of about 1.5, 3, 5, 10, and 20 Hz for the CNA region. High-amplitude reflections of the seismic waves at the Moho can be observed at a hypocentral distance of about 50 km, where the attenuation rate decays relative to closer distances. This type of plot is ideal for a small dataset or for a quick assessment of PSA, but it is not practical for comparing large amounts of data. Attenuation plots were mostly used to verify computations and to better understand trends observed in other types of plots. In contrast, Figures 4.3 and 4.4 show scatter and contour plots, which are a better representation for the larger, aggregated datasets.

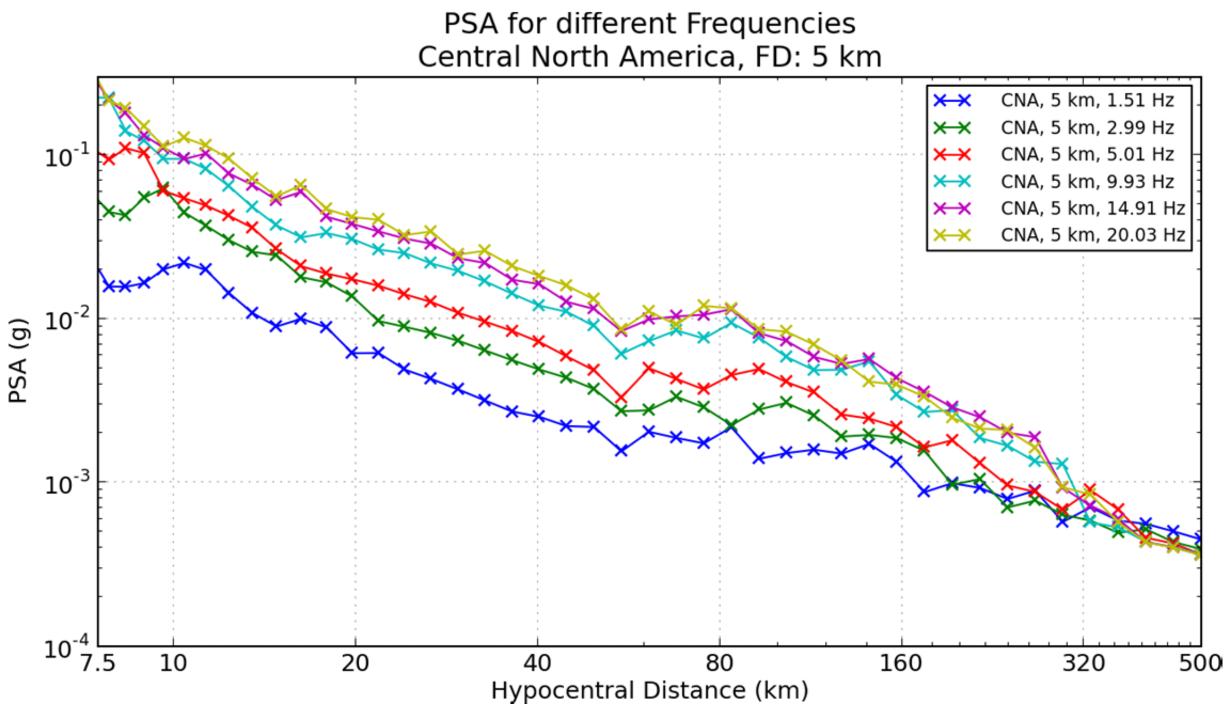

Figure 4.2 **5%-damped PSA for different frequencies (1.5, 3, 5, 10, 15, and 20 Hz) within CNA for an event with a source depth of 5 km.**

Scatter Plot

The scatter plot (Figure 4.3) shows color-coded PSA values in a map space defined by frequency and hypocentral distance. The PSA for each frequency-distance pair is represented by a colored symbol (circle). Those 43 × 200 circles are clearly separated on the *X*-axis for distances >10 km; they are overlapping on this axis for distances closer than 10 km and are also overlapping on the *Y*-axis. The scatter plot shows the raw data without smoothing or interpolation.

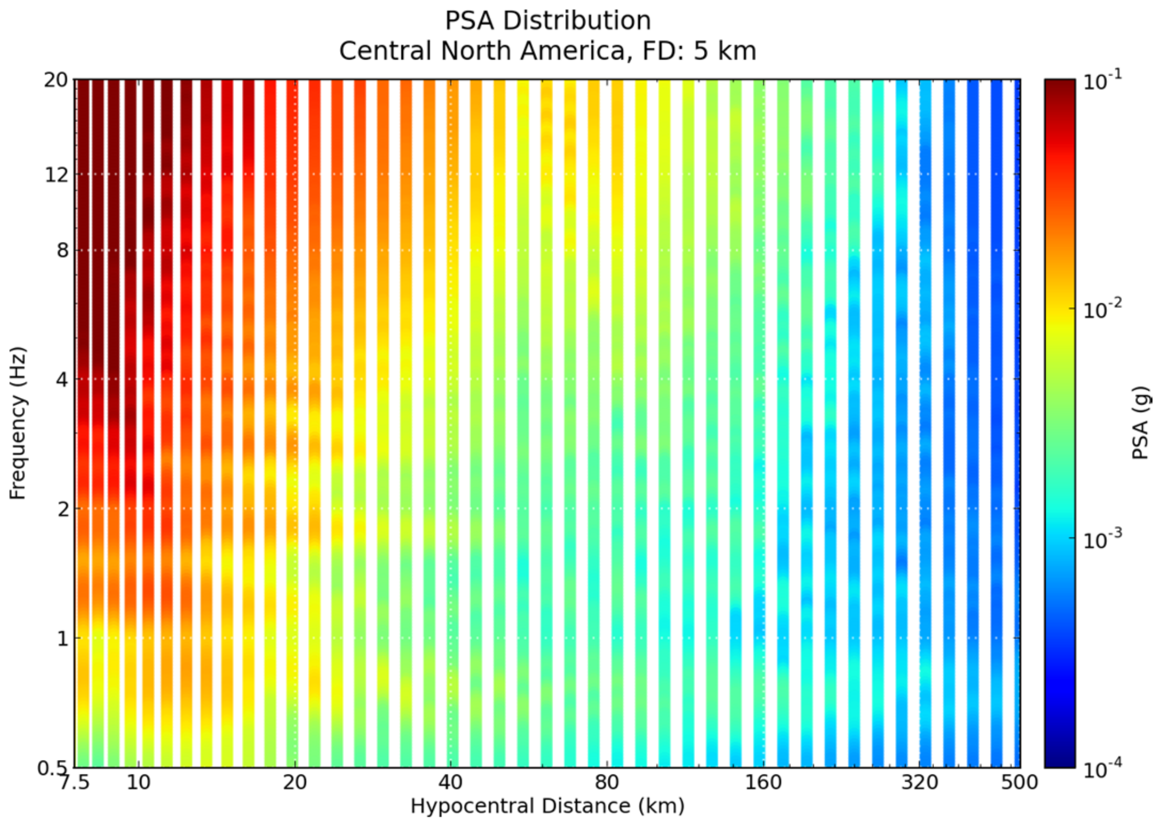

Figure 4.3 **Scatter plot showing unsmoothed and not interpolated ground response of an earthquake at 5 km depth and within the CNA region; PSA is plotted as the third dimension.**

Contour Plot

The same data illustrated in Figure 4.3 is shown as a contour plot in Figure 4.4 The illustration looks much smoother, but the data is neither smoothed, nor interpolated. One can easily visualize that increasing the size of the PSA symbols in the scatter plot will lead to the contour plot. Both 2D plots (Figures 4.3 and 4.4) present the same information, but the contour plot lacks the visual discontinuities and is easier to interpret.

This illustration of PSA is quite effective. Using a 2D illustration of the PSA data, a much larger set of data can be shown with fewer figures (compared to the attenuation plots). Only four plots are needed to show the distance and frequency-dependent PSA distribution within one region (in this case, the CNA region); one plot per focal depths. For all the contour plots in this report, the PSA color bar scheme is fixed and ranges from 10^{-4} to 10^{-1}*g* to allow direct comparisons between simulation sets (i.e. different regions and/or focal depths).

For the specific set of simulations shown on Figure 4.4 (CNA region, 5 km focal depth), the highest PSA is around 0.1–0.3*g,* which occurs at frequencies between 10–20 Hz and at hypocentral distances between 7.5 and 12 km. The PSA decreases with distance and is reduced to about 4 X 10^{-4}*g* at distances of 500 km. The lower the frequency, the lower the PSA; the rate of attenuation is also frequency-dependent. At distances of 60–100 km and at all frequencies above 2 Hz, the Moho reflections become prominent, which causes an increase in PSA. This effect is more pronounced for higher frequencies. From about 7.5 to 12 km for frequencies larger than 2 Hz or so, there is a band of higher energy. This is caused by strong reflections from the bottom of the uppermost crustal layer.

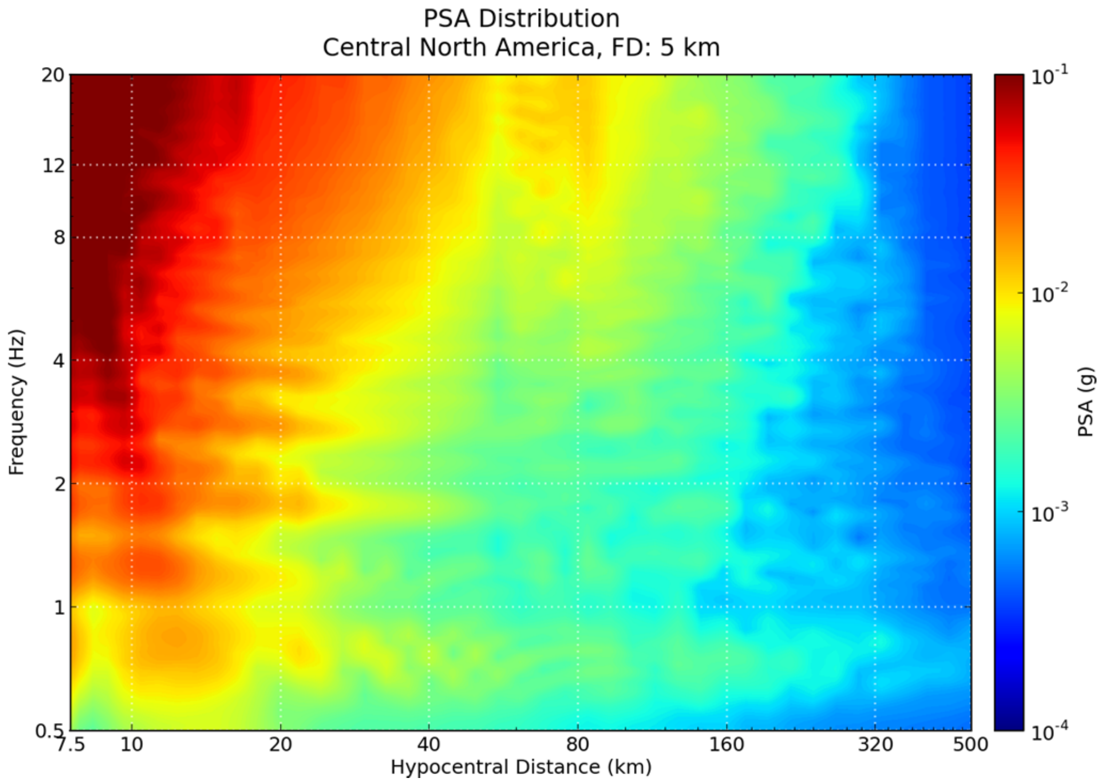

Figure 4.4 Contour plot showing unsmoothed and un-interpolated ground response of an earthquake at a depth of 5 km within the CNA region; PSA is plotted as the third dimension.

4.5 METHODS OF COMPARISON

The methods of comparison are used to identify and quantify differences in attenuation between the different CENA regions in terms of the natural log of PSA, ln(PSA). This is accomplished by comparing the distributions of ln(PSA) for a subset of binned data (bins defined by frequency and distance ranges) between regions. Ideally, a set of profiles representing the expected profile variability within each region should be defined and simulations run for each profile. Because some regions are relatively small and do not have a large number of profiles available, this was not possible. The comparisons are using CNA as the reference region to determine whether the attenuation in a region is similar or different from that of CNA. This forms the basis for grouping the tested region with CNA or assigning it to a different attenuation group. The CNA is the largest of the regions considered and had the most velocity profiles available. Based on the distributions shown in Chapter 3, a range of alternate profiles could be defined for that region. The analyses described below are based on the following: (1) the ln(PSA) variability of all regions is assumed similar to that of the CNA region (for which a range of alternate profiles was considered) and (2) for a subset of binned data, ln(PSA) follows a distribution close to a normal distribution. This second assumption was verified and judged acceptable for comparison purposes.

4.5.1 CNA Alternate Profiles

This section describes the series of alternate crustal models defined for CNA. The layer boundary and velocity sensitivity tests are an important step in estimating the influence of boundary and velocity variations relative to the representative profile. A range of uncertainty was estimated for each layer using the 2D histogram shown in Figure 3.11(b).

Figure 4.5(a) shows the velocity variations considered (layer thicknesses are fixed). The variations range between -0.2 and + 0.4 km/sec. The velocity range was set to be asymmetric to avoid very low velocity zones within the crust. Models with variations were calculated one at a time. Figure 4.5(b) shows the variations of the layer boundary depth with respect to the representative model (layer velocities are fixed). The modifications are symmetrical and in the range of ±6 km. This study considers eighteen crustal velocity models, whereby each model has only one modification at a time.

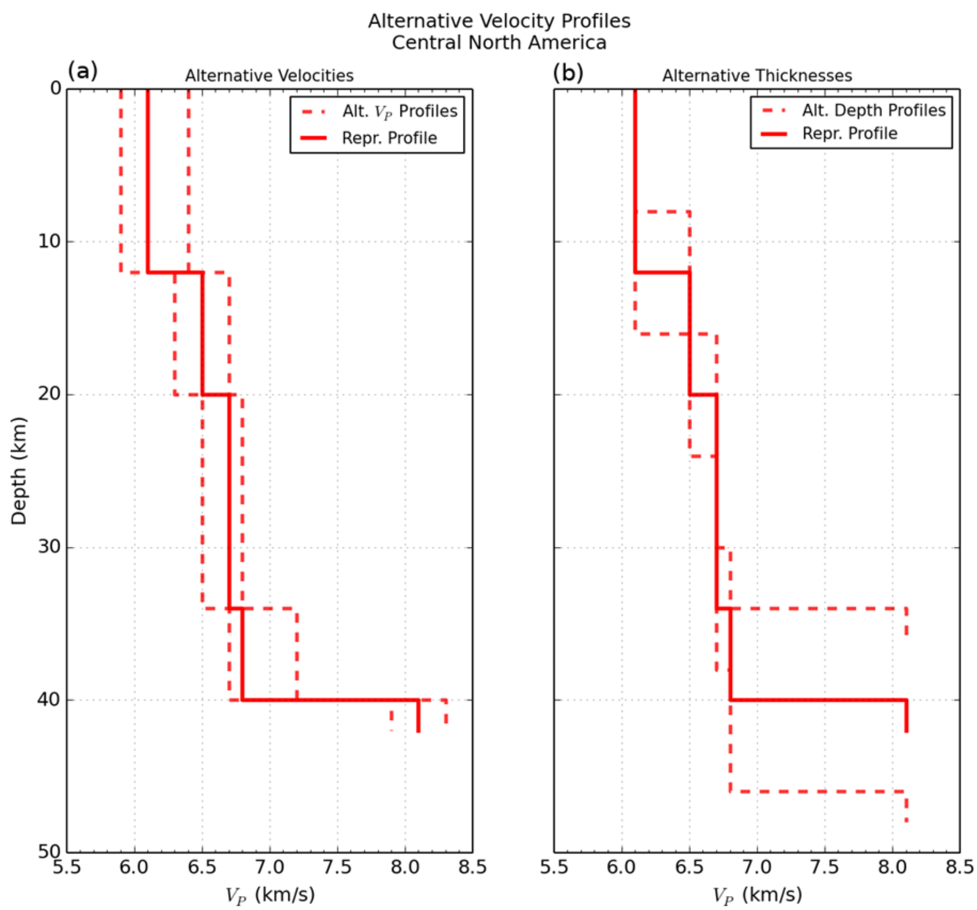

Figure 4.5 **(a) Alternative velocity profiles modifying *P*-wave velocity with fixed layer boundary depths; and (b) alternative seismic velocity profiles modifying layer thickness (i.e., boundary depths) with fixed layer velocities.**

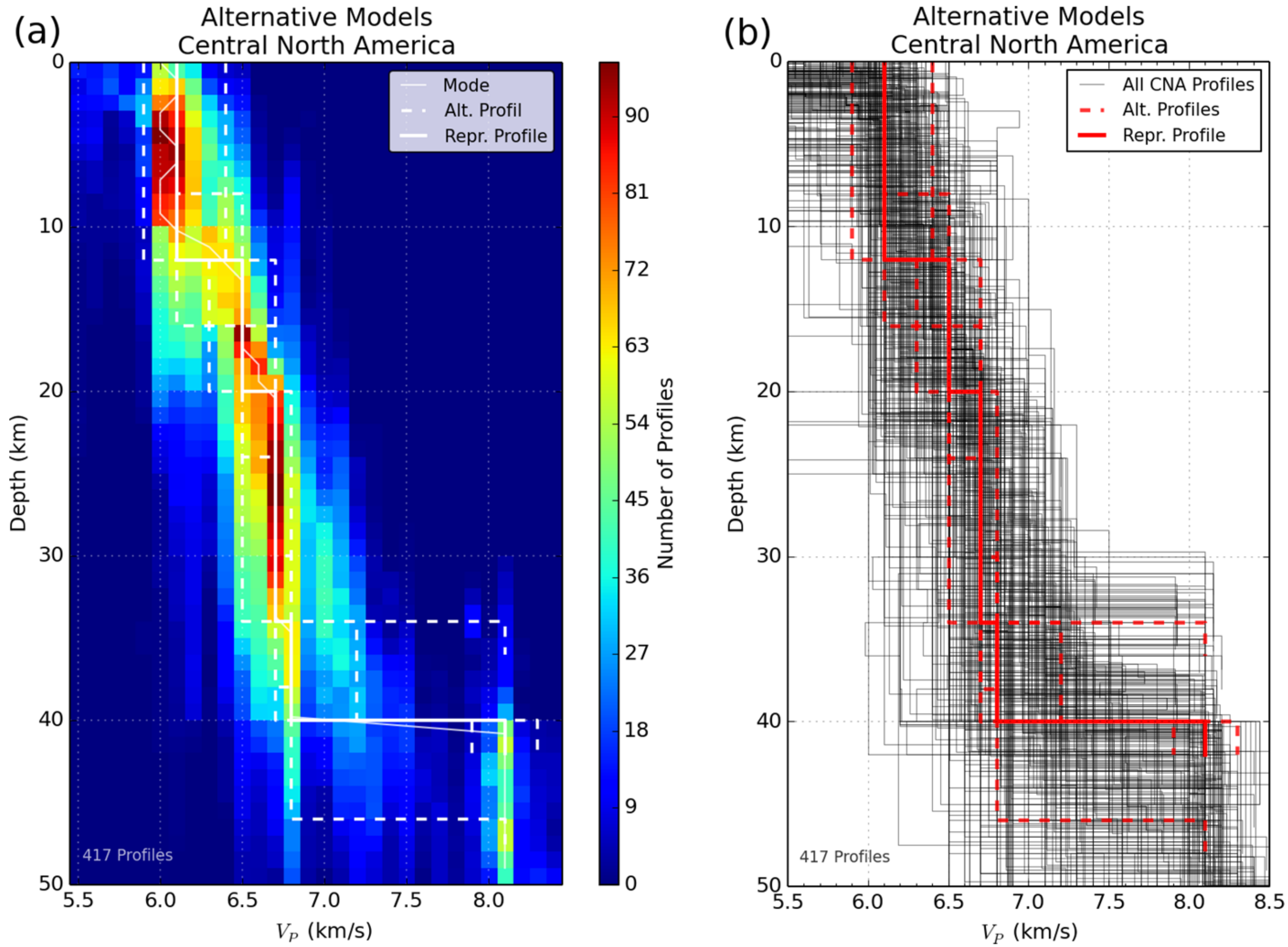

Figure 4.6 **Representative and alternative velocity profiles on top of the available seismic velocity profiles for CNA, as shown in Figure 3.11.**

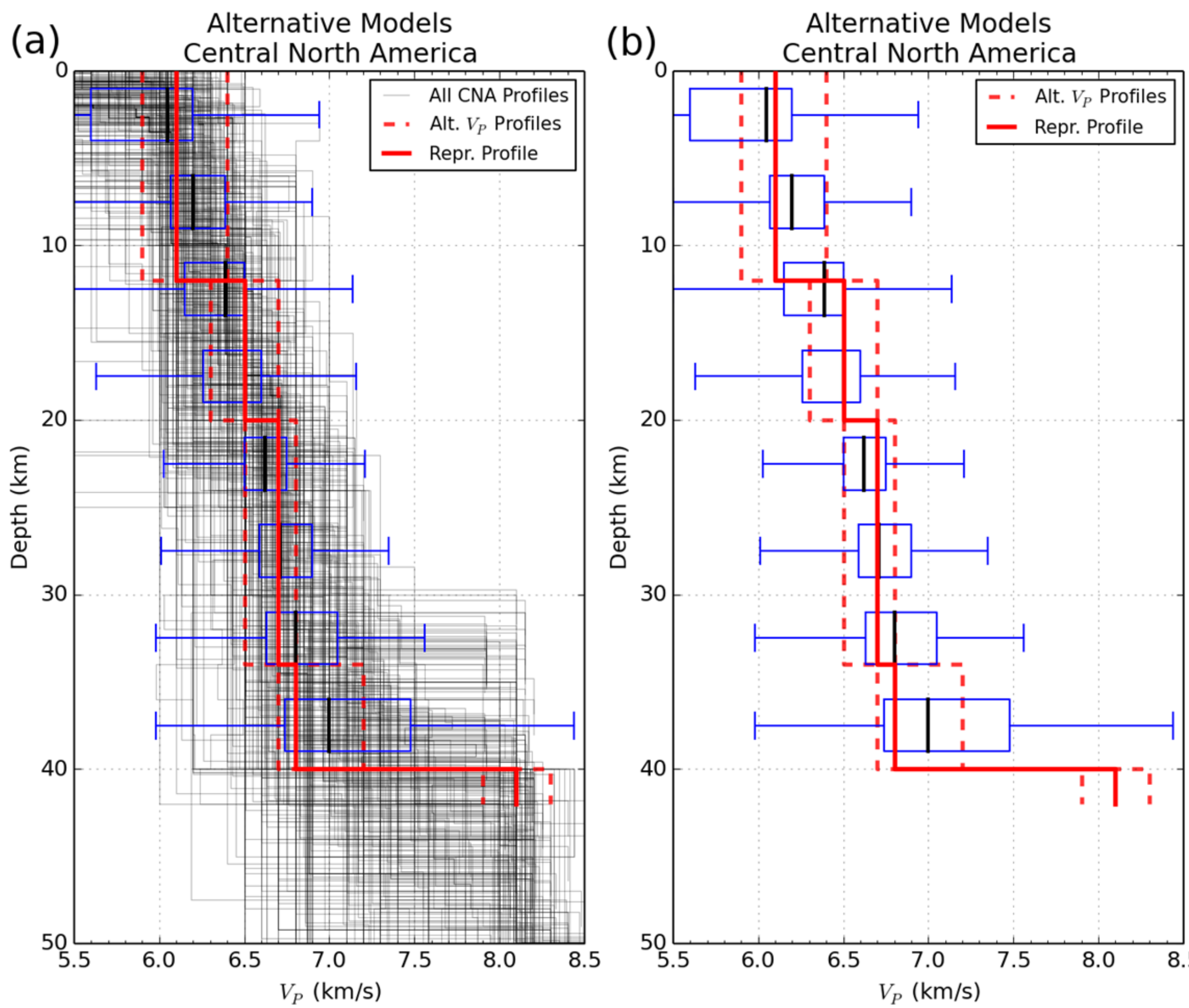

Figure 4.7 (a) Representative and alternative crustal models on top of the selected velocity profiles of CNA. Additionally, box-and-whiskers for seismic velocity uncertainties with box interval of ±25% and whiskers (blue "error bars") at ± 45% (black line within the box represents the median); and (b) box-and-whiskers without the velocity profiles.

Figure 4.7(a) shows box-and-whiskers plots of the selected velocity profiles for CNA. The profiles are plotted in the background. The boxes are placed every 5 km; if the box is at 7.5 km depth, the box shows the velocities between 5 to 10 km. Fifty percent of the profiles can be found within the box, with a median marked as the black line. The whiskers encompass a range of 5% to 95%, where 90% of the velocity profiles lie. Figure 4.7(b) shows box-and-whiskers plots and superimposed are our preferred representative profile and two alternatives. It is evident that the selected representative profile lies completely within the box and very often very close to the median, with two depth intervals being congruent (15–20 and 25–30 km). There are 18 alternative crustal structures for the CNA region as well, which offer 18 additional ground motion patterns. These alternatives were combined to form a matrix with a dimension of 43 distances × 200 frequencies (at focal depth 5 km), and 18 ln(PSA) values assigned to each distance-frequency pair (hence 43 × 200 × 18 values).

All the regions are associated with their own representative profile, as defined in Chapter 3. The short-hand REG_{Rep} is used to represent ln(PSA) from the representative profile, where REG is replaced with the appropriate three-letter acronym of the specific region referenced. The CNA is the only region to have ln(PSA) associated with simulations from the suite of alternate profiles defined above. These ln(PSA) values are referred to as CNA_{Alt}. This notation is used in the following sections and clarified for each comparison method, as appropriate.

Statistical Distribution

The PSA domain shown in Figure 4.4 was subdivided into smaller bins, summarized in Table 4.2. The same bins are illustrated on the contour plot in Figure 4.5.

Table 4.2 Distance and frequency bands of interest for statistical analyses.

Distances (km)	Frequencies (Hz)
35–70	0.5–1; 5–10
70–140	0.5–1; 5–10
140–280	0.5–1; 5–10
280–500	0.5–1; 5–10

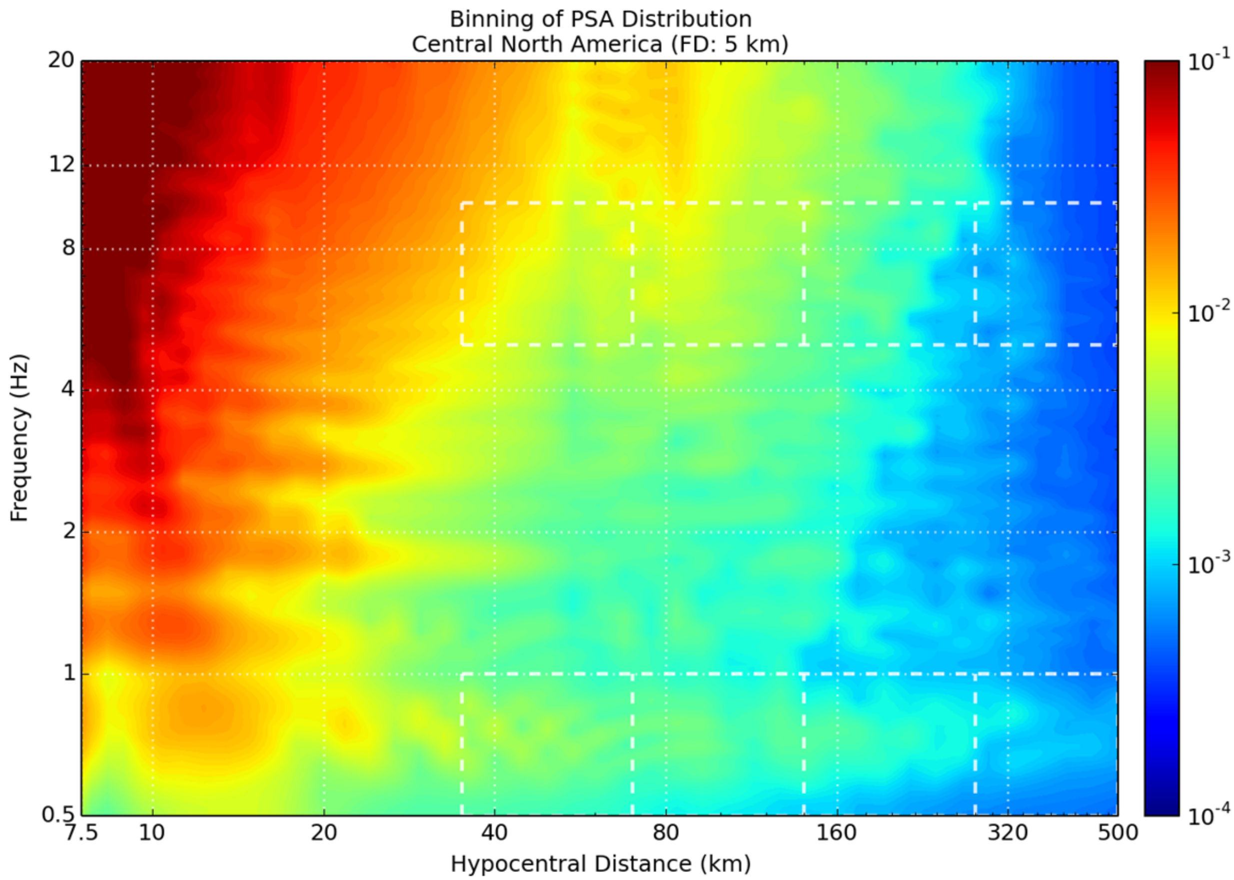

Figure 4.8 **The PSA distribution overlaid by a grid showing the distance and frequency bands of interest.**

The two frequency groups were selected to represent relatively low frequencies (0.5−1 Hz) and high frequencies (5−10 Hz). As shown on Figure 4.5, those two groups show systematic differences in the rate of attenuation, with the low frequencies attenuating more slowly than the high frequencies with distance. The distance bins were defined to capture (1) the important features of the Moho reflections, which generally occur in the distance range of 40−120 km and (2) the effect of anelastic attenuation (*Q*) at distance larger than 70−120 km. Basically, the selected distance and frequency bins are used to disaggregate the contour plots into data subsets where differences are expected between regions. The selected binning also allows an easier interpretation of general trends of attenuation with respect to distance and frequency.

Histograms of ln(PSA) for those selected distance and frequency bins are used to compare PSA within CNA and across regions (see example shown in Figure 4.6). Essential variables for this analysis are the mean and standard deviation for each logarithmic normal distribution.

The histogram illustrated in Figure 4.6 shows the distributions of ln(PSA) values of two datasets defined in the 35–70 km distance for a 5-km-deep source and the 5–10 Hz frequency band. The green colored bars show the ln(PSA) values for the CNA representative model (CNA_{Rep}), while the transparent white colored bars show the distribution for the alternative models considered (CNA_{Alt}), which are intended to represent the uncertainty within the region. Note that the light green color originates from the overlying of the transparent white on top of the green distribution (there is no third distribution). The top right corner of the plot provides the mean (μ) and the standard deviation (σ) from both distributions. The mean and standard deviation terms are always associated with the distribution of ln(PSA). The abbreviations are explained in Table 4.3.

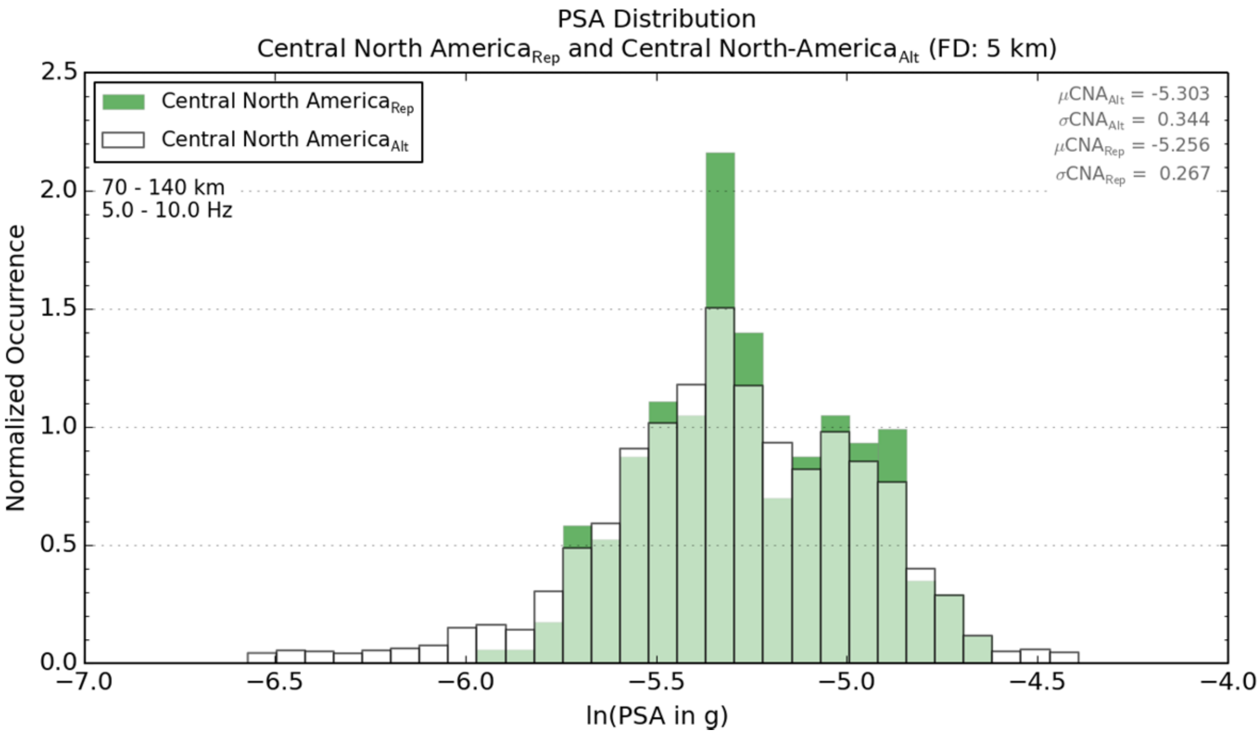

Figure 4.9 **ln(PSA) distribution from CNA's representative and alternative models. The histogram shows the ln(PSA)-values of the 70–140 km distance and the 5–10 Hz frequency bin. The top right corner shows information about the mean and the standard deviation of each distribution.**

Table 4.3 **Abbreviations of ln(PSA) for statistical distribution.**

Abbreviations for log-normal PSA distribution	Explanation
μCNA_{Rep} and σCNA_{Rep}	μ and σ define the log-normal distribution of PSA-values within a distance and frequency band as defined in Table 4.2. μ and σ are two digits. Used input data are from the *representative model of Central North America*.
μCNA_{Alt} and σCNA_{Alt}	μ and σ define the log-normal distribution of PSA-values within a distance and frequency band as defined in Table 4.2. μ and σ are two digits. Used input data are from the *alternative models of Central North America*.
μREG_{Rep} and σREG_{Rep}	μ and σ define the log-normal distribution of PSA-values within a distance and frequency band as defined in Table 4.2. μ and σ are two digits. Used input data are from the *representative model of a region, e.g., of the Appalachians (REG=APP)*.

The ground motion generated using the set of alternative velocity profiles includes the uncertainty of ground motion within the CNA region itself. The $\mu\,\mathrm{CNA}_{Rep}$ and $\mu\,\mathrm{CNA}_{Alt}$ are -5.26 and -5.30, respectively, and $\sigma\,\mathrm{CNA}_{Rep}$ and $\sigma\,\mathrm{CNA}_{Alt}$ are 0.27 and 0.34, respectively. The means of both distributions are very close. The ln(PSA) distribution from CNA_{Rep} lies within the broader distribution of CNA_{Alt}, confirming that the representative profile accurately reflects the velocity structure of the region in term of ground motions. It can also be confirmed that the same is valid for the other distance and frequency bands and focal depths (see Appendix D). All regions will be compared to CNA using $\left(\mu\mathrm{CNA}_{Alt}\right)$ and $\left(\sigma\mathrm{CNA}_{Alt}\right)$. Tables of μ and σ for each region's bins and focal depths can be found in Appendix D.

Moving Average on Attenuation Plots

One type of comparison between regions is performed in the attenuation plot space using a moving window average. Figure 4.7 summarizes the moving window average process and Figure 4.8 shows an example set of results. Each of the black line on Figure 4.7 corresponds to a PSA vector at a given distance (set of PSA values from a frequency range such as, for example, 5–10 Hz). For a focal depth of 5 km, there are 43 vectors for each of the 43 distances. The moving window averages the data over three distances for the given frequency band, and assigns the average PSA value (μ), and the standard deviation (σ) to the middle distance. This smoothing process reduces the number of distances by a factor of two and leads to a maximum hypocentral distance of 450 km. Applying the moving window to a region results in distance-dependent vectors of μ and σ. The moving average method considers the ln(PSA) statistics over a frequency band for a fixed distance, one distance at-a-time. This is referred to as a 1D statistics approach.

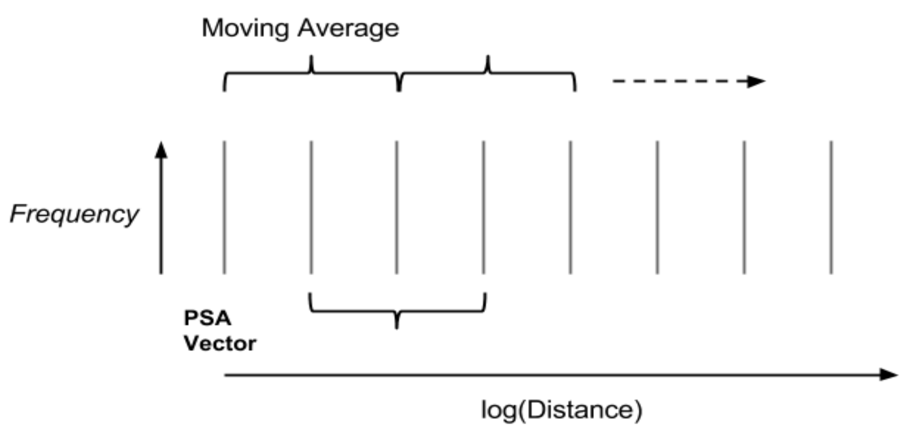

Figure 4.10 Principle of computing the mean and standard deviation using a moving window average over three distances and a frequency band.

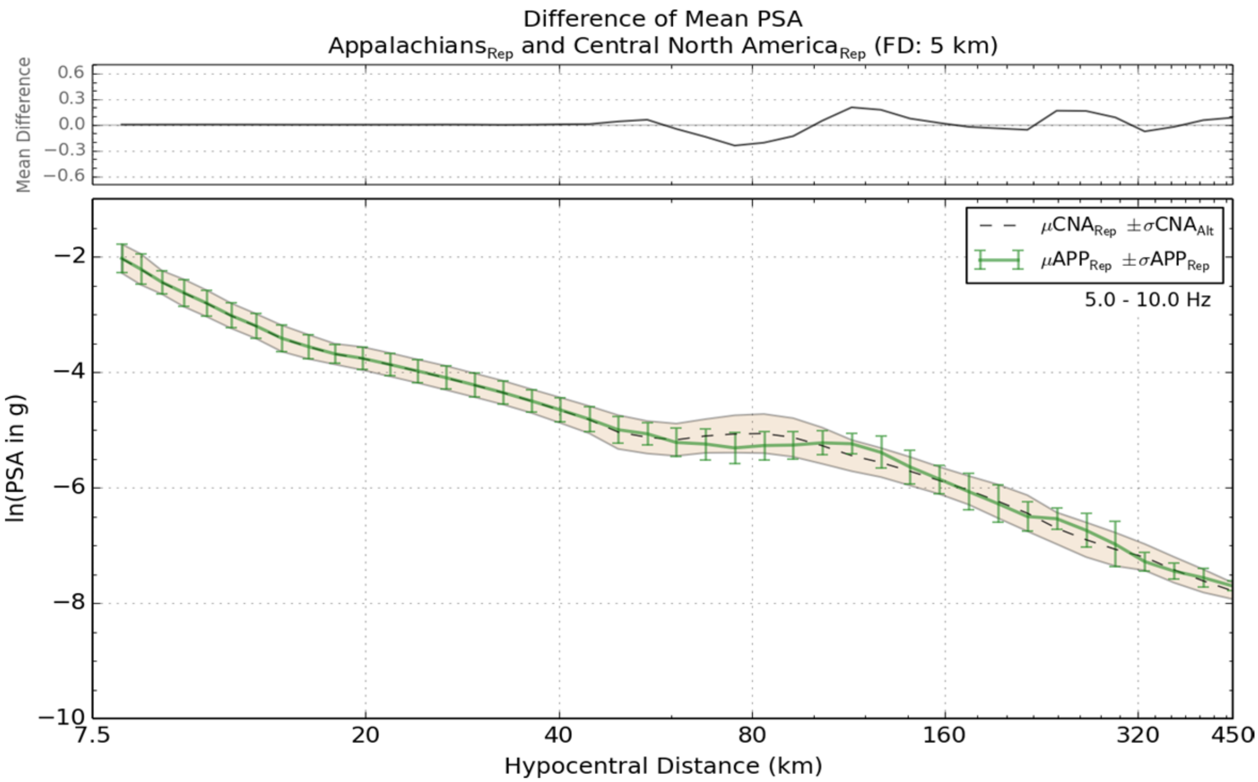

Figure 4.11 **Comparison of ln(PSA) mean values for the representative crustal models for the APP and CNA regions within the standard deviation of CNA ground motion varieties using the alternative model. The method of moving averages was used over three distances and for the frequency bin 5–10 Hz. The upper plot represents the difference of the PSA mean of the two representative regions.**

Table 4.4 **Abbreviations of ln(PSA) for moving average method.**

Abbreviations for moving average method	Explanation
μCNA_{Rep} and σCNA_{Rep}	μ and σ are PSA-vectors dependent on distance. They contain PSA-values, averaged over distance and a frequency bin. Used input data are from the *representative model of Central North America (CAN).*
μCNA_{Alt} and σCNA_{Alt}	μ and σ are PSA-vectors dependent on distance. They contain PSA-values, averaged over distance and a frequency bin. Used input data are from the *alternative models of Central North America*.
μREG_{Rep} and σREG_{Rep}	μ and σ are PSA-vectors dependent on distance. They contain PSA-values, averaged over distance and a frequency bin. Used input data are from the *representative model of a region, e.g., of the Appalachians (REG=APP).*

Figure 4.8 shows a comparison between the APP and CNA regions. The $\mu\mathrm{CNA}_{Rep}$ is represented by a dashed black line, and the region's standard deviation including the variability due to the alternate profiles $\sigma\mathrm{CNA}_{Alt}$ is indicated through a beige shaded band with a width of 2σ. The ground motions of a given region (the APP region in this case) are always compared to CNA. The values of μ and σ for other regions are displayed with a solid green line and the whiskers also span the 2σ. range. The top plot on Figure 4.8 shows the differences of the means between CNA_{Rep} and the region considered. Table 4.4 shows abbreviations and definitions used on moving average plots.

The criterion for deciding whether or not the ground motion of the four regions are significantly different from those of CNA is whether or not the mean of a region lies within the range of $\mu\mathrm{CNA}_{Rep}$ +/- $\sigma\mathrm{CNA}_{Alt}$. If it does lie within this range, and the standard deviation is also within $\sigma\mathrm{CNA}_{Alt}$, then the region can be placed in the same attenuation group as CNA. If a region's mean is significantly different from $\sigma\mathrm{CNA}_{Alt}$ then that region most likely belongs to another attenuation group.

Mean Difference (Normalized Mean Difference Method)

The application of the method called mean difference consists of three steps:

1. compute the mean difference between a region and CNA:

$$\mu\mathrm{REG}_{Rep} - \mu\mathrm{CNA}_{Rep}$$

2. compute the standard deviation of $\mathrm{CNA}_{\mathrm{Alt}}$:

$$\sigma\ CNA_{Alt}$$

3. normalize the mean difference by the standard deviation from $\mathrm{CNA}_{\mathrm{Alt}}$:

$$\frac{\mu REG_{\mathrm{Re}p} - \mu CNA_{\mathrm{Re}p}}{\sigma CNA_{Alt}} \tag{4.1}$$

In the mean difference method, the statistics include data for both dimensions of the frequency−distance bins. This is referred to as a 2D statistics method. This 2D method results in matrices of the mean difference (step one from above, Figure 4.9) and a matrix of the standard deviation for $\mathrm{CNA}_{\mathrm{Alt}}$ (step two from above, Figure 4.10). The final matrix comes from equation 4.1. Both matrices involved in Equation 4.1 have the same dimensions and the subtraction and division of the two matrices are made "point by point" (Figure 4.11).

The criterion for whether or not the ground motions of the four regions are significantly different from those of CNA is whether or not the mean of a region lies within the range of $\mu\mathrm{CNA}_{Rep}$ +/- $\sigma\mathrm{CNA}_{Alt}$. If the majority of the 2D map (Figure 4.11) fulfills the following constraint:

$$\frac{\mu \mathrm{REG}_{Rep} - \mu \mathrm{CNA}_{Rep}}{\sigma \mathrm{CNA}_{Alt}} < 1 \tag{4.2}$$

then the mean of the representative region $\left(\mathrm{REG}_{Rep}\right)$ lies mostly within the standard deviation of CNA_{Alt} and the region can be placed in the same attenuation group as CNA. If the majority of the 2D map does not fulfill Equation (4.2), but rather the following relation:

$$\frac{\mu \mathrm{REG}_{Rep} - \mu \mathrm{CNA}_{Rep}}{\sigma \mathrm{CNA}_{Alt}} > 1 \tag{4.3}$$

then the region's mean is significantly outside of $\sigma \mathrm{CNA}_{Alt}$ and the region most likely belongs to an alternative attenuation group.

Table 4.5 Abbreviations of ln(PSA) for mean differences, normalized by the CNA standard deviation.

Abbreviations for normed mean difference	Explanation
$\mu \mathrm{CNA}_{Rep}$ and $\sigma \mathrm{CNA}_{Rep}$	μ and σ are PSA-matrices. They contain PSA-values, averaged over distance, but not over frequency. Used input data are from the *representative model of Central North America*.
$\mu \mathrm{CNA}_{Alt}$ and $\sigma \mathrm{CNA}_{Alt}$	μ and σ are PSA-matrices. They contain PSA-values, averaged over distance, but not over frequency. Used input data are from the *alternative models of Central North America*.
$\mu \mathrm{REG}_{Rep}$ and $\sigma \mathrm{REG}_{Rep}$	μ and σ are PSA-matrices. They contain PSA-values, averaged over distance, but not over frequency. Used input data are from the *representative model of a region, e.g., of the Appalachians (REG=APP).*

Figure 4.9 shows an example of difference in the means, which was obtained by subtracting the mean of CNA from the APP mean. Figure 4.10 shows the standard deviation of the ground motions for the 18 alternative models of CNA. It is assumed that the other regions have the same variability as CNA. The range of $\sigma \mathrm{CNA}_{Alt}$ is mostly between 0.1 and 0.3 ln(PSA), reflecting a difference of 10–30%. Figure 4.11 shows the final product of the comparison between the APP and CNA regions using the normalized difference method. The plot is mainly characterized by normalized mean differences spanning the -1 and 1 range. At larger distances there are values slightly greater than 1 and a few are slightly lower than -1. A ratio of -1 or 1 implies that the difference of the means of CNA and the region being compared is as high as the standard deviation (including the alternative models); therefore, the difference is therefore within the uncertainty for the CNA region. If one projects this statement to the moving window method, a ratio between -1 and 1 implies that the mean of the region (i.e., the APP region, continuous green line) lies within the standard deviation of CNA (alternative models are shown

as beige shaded area). If the ratio is outside this interval, the mean line (continuous green line) lies outside the uncertainty of CNA (beige shaded band). As shown on Figure 4.11, the distribution of ln(PSA) from the APP region fit very well within the values for CNA. Thus, the mean values of PSA for the representative crustal models are relatively close. Considering an event with a focal depth of 5 km, the percentage of APP ratios (percentage of the area in Figure 4.11) that fulfill Equation (4.1) is 91.2%.

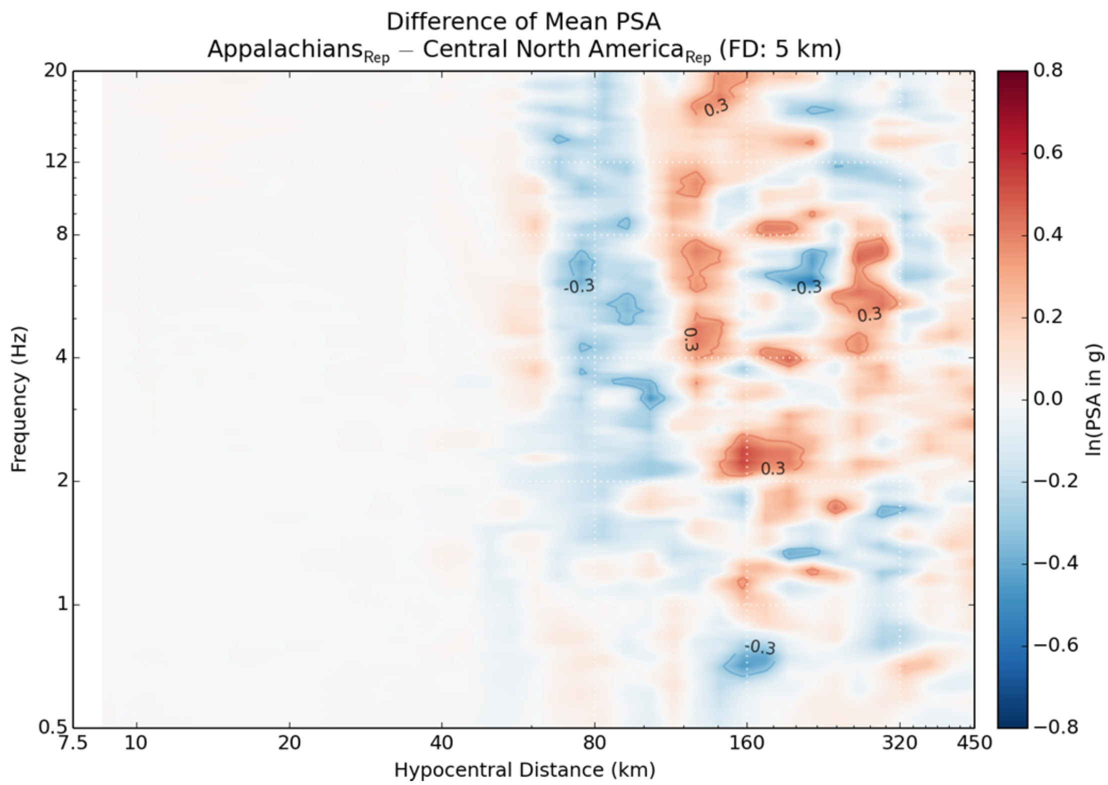

Figure 4.12 **Difference of mean PSA: compared is the APP region to can region at an event's focal depth of 5 km. Contour lines are at -0.6, -0.3, 0.3, and 0.6.**

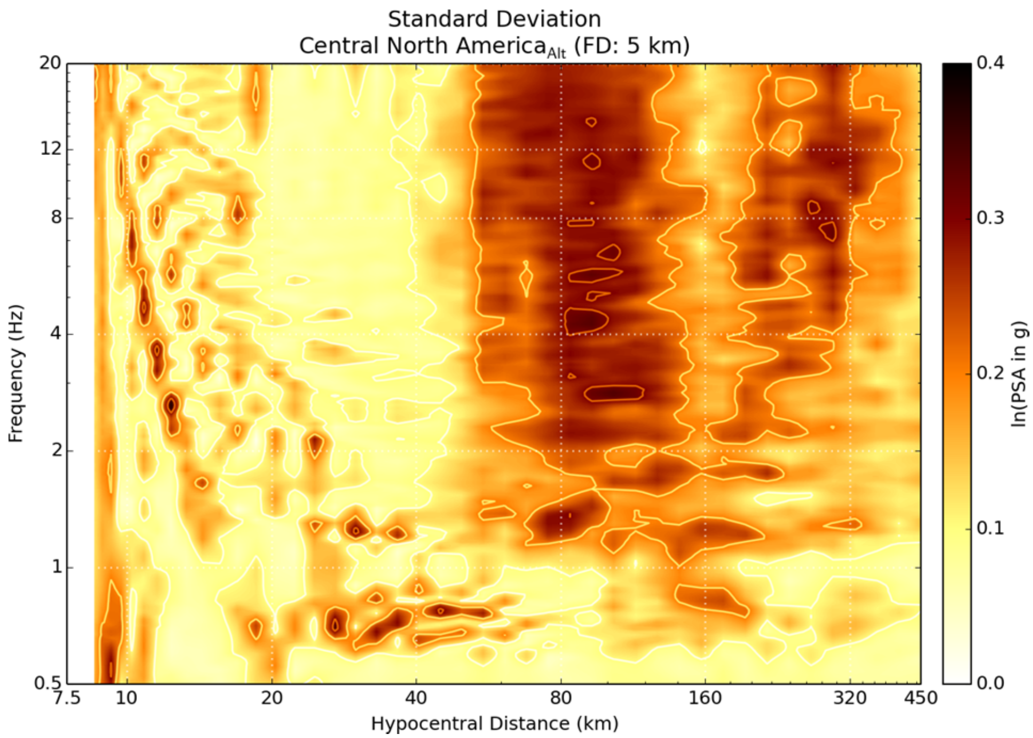

Figure 4.13 Standard deviation for CNA using all alternative models for this region at an event's focal depth of 5 km. Contour lines are at 0, 0.1, 0.2, 0.3, and 0.4.

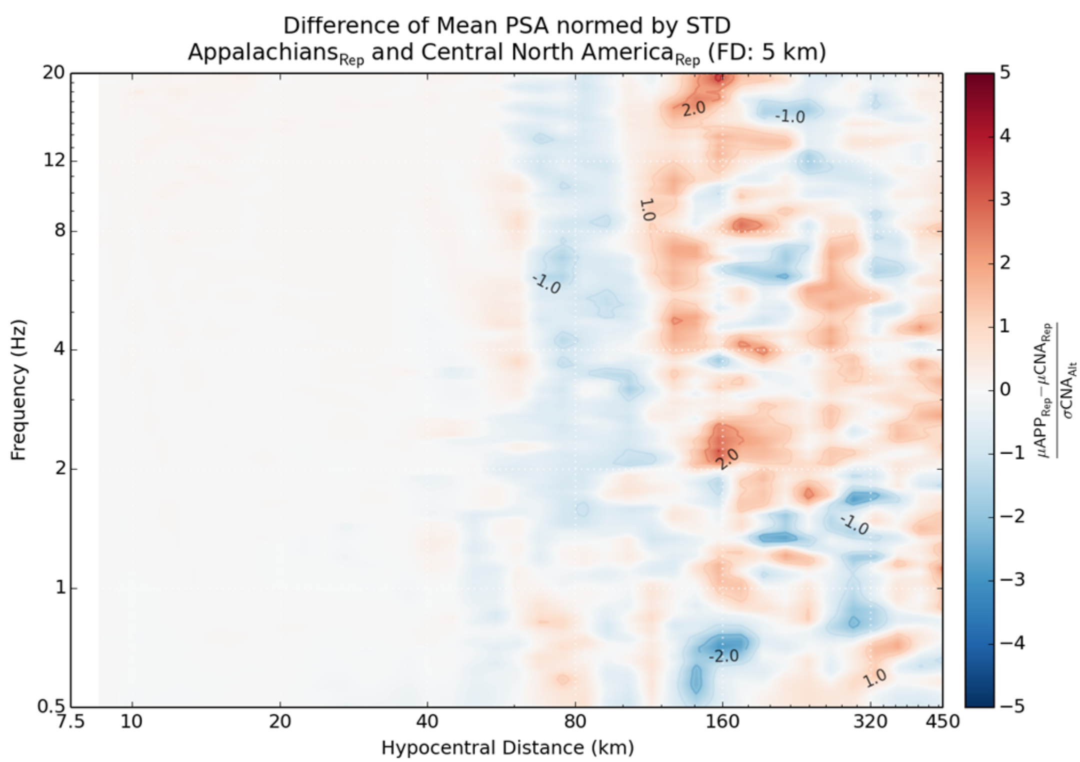

Figure 4.14 Difference of mean PSA normed by standard deviation (STD). Compared is the APP region to can region for an event with a focal depth of 5 km. Mean PSA values range between -5 and 5.

5 Results: Frequency-Independent *Q*

This chapter presents samples results from intermediate products generates with the program *FK* and summarizes the results from computations described in Chapter 5, for all the regions.

5.1 SYNTHETIC TIME SERIES

Sample synthetic time series generated with *FK* [Zhu 2012] are shown in Figures 5.1–5.7. While Figures 5.1–5.3 show traces of displacement (for easy comparison of waveforms), Figures 5.4–5.7 show record sections of radial velocity. The horizontal radial component shows the highest amplitudes of ground motion, whereas the transverse component, because of the chosen focal mechanism and azimuth of stations (Sections 3.5 and 3.10), shows almost no displacement (Figure 5.1). A sample set of time series for all regions is shown in Figures 5.2 and 5.3 for two different distances of a 5-km-deep source. Waveforms in Figure 5.2 are quite similar due to the shallow earthquake source and relatively close distance. More regional differences are visible in Figure 5.3; the 54 km distance allows a few more reflections to affect the time series. Additional record sections show synthetic ground velocity caused by earthquakes with focal depths of 5 km and 30 km, respectively, within the CNA and MEM regions (Figures 5.4–5.7).

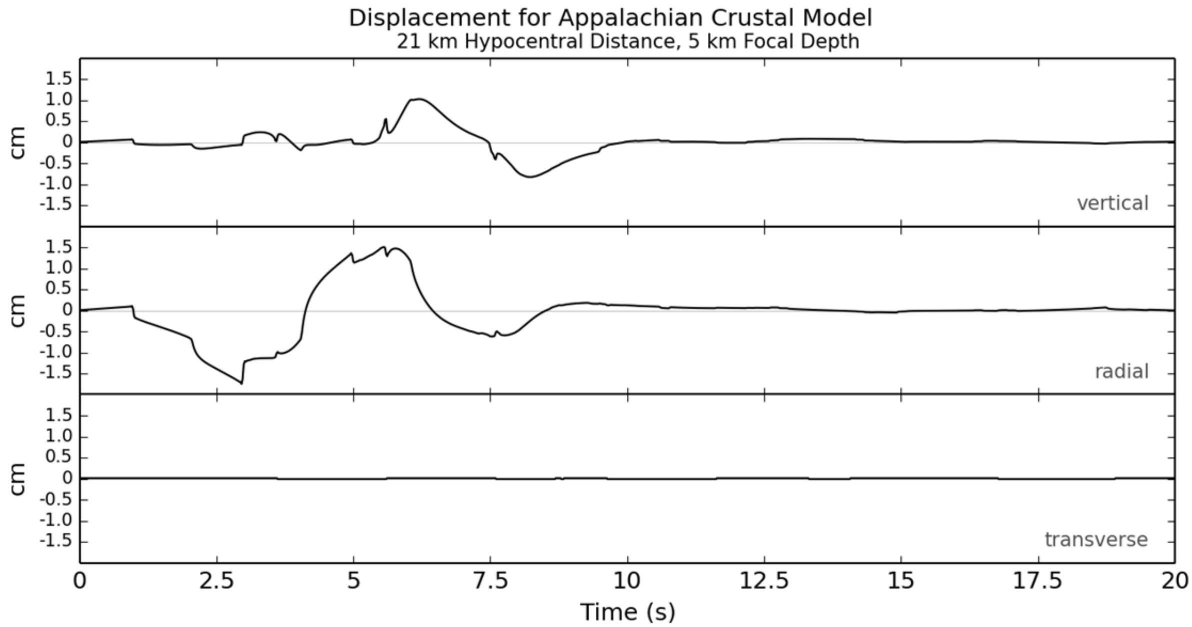

Figure 5.1 **Displacement for components vertical, radial, and transverse for the APP region at a hypocentral distance of 21 km for an event with a focal depth of 5 km.**

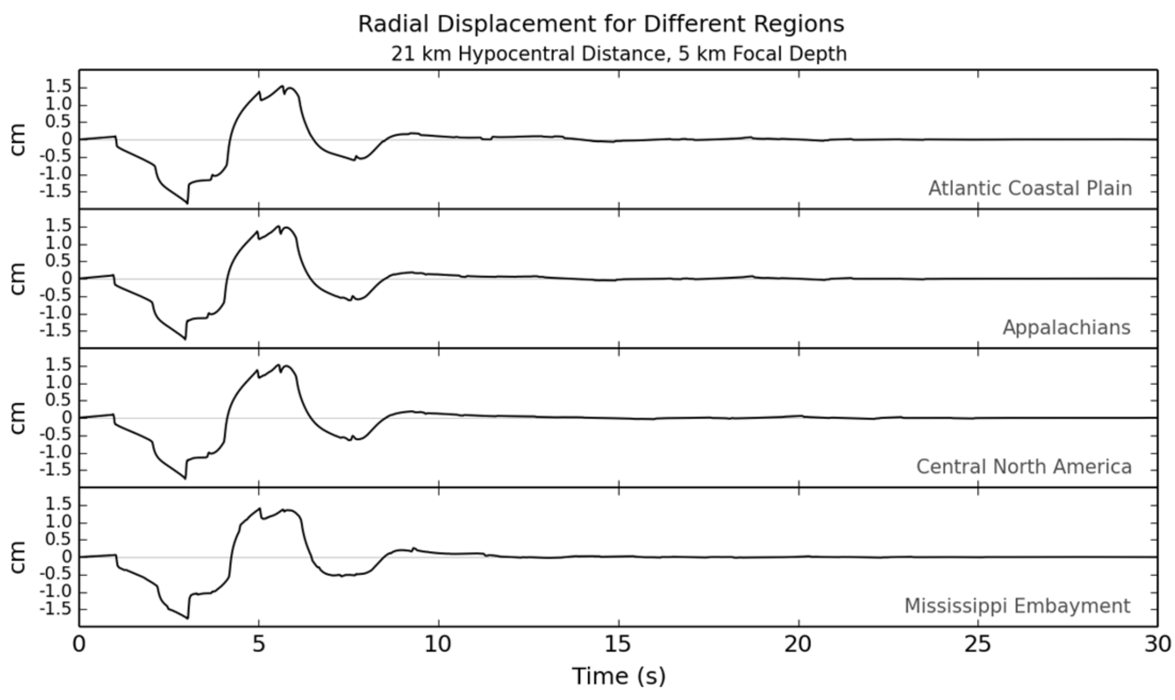

Figure 5.2 **Radial displacement for all regions at a hypocentral distance of 21 km for an event with a focal depth of 5 km.**

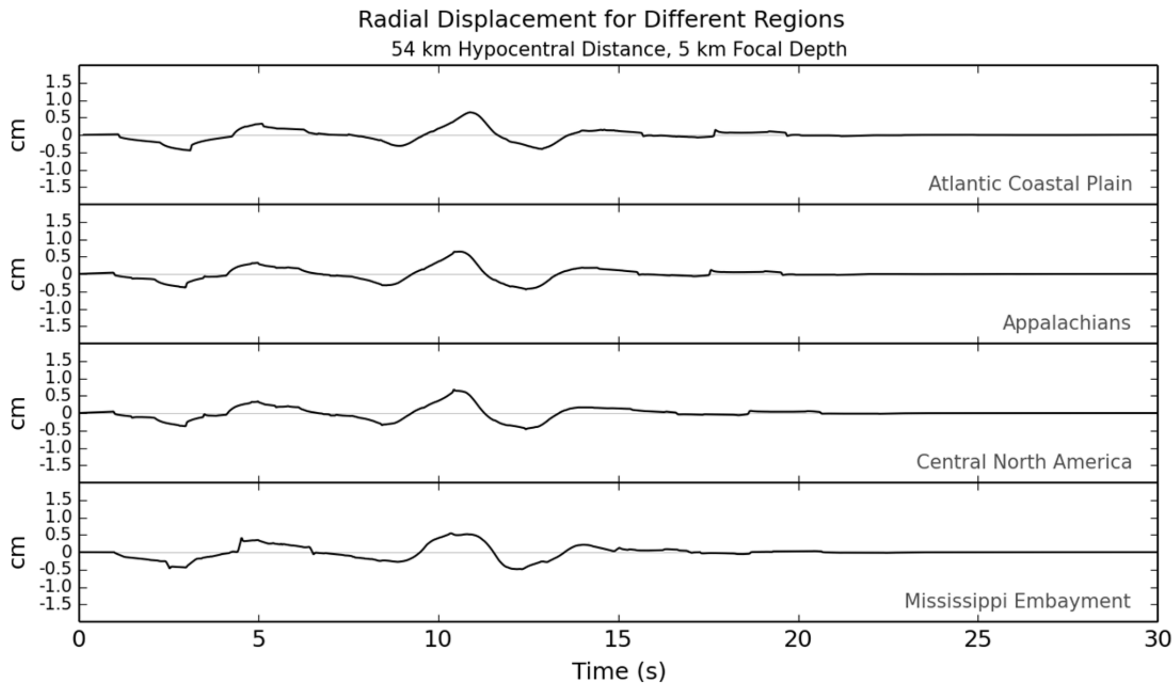

Figure 5.3 **Radial displacement for all regions at a hypocentral distance of 54 km for an event with a focal depth of 5 km.**

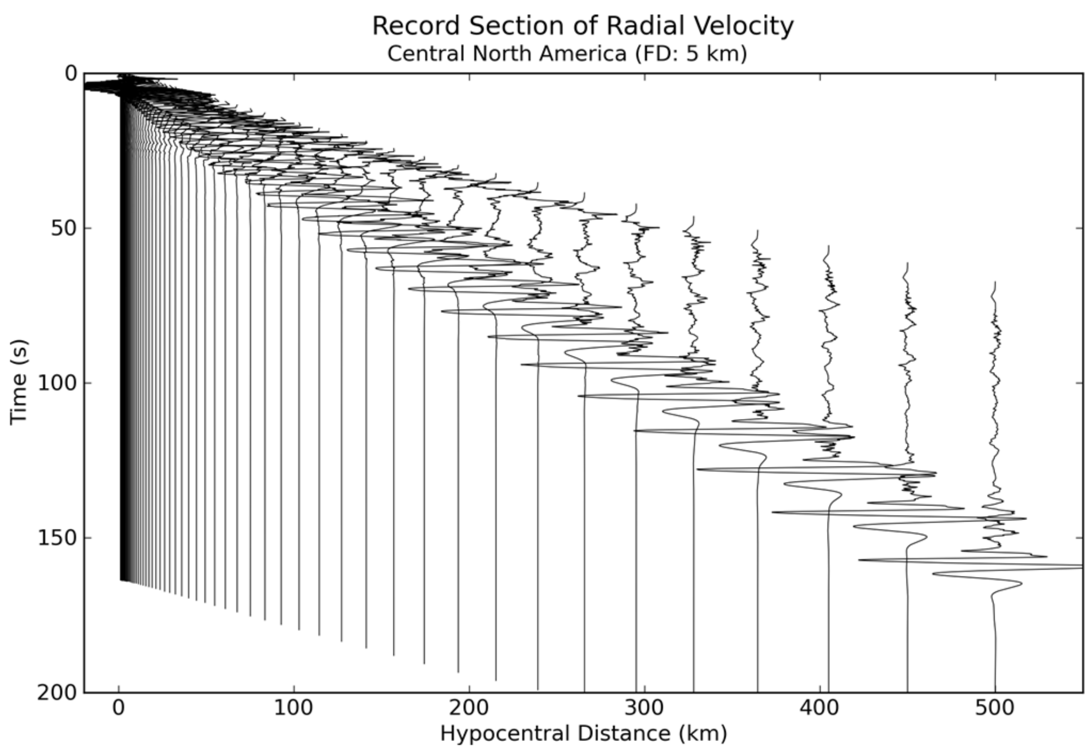

Figure 5.4 **Record section of the radial component for CNA for an event with a focal depth of 5 km.**

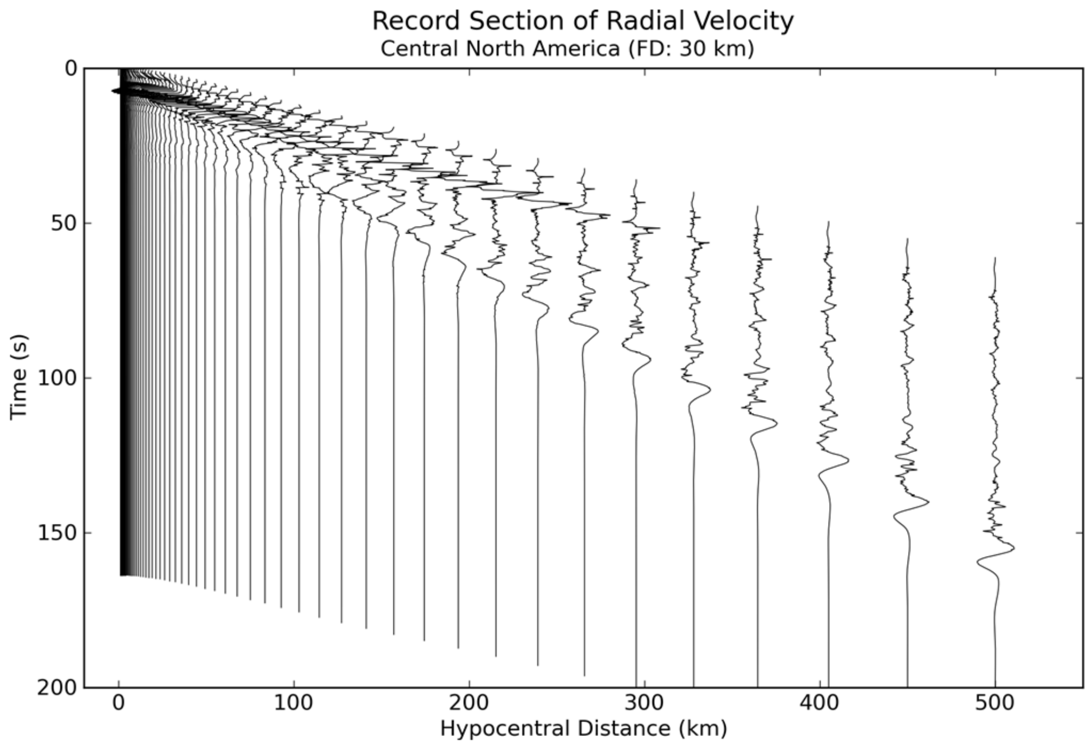

Figure 5.5 **Record section of the radial component for CNA for an event with a focal depth of 30 km.**

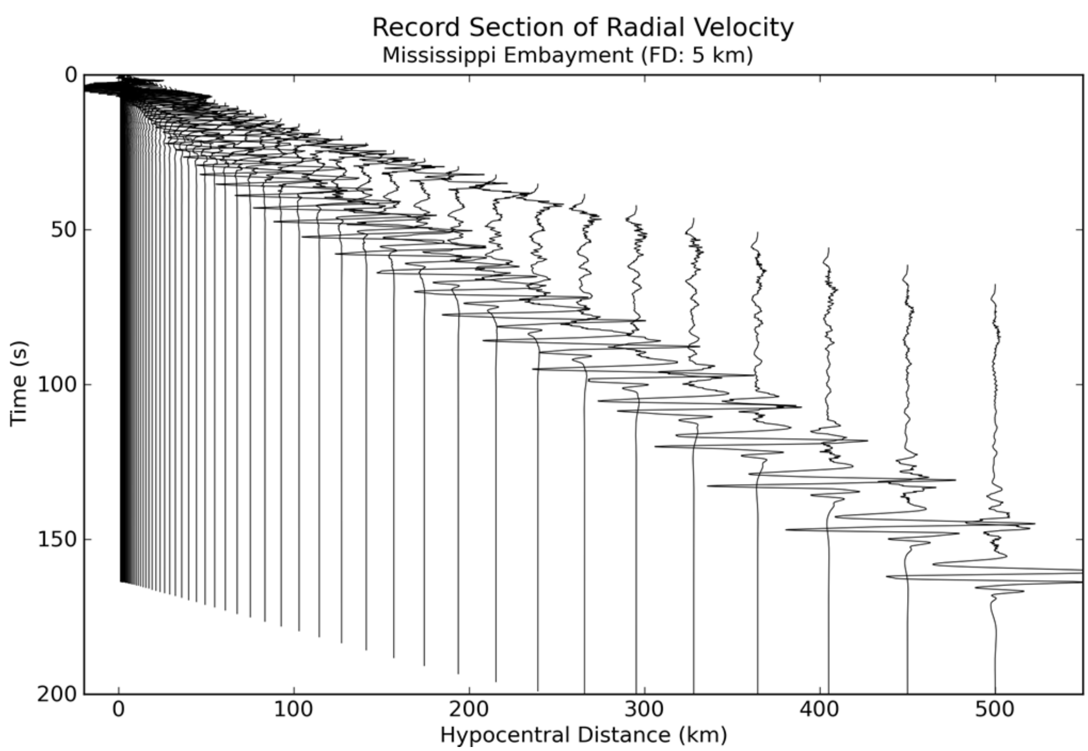

Figure 5.6 **Record section of the radial component for the MEM region for an event with a focal depth of 5 km.**

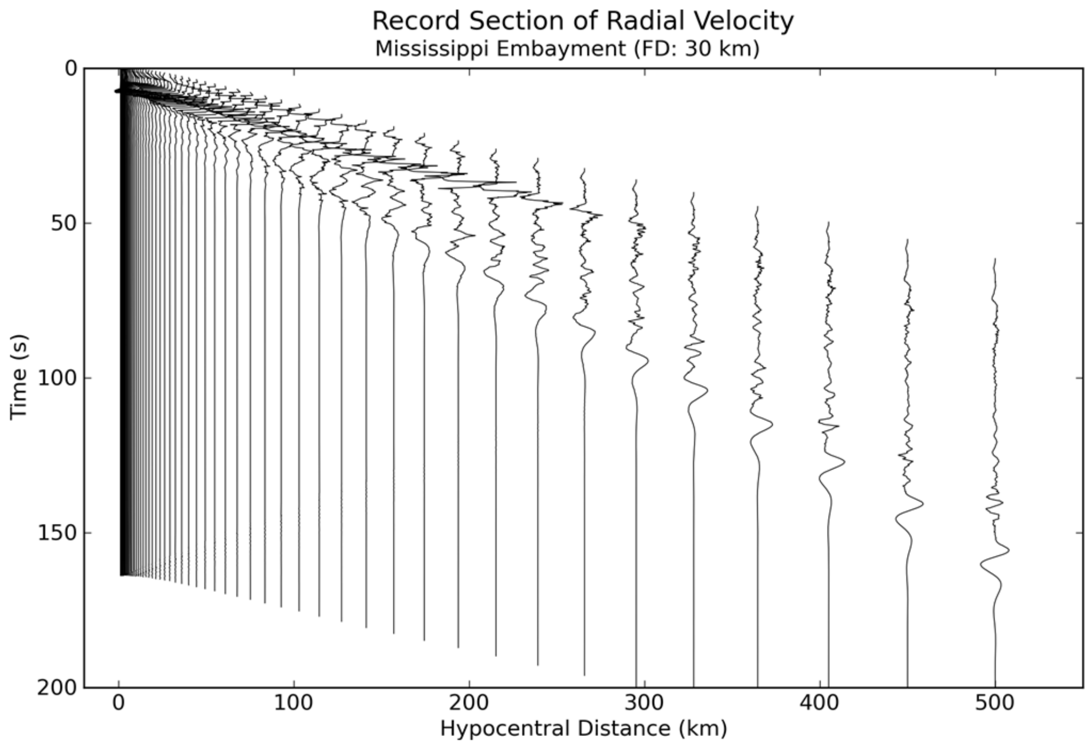

Figure 5.7 **Record section of the radial component for the MEM region for an event with a focal depth of 5 km.**

5.2 5%-DAMPED PSA

Figures 5.8−5.10 show ground motions as attenuation plots, PSA versus distance, for CNA. The illustrations show the attenuation dependence on frequency (ca. 1.5, 3, 5, 10, 15, and 20 Hz) for different focal depths. A comparison of the four regions at a frequency of 5 Hz for different focal depths can be found in Appendix D (Figures D.1−D4). The APP, ACP, and the MEM regions show strong Moho reflections starting at 45–80 km hypocentral distance for all four focal depths. The most significant differences in ground motions between the regions lie within a 70–140 km distance.

Figures 5.11−5.14 show the 2D PSA distribution for all regions for a hypocentral distance range of 1.5 * focal depth–500 km and a frequency range of 0.5–20 Hz. Figure 5.11 illustrates the distribution of ground motion for an event with a focal depth of 5 km in each of the four regions: the ACP, the APP, MEM region shows a clear difference in PSA at frequencies > 3 Hz and distances within the ranges of 30–70 and 80–160 km. Note that within the first distance range there are higher accelerations, and in the second range there are relatively low accelerations. This is also partly visible in the attenuation plot in Figure D.1 for 5 Hz. For lower frequencies, the PSA of the MEM region does not look significantly different in comparison with the other regions.

Similar patterns can be observed for an event with a focal depth of 10 km. The MEM region shows higher accelerations at frequencies > 1 Hz and a distance range of 30–60 km in comparison with the other regions; at a distance range of 60–120 km, the MEM region shows slighter lower accelerations (c.f., Figure D.2) The ACP shows distance-dependent increasing of PSA-values at hypocentral distances of 80, 105, and 160 km.

For an event with a focal depth of 5 km, the CNA and the APP regions show relatively good agreement in amplitude versus distance of PSA. Within the APP region there are slightly higher PSA values at a distance of 60 ± 5 km at frequencies >10 Hz. This is also true at a hypocentral distance of about 160 km, where the distance-dependent distribution of PSA values is more limited to frequencies of approximately 1.1 Hz. The MEM region shows increased values at a distance of 50–80 km at frequencies between 2 and 6 Hz. The PSA distribution also shows significant differences at hypocentral distances of about 160 and 200 km compared to the other three regions. After 220 km (frequency > 4 Hz), the PSA decreases to an amplitude of 10^{-3}, while the other regions experience this amplitude at distances of 240–260 km (APP) and 260–280 km (CNA). The ACP shows a different pattern than the other three regions. In general, the accelerations are higher and the amplitude-distance pattern tends to be different (especially at frequencies > 5 Hz). The ACP also shows a significant influence of the focal depth. As shown in Section 3.2, the ACP's representative crustal structure contains a layer boundary at a depth of 20.5 km. This layer boundary and the focal depth of 20 km result in stronger theoretical ground motions at closer distances. This is due to the strong reflection of waves from this layer boundary. The direct waves (directly going upward from the source) and the reflected waves from the 20.5 km interface (going upward with just a slight delay with respect to the direct waves) interfere, causing high amplitudes. This interference changes significantly the theoretical ground motion pattern. Although there was an attempt to prevent these extreme source-reflector interactions, this case remained in the simulations. All cases with a source very close to a boundary would lead to similar conclusions and are not very helpful in explaining regional differences.

Figure 5.14 shows the response spectral acceleration for all the regions for an event with a focal depth of 30 km. As before, the MEM region shows a band of high PSA values at the distance range of 50–80 km and at frequencies > 4 Hz. There are also significant differences in the theoretical amplitudes at hypocentral distances of 160 ± 40 km and low frequencies (0.5–3 Hz).

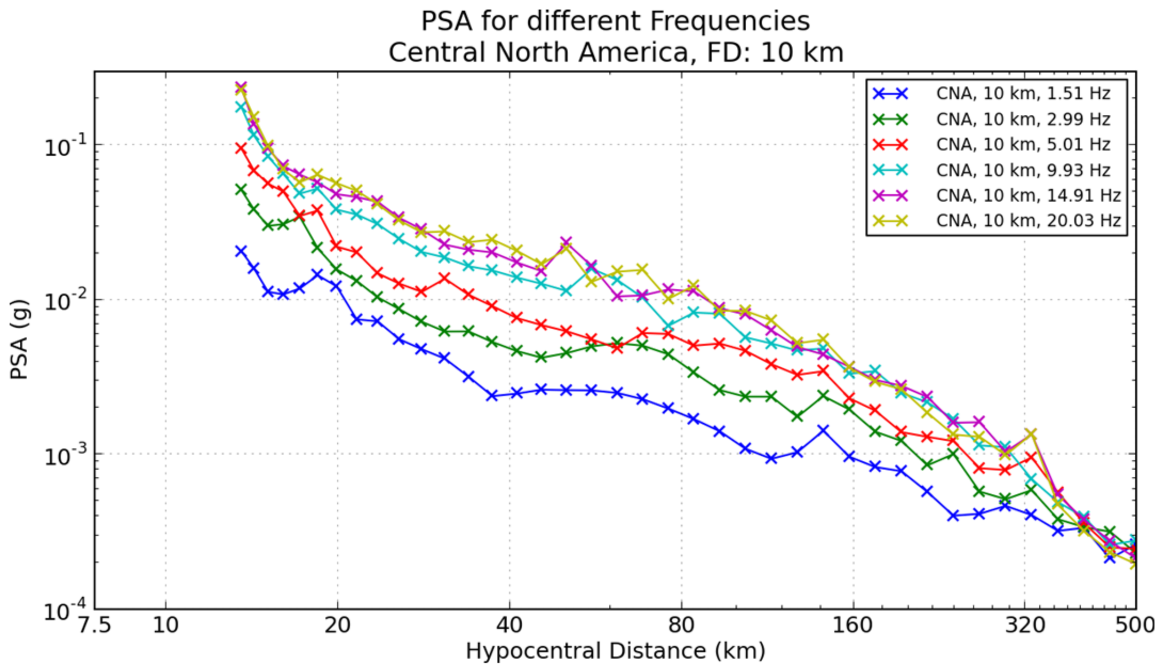

Figure 5.8 **PSA for different frequencies (ca. 1.5, 3, 5, 10, 15, and 20 Hz) within CNA for an event at 10 km depth.**

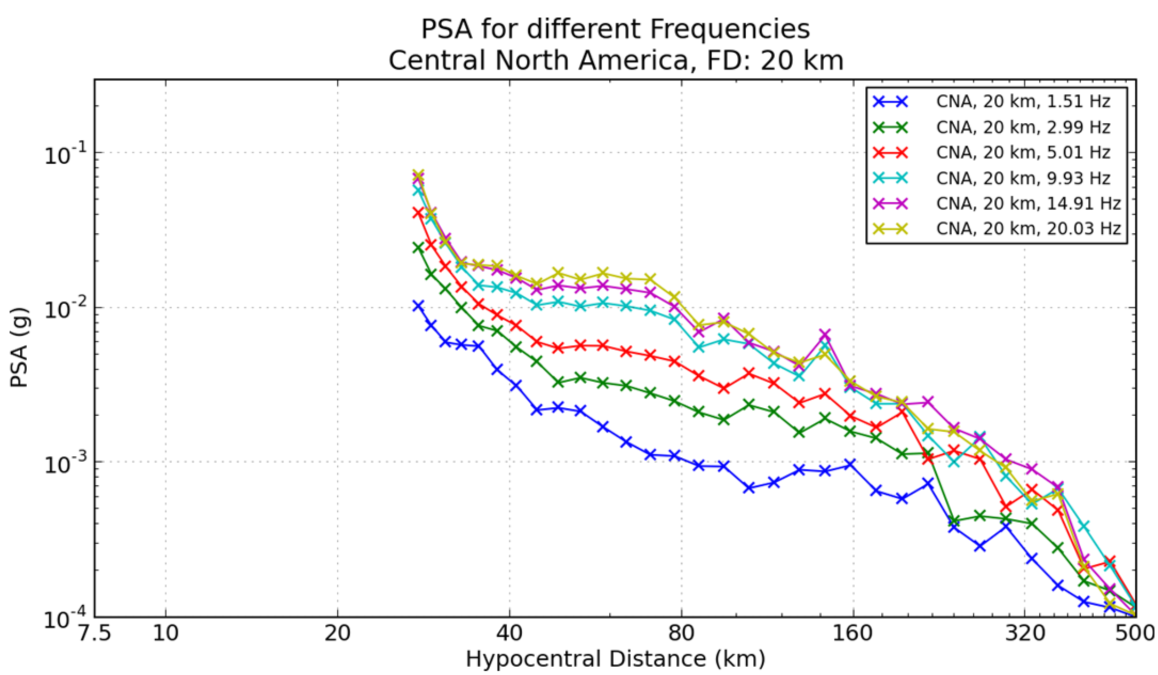

Figure 5.9 **PSA for different frequencies (ca. 1.5, 3, 5, 10, 15, and 20 Hz) within the CNA region for an event at 20 km depth.**

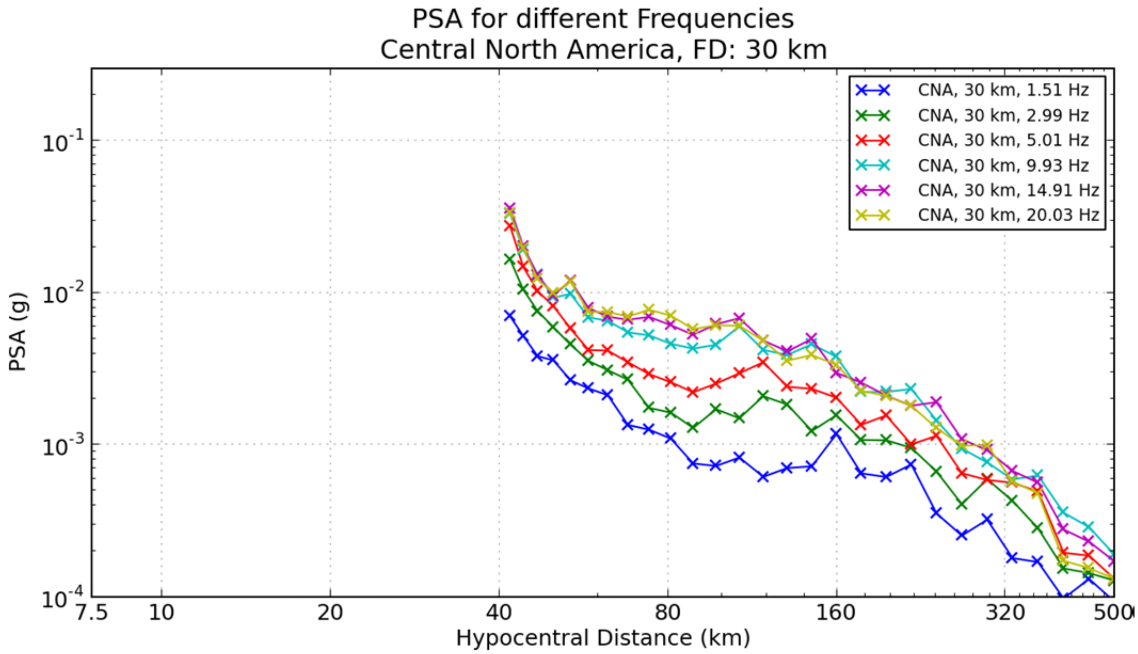

Figure 5.10 **PSA for different frequencies (ca. 1.5, 3, 5, 10, 15, and 20 Hz) within the CNA region for an event at 30 km depth.**

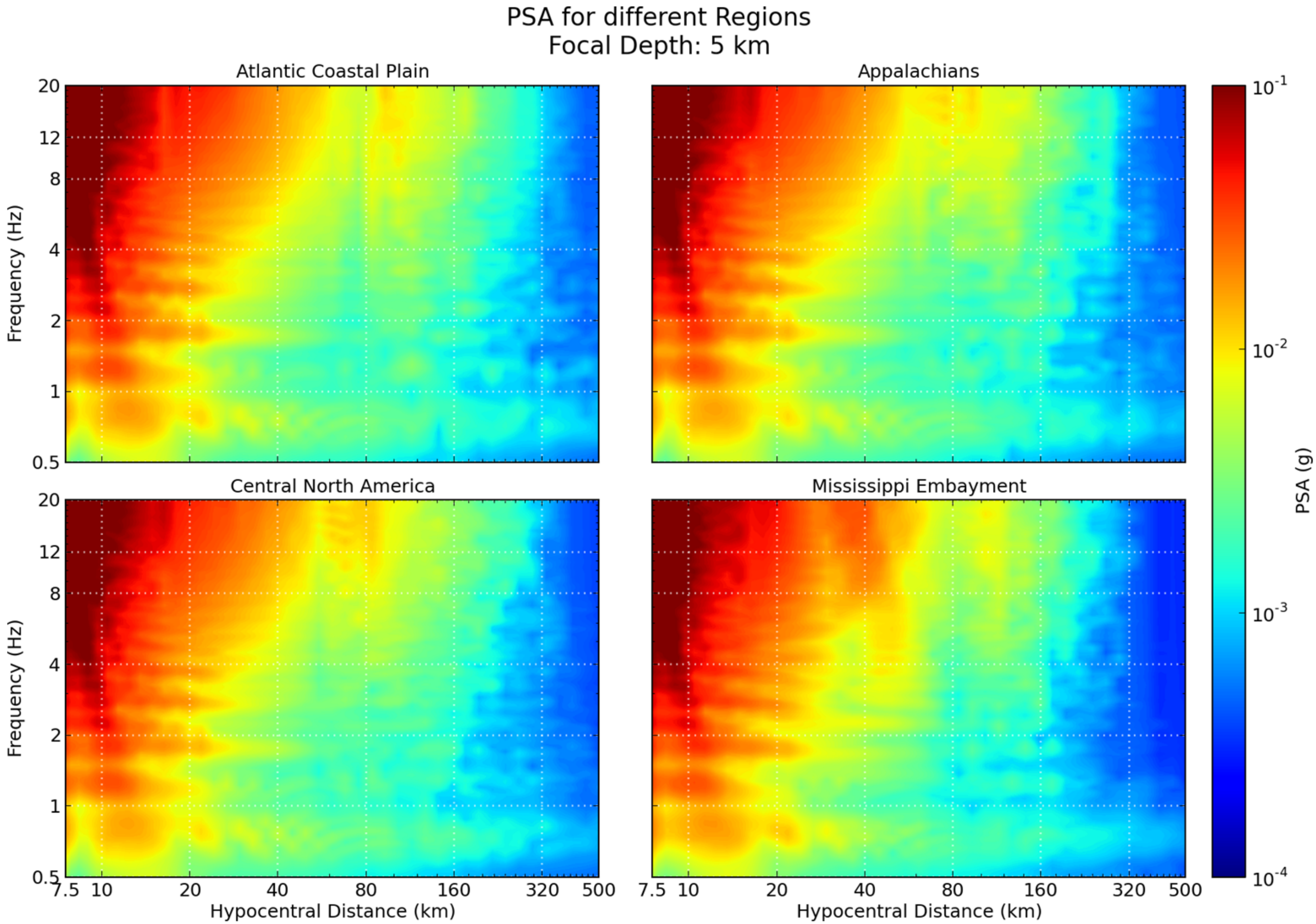

Figure 5.11 The PSA for the ACP, APP, CNA, and MEM regions for an event with focal depth of 5 km.

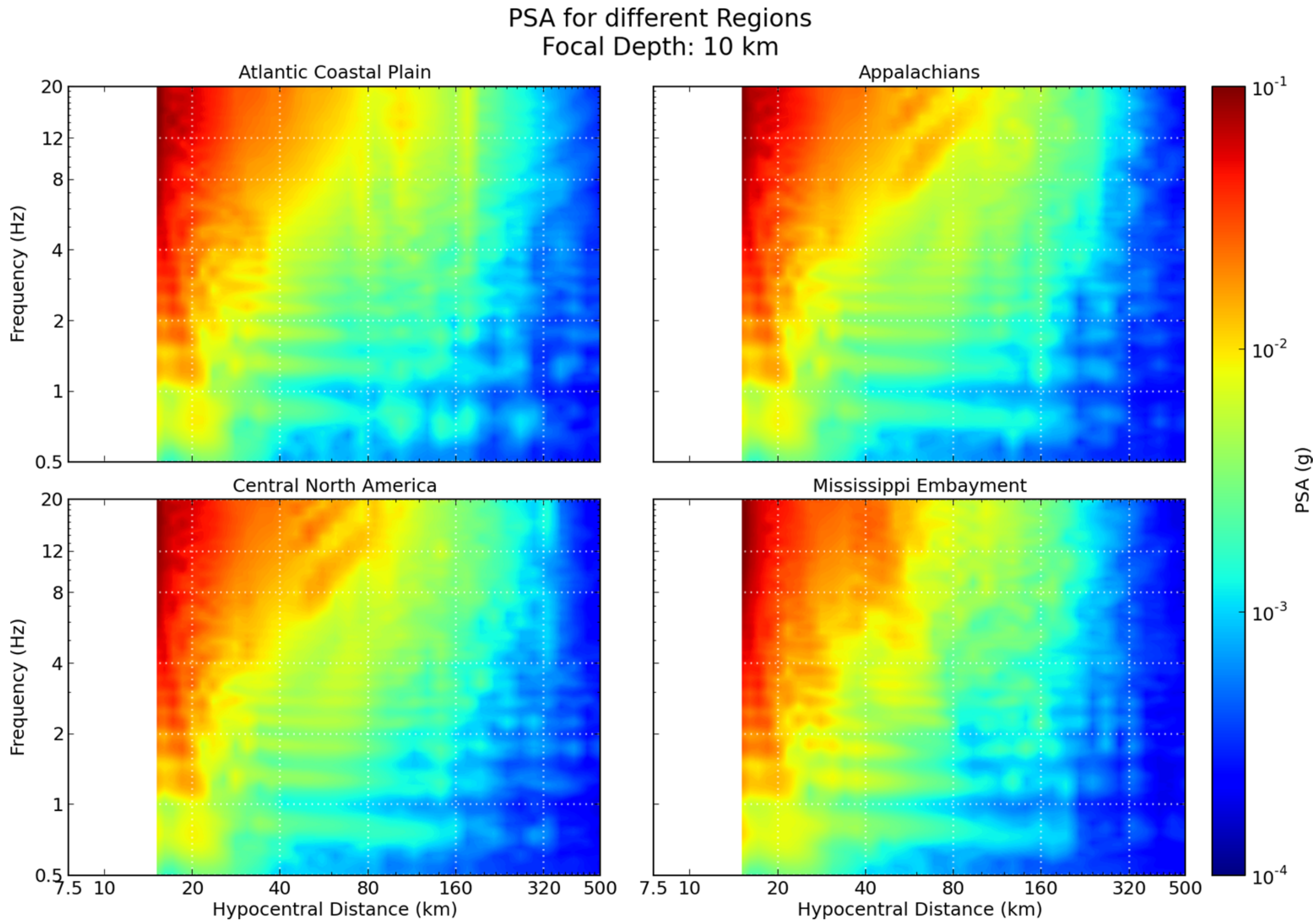

Figure 5.12 The PSA for the ACP, APP, CNA, and MEM regions for an event with a focal depth of 10 km.

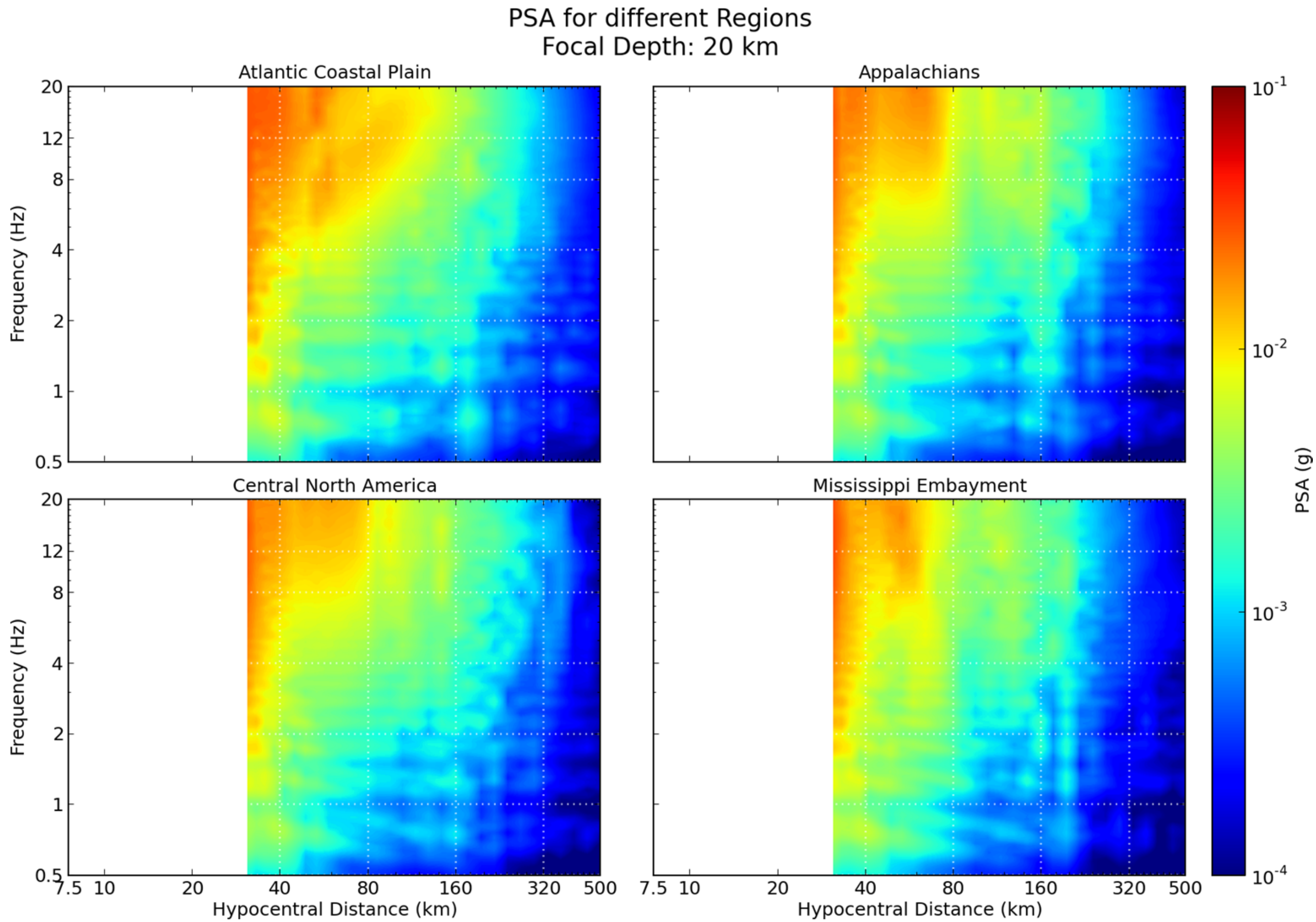

Figure 5.13 **The PSA for the ACP, APP, CNA, and MEM regions for an event with a focal depth of 20 km.**

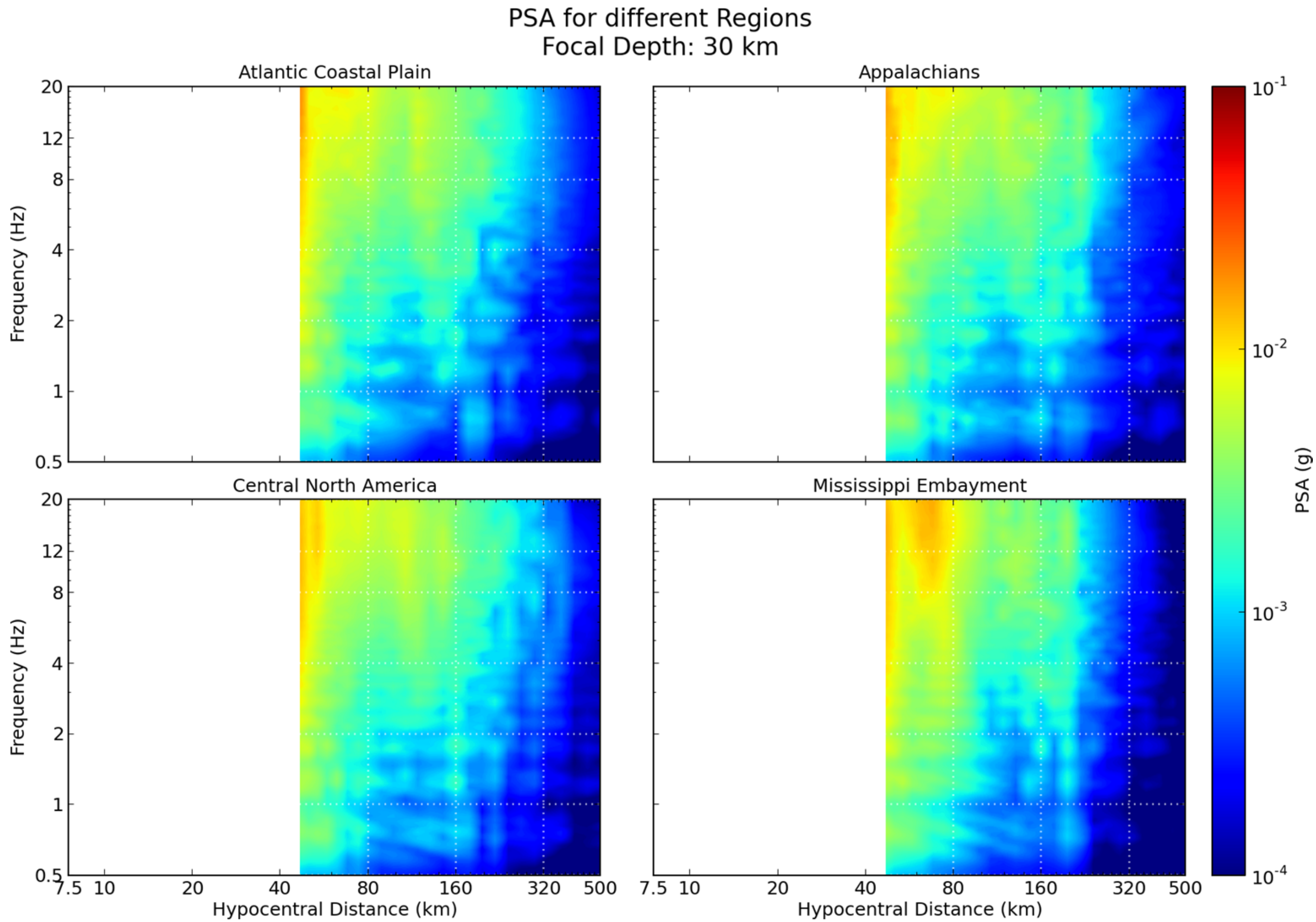

Figure 5.14 The PSA for the ACP, APP, CNA, and MEM regions for an event with a focal depth of 30 km.

5.3 CONSIDERATION OF PROFILE VARIABILITY EFFECTS ON GROUND MOTION DISTRIBUTIONS

This section presents key results of PSA attenuation and distribution for the CNA alternative models. Figure 5.15 and 5.16 show the attenuation of PSA with distance at a frequency of 5 Hz. Illustrated are all 18 attenuation curves for the alternative crustal models. A clear pattern emerges at a focal depth of 5 km: up to a hypocentral distance of 40 km the curves are relatively close and parallel to each other. Between 40 and 140 km the curves separate, which is caused by the Moho reflections. At distances greater than 140 km, the PSA curves approach each other again and seem to show similar attenuation. This trend with three distinct attenuation zones is also visible for an event's focal depth of 10 km (Figure 5.16). This pattern is less distinct for a focal depth of 20 km (Figure 5.17), but it is prominent again for a source focal depth of 30 km (Figure 5.18). These trends are consistent with the focal depth location relative to the main reflectors depths.

The PSA distributions are shown in Figures 5.19–5.23 for different distance and frequency bins, and for focal depths of 5 and 10 km. Figures 5.19 shows the 35–70 km and 5–10 Hz bin. The trends in distribution and the means are very close while the standard deviation within CNA_{Alt} is broader than the one for CNA_{Rep} ($difference_{Alt\text{-}Rep}$: 0.019), as expected. Looking at the same focal depth and frequency bin, but for the 70–140 km distance bin that includes the arrival of the Moho reflection (Figure 5.20), one observes a much broader difference in standard deviations for CNA ($difference_{Alt\text{-}Rep}$: 0.077). For a lower frequency band (Figure 5.21), the widths of the two PSA distributions are similar ($difference_{Alt\text{-}Rep}$: 0.006). The distribution also shifts to lower values and is narrower (smaller standard deviation) for the lower frequency band (Figure 5.21), relative to the higher frequency band (Figure 5.20).

For an event with a focal depth of 10 km the same pattern is visible (Figure 5.22 and 5.23 for high and low frequencies, respectively). Here again, the means of the two distributions within a given figure are very close. For higher frequencies, the distributions of the alternative crustal model's PSA values within the Moho-distance bin are much wider than the ones for the representative model ($difference_{Alt\text{-}Rep}$: 0.055). For the lower frequency band, the distribution of CNA_{Alt} still shows a bigger width than the one for CNA_{Rep} ($difference_{Alt\text{-}Rep}$: 0.018), but less broad than what is observed at higher frequencies.

Table D.1 in Appendix D tabulates all the means and standard deviations for CNA (CNA_{Rep} and CNA_{Alt}) within each distance and frequency band. Additional distributions are presented in Figures D.7–D12.

In general, the differences of the means of the two distributions are very small. The absolute differences are within the range 0.003 to 0.068, but are generally less than 0.03. The exception is for the focal depth of 30 km within the 35–70 km distance bin. However, due to the reduced number of samples (PSA available from 45 km = 1.5 * focal depth) within this bin, the statistics may not be reliable. The means for this limited dataset have absolute differences of 0.5–0.8. Nevertheless, the representative PSA-distribution consistently lies within the alternative distribution.

The differences of the standard deviations generally follow a distinct pattern: the higher the frequency band, the higher the differences between results from the representative and alternative profiles. The largest differences are within the 70–140 km hypocentral distance bin (Moho reflection zone). The range of absolute differences of the two distributions standard deviations range between 0.003 and 0.077, with the exception of an event with a focal depth of 30 km for the distance bin of 35–70 km (0.2–0.6).

Figure 5.24 shows the standard deviations of CNA_{Alt} as a 2D contour plot. The standard deviations are between 0 and 0.5 ln(PSA). Small values generally appear at closer distances and higher values at higher distances. This pattern is visible for an event with a focal depth of 5 km. At about 40 km the values increase abruptly due to the arrival of high-amplitude Moho reflections. At larger distances, the pattern remains similar but with shifted Moho arrivals and shifted increased PSA values. This study uses these 2D matrices of standard deviations when normalizing the 2D mean difference matrices for CNA and the other regions, as described in Section 4.5.

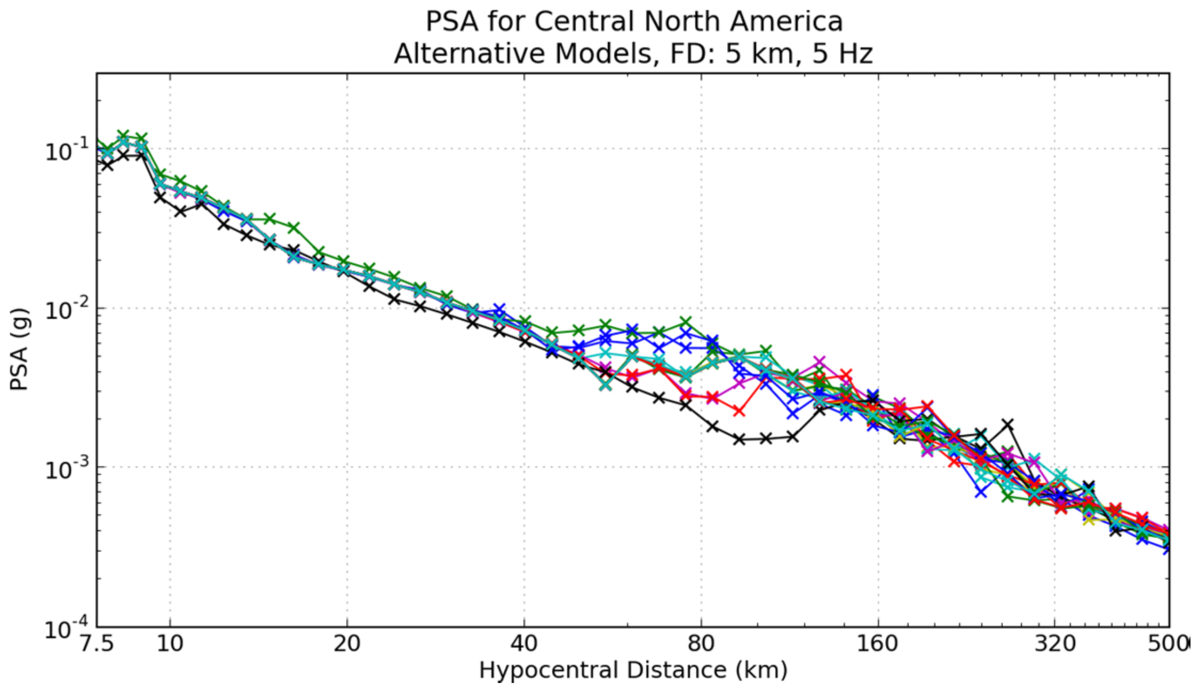

Figure 5.15 **The PSA at 5 Hz for CNA and its alternative profiles for an event with a focal depth of 5 km.**

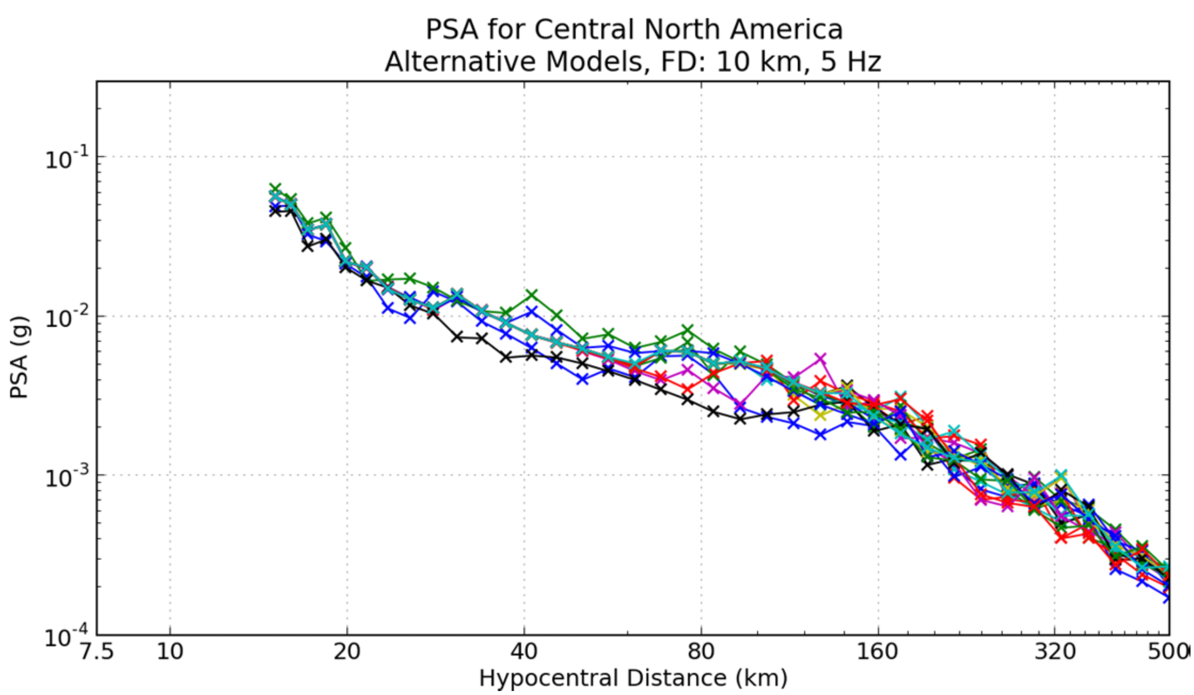

Figure 5.16 **The PSA at 5 Hz for CNA and its alternative profiles for an event with a focal depth of 10 km.**

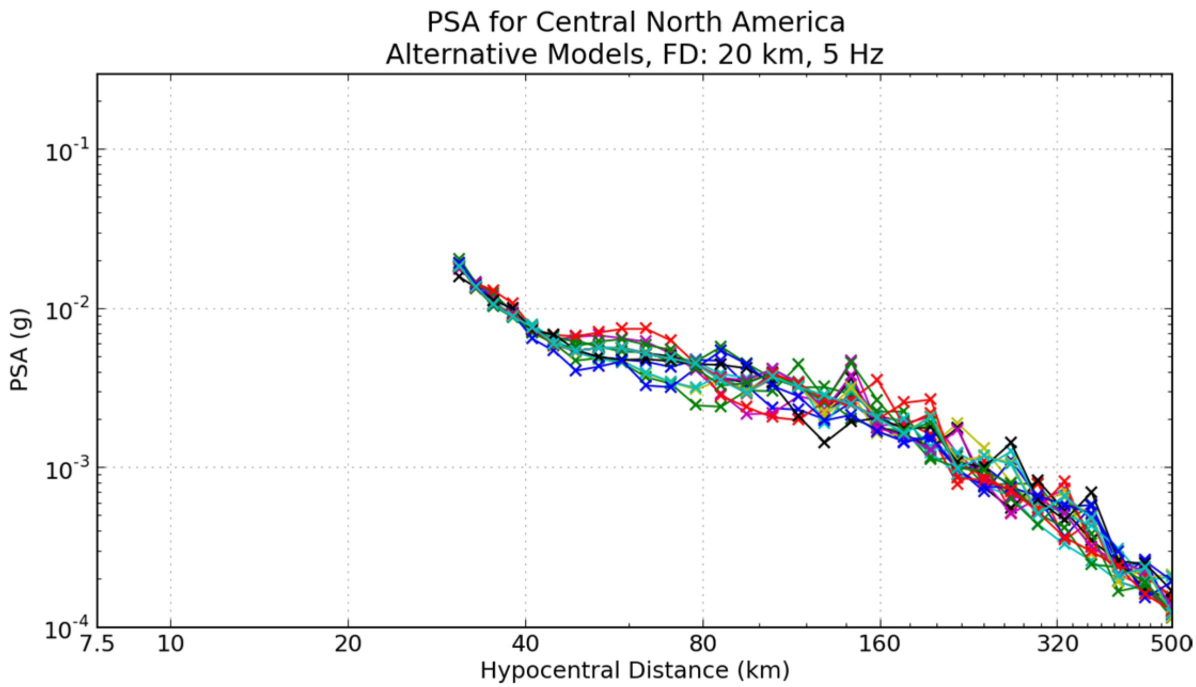

Figure 5.17 Response spectral acceleration at 5 Hz for CNA and its alternative profiles for an event with focal depth 20 km.

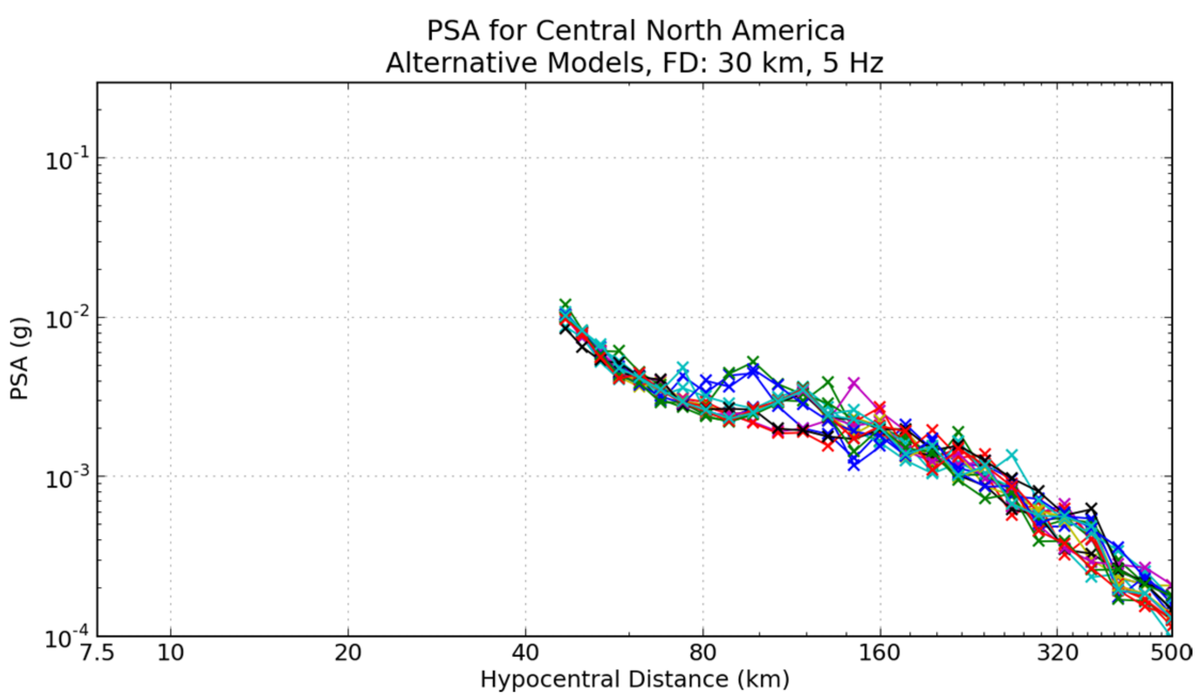

Figure 5.18 Response spectral acceleration at 5 Hz for CNA and its alternative profiles, for an event with focal depth 30 km.

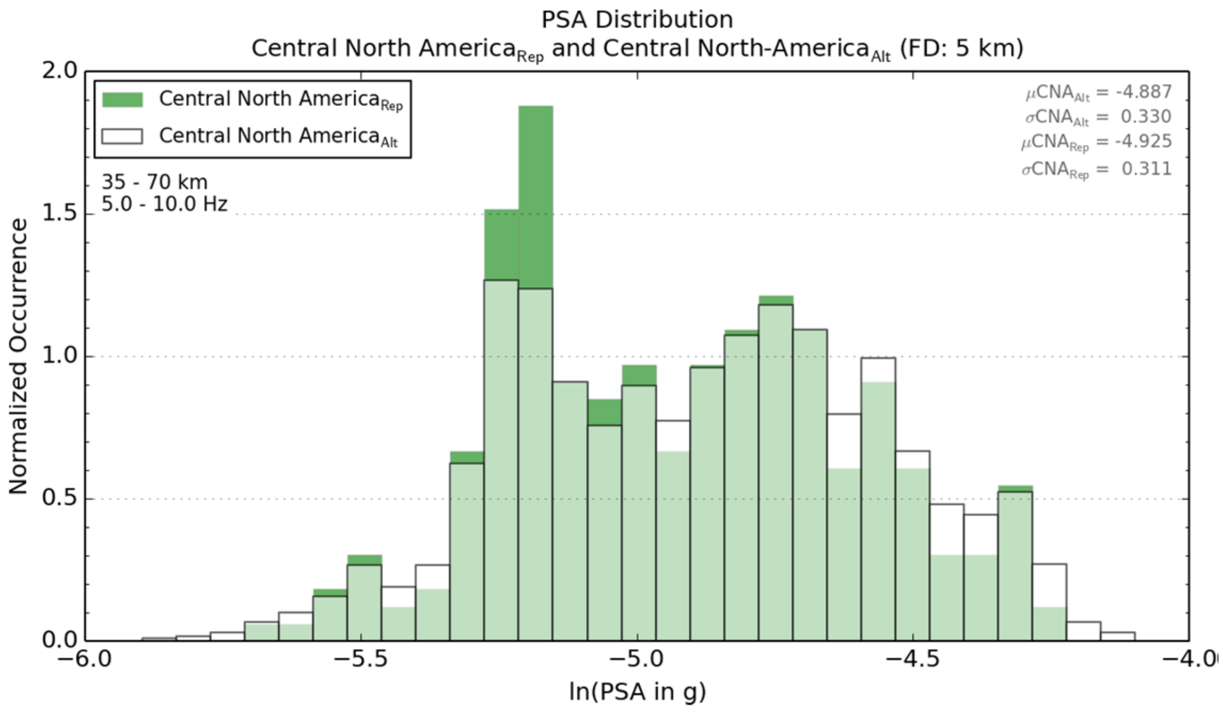

Figure 5.19 **The PSA distribution for CNA illustrated for representative and alternative models at distances of 35–70 km and frequencies of 5–10 Hz for an event with a focal depth of 5 km**

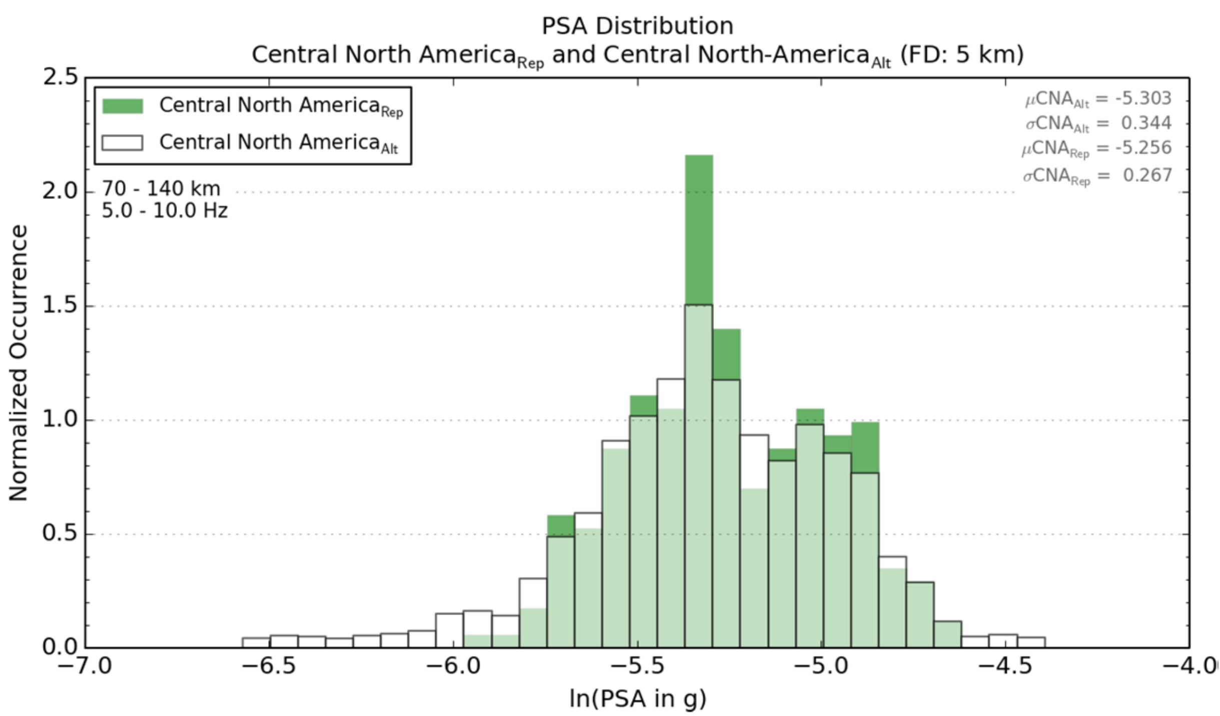

Figure 5.20 **The PSA distribution for CNA illustrated for representative and alternative models at distances of 70–140 km and frequencies of 5–10 Hz for an event with a focal depth of 5 km.**

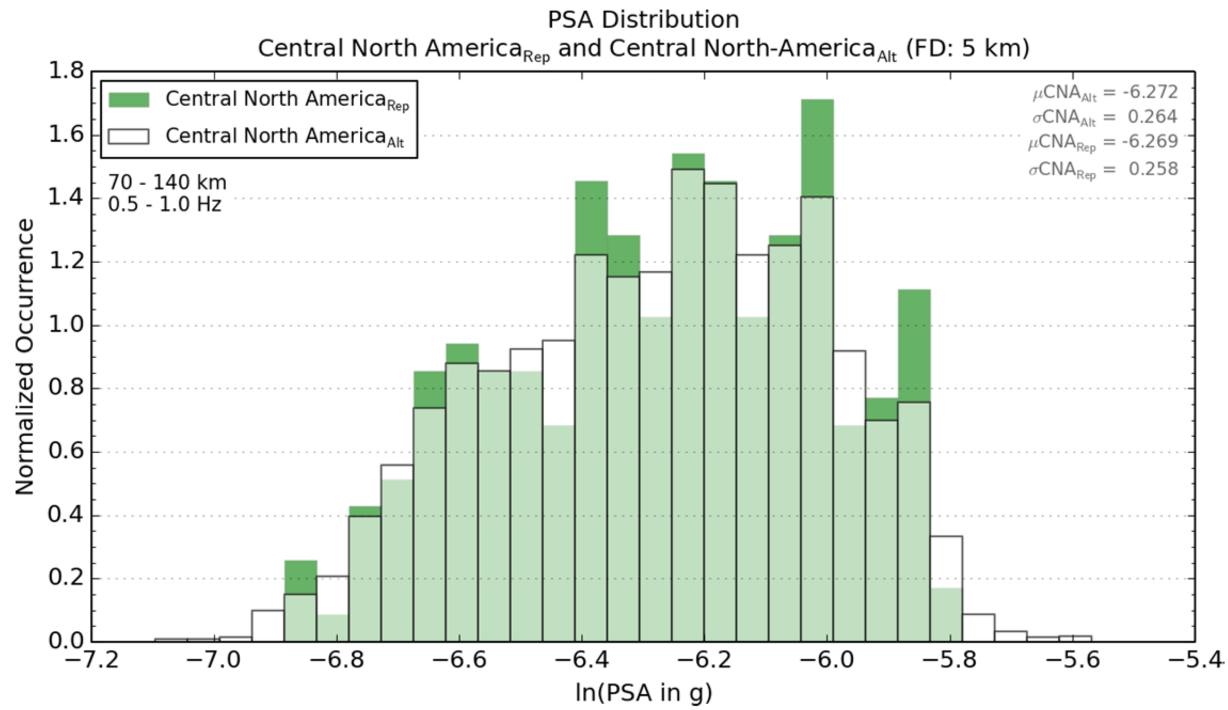

Figure 5.21 The PSA distribution for CNA illustrated for representative and alternative models at distances of 70–140 km and frequencies of 0.5–1 Hz for an event with a focal depth of 5 km

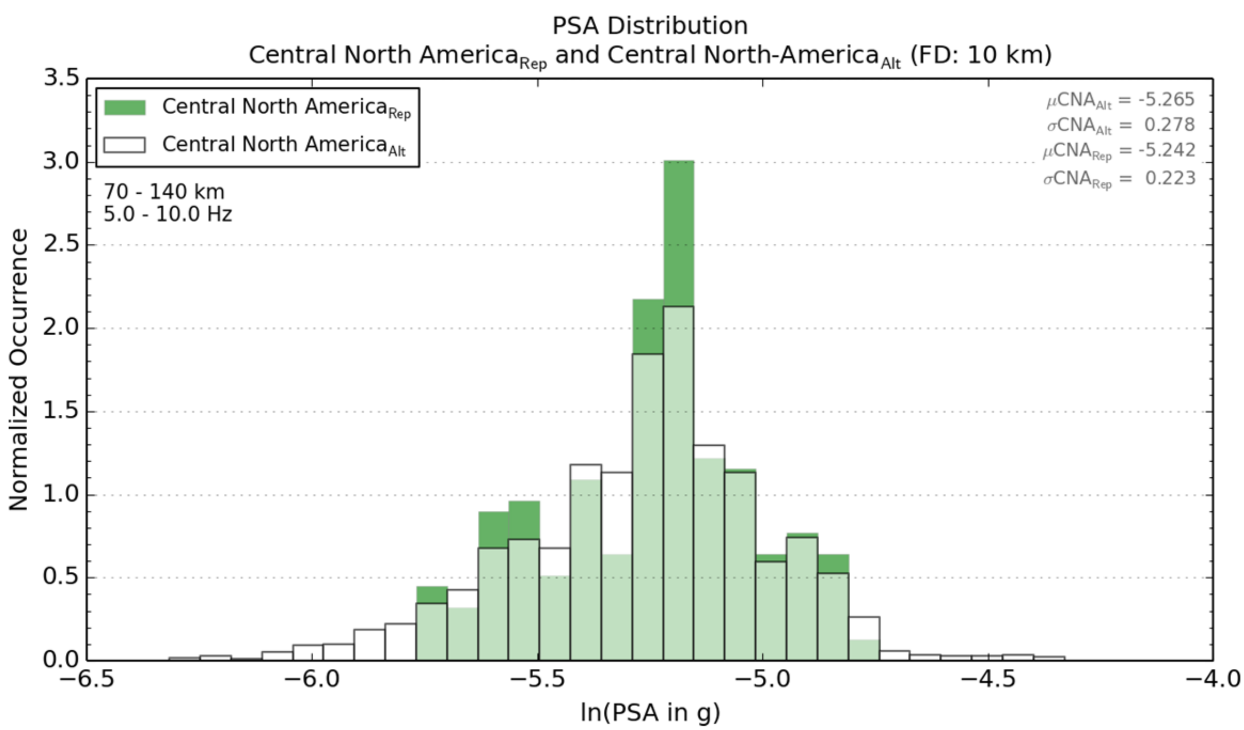

Figure 5.22 The PSA distribution for CNA illustrated for representative and alternative models at distances of 70–140 km and frequencies of 5–10 Hz for an event with a focal depth of 10 km.

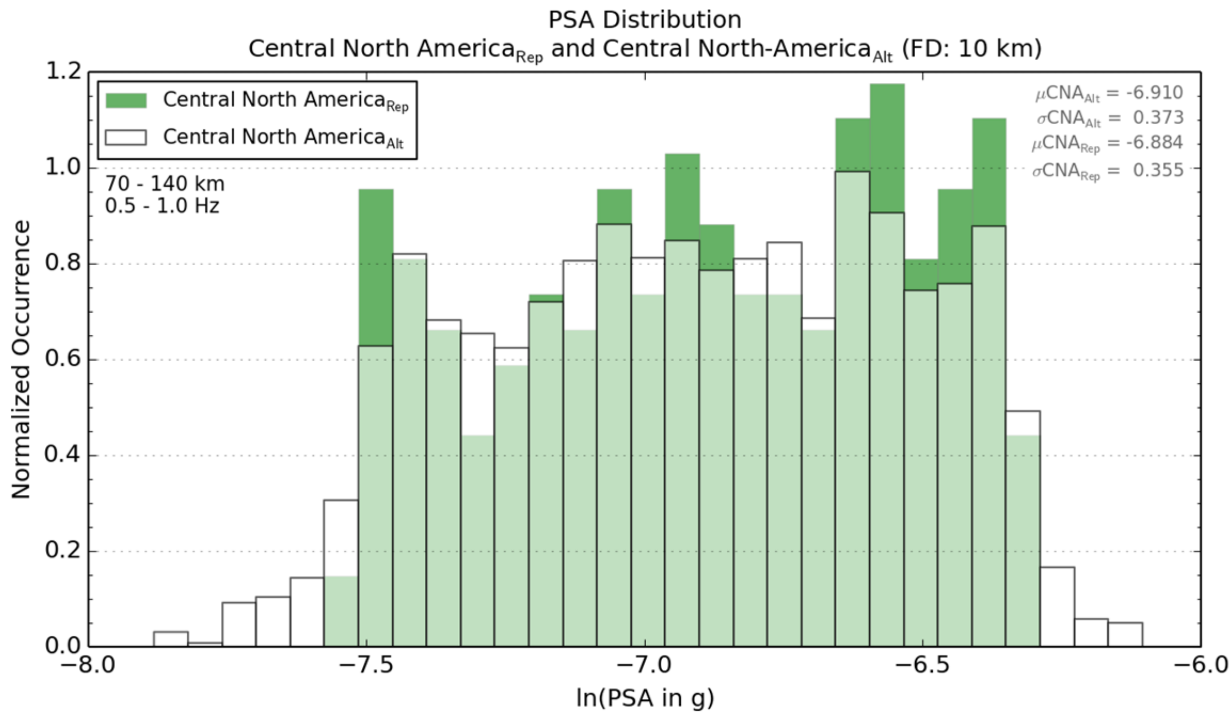

Figure 5.23 The PSA distribution for CNA illustrated for representative and alternative models at distances of 70–140 km and frequencies of 0.5–1 Hz for an event with a focal depth of 10 km.

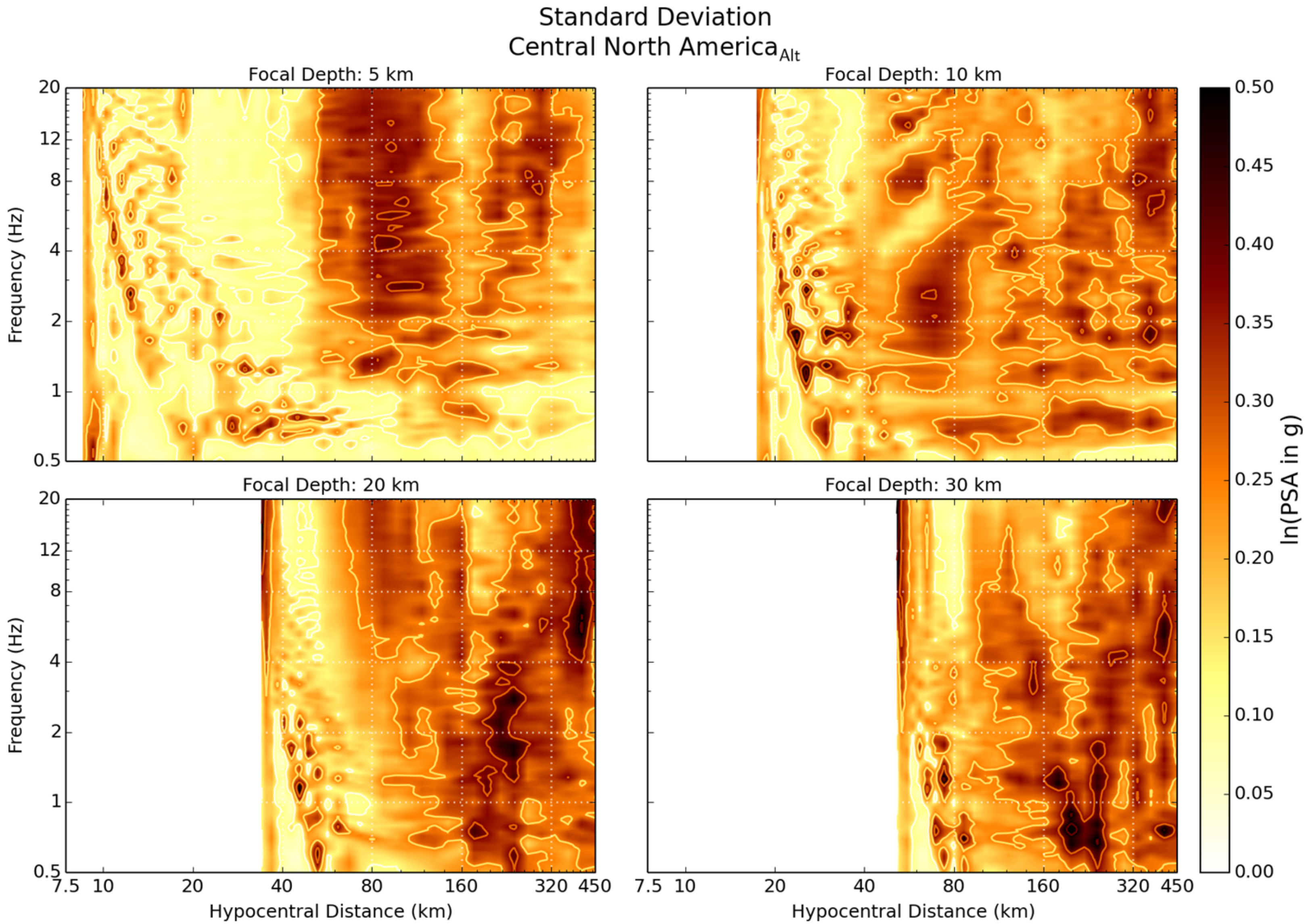

Figure 5.24 **Standard deviation of CNA and its 18 alternative models. Event focal depths are at 5, 10, 20, and 30 km.**

5.4 REGIONAL COMPARISONS

The moving window average and the normalized mean difference (Section 4.5) were applied to determine whether or not there are significant differences of PSA for the four regions. A selected subset of plots is shown in Figures 5.25–5.30 (remaining plots are in Appending D: Figures D.13–D.28). Table 5.1 presents a summary of results with the following entries:

Region

Atlantic Coastal Plain (ACP), Appalachians (APP) and Mississippi Embayment (MEM).

Focal Depth (FD)

5, 10, 20, and 30 km deep events. The FD=20 km event was excluded for the Atlantic Coastal Plain due to the presence of a layer boundary at 20.5 km depth that invalidates the resulting calculations.

Frequency Range

0.5–1 and 5–10 Hz bins.

$|(\mu\, REG_{Rep} - \mu\, CNA_{Rep})| < 0.3$ *and* $|(\mu\, REG_{Rep} - \mu CNA_{Rep})| < \sigma\, CNA_{Alt}$:

Does the mean of the region under consideration (REG) lie within the range of $\mu\mathrm{CNA}_{Rep}$ +/- $\sigma\mathrm{CNA}_{Alt}$?

Yes = completely:

REG is judged to belong to the same attenuation group as CNA.

(Yes) = almost completely:

REG could belong to the same attenuation group as CNA, apply judgment regarding range(s) for which large differences exist.

No or mostly not:

REG is not judged to belong to the same attenuation group as CNA.

$|(\mu\, REG_{Rep} - \mu CNA_{Rep})| > \sigma\, CNA_{Alt}$::

Evaluate distance and frequency ranges, where $\mu\, REG_{Rep}$ is not within $\mu\mathrm{CNA}_{Rep}$ +/- $\sigma\mathrm{CNA}_{Alt}$.

The key column of interest in Table 5.1 is the fifth one (gray shading). For the APP and ACP regions, and for both frequency bands at most distances, $\mu\, REG_{Rep}$ is completely or mostly contained in the $\mu\mathrm{CNA}_{Rep}$ +/- $\sigma\mathrm{CNA}_{Alt}$ range. The MEM region looks quite unique. Particularly for the higher frequency band, the mean of the MEM region lies mostly outside the bounds for CNA and its alternative, with the difference in the means often exceeding an absolute value of 0.3 (up to 0.6). This implies that MEM region attenuates significantly differently from the APP region. For lower frequencies, the PSA values of the MEM region fit relatively well to the CNA region, for the range of distances considered.

The mean difference of ln(PSA) for each of the other three regions compared to CNA are presented in Appendix D (Tables D.2–D.4) for the distinct distance and frequency bins as defined in Chapter 4. Based on the established criteria and the statistics summarized in these tables, the MEM region is judged to belong to a different attenuation group and the APP region is judged to belong to the same group as CNA. The ACP region also seems to belong to the same group as can region, but the agreement is not as close as found for the APP region.

Table 5.1 Comparing the three regions (Appalachians, Atlantic Coastal Plain, and Mississippi Embayment) to the CNA region. This table is based on the moving average method, which shows how well a region fits into the CNA PSA distribution.

Region (REG)	FD (km)	Frequency range (Hz)	$\lvert(\mu\, REG_{Rep} - \mu\, CNA_{Rep})\rvert < 0.3$	$\lvert(\mu\, REG_{Rep} - \mu\, CNA_{Rep})\rvert < \sigma\, CNA_{Alt}$	$\lvert(\mu\, REG_{Rep} - \mu\, CNA_{Rep})\rvert > \sigma\, CNA_{Alt}$ at distance range (km)	illustration
ACP	5	0.5–1	Yes	Yes		
ACP	10	0.5–1	(Yes)	(Yes)	240–300	Figure 5.
~~ACP~~	~~20~~	~~0.5–1~~	~~No~~	~~(Yes)~~	~~160–220~~	
ACP	30	0.5–1	(Yes)	Yes		
ACP	5	5–10	Yes	Yes		
ACP	10	5–10	(Yes)	(Yes)	160–180	Figure 5.
~~ACP~~	~~20~~	~~5–10~~	~~No~~	~~No~~	~~35–130~~	
ACP	30	5–10	Yes	Yes		
APP	5	0.5–1	Yes	Yes		
APP	10	0.5–1	Yes	Yes		
APP	20	0.5–1	Yes	Yes		
APP	30	0.5–1	(Yes)	Yes		
APP	5	5–10	Yes	Yes		Figure 5.
APP	10	5–10	Yes	Yes		
APP	20	5–10	Yes	Yes		
APP	30	5–10	(Yes)	(Yes)	300–360	
MEM	5	0.5–1	Yes	Yes		
MEM	10	0.5–1	Yes	Yes		
MEM	20	0.5–1	(Yes)	Yes		
MEM	30	0.5–1	No	No	260–450	Figure 5.
MEM	5	5–10	No	No	40–55, 70–95, 240–450	Figure 5.
MEM	10	5–10	No	No	75–120, 230–360	
MEM	20	5–10	No	No	80–110, 230–360	
MEM	30	5–10	No	No	60–85, 100–130, 240–450	Figure 5.

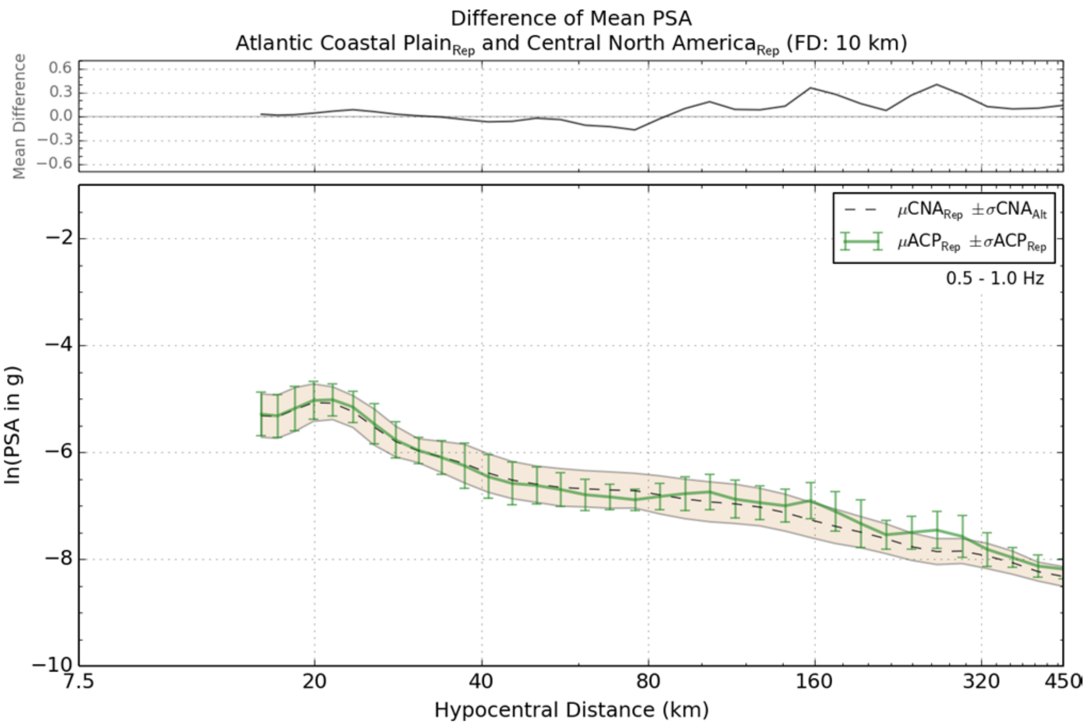

Figure 5.25 **Representative mean comparison: ACP and CNA regions within the standard deviation of CNA_{Alt} at a frequency bin of 0.5–1 Hz and focal depth of10 km.**

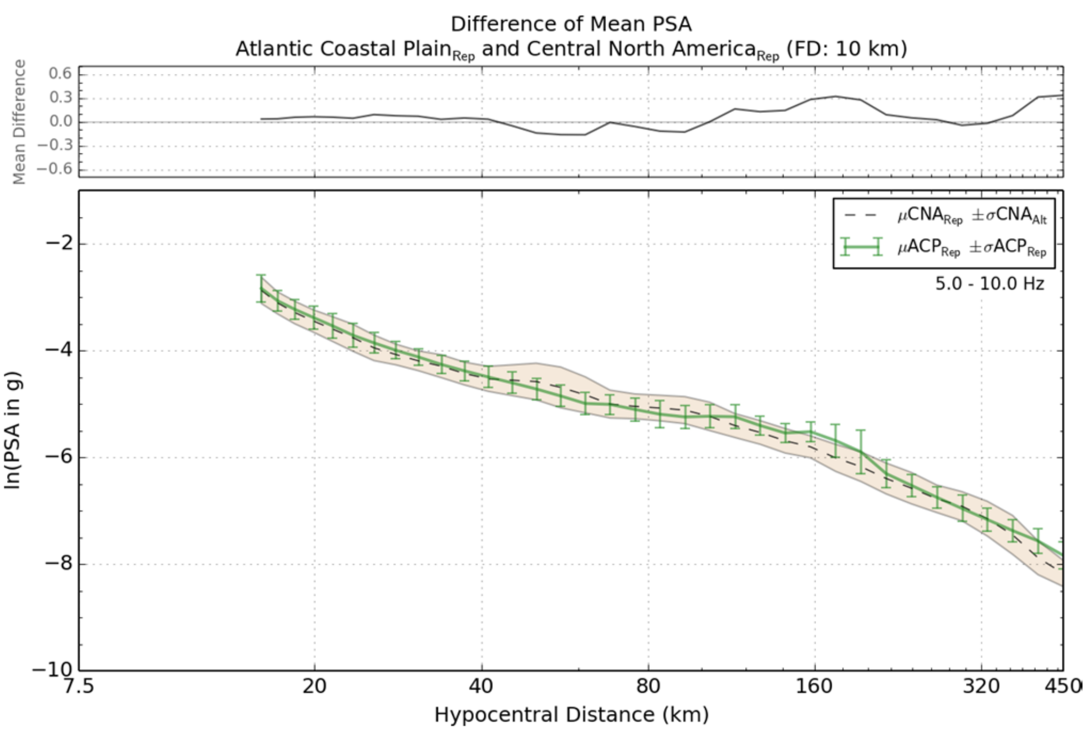

Figure 5.26 **Representative mean comparison: ACP and CNA regions within the standard deviation of CNA_{Alt} at a frequency bin of 5–10 Hz and focal depth of 10 km.**

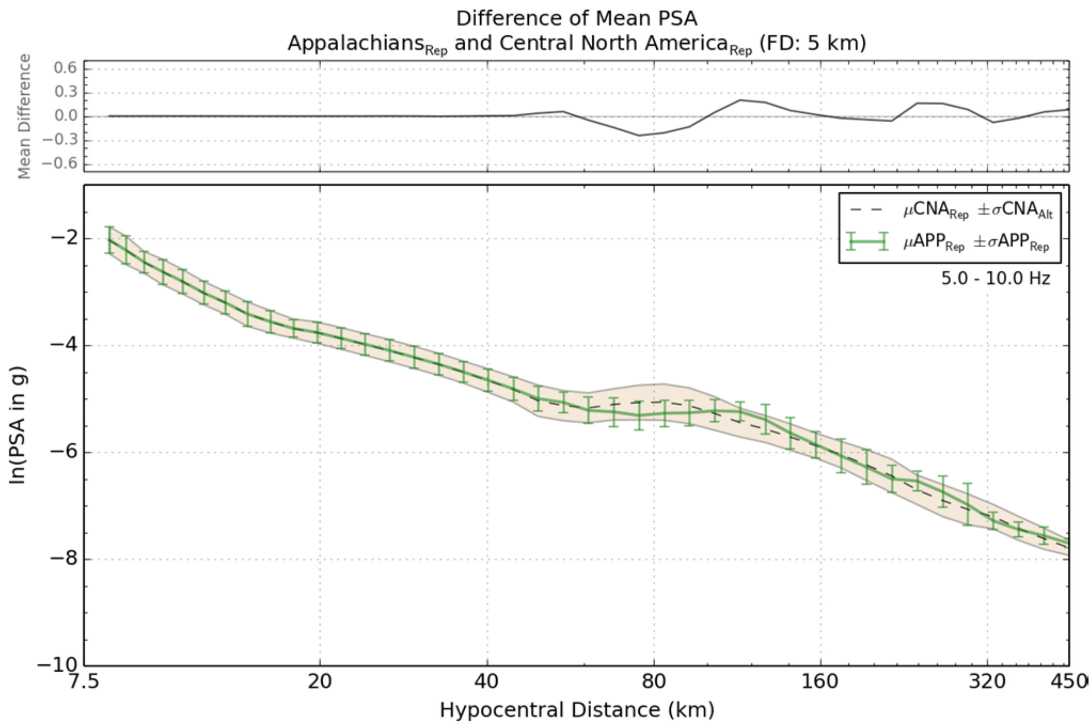

Figure 5.27 **Representative mean comparison: APP and CNA regions within the standard deviation of CNA$_{Alt}$ at a frequency bin of 5–10 Hz and focal depth of 5 km.**

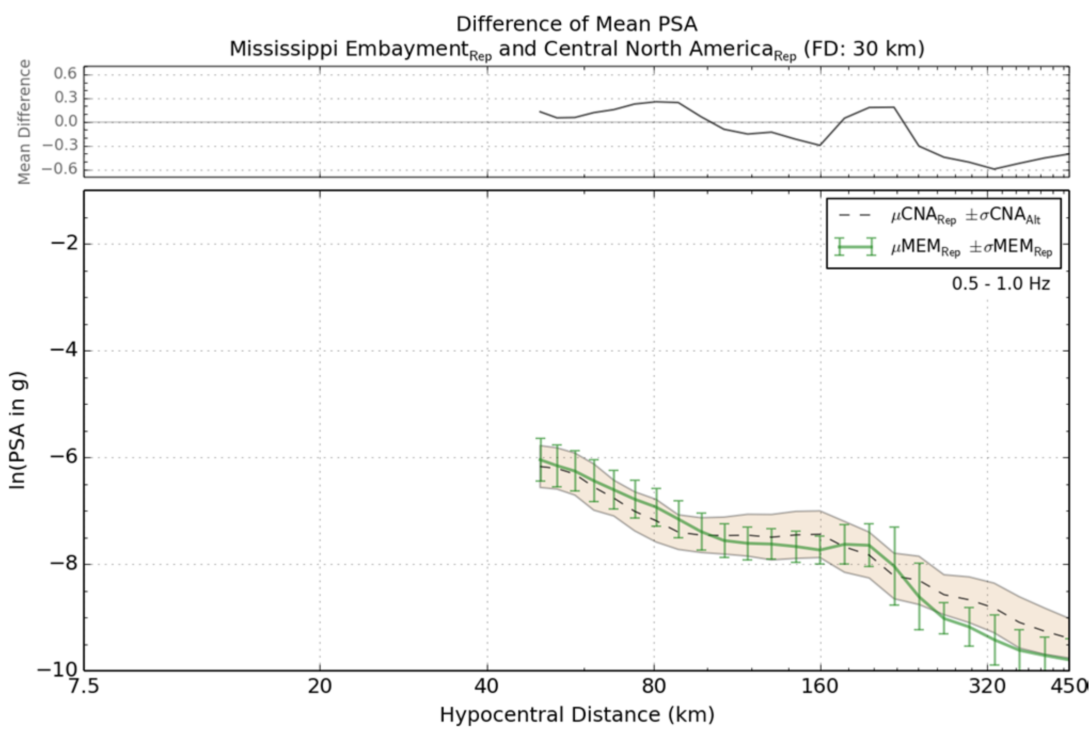

Figure 5.28 **Representative mean comparison: MEM and CNA regions within the standard deviation of CNA$_{Alt}$ at a frequency bin of 0.5–1 Hz and focal depth of 30 km.**

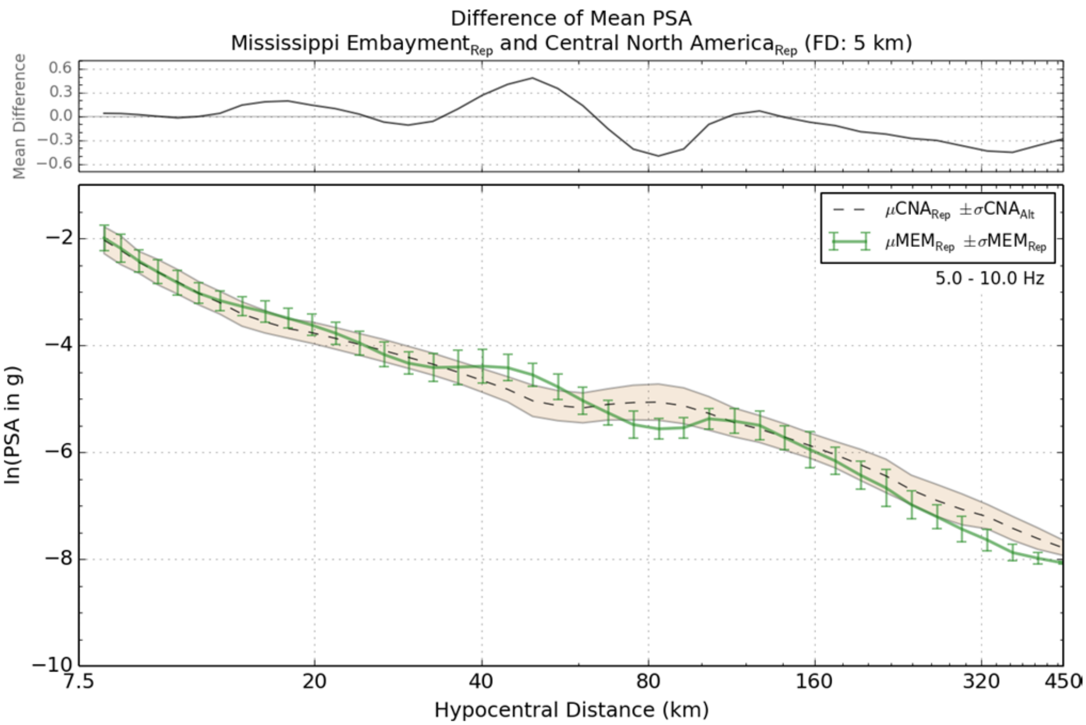

Figure 5.29 **Representative mean comparison: MEM and CNA regions within the standard deviation of CNA$_{Alt}$ at a frequency bin of 5–10 Hz and focal depth of 5 km.**

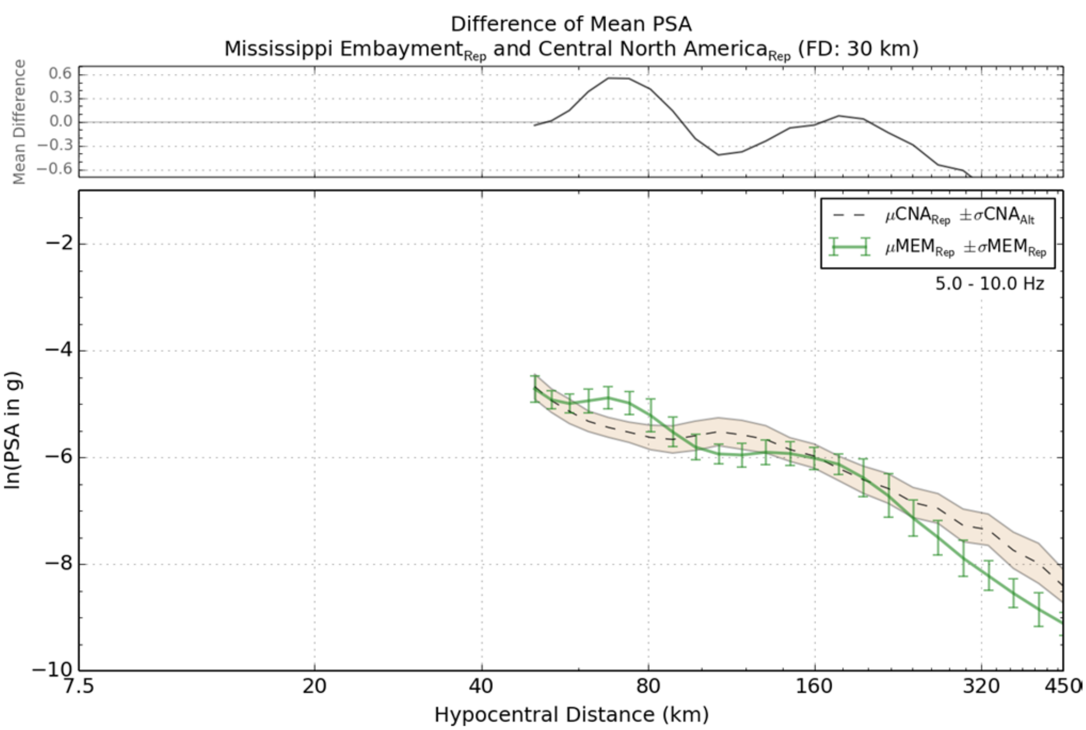

Figure 5.30 **Representative mean comparison: MEM and CNA regions within the standard deviation of CNA$_{Alt}$ at a frequency bin of 5–10 Hz and focal depth of 30 km.**

Figures 5.31–5.36 show the 2D analyses to illustrate the comparison of the four crustal regions. These figures show the difference of the mean as well as the normalized difference of the mean from each region relative to the can region. A distinct pattern in the difference is evident. Table 5.2 summarizes the results obtained from the 2D plots regarding the respective attenuation groups.

Table 5.2 Percentage of values, which lie within specific ranges (see Section 4.3). Difference of means and normalized difference of means from a region relative to CNA are summarized: note that highlighted values are judged significantly different.

REG		$X = \mu\mathrm{REG}_{Rep} - \mu\mathrm{CNA}_{Rep}$		$Y = \dfrac{\mu\mathrm{REG}_{Rep} - \mu\mathrm{CNA}_{Rep}}{\sigma\mathrm{CNA}_{Alt}}$	
Region	**Focal Depth (km)**	**|*X*| < 0.3**	**|*X*| < 0.6**	**|*Y*| < 1**	**|*Y*| < 3**
ACP	5	93.4%	99.8%	71.0%	99.5%
ACP	10	86.4%	99.0%	68.5%	98.7%
~~ACP~~	~~20~~	~~56.8%~~	~~96.6%~~	~~35.0%~~	~~82.3%~~
ACP	30	91.7%	99.4%	73.8%	98.5%
APP	5	97.2%	100.0%	91.2%	100.0%
APP	10	96.1%	100.0%	89.0%	100.0%
APP	20	92.3%	99.9%	75.3%	99.6%
APP	30	87.9%	99.5%	72.7%	99.6%
MEM	5	78.2%	97.4%	49.4%	91.4%
MEM	10	75.1%	96.3%	49.2%	95.1%
MEM	20	69.4%	96.4%	48.5%	94.2%
MEM	30	57.4%	84.7%	40.8%	84.0%

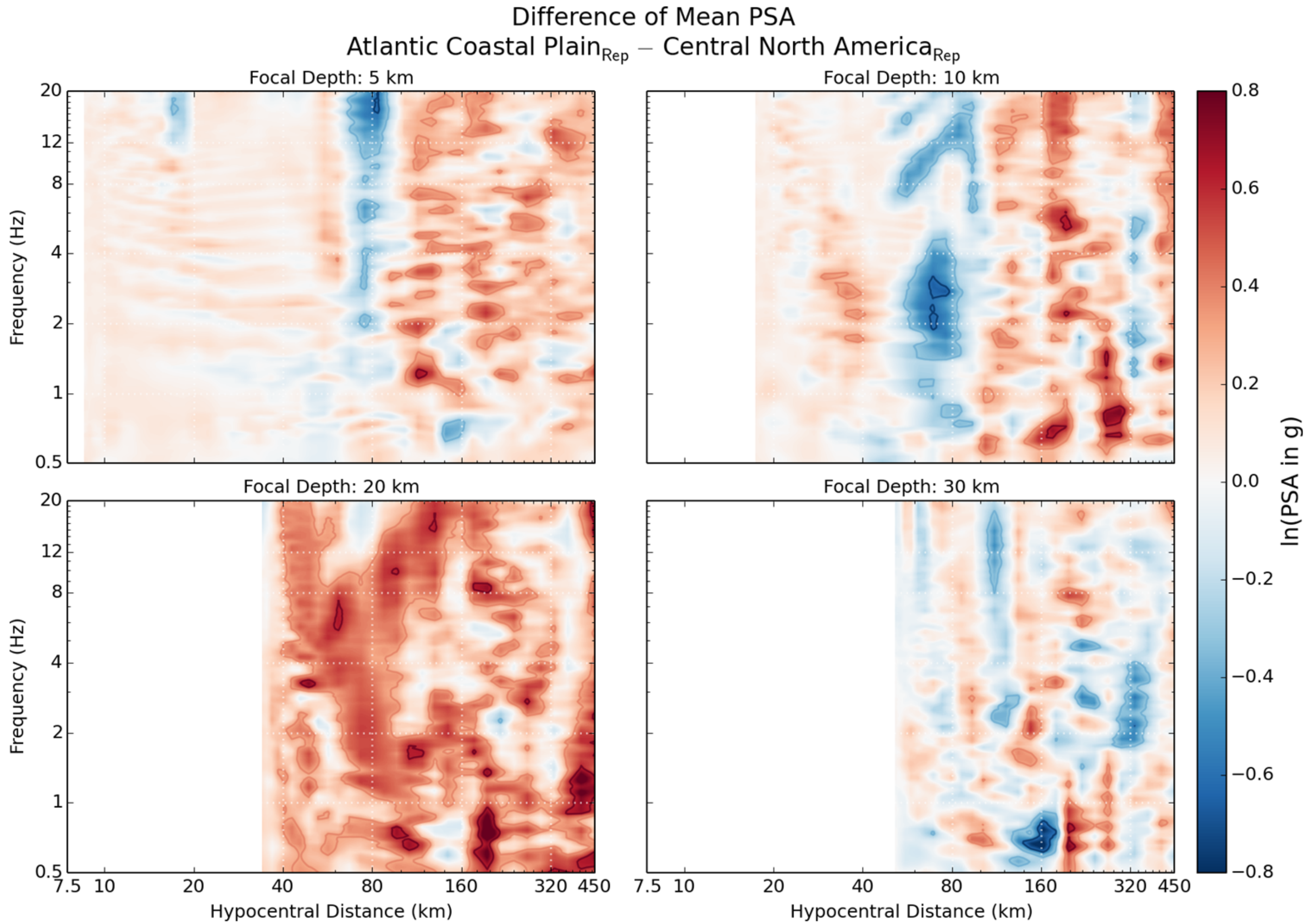

Figure 5.31 Difference of mean ln(PSA) for the ACP region relative to CNA regions at different focal depths.

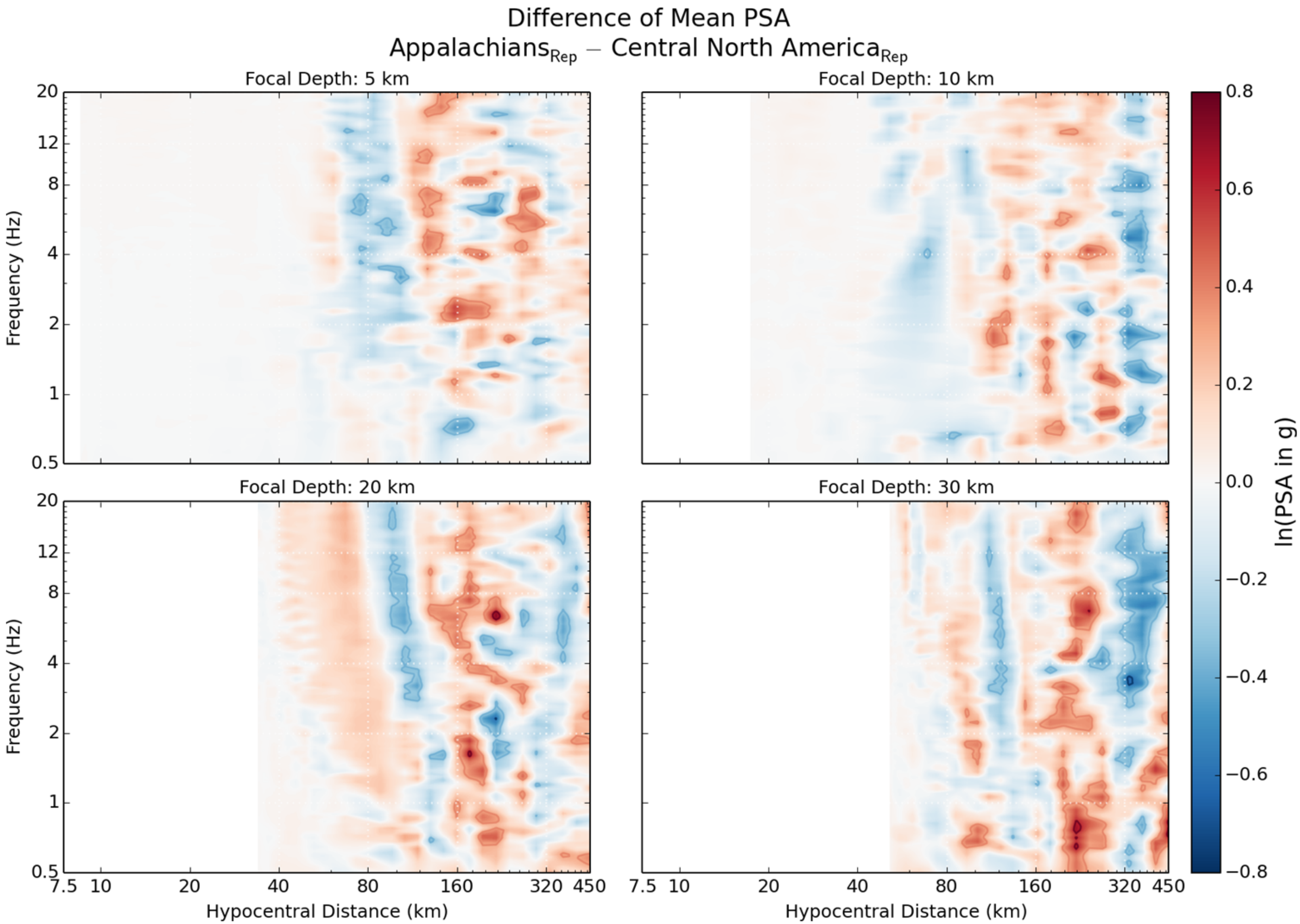

Figure 5.32 Difference of mean ln(PSA) for the APP region relative to CNA regions at different focal depths.

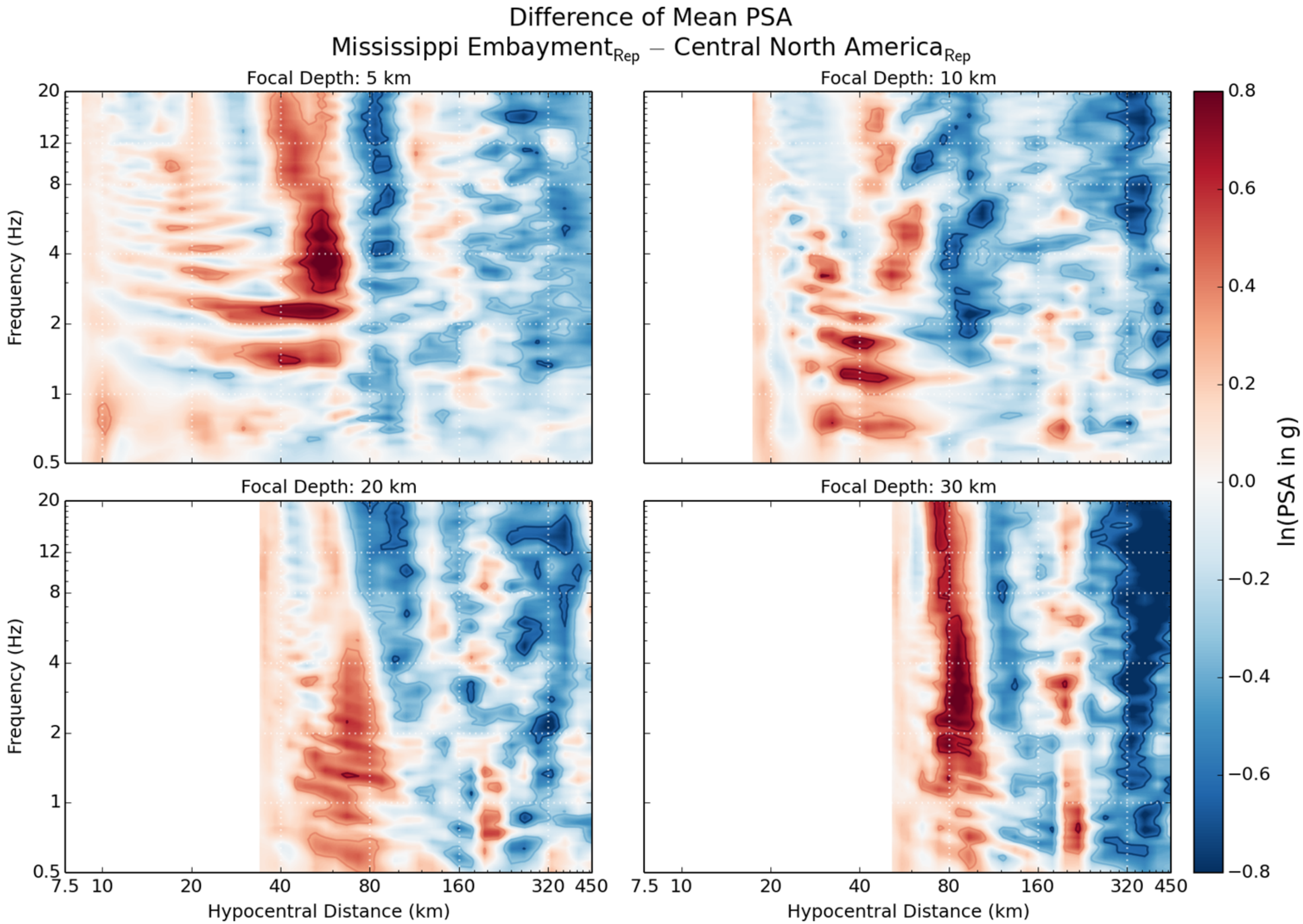

Figure 5.33 **Difference of mean ln(PSA) for the MEM region relative to CNA regions at different focal depths.**

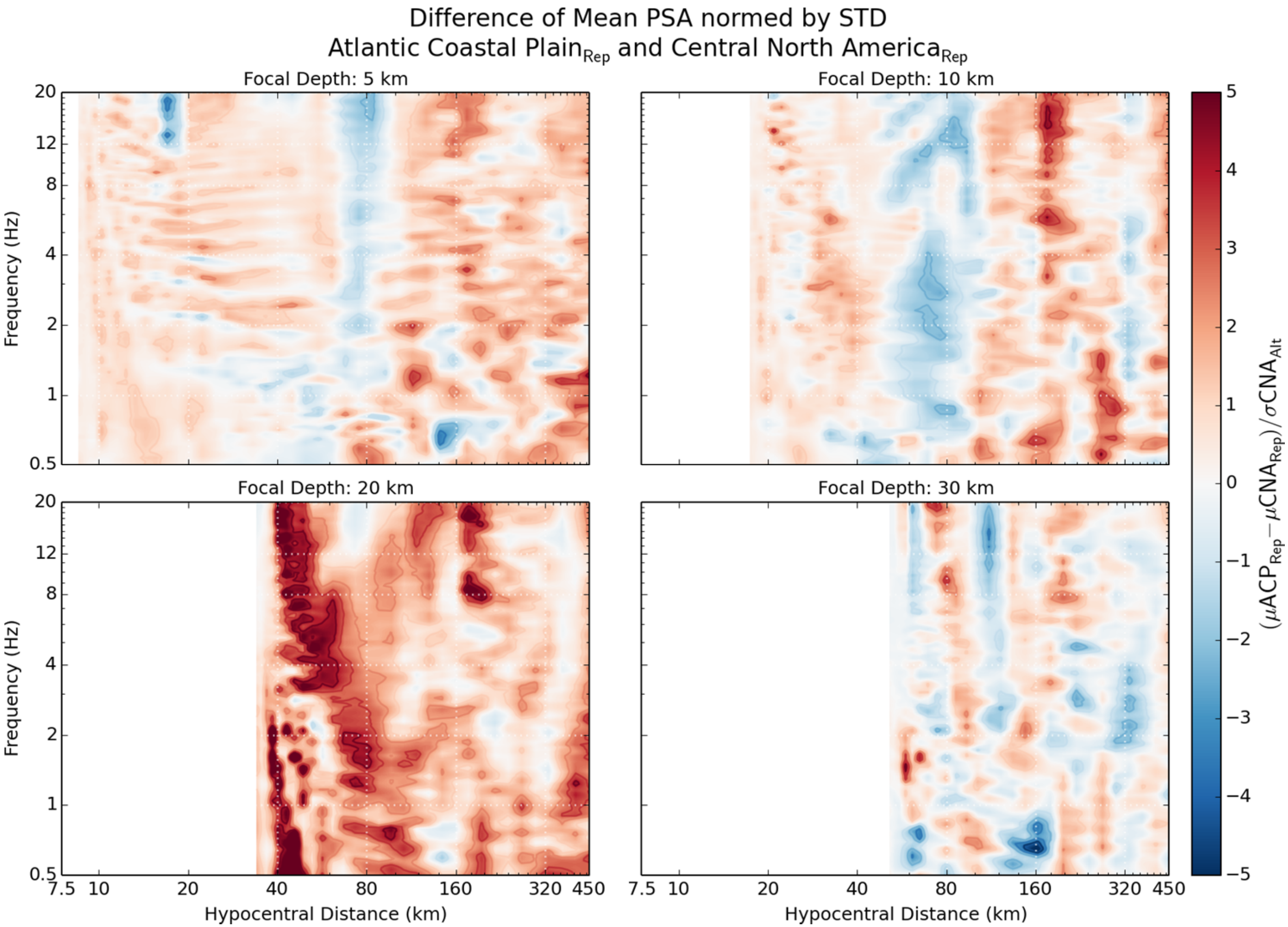

Figure 5.34 **Normalized difference of means of ln(PSA) for the ACP region relative to CNA at different focal depths.**

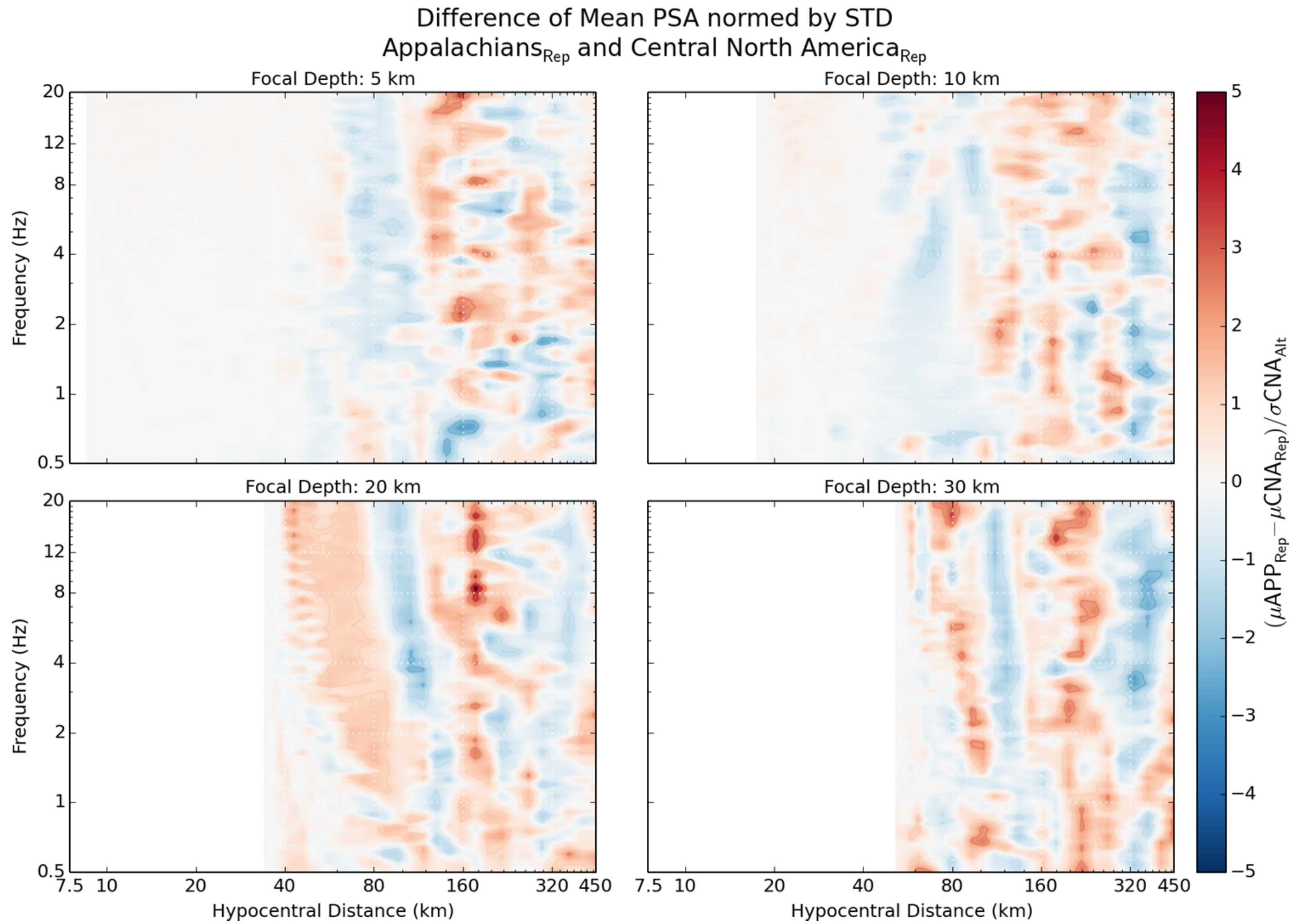

Figure 5.35 Normalized difference of means of ln(PSA) for the APP region relative to CNA at different focal depths.

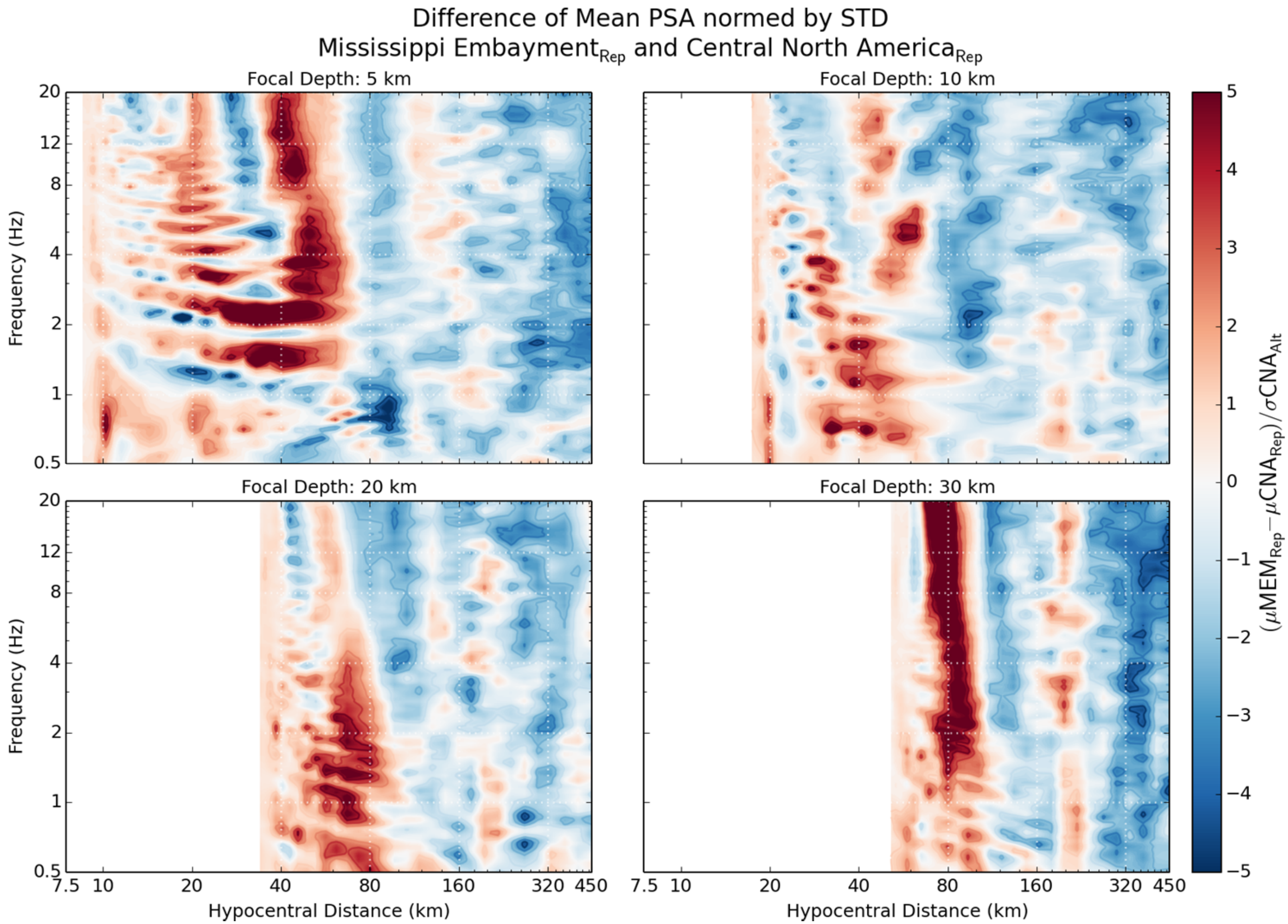

Figure 5.36 **Normalized difference of means of ln(PSA) for the MEM region relative to CNA at different focal depths**

5.5 SUMMARY AND INTERPRETATION

In summary, the statistics of the ln(PSA) histograms demonstrate that the ln(PSA) means of the representative APP and CNA crustal models are very close to each other (the absolute difference is almost always < 0.1). This is true regardless of the focal depth at which the event occurs; only at larger hypocentral distances (>100 km) do the values show noticeable differences. These differences are comparable to the differences in mean from the alternative CNA models (i.e., the variability within CNA model itself, see Table D.1). The absolute values of the normalized difference in means (see Section 4.3) are always smaller than 1, the majority even smaller than 0.3. The percentage of map area (Table 6.2) for which the normalized difference in means in within the range of CNA_{Alt} is between 73% and 91%, depending on the focal depth. The means of the representative models for ACP and CNA, respectively, are also very close together (with an absolute difference mostly < 0.1), and are almost comparable to the differences in mean from within CNA (due to alternate profiles). The absolute values of the normalized difference in means are always smaller than 1, the majority even smaller than 0.4. The fraction of area within the limits of the CNA range (normalize difference of the means) is about 70% for each of the different focal depths (Table 6.2), with the exception of the 20 km source depth, which was excluded due to the existence of a layer boundary at 20.5 km depth that produced strong model-dependent artifacts in the PSAs. However, the results from all other focal depths imply that the ACP belongs to the same attenuation group as CNA. It is worth reiterating is that the agreement between the ACP and CNA is not as close as that between the APP and CNA regions.

The means of the representative MEM and CNA regions are very different (absolute difference mostly between 0.1–0.35). The absolute values of the normalized difference of the means are widely spread, mostly between 0.3–1 with a few values exceeding 1. The fraction of area within the CNA range (normalize difference of the means) is always less than 50%. (see Table 6.2). Our findings are in agreement with previous analyses that concluded that this region is significantly different from other crustal regions within North America.

From these results, we propose two distinct attenuation groups:

- GROUP 1: Central North America, Appalachians, Atlantic Coastal Plain
- GROUP 2: Mississippi Embayment/Gulf Coast

The frequency independent *Q*-factors for the four regions are relatively similar. Thus, the crustal seismic velocity-depth structure is by far the major parameter determining the ground motion results. The presence of a high velocity (7.3 km/sec) lower crustal layer in the MEM region is probably the driving factor for the differences relative to other three regions.

6 Results: Frequency-Dependent *Q*

6.1 INTRODUCTION

Chapters 3–5 summarized the work of the J. Dreiling, M. P. Isken, and W. D. Mooney team on assessing regional differences in attenuation. The previous chapters summarized the development and comparison of representative crustal structure models for four regions of CENA: the Atlantic Coastal Plain (ACP_{Rep}), the Appalachians (APP_{Rep}), Central North America (CNA_{Rep}), and the Mississippi Embayment and Gulf Coast (MEM_{Rep}). The team created synthetic seismograms for a reverse focal mechanism at a range of focal depths and generated seismograms for the radial component of horizontal motion along a profile with source-receiver distances ranging from 1 to 500 km. They then made statistical comparisons of PSA responses for four different geologic regions of CENA. Based on those comparisons, they concluded that three of the four regions were statistically similar enough to be considered one region; see Chapter 5

These synthetic seismograms used frequency-independent *Q*, whereas studies have demonstrated that apparent *Q* for high-frequency *S*-*Lg* waves is frequency dependent. Also, ground motion amplitudes depend on the radiation pattern from the source, and amplitudes vary among the three components of motion. For these reasons, synthetic seismograms were generated for vertical, radial, and transverse components of motion using frequency-dependent *Q* along profiles covering a range of source-receiver azimuths. We also examined several focal depths in addition to those considered in Chapter 5.

Our modeling uses the same source-time function, crustal structure models, and *Q* models (except frequency dependent) defined in Chapter 3. We calculated elemental Green's functions using a modified version of the computer program *hspec96* [Herrmann 2013a; 2013b], which uses frequency-wavenumber integration to generate full wave-field synthetics for horizontally layered Earth crustal structures. We modified *hspec96* to support frequency-dependent *Q* (see Chapman and Godbee [2012]). Chapter 5 showed results from the computer program *FK* by Zhu [2012], which also generates synthetic seismograms using frequency-wavenumber integration.

The PSA responses were computed at the same oscillator frequencies and using the same distance averaging method developed in the previous chapters. This was intentional to allow our results to be directly compared to theirs. We generated a comprehensive set of figures, using the same PYTHON scripts (Chapter 4), with the same layout, scale, etc., for a direct comparison of results figures. To investigate whether comparing the regional models using a single source-receiver azimuth (90°) and component of motion (radial) is representative of the models' differences, we generated figures showing PSA comparisons of the transverse component of motion, as well as a range of source-receiver azimuths and a wider range of focal depths,.

6.2 PARAMETERS

The source and receiver parameters were chosen to be identical to those defined in Chapter 3 and used in Chapter 5. We specified additional focal depths and source-receiver azimuths, but these additional parameters did not affect any data used in comparisons with the original study. The crustal structure models used are identical to those defined in Chapter 3 and used in Chapter 5, with the only difference being that we used frequency-dependent Q instead of constant Q. All time-series records contain 8192 samples with a sampling interval of 0.02 sec.

6.2.1 Source Parameters

- Source type: point source
- Source-time function: triangle pulse, 4 sec duration
- Moment magnitude: 6.0
- Focal mechanism: reverse fault with 180° strike, 45° dip, and 90° rake
- Focal depths: 5, 10, 15, 20, 25, and 30 km

6.2.2 Receiver Parameters

- Source-receiver distances: 1 to 500 km in 60 $\log_{10}$-spaced steps
- Source-receiver azimuths: 0°, 22.5°, 45°, 67.5°, and 90°
- Components of motion: vertical, radial, and transverse

6.2.3 Earth Structure Models

The Q versus frequency relation for each Earth structure model is given by $Q_p(f) = Q_p\left(\frac{f}{f_p}\right)^{\eta_p}$ for P-waves and $Q_s(f) = Q_s\left(\frac{f}{f_s}\right)^{\eta_s}$ for S-waves.

Table 6.1 Summary of crustal structure parameters.

Layer thickness (km)	V_p (km/sec)	V_s (km/sec)	Layer density (g/cm^3)	Q_p	Q_s	η_p	η_s	f_p	f_s
Atlantic Coastal Plain Representative Model (ACP$_{Rep}$)									
20.5	6.0	3.46	2.690	1256.0	628.0	0.38	0.38	1.0	1.0
15.5	6.7	3.87	2.914	1256.0	628.0	0.38	0.38	1.0	1.0
∞	8.1	4.68	3.362	1256.0	628.0	0.38	0.38	1.0	1.0
Appalachians representative model (APP$_{Rep}$)									
12.0	6.1	3.52	2.722	1426.0	713.0	0.39	0.39	1.0	1.0
8.0	6.4	3.70	2.818	1426.0	713.0	0.39	0.39	1.0	1.0
17.0	6.7	3.87	2.914	1426.0	713.0	0.39	0.39	1.0	1.0
∞	8.1	4.68	3.362	1426.0	713.0	0.39	0.39	1.0	1.0
Central North America representative model (CNA$_{Rep}$)									
12.0	6.1	3.52	2.722	1260.0	630.0	0.40	0.40	1.0	1.0
8.0	6.5	3.75	2.850	1260.0	630.0	0.40	0.40	1.0	1.0
14.0	6.7	3.87	2.914	1260.0	630.0	0.40	0.40	1.0	1.0
6.0	6.8	3.93	2.946	1260.0	630.0	0.40	0.40	1.0	1.0
∞	8.1	4.68	3.362	1260.0	630.0	0.40	0.40	1.0	1.0
Mississippi Embayment representative model (MEM$_{Rep}$)									
4.0	5.9	3.41	2.658	1228.0	614.0	0.32	0.32	1.0	1.0
12.5	6.2	3.58	2.754	1228.0	614.0	0.32	0.32	1.0	1.0
13.5	6.6	3.81	2.882	1228.0	614.0	0.32	0.32	1.0	1.0
11.0	7.3	4.21	3.106	1228.0	614.0	0.32	0.32	1.0	1.0
∞	8.0	4.62	3.330	1228.0	614.0	0.32	0.32	1.0	1.0

6.3 WORKFLOW

The workflow for generating the data and figures was divided into four steps that were run in sequence: the Green's functions were calculated, acceleration seismograms from those Green's functions were calculated, from which PSA was computed. The figures were then generated for PSA comparison between regions. In order to reduce the amount of time it took for the workflow to run to completion, each of the four steps were divided into a series of smaller tasks that were run in parallel.

6.3.1 Green's Functions

Sets of elemental Green's functions were calculated for all combinations of the four Earth crustal structure models, the six focal depths, and the 60 source-receiver distances (for a total of 1440 sets of Green's functions), using Herrmann's computer software [2013a; 2013b], and included the modified version of *hspec96*.

Figure 6.1 shows the flow of data and parameters through the various CPS programs implementing wavenumber integration and conversion of CPS's "file96" format to SAC files (see *SAC Data File Format* [2012]). Red ovals and arrows represent command-line parameters passed to the *run-herrmann* Bourne shell script that controls this workflow. Boxes with white backgrounds represent input and/or output files, while boxes with gray backgrounds represent programs. Black arrows represent the flow of files into and out of programs.

The *run-herrmann* script accepts two command-line parameters: the region name and the focal depth (in km).

distance.dat is a text file that contains source-receiver distances, the sampling interval (in seconds), the number of samples, the time offset of the first sample (in seconds), and the reducing velocity (in km/sec).

The *velmod_[model].dat* text files contain the representative crustal structure models used by Dreiling et al. team. *[model]* contains the all-lowercase name of a model, such as "acp_rep" for the Atlantic Coastal Plain representative model. These files contain all of the parameters specified in Section 6.2.3 above, as well as other model-related parameters that affect *hspec96*'s operation.

The *B[rrr][nn][NNN].sac* files contain the Green's functions as time-series data in SAC binary format and are the output of this step. In these files' names, *[rrr]* is the receiver number (001–060), *[nn]* is a CPS-specific number corresponding to a specific Green's function (01–10), and *[NNN]* is a CPS-specific abbreviation for a Green's function (*ZDD*, *RDD*, *ZDS*, *RDS*, *TDS*, *ZSS*, *RSS*, *TSS*, *ZEX*, or *REX*). For example, *B01708TSS.sac* contains the tangential component vertical strike slip Green's function for the 17th receiver listed in *distance.dat*. These files are organized in directories that correspond to their region and focal depth.

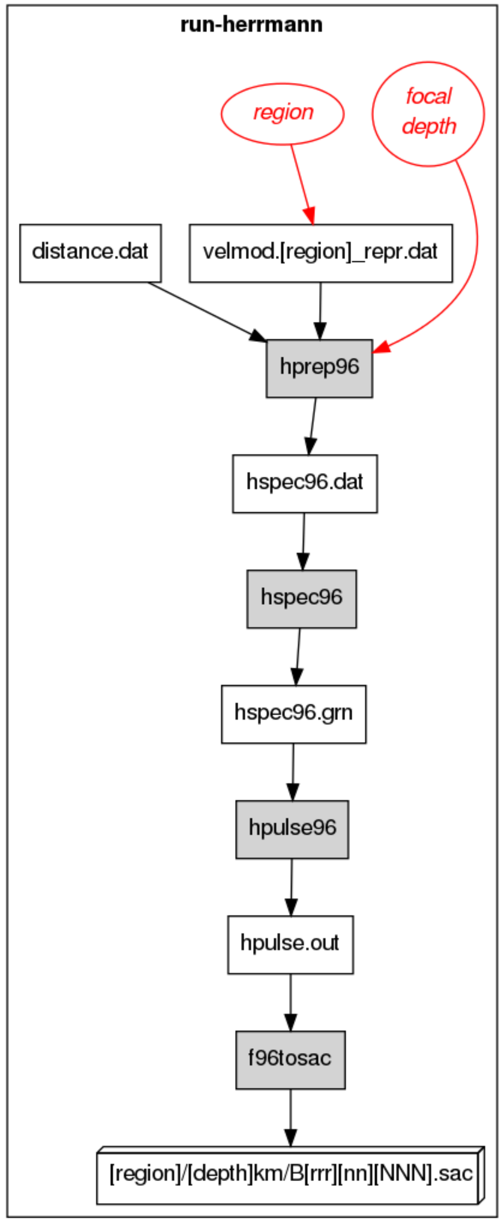

Figure 6.1 **Flow of data and parameters in the generation of Green's functions by the *run-herrmann* script.**

6.3.2 Acceleration Seismograms

The *answer* computer program was developed (see the Appendix of Chapman and Godbee [2012]) to combine the source-time function with the 1440 sets of Green's functions computed in the previous step and create three-component acceleration seismograms for the five source-receiver azimuths (7200 three-component seismograms).

Figure 6.2 shows the flow of data and parameters through the *answer* program. Red ovals and arrows represent command-line parameters passed to the *run-answer* Bourne shell script that controls this workflow. Light gray ovals and arrows represent parameters "baked into" the *run-answer* script. (Since only one fault orientation was used in this study, these fault orientation parameters never changed.) Boxes with white backgrounds represent input or output files, while boxes with gray backgrounds represent programs. Black arrows represent the flow of files into and out of programs.

The *run-answer* script accepts three command-line arguments: the region, the focal depth (in km), and the source-receiver azimuth.

triangle_source_pulse.dat is a text file containing a time-series record of the source pulse's moment rate. The file has two columns containing the time (in seconds) and moment rate (in dyne·cm/sec) of each of the 8192 samples in the record. The total moment of the source pulse used in this study was 1.122×10^{25} dyne·cm, corresponding to an M_W 6.0 earthquake.

The *B[rrr][nn][NNN].sac* files correspond to the Green's functions computed in the previous step.

The *answer.[rrr].[cc].sac* files are three-component acceleration seismograms in SAC binary format. In these files' names, *[rrr]* is the receiver number (001–060) and *[cc]* is the component of motion (*z* for vertical, *r* for radial, or *t* for transverse). These files are organized in directories that correspond to their model, focal depth, and source-receiver azimuth.

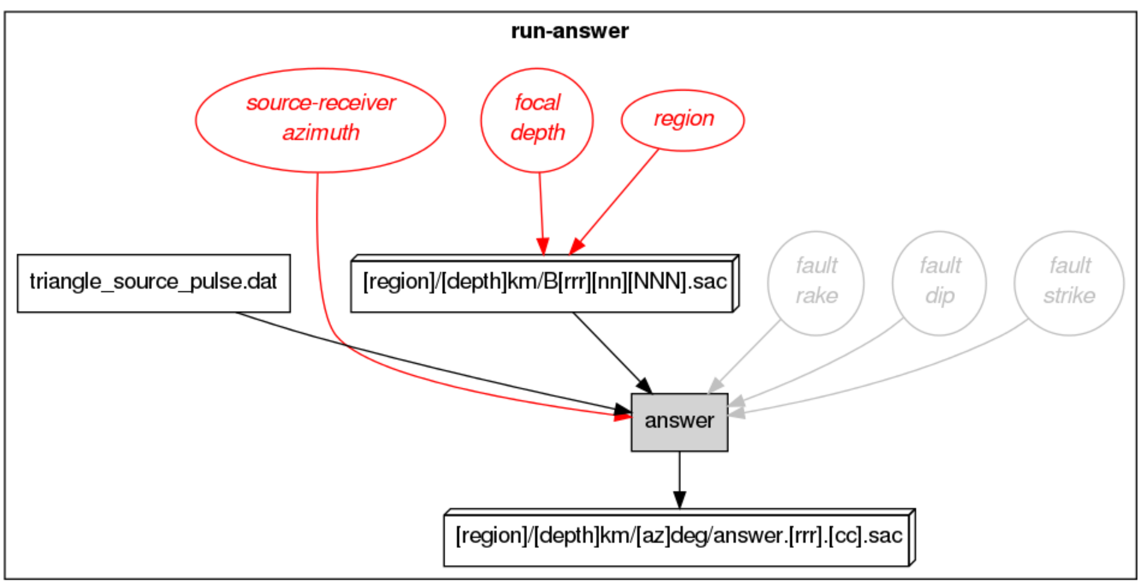

Figure 6.2 Flow of data and parameters in the generation of acceleration seismograms by the *run-answer* script.

6.3.3 PSA Response

The vertical, radial, and transverse component PSA response spectra (5% damping) were computed using the program *acc2rspect*, which uses the Nigam and Jennings [1969] method. Following Dreiling et al. team's protocol, the response was calculated at 200 $\log_{10}$-spaced frequencies between 0.1 and 100 Hz for all 7200 sets of three-component seismograms generated in the previous step.

Figure 6.3 shows the flow of data and parameters through the *acc2rspect* program. Red ovals and arrows represent command-line parameters passed to the *run-rspect* Bourne shell script that controls this workflow. Boxes with white backgrounds represent input or output files, while boxes with gray backgrounds represent programs. Black arrows represent the flow of files into and out of programs.

The *run-rspect* script accepts three command-line arguments: the region, the focal depth (in km), and the source-receiver azimuth. The *answer.[rrr].[cc].sac* files correspond to the acceleration seismograms computed in the previous step. The *acc2rspect_[cc].out* files are text files containing PGV, PGA, and PSA data. In these files' names, *[cc]* is the component of motion (*ZZ* for vertical, *rad* for radial, or *tran* for transverse). Each line in the file corresponds to a receiver; for example, line 28 corresponds to receiver number 28. The columns in the file are as follows:

- Column 1: Source-receiver distance (epicentral)
- Column 2: Source-receiver distance (hypocentral)
- Column 3: PGV (cm/sec)
- Column 4: PGA (cm/sec^2)
- Columns 5–204: PSA (cm/sec^2) for frequencies 1–200

These files are organized in directories that correspond to their model, focal depth, and source-receiver azimuth.

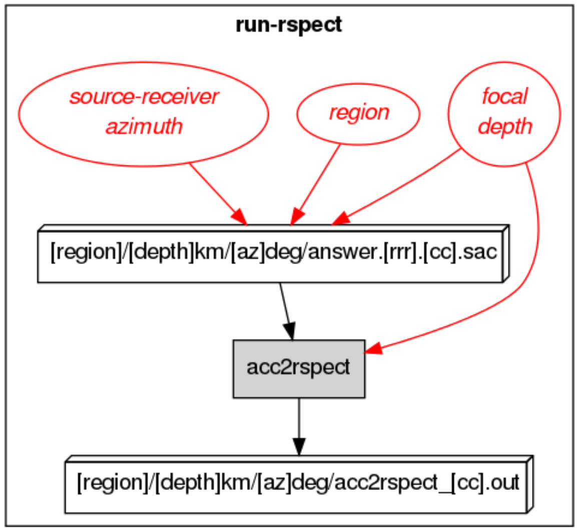

Figure 6.3 **Flow of data and parameters in the generation of PSA response spectra by the *run-rspect* script.**

6.3.4 Figures

As described in Chapter 5, a module (*pyPSA*) and a set of programs written in the PYTHON programming language was developed to read PSA data and generate the various figures using *matplotlib*, a 2D graphics package for PYTHON written by Hunter [2007]. An initial investigation tried to modify *pyPSA* to read PSA data file format, but in the course of doing so, it was discovered that *pyPSA* would try to read datasets not included in this in this part of the study, such as the PSA data for the CNA_{Alt} crustal structure models..

Rather than modify *pyPSA* to read the data file format,, it was decided that it would be more straightforward to write a new set of programs that could read the PSA data files and generate the figures using *pyPSA* as a guide for what *matplotlib* functions and parameters to use. This effort resulted in the creation of three PYTHON programs:

- *regions-psa.py* generates figures containing four filled 2D contour plots of PSA response over hypocentral distance and frequency, one plot per representative Earth structure model. The figures generated by this script correspond to Figures 5.11–5.14..
- *mean-difference-psa.py* generates figures containing two line plots: one showing the mean PSA response of the CNA_{Rep} Earth structure model and the mean PSA of another representative Earth structure model (plus error bars $\pm\sigma$ of the comparison model), and the other showing the difference between the two mean PSAs. The figures generated by this script correspond to Figures 5.25–5.30.
- *mean-difference-psa-contour.py* generates figures containing four filled 2-D contour plots of the difference of the mean PSA response of the CNA_{Rep} Earth structure model and the mean PSA response of another representative Earth structure model over hypocentral distance and frequency, one plot per focal depth.

The figures generated by this script correspond to Figures 5.31–5.33 from Chapter 5.

The figures these scripts generate aim to be identical in style to the figures from those shown in Chapters 4 and 5, but there are a few differences worth noting:

- The figures generated by *mean-difference-psa.py* do not include the $\pm\sigma \text{CNA}_{Alt}$ error band because we did not generate synthetics for CNA_{Alt}.
- All of the figures have a small annotation in the upper right corner of the figure (or the main plot within the figure) showing which source-receiver azimuth and component of motion that figure represents. The figures in Chapter 5 all show data from the radial component of motion using receivers with a source-receiver azimuth of 90°, but we also generated figures for other components of motion and source-receiver azimuths.
- All of the figures have a small annotation in the lower right corner with the authors' initials ("mcc/rwg"). Since our figures are very similar in appearance to those from Chapter 5, this provides a quick method to identify our figures.

Additionally, we developed a fourth PYTHON script, *mean-difference-psa-rad+tran.py*. This script generates the same style of plot as *mean-difference-psa.py*, but it shows both the radial and transverse components instead of only the radial component.

6.3.5 Parallel Execution

Every step in the workflow is "perfectly parallel"; that is, each step can be divided into separate tasks that have no dependencies on each other. Therefore, the tasks in each step can be run concurrently without any special programming considerations. We wrote three Bourne shell scripts that use Tange's GNU Parallel program [2011] to manage running the tasks described in Sections 6.3.1, 6.3.2, and 6.3.3.

- *run-herrmann-all* uses GNU Parallel to manage running *run-herrmann* script for all combinations of the four Earth structure models, six focal depths, and 60 source-receiver distances.
- *run-answer-all* uses GNU Parallel to manage running the *run-answer* script for all combinations of the four Earth structure models, six focal depths, 60 source-receiver distances, and five source-receiver azimuths.
- *run-rspect-all* uses GNU Parallel to manage running the *run-rspect* script for all combinations of the four Earth structure models, six focal depths, 60 source-receiver distances, five source-receiver azimuths, and three components of motion.

The three PYTHON programs used to generate the figures contain code to generate their figures in parallel using PYTHON's *multiprocessing* module, so GNU Parallel was not used to run those programs. Both GNU Parallel and PYTHON's *multiprocessing* module can detect the number of CPUs available and were configured to limit the number of tasks they ran concurrently to that number so the CPUs weren't oversubscribed.

6.4 RESULTS: COMPARISON TO RESULTS OBTAINED IN CHAPTER 5

The results shown in Figures 6.4–6.7 are compared to Figures 5.11–5.14 in Chapter 5 The figures show PSA response amplitude as a function of frequency and distance for all four Earth structure models, at focal depths of 5, 10, 20, and 30 km.

Figures 6.8–6.13 compare Figures 5.25–5.30 and D.29 (top two panels) with the corresponding figures generated in this study (bottom two panels). The figures show PSA amplitudes for the CNA region and PSA amplitudes for each of the three other regions versus hypocenter distance, as well as the difference of the two sets of PSA amplitudes versus hypocenter distance. The purpose of these figures is to quantify the differences between the results from APP_{Rep}, ACP_{Rep}, and MEM_{Rep} crustal structure models and the ones from the CNA_{Rep} model. In the lower panel, the dashed black lines show the mean PSA amplitudes for the CNA_{Rep} model, and the solid green lines and error bars show the mean ± one standard deviation of PSA amplitudes for the model being compared to the CNA_{Rep} model in a series of hypocenter distance bands. In the upper panel, the solid black line shows the mean PSA amplitudes of the model being compared (either APP_{Rep}, ACP_{Rep}, or MEM_{Rep}) minus the mean PSA amplitudes of the CNA_{Rep} model.

Figures 6.14–6.16 compare Figures 5.31–5.33 with the corresponding figures generated in this part of the study. Each figure shows the mean PSA amplitudes (as functions of hypocenter distance and frequency) of the model being compared (either APP_{Rep}, ACP_{Rep}, or MEM_{Rep}) minus the mean PSA amplitudes of the CNA_{Rep} model at focal depths of 5, 10, 20, and 30 km

Examination of the figures below shows very minor differences due to our treatment of anelastic attenuation using frequency-dependent *Q*. The differences between the APP_{Rep}, ACP_{Rep}, and MEM_{Rep} models and the CNA_{Rep} model are largest at frequencies greater than 5 Hz and at epicentral distances greater than 100 km. At smaller distances, the differences are negligible. We concluded that the issue of *Q* models has no impact on questions concerning regionalization.

.

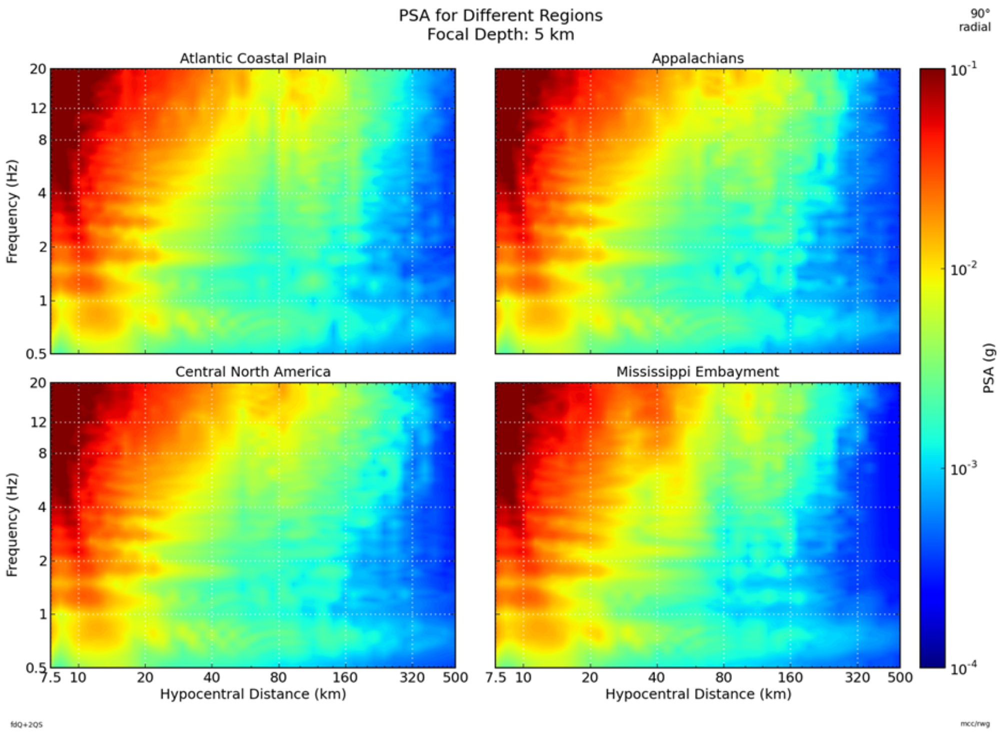

(a)

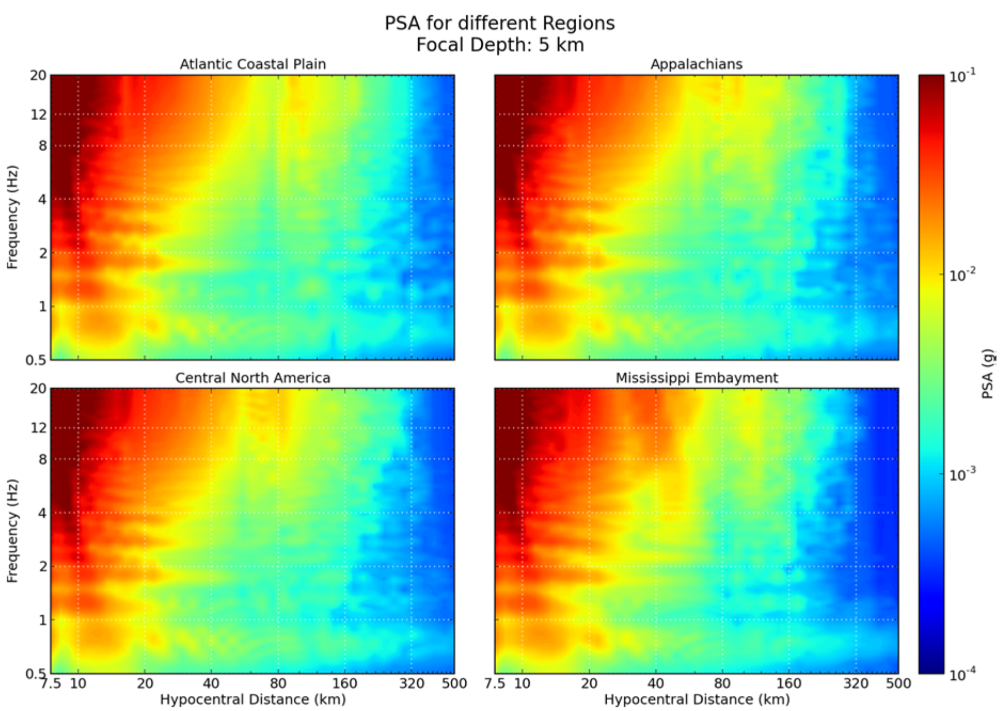

(b)

Figure 6.4 PSA for different regions: (a) Figure 5.11 compared to (b) analogous results from using frequency-dependent *Q* at a focal depth of 5 km.

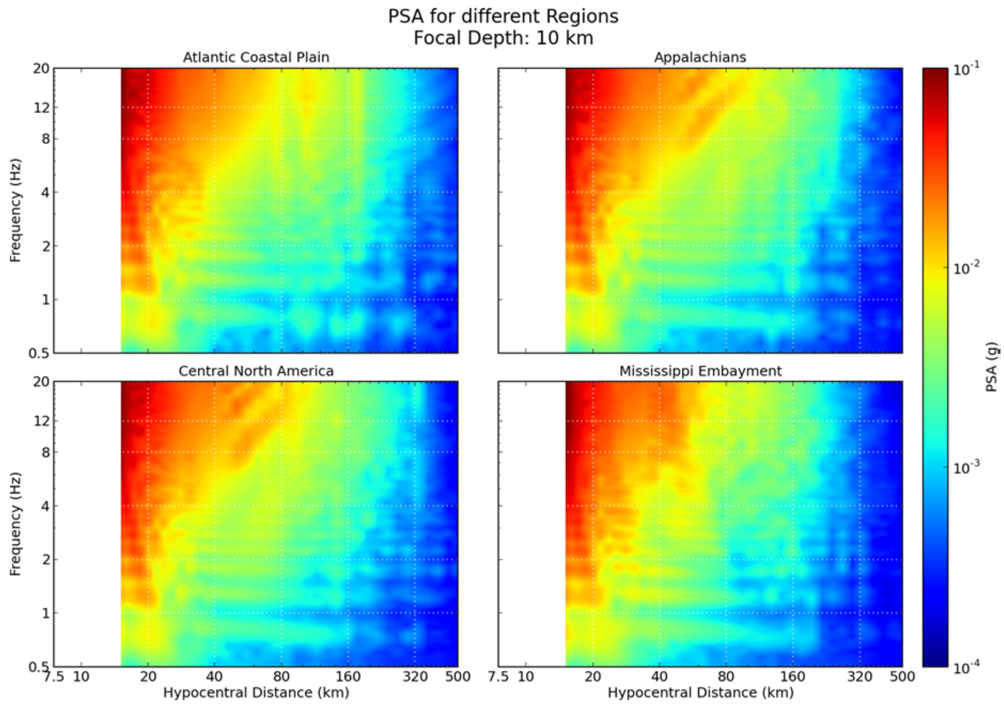

(a)

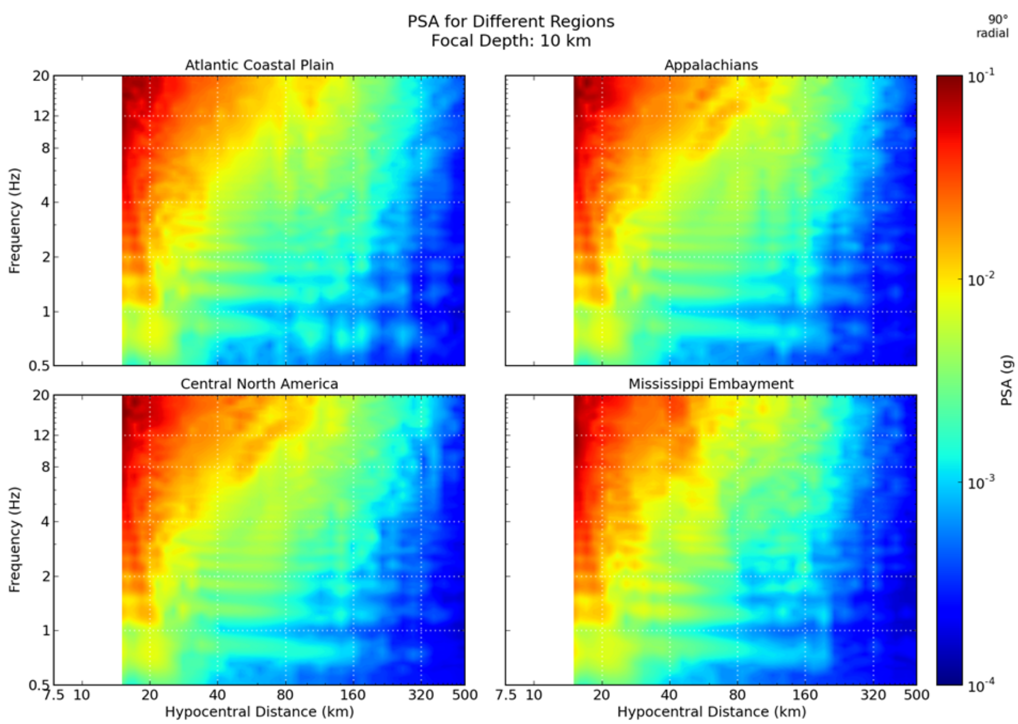

(b)

Figure 6.5 PSA for different regions: (a) Figure 5.12 compared to (b) analogous results from using frequency-dependent *Q* at a focal depth of 10 km.

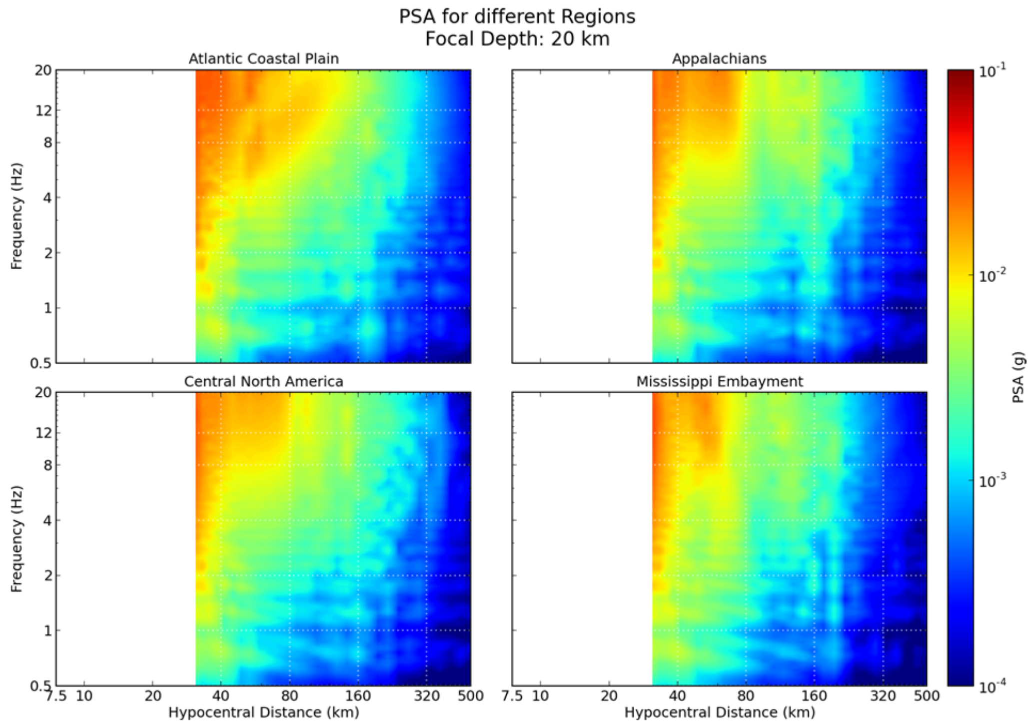

(a)

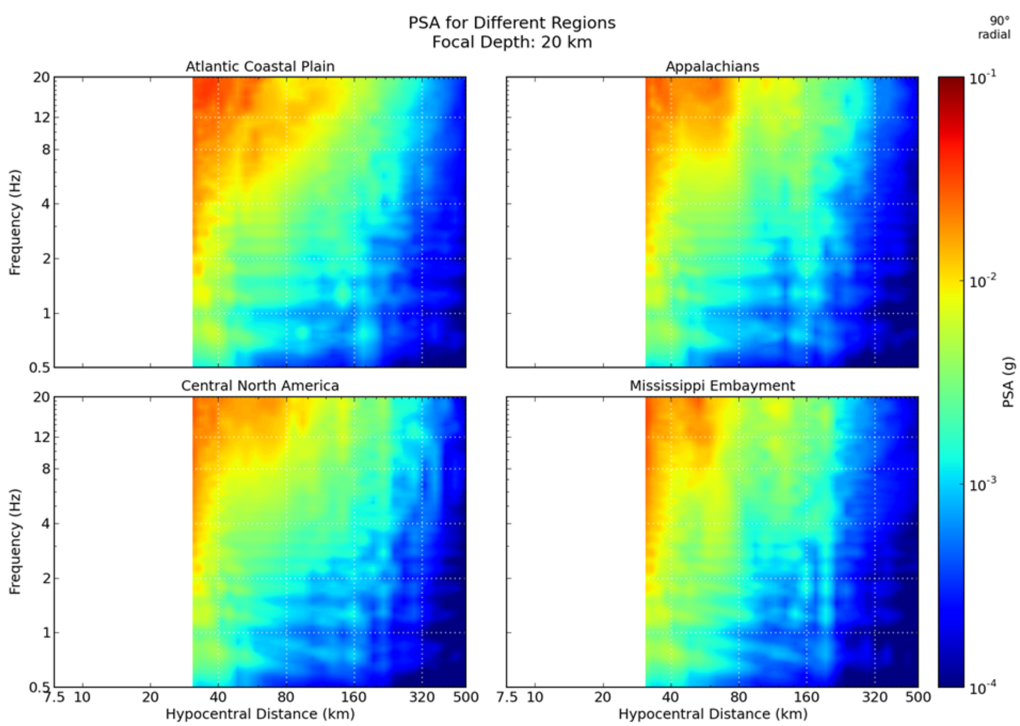

(b)

Figure 6.6 **PSA for different regions: (a) Figure 5.13 compared to (b) analogous results from using frequency-dependent *Q* at a focal depth of 20 km.**

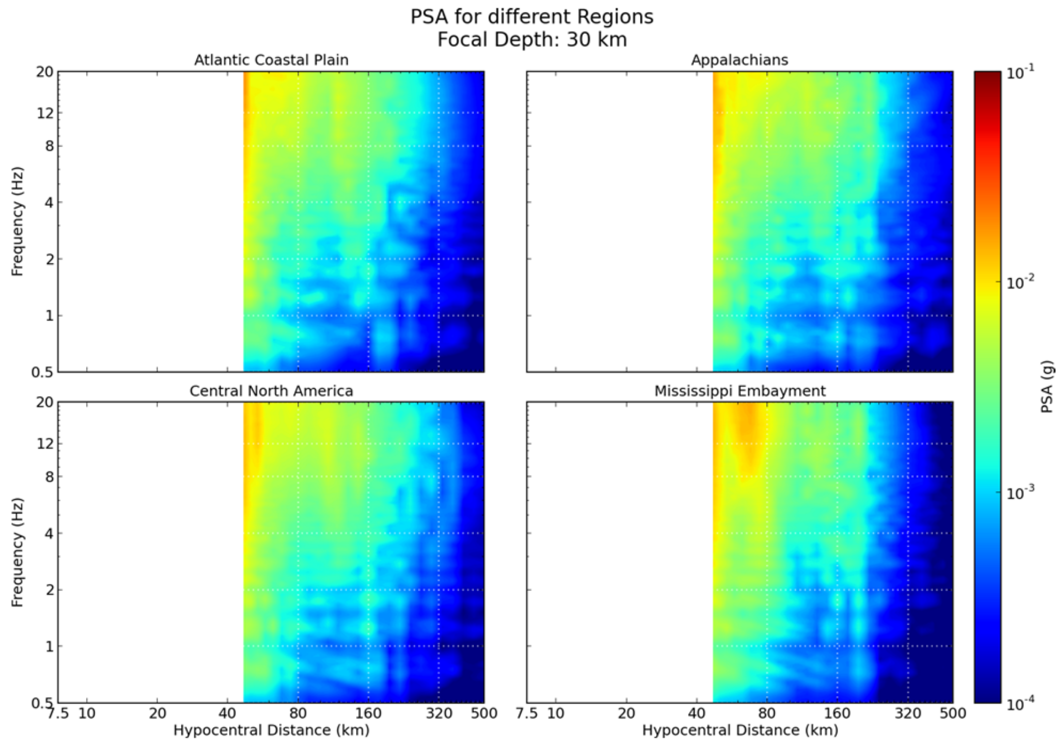

(a)

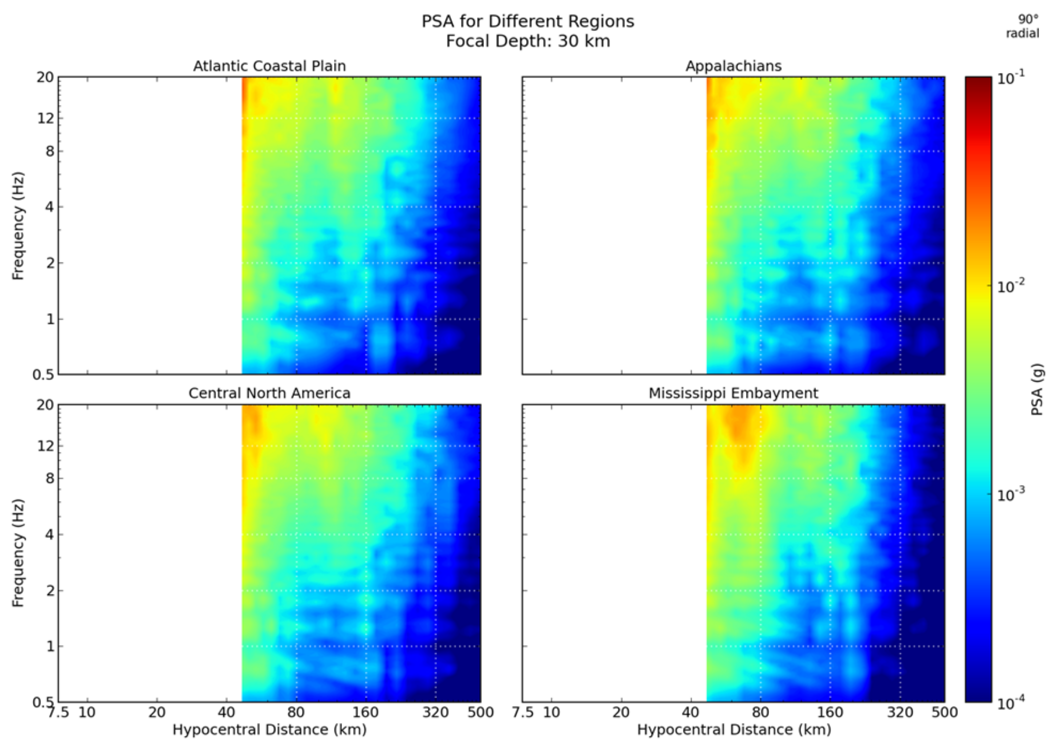

(b)

Figure 6.7 **PSA for different regions: (a) Figure 5.14 compared to (b) analogous results from using frequency-dependent *Q* at a focal depth of 30 km.**

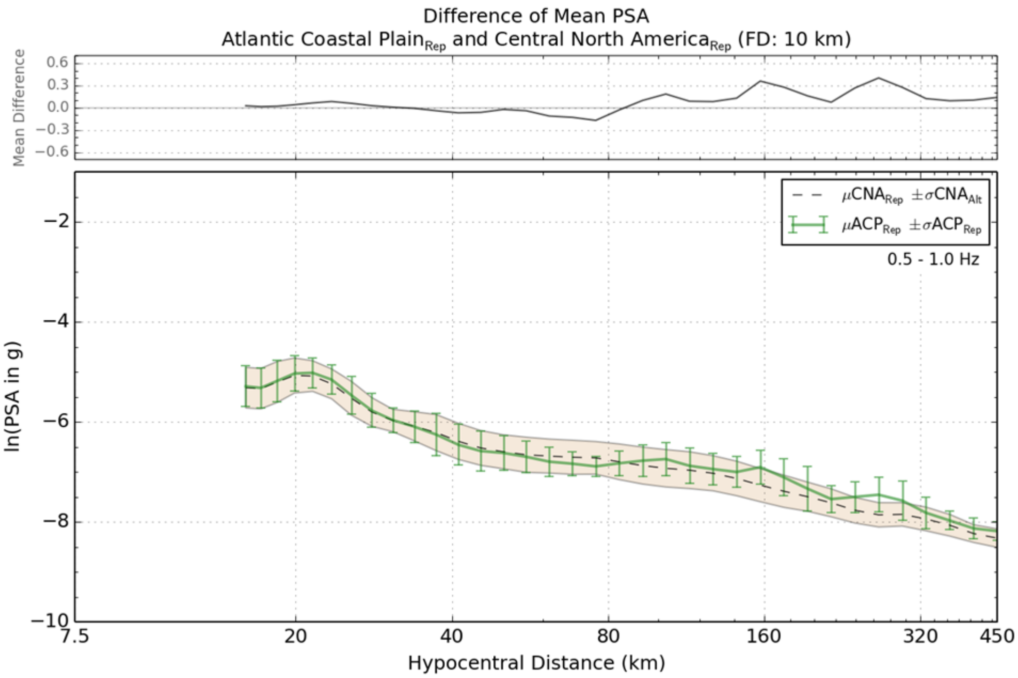

(a)

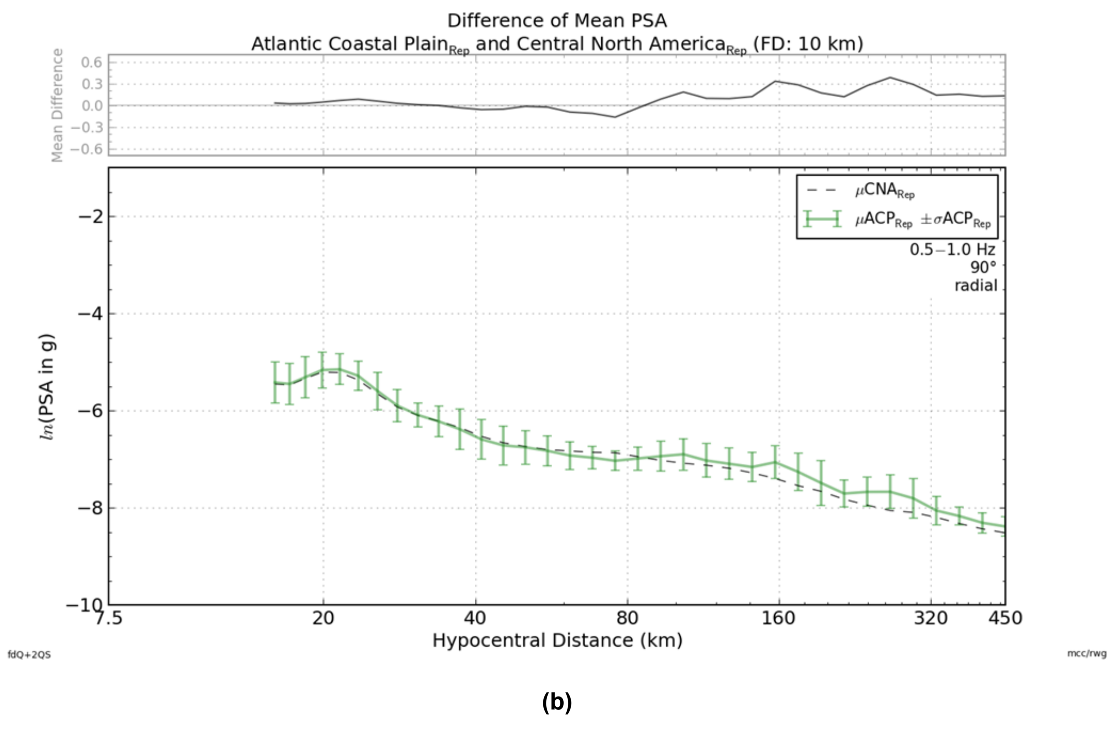

(b)

Figure 6.8 Difference of mean PSA: (a) Figure 5.25 compared to (b) analogous results from using frequency-dependent *Q* at a focal depth of 10 km and 0.5–1.0 Hz.

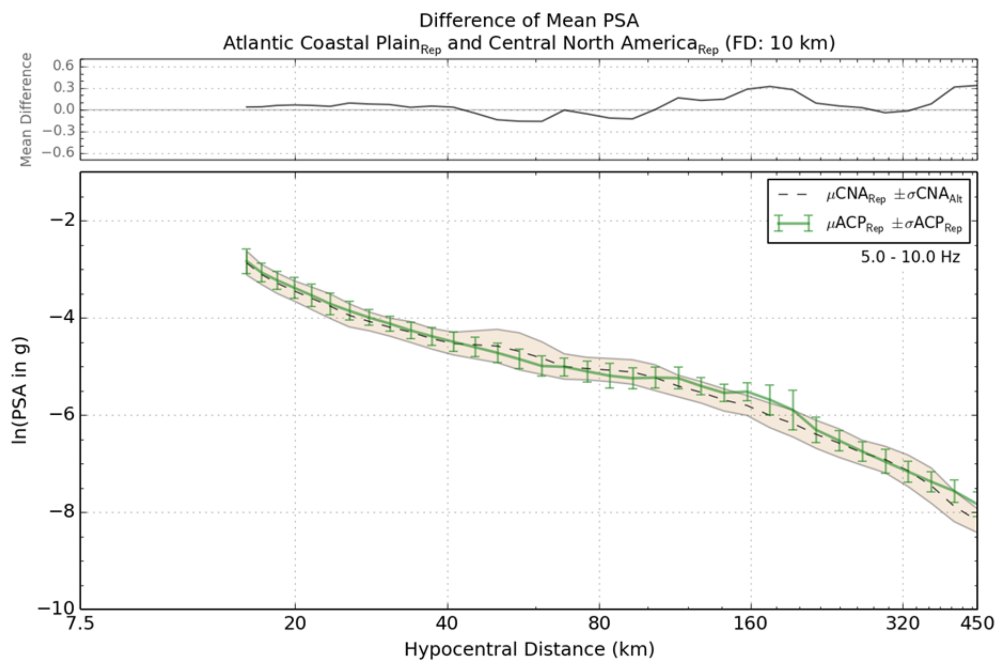

(a)

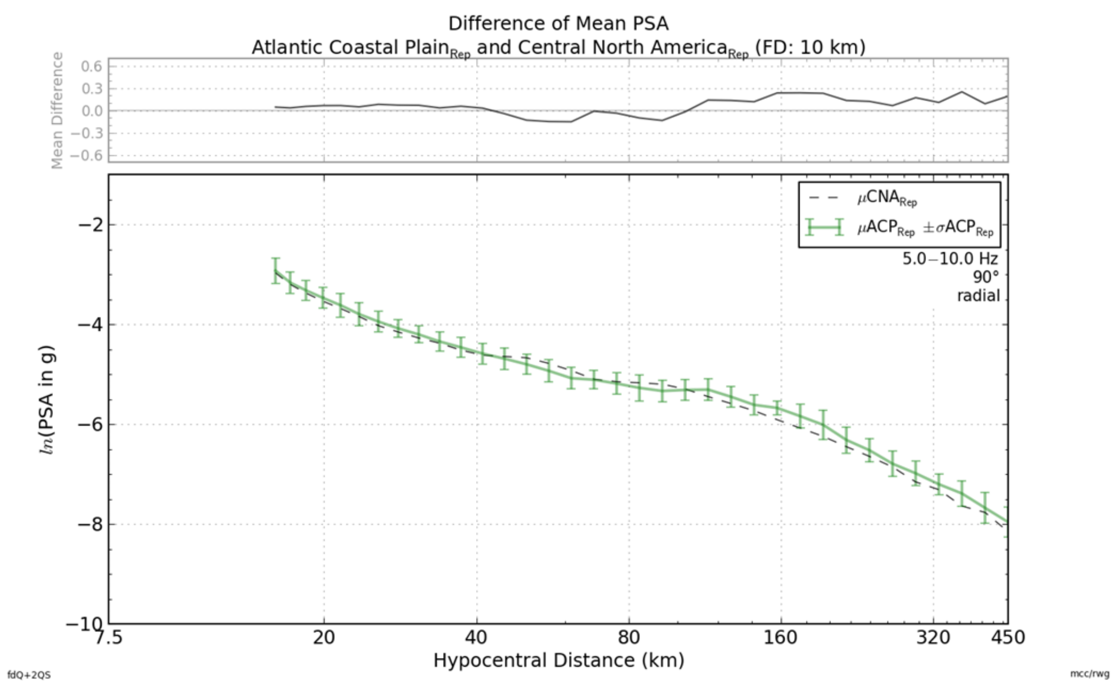

(b)

Figure 6.9 **Difference of mean PSA: (a) Figure 5.26 compared to (b) analogous results from using frequency-dependent *Q* at a focal depth of 10 km and 5.0–10.0 Hz.**

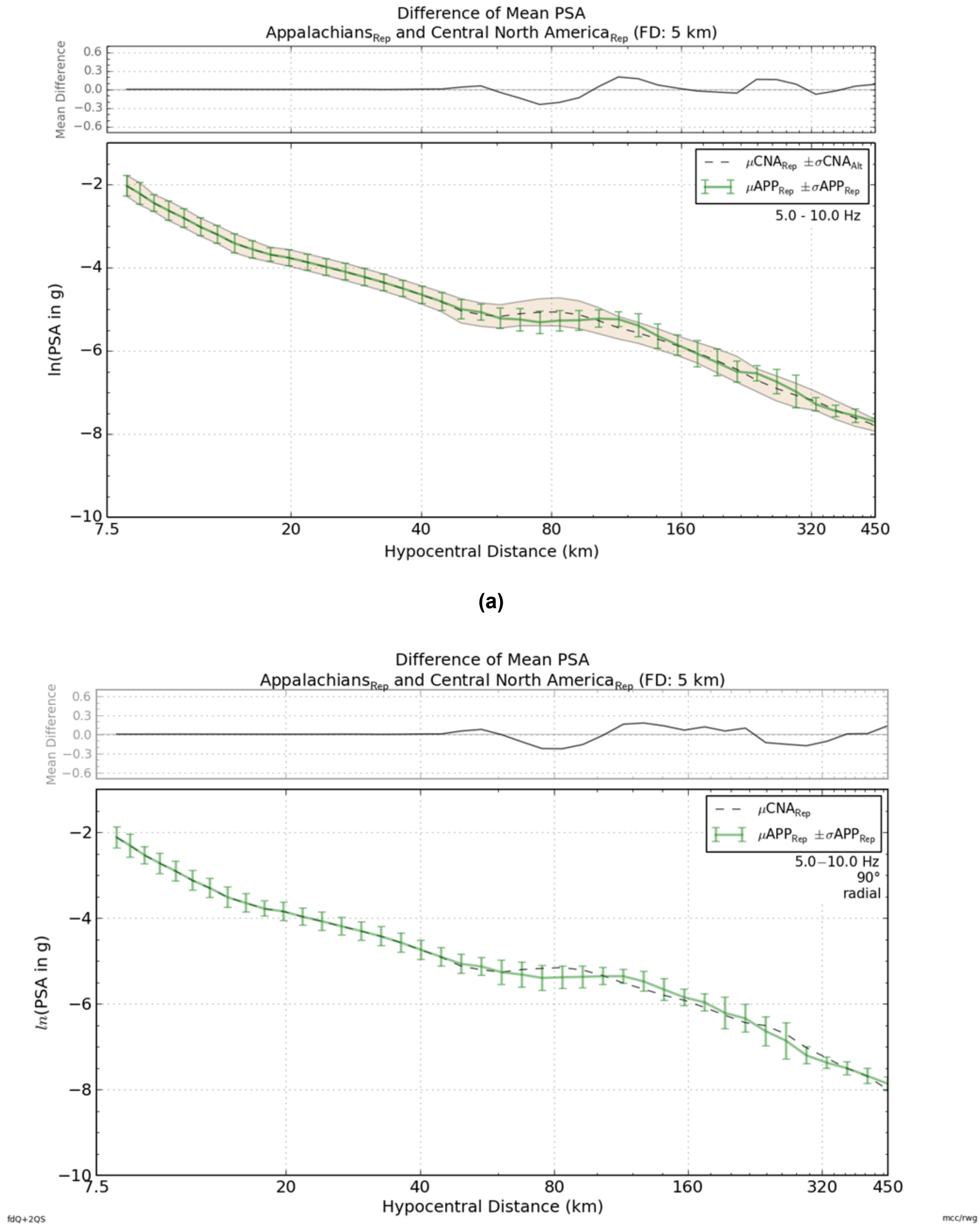

(a)

(b)

Figure 6.10 **Difference of mean PSA: (a) Figure 5.27 compared to (b) analogous results from using frequency-dependent *Q* at a focal depth of 5 km and 5.0–10.0 Hz.**

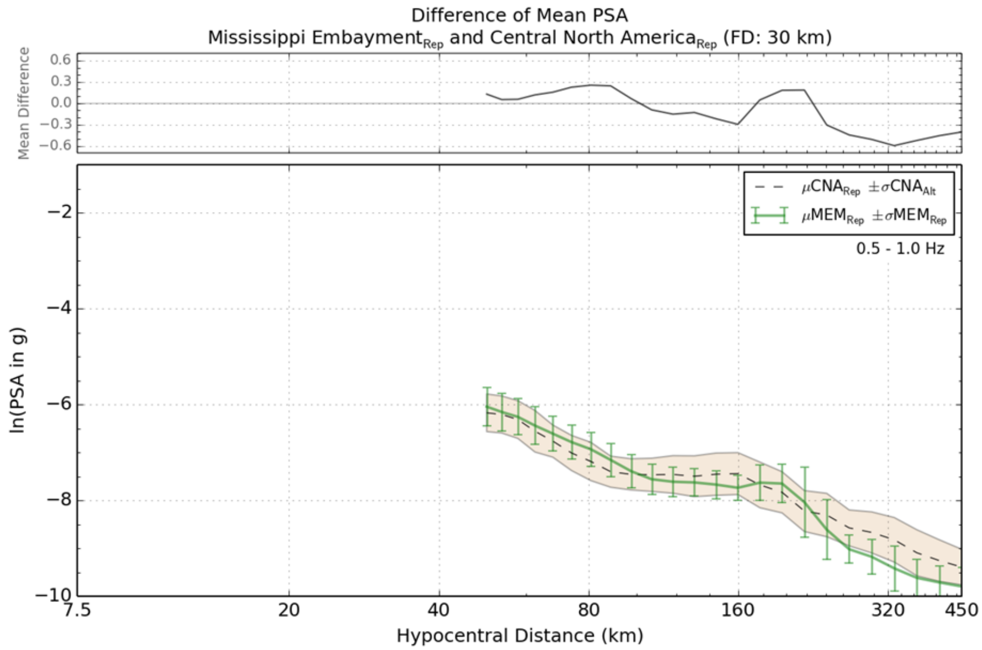

(a)

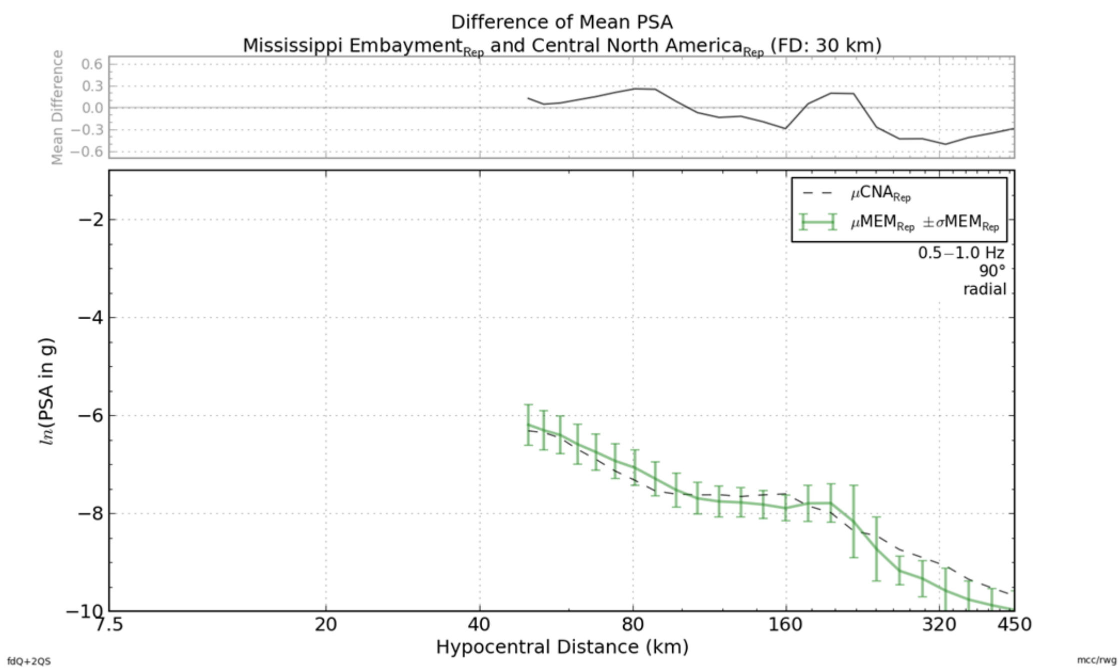

(b)

Figure 6.11 Difference of mean PSA: (a) Figure 5.29 compared to (b) analogous results from using frequency-dependent *Q* at a focal depth of 30 km and 0.5–1.0 HZ.

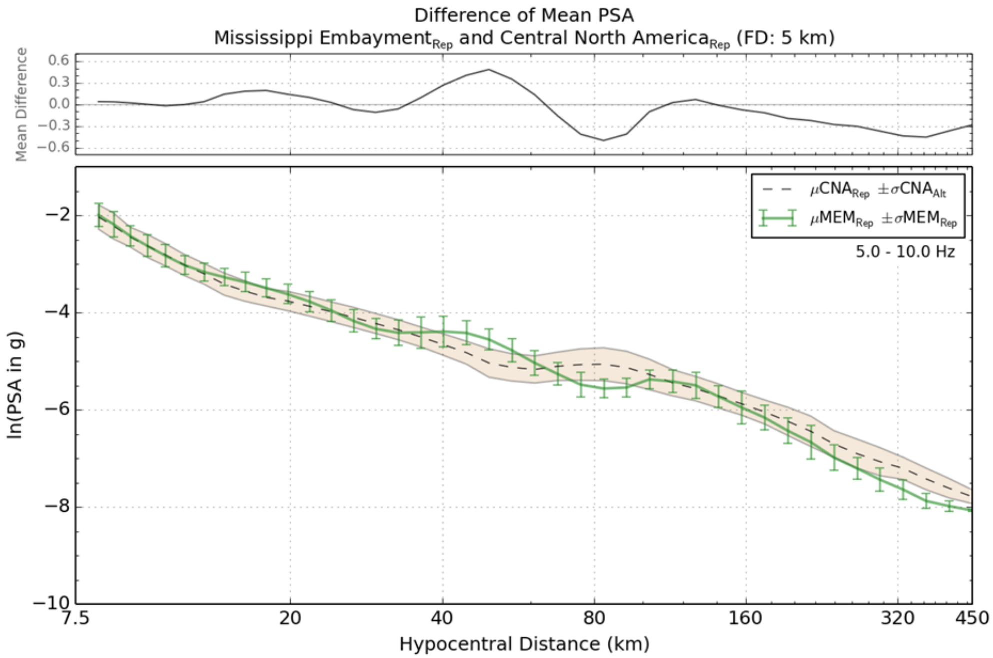

(a)

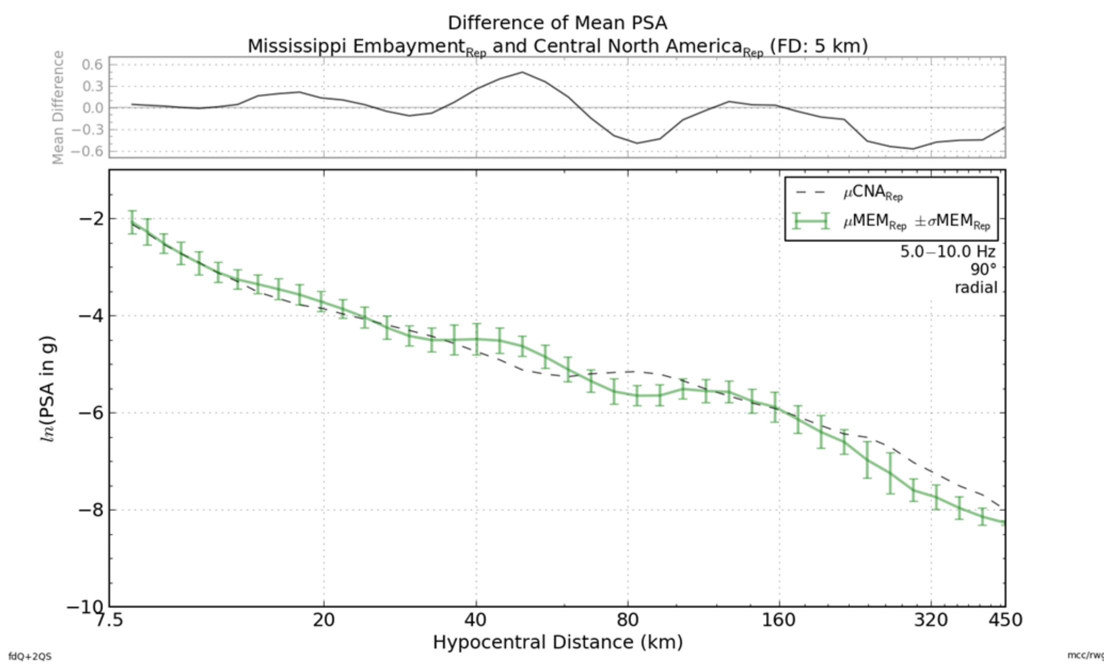

(b)

Figure 6.12 Difference of mean PSA: (a) Figure 5.30 compared to (b) analogous results from using frequency-dependent *Q* at a focal depth of 5 km and 5.0–10.0 Hz.

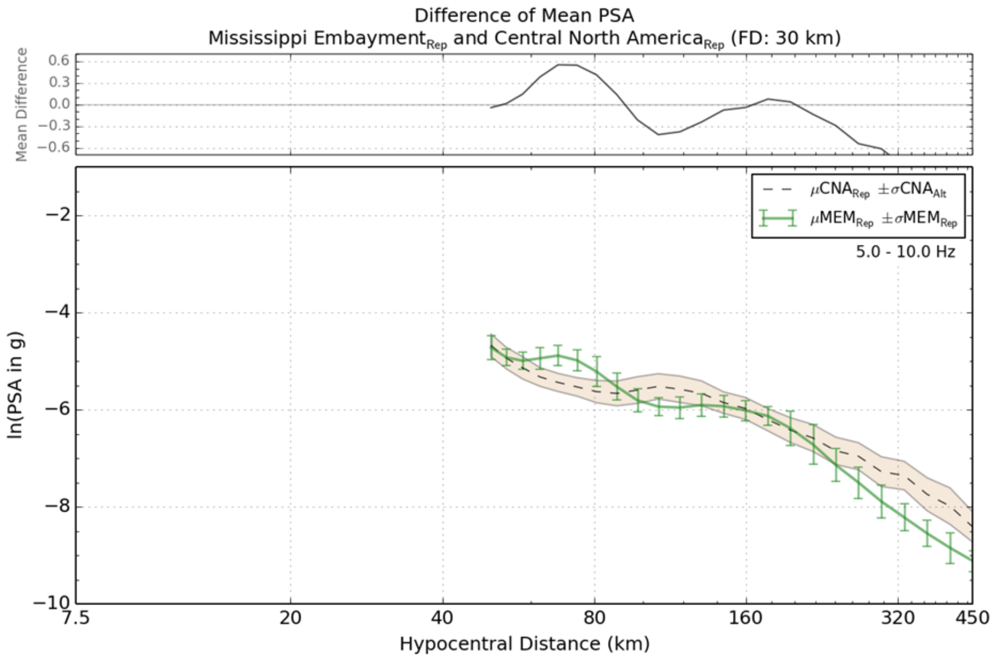

(a)

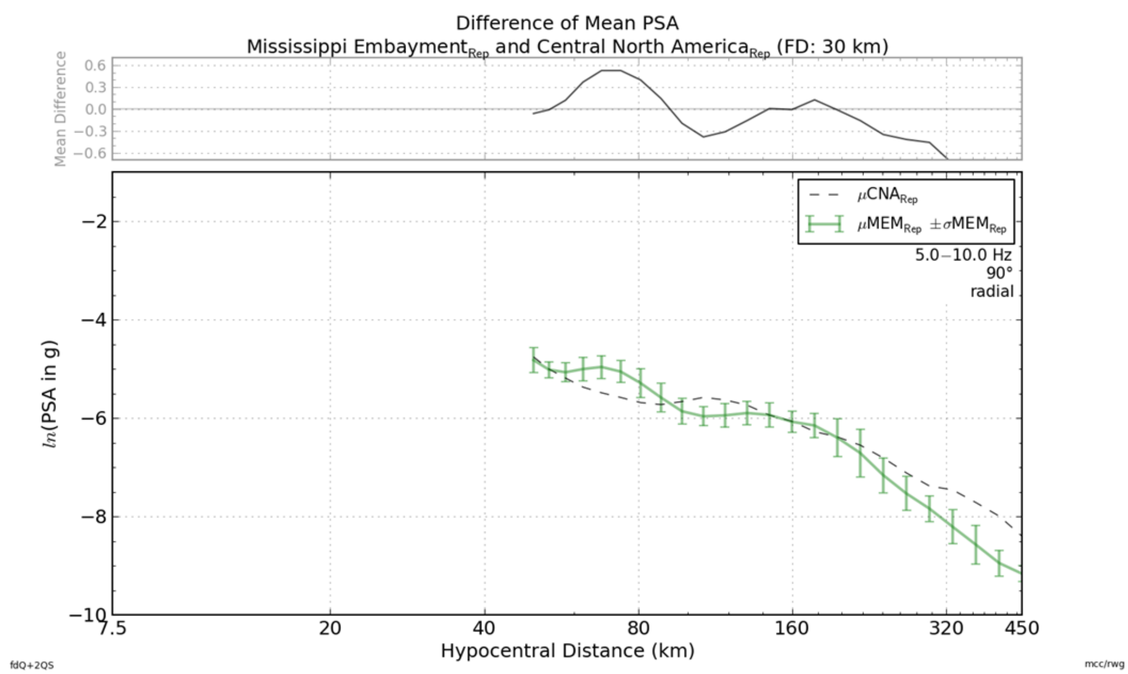

(b)

Figure 6.13 Difference of mean PSA: (a) Figure D.29 compared to (b) analogous results from using frequency-dependent *Q* at a focal depth of 30 km and 5.0–10.0 Hz.

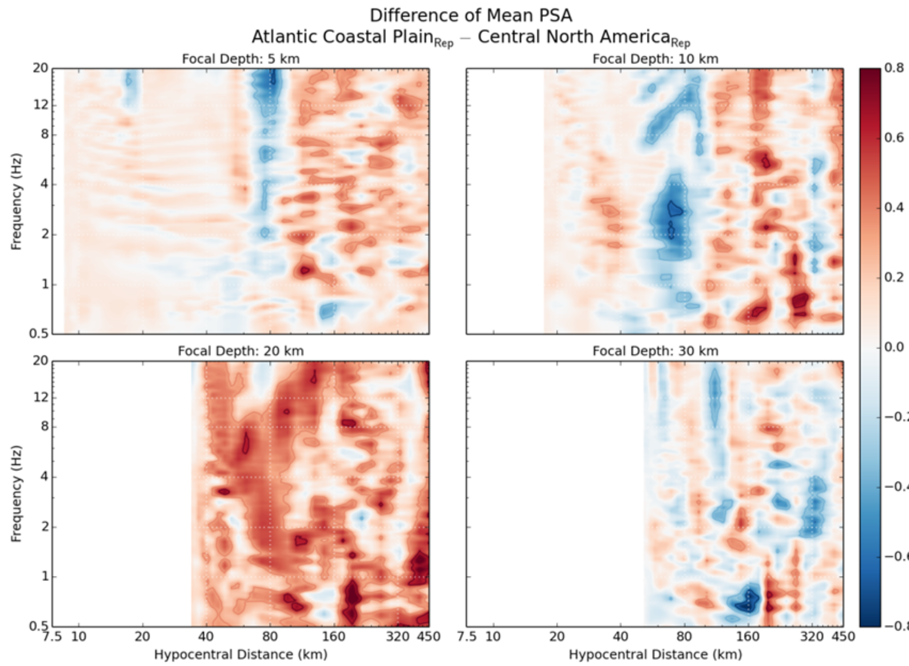

(a)

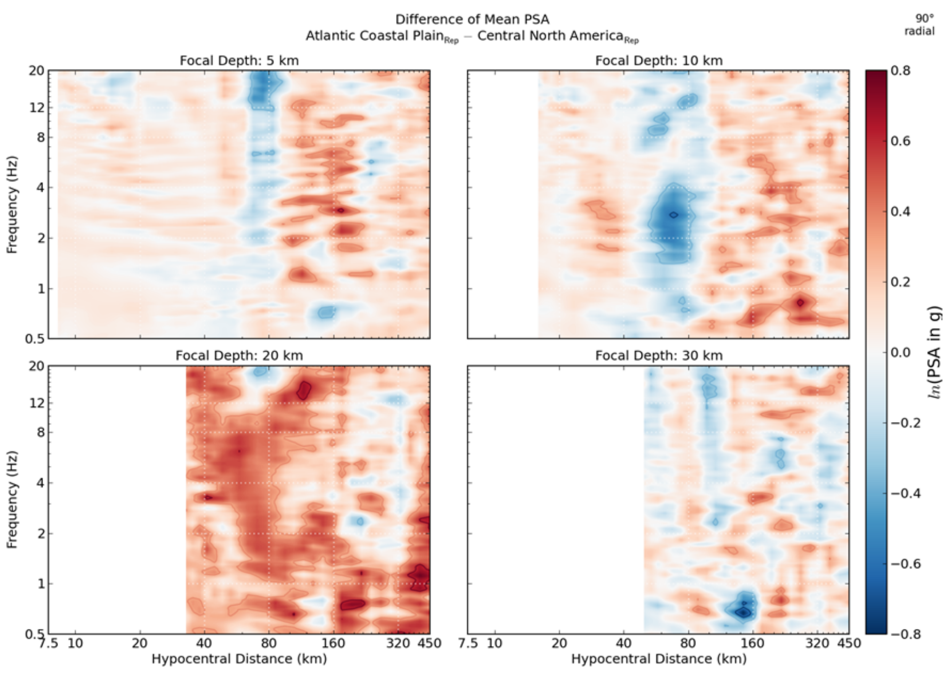

(b)

Figure 6.14 **Difference of mean PSA for ACP$_{Rep}$ and CNA$_{Rep}$: (a) Figure 5.31 compared to (b) analogous results from using frequency-dependent *Q*.**

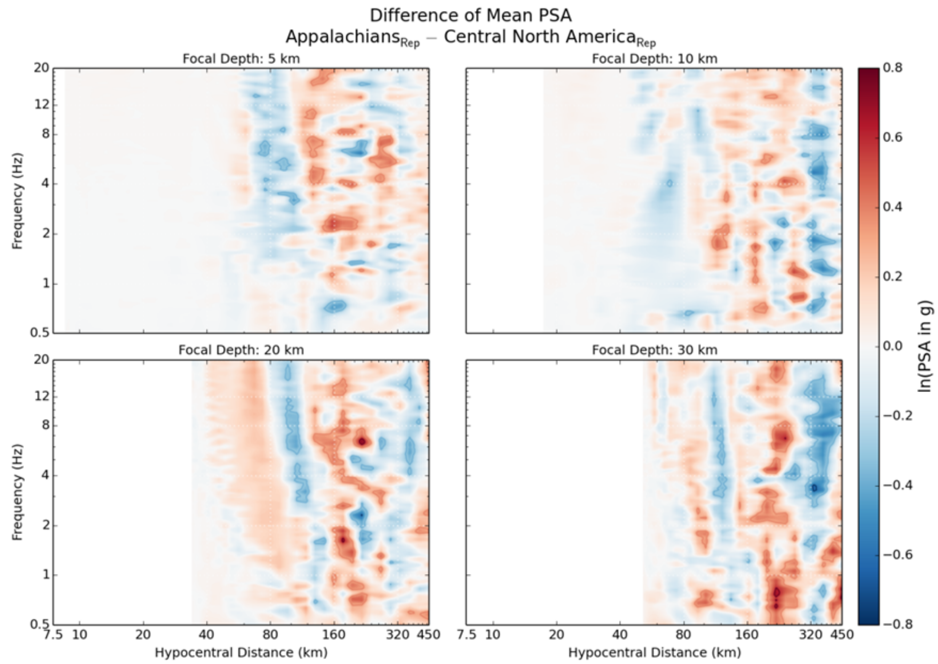

(a)

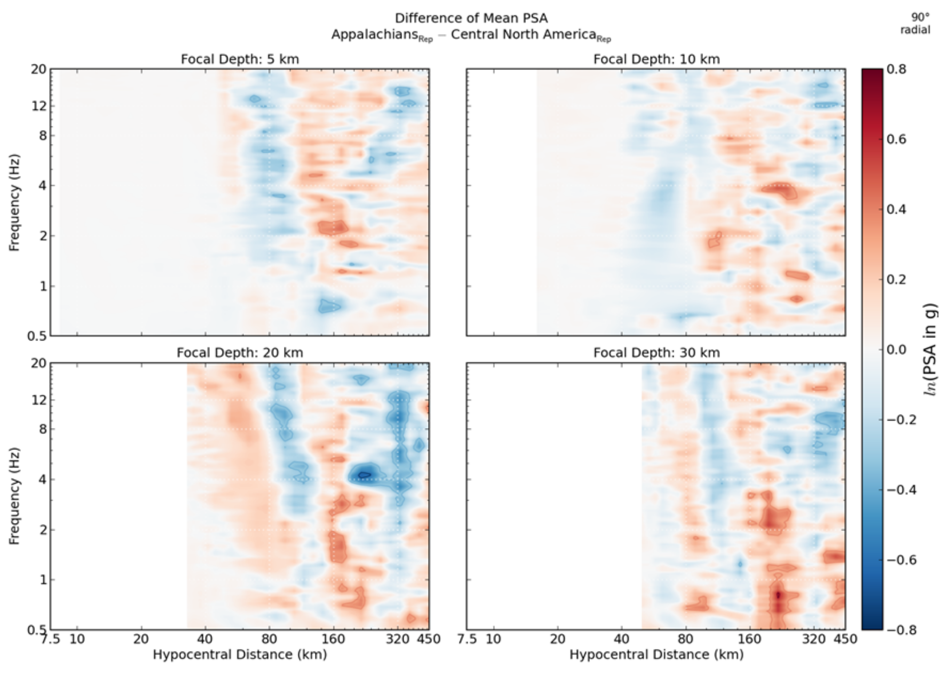

(b)

Figure 6.15 Difference of mean PSA for APP$_{Rep}$ and CNA$_{Rep}$: (a) Figure 5.32 compared to (b) analogous results from using frequency-dependent Q.

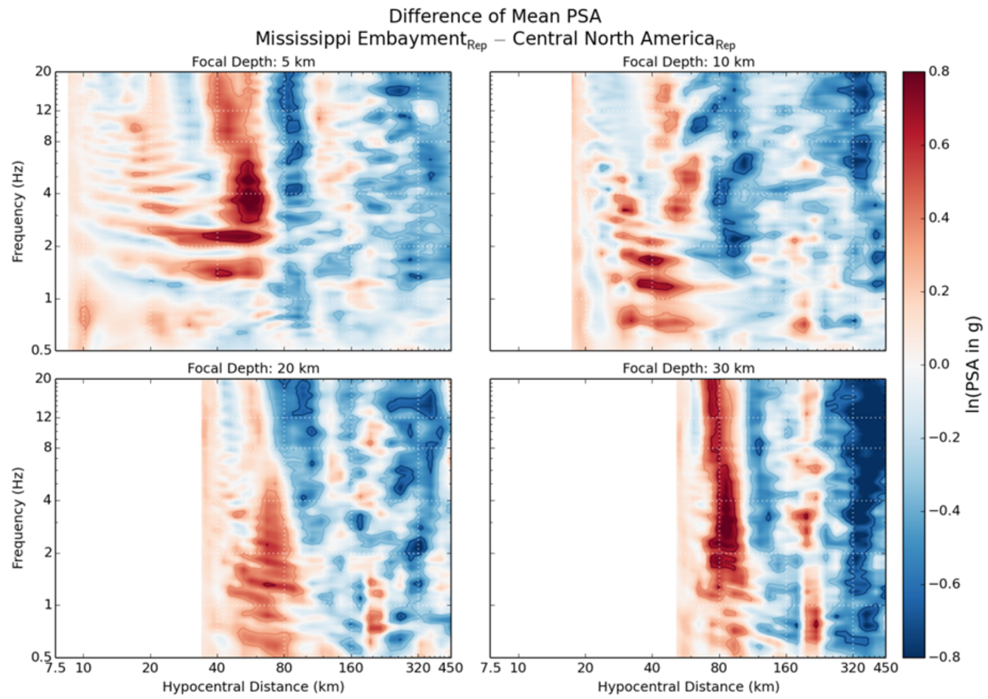

(a)

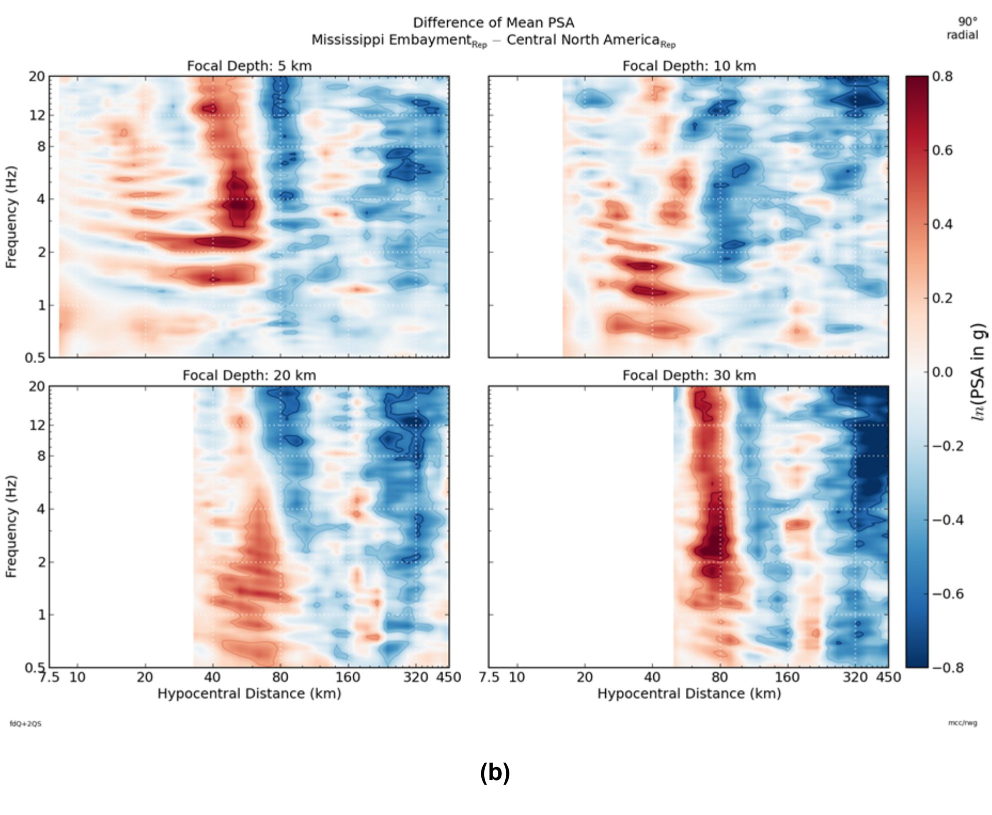

(b)

Figure 6.16 Difference of mean PSA for MEM$_{Rep}$ and CNA$_{Rep}$: (a) Figure 5.33 compared to (b) analogous results from using frequency-dependent *Q*.

6.5 RESULTS: COMPARISONS OF RADIAL AND TRANSVERSE COMPONENT AMPLITUDES AS A FUNCTION OF DISTANCE AND SOURCE-RECEIVER AZIMUTH

The focal mechanism of the earthquake modeled here is pure reverse motion on a South-striking (N180°E), west-dipping fault (45°) in a horizontally layered Earth model. As a result, the transverse horizontal component of motion is zero for receiver azimuths N0°E, N90°E, N180°E, and N270°E. However, for the majority of combinations of focal depth, distance, and regional velocity models examined, the transverse component PSA response amplitudes are larger than that of the radial component for azimuths in the range N22.5°E–N67.5°E due to radiation pattern symmetry. This also holds for azimuths in the range N112.5°E–N157.5°E. The transverse component PSA amplitudes are due to waves of the *SH* type, whereas the horizontal radial component PSA amplitudes are due to *SV*- and *P*-waves. The *SH*-, *SV*-, and *P*-waves exhibit different scattering behavior when they encounter impedance contrasts along the path from source to receiver; therefore, one can expect different amplitude-distance behavior of the two horizontal components. The degree to which these differences may impact considerations regarding regionalization of ground motion prediction models was examined by generating a full suite of three-component synthetics for the four studied regions, exploring five different source-receiver azimuths and six different focal depths.

Three-component synthetic seismograms using the Earth structure and *Q* models of Chapter 5 were computed for the four Earth structure regions along profiles oriented at azimuths of N0°E, N22.5°E, N45°E, N67.5°E, and N90°E. The synthetics incorporate frequency-dependent *Q*.

The discussion here focuses on the results obtained for the APP and the ACP regions, in comparison to the CNA region, as defined in Chapter 5. The MEM region was previously recognized as requiring separate treatment for ground motion modeling; see Chapter 5. At issue here is whether or not significant differences exist between the other three regions (ACP, APP, and CNA regions).

The electronic appendices (Appendices F-I) to this report contain figures that illustrate the PSA response amplitude as a function of hypocenter distance, focal depth, and oscillator frequency for the vertical, radial, and transverse components of motion. A subset of selected figures is shown below to support the discussion. Examination of those results led to the observations described in the next sub-sections.

6.5.1 Appalachian Region Compared to the Central North America Region

- No significant differences were observed in the attenuation of the radial component PSA response amplitudes between the APP region and the CNA region.

  A systematic difference involving the transverse component amplitudes was observed for the APP region relative to the CNA region. This difference occurs for focal depths of 15 and 20 km and is most apparent in the 5−10 Hz oscillator band, for azimuths in the range N22.5°E–N67.5°E. The transverse component amplitudes average a factor of approximately 1.25 larger in the Appalachian region in the distance range of approximately 50–450 km. The largest PSA amplitude observed for the APP region, relative to the CNA region, amounts to a factor of approximately 1.5 times larger, for a focal depth of 20 km at a hypocenter distance of 240 km (see Figure 6.15).

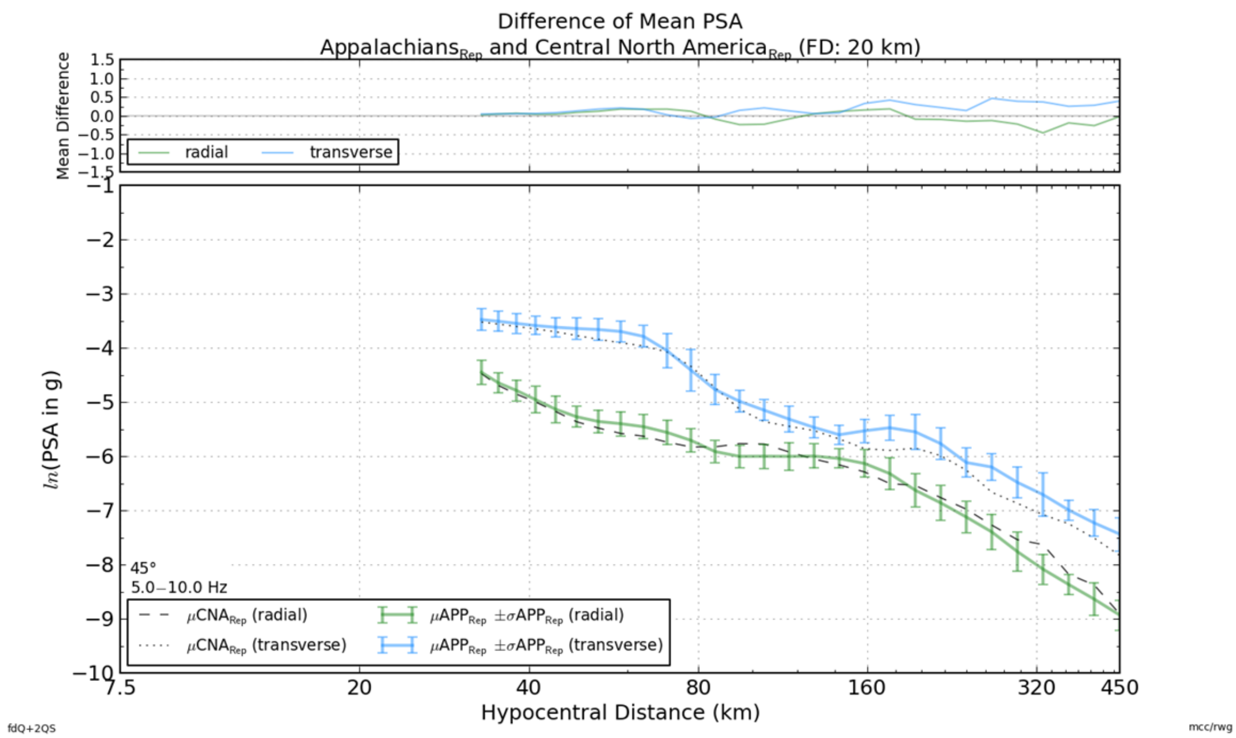

Figure 6.15 **Comparison of mean PSA response amplitudes between the APP$_{Rep}$ and CNA$_{Rep}$ models for the radial and transverse components.**

6.5.2 Atlantic Coastal Plain Region Compared to the Central North America Region

Systematic differences between the two regions were observed for both components of motion, and the largest differences were observed for focal depths 15 and 20 km.

- For focal depths 5 and 10 km, the ACP region's transverse component PSA amplitude is smaller than the CNA region's amplitude at hypocenter distances exceeding 100 km, by a factor of approximately 0.6–0.8 (e.g., Figure 6.16 and Figure 6.17).
- For focal depths 15 and 20 km, the ACP region's transverse component PSA response amplitudes are larger than those found for the CNA region at distances exceeding approximately 70 km and for source-receiver azimuths N22.5°E, N45°E, and N67.5°E. For the 5–10 Hz oscillator response, the ACP region's amplitudes at 120 km hypocenter distance are as much as a factor of 3.5 larger than those for the CNA region (e.g., Figures 6.18 and 6.19).
- For focal depths 15 and 20 km, the ACP region's radial component PSA response amplitudes are larger than those found for the CNA region at all distances and azimuths. Radial component response amplitudes are particularly large relative to the CNA region in the near-source 40–80 km hypocenter distance range. For the 5–10 Hz oscillator response, the ACP region's amplitudes at 50 km hypocenter distance for azimuths of N0°E and N22.5°E exceeded those of the CNA region by a factor of approximately 2.7 (e.g., Figures 6.20 and 6.21).

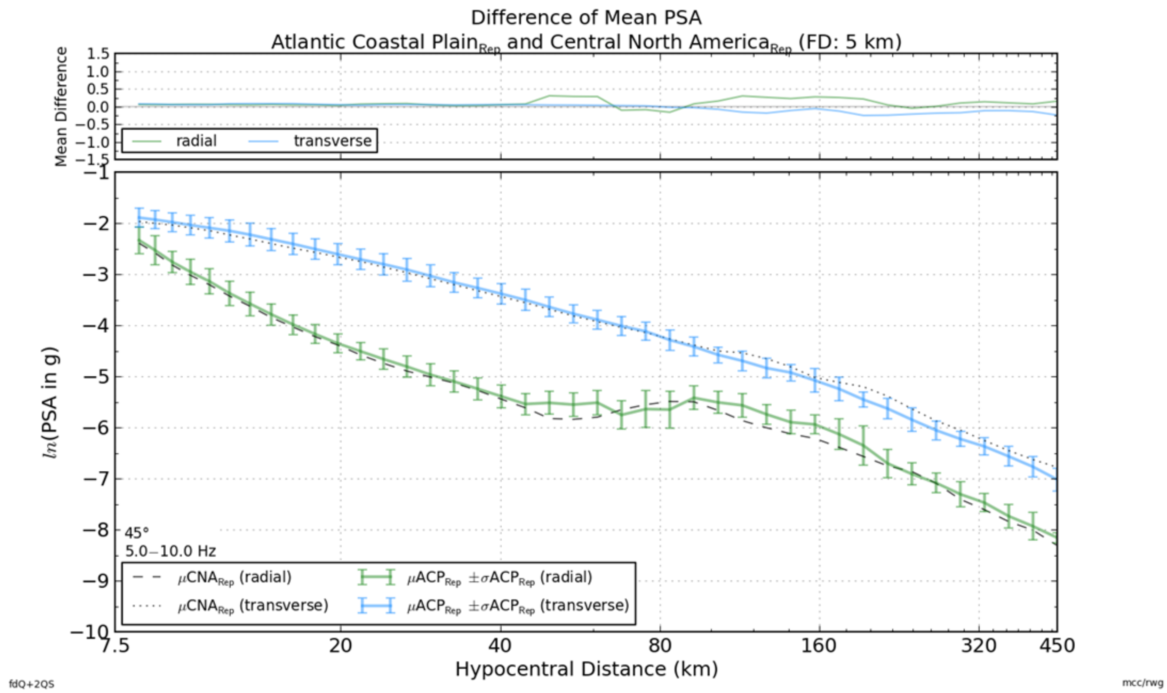

Figure 6.16 **Comparison of mean PSA response amplitudes between the ACP$_{Rep}$ and CNA$_{Rep}$ models at a focal depth of 5 km for the radial and transverse components.**

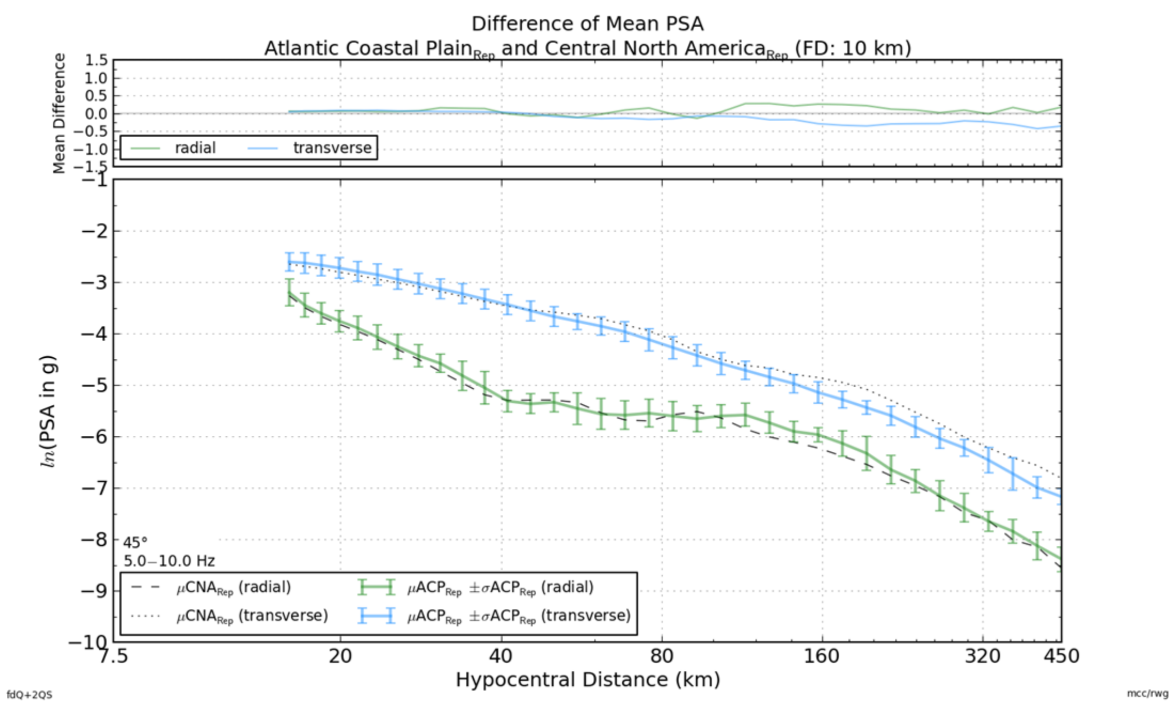

Figure 6.17 **Comparison of mean PSA response amplitudes between the ACP$_{Rep}$ and CNA$_{Rep}$ models at a focal depth of 10 km for the radial and transverse components.**

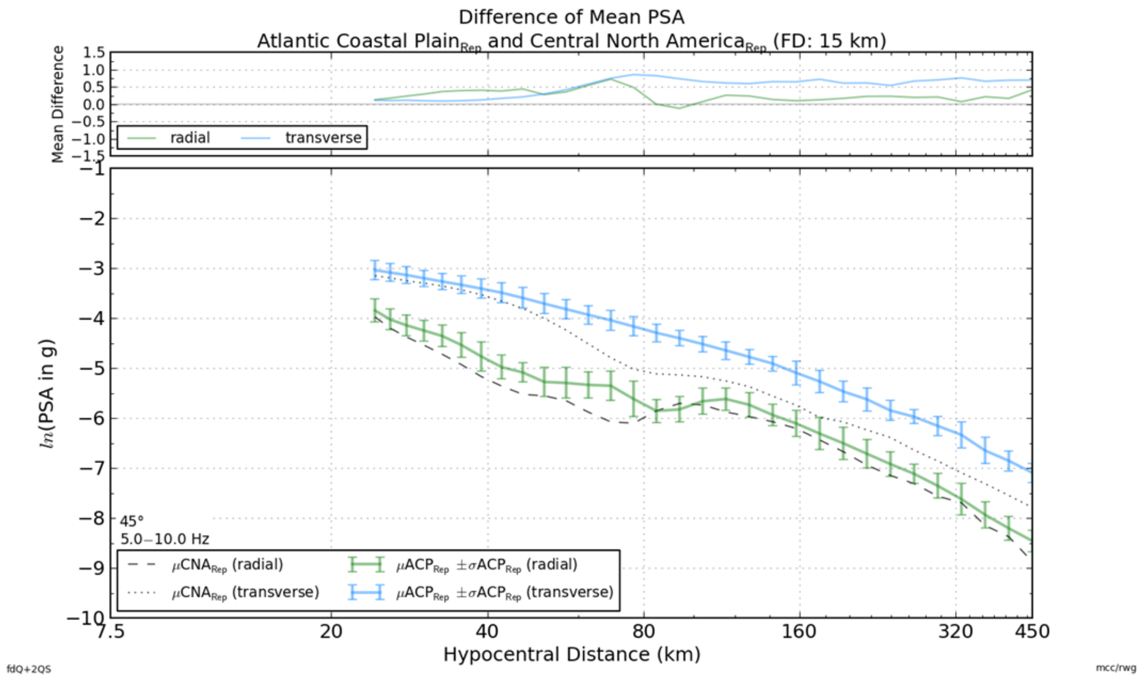

Figure 6.18 **Comparison of mean PSA response amplitudes between the ACP$_{Rep}$ and CNA$_{Rep}$ models at a focal depth of 15 km for the radial and transverse components.**

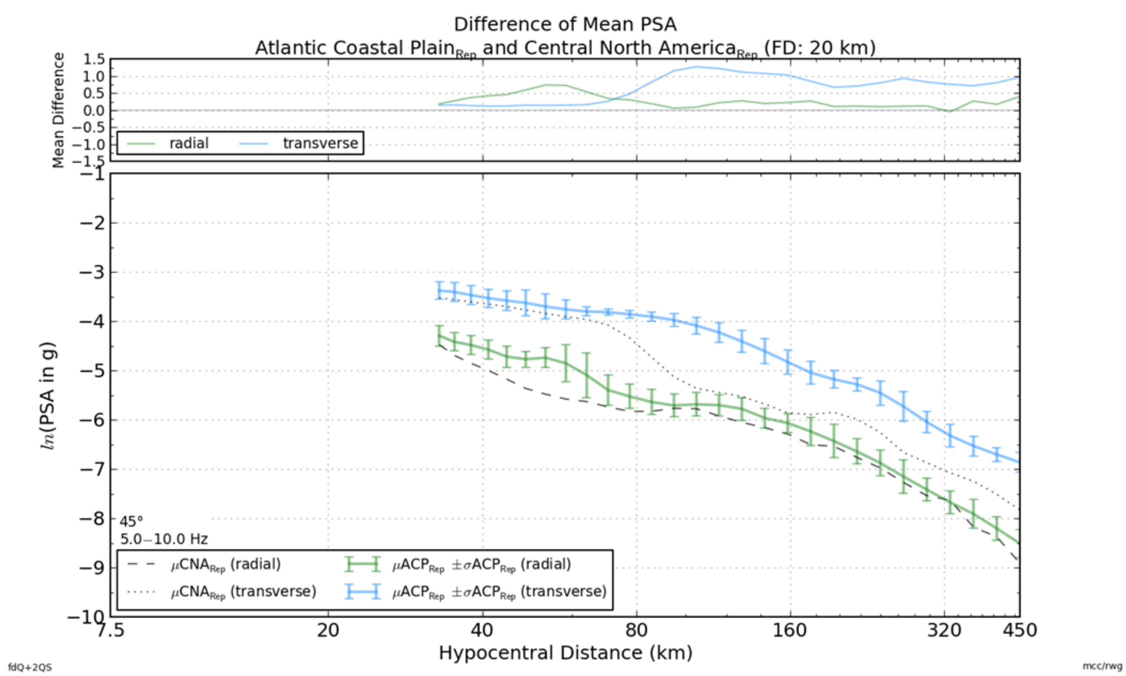

Figure 6.19 **Comparison of mean PSA response amplitudes between the ACP$_{Rep}$ and CNA$_{Rep}$ models at a focal depth of 20 km for the radial and transverse components.**

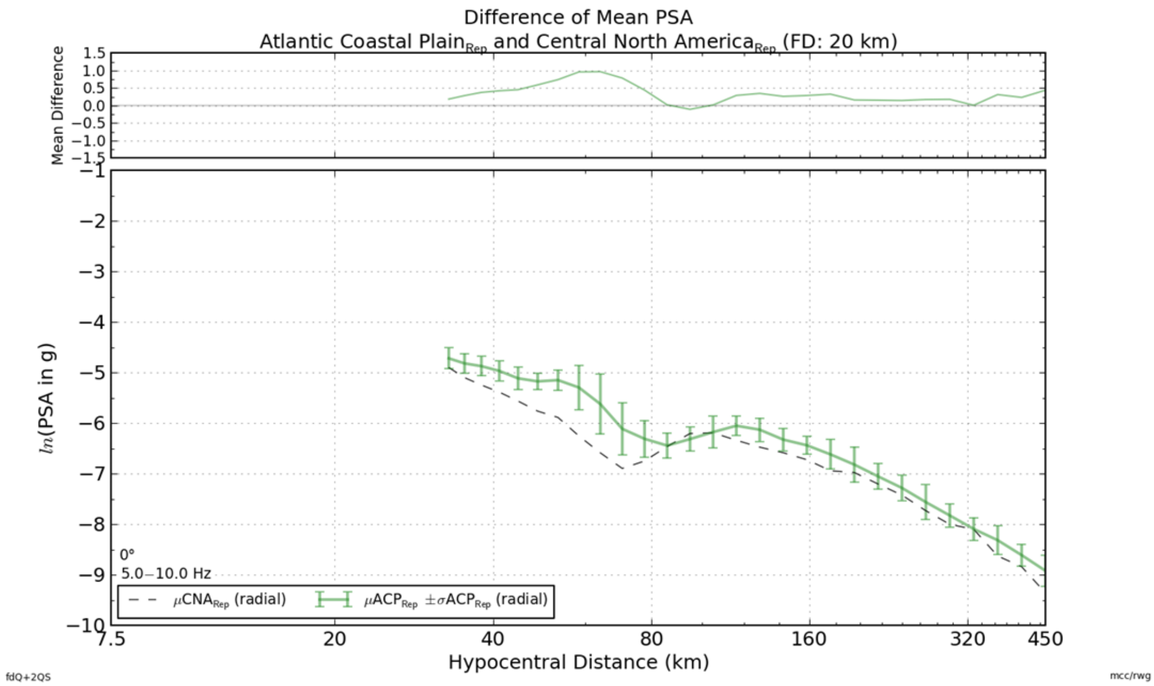

Figure 6.20 Comparison of mean PSA response amplitudes between the ACP$_{Rep}$ and CNA$_{Rep}$ models at a source-receiver azimuth of 0° for the radial component.

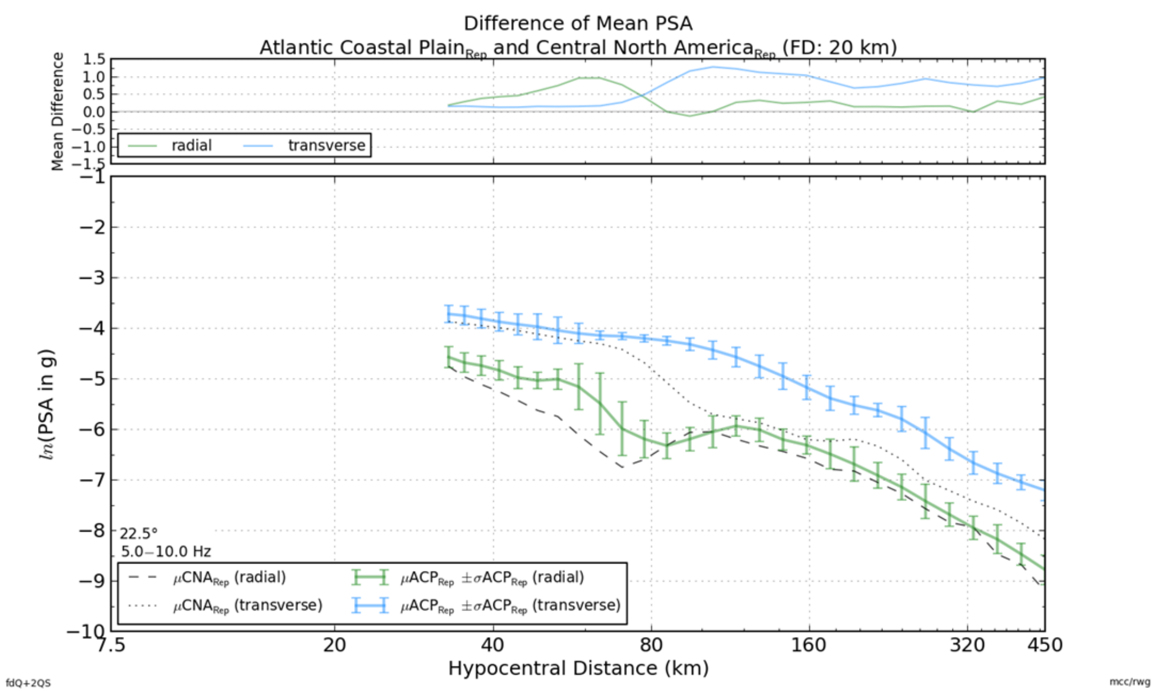

Figure 6.21 Comparison of mean PSA response amplitudes between the ACP$_{Rep}$ and CNA$_{Rep}$ models at a source-receiver azimuth of 22.5° for the radial and transverse components.

6.5.3 Mid-Crustal Velocity Contrasts

The large PSA response amplitudes computed for the ACP region at focal depths of 15 and 20 km are due to a strong velocity contrast at 20.5 km depth in that model. Figure 6.22, which is reproduced from Figure 3.16, shows that this velocity contrast is the largest mid-crustal velocity contrast in any of the models considered. Sources at depths between approximately 12 km and 20 km generate strong post-critical reflections from this interface that return to the surface with large amplitudes at epicenter distances in excess of approximately 50 km. In effect, the velocity contrast sets up a wave guide for post-critically reflected *P*- and *S*-waves in the ACP model that is most efficient for a focal depth range of approximately 12–20 km. Although the radial component amplitudes show the same effect due to *SV* reflection from this mid-crustal velocity contrast, *SH*-wave amplitudes are significantly stronger than *SV* for the reverse focal mechanism studied here, with the result that the transverse component shows the largest difference between the ACP and CNA models.

Figure 6.23 shows synthetic radial and transverse component velocity seismograms along a profile oriented N67.5°E for a focal depth of 15 km. The upper panel represents the ACP region, and the lower panel represents the CNA region. The amplitudes of the traces were high-pass filtered at 1 Hz and scaled to correct for geometrical spreading. The purpose of this figure is to illustrate the difference in amplitude between the radial and transverse components in both regions and the larger amplitudes of the *S*-*Lg* components in the ACP region (relative to the CNA region) at distances greater than approximately 60 km.

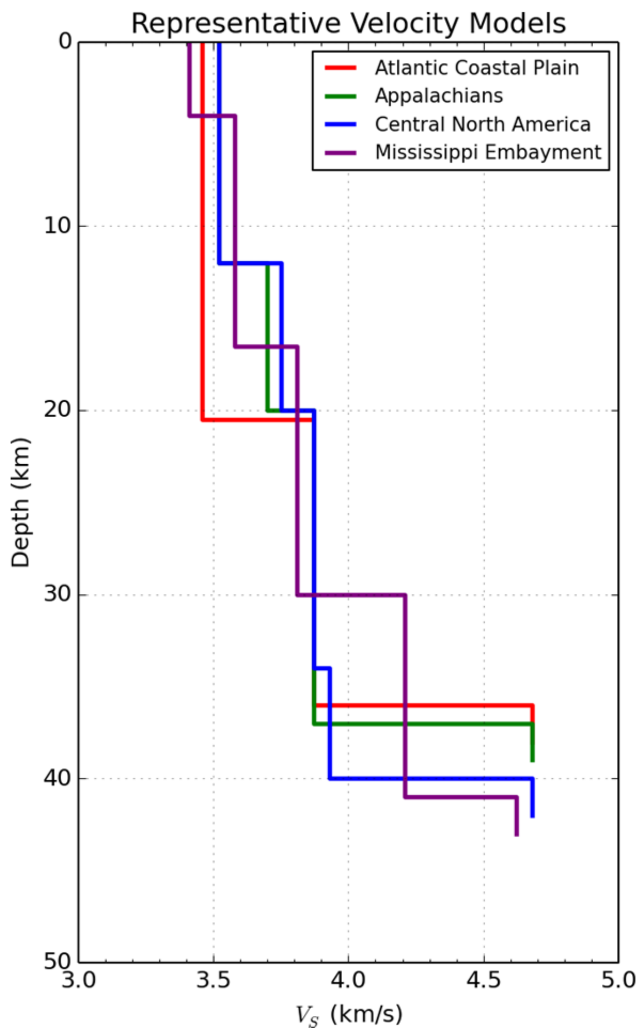

Figure 6.22 **Representative velocity structure models for four regions of central and eastern North America (reproduced from Figure 3.16).**

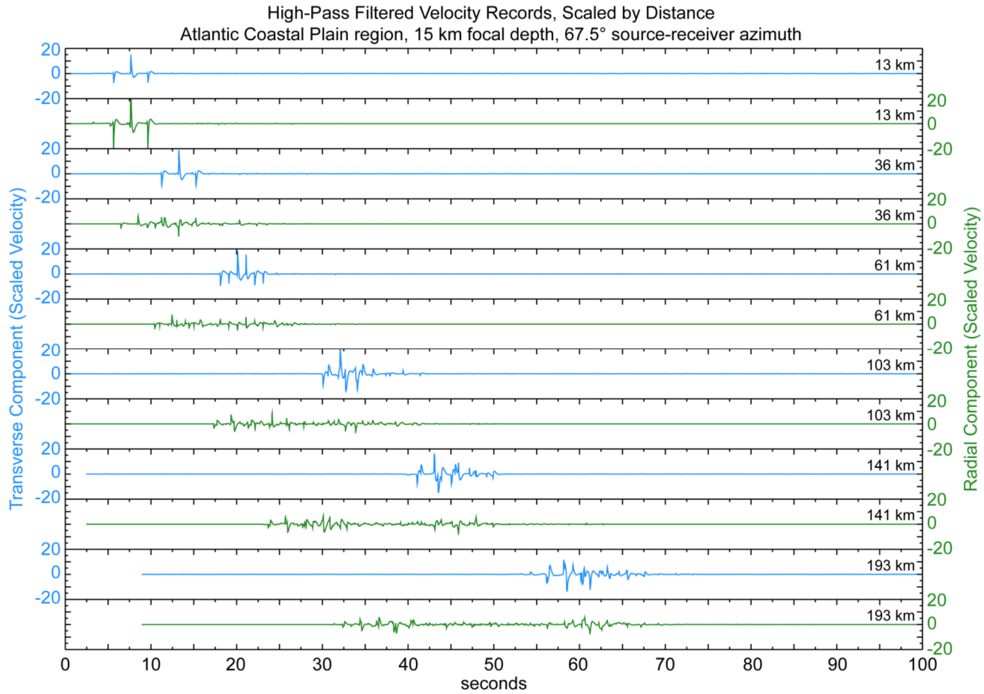

(a)

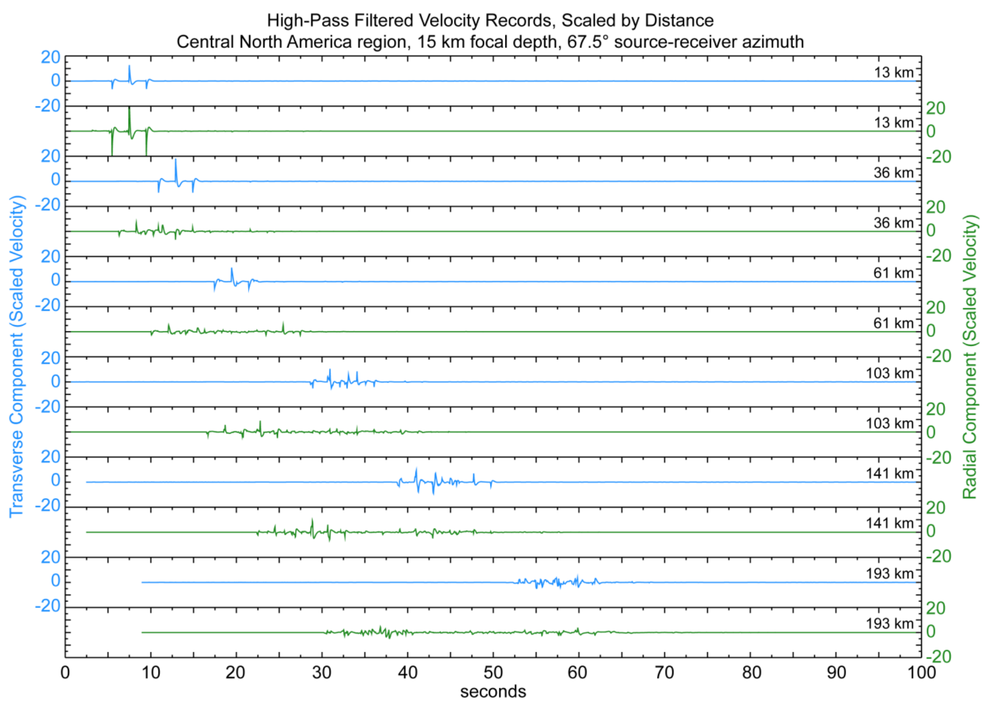

(b)

Figure 6.23 **(a) Profile along azimuth N67.5°E for the ACP region. Blue and green traces represent transverse and radial components, respectively; and (b) corresponding profile for the CNA region. The traces represent high-pass filtered (1 Hz corner frequency) velocity traces multiplied by hypocentral distance to correct for geometrical spreading.**

6.6 SUMMARY AND INTERPRETATION

A comparison of the results presented in this chapter to those results obtained by the Dreiling et al.'s team (see Chapter 5) shows that the computed differences in PSA amplitudes among the regions studied here are insensitive to the use of frequency-dependent or constant *Q* models or to the use of a specific code (i.e., *FK* [Zhu 2012] or *hspec96* [Herrmann 2013a; 2013b]).

The study presented in Chapter 6 reached the same conclusion as the study presented in Chapter 5 regarding regionalization for most of the focal depths and source-receiver azimuths investigated in this report. However, examination of the transverse component of motion for earthquakes in the focal depth range of 15–20 km shows significant differences between the ACP and CNA regions, whereas the CNA and APP regions are similar in that regard. This difference results from a strong mid-crustal velocity contrast present in the ACP representative model that is lacking in the CNA and APP representative models. This feature of the model results in large PSA response amplitudes on the transverse component over a wide source-receiver azimuth range.

The question arises as to whether or not this velocity contrast is pervasive throughout the ACP region, and whether or not it is an abrupt change as modeled or might rather be a more gradual velocity increase with depth. If the latter is the case, then the distinction between the ACP representative model and the CNA and APP representative models would be less pronounced.

Recent results derived from the 2011 Mineral, Virginia, earthquake show azimuthally dependent attenuation [McNamara et al. 2014; Chapman 2014]. The attenuation appears to be related to the northeast-trending structural fabric of the Appalachian orogenic belt. The orogenic belt includes the APP and ACP regions as defined in this study. The recent studies show that attenuation is stronger perpendicular to the northeast-trending orogenic belt. This effect cannot be effectively modeled using 1D horizontally layered velocity structure models as were used in this study, raising the question: How meaningful are the results obtained in this study? If three-dimensional (3D) scattering effects dominate ground motion attenuation, then the calculated differences between the ACP region and the CNA and APP regions may not be significant.

7 Summary

An important aspect of the PEER NGA-East project is the determination of distance-dependent attenuation of pseudo-spectral acceleration (PSA) at specific oscillator frequencies in major regions of Central and Eastern North America (CENA). To achieve this goal, CENA was divided into four regions based on regional geology, tectonic setting, and by considering previous regionalization work. The seismic velocity-depth structure and intrinsic seismic damping (as related to the quality factor, *Q*) of the crust directly influence the attenuation of seismic ground motions for each region. Herein we quantitatively evaluated these path effects.

We evaluated the attenuation of PSA in the four crustal provinces: the Atlantic Coastal Plain (ACP), the Appalachians (APP), Central North America (CNA), and the Mississippi Embayment/Gulf Coastal Region (MEM). The regions were described by a statistically representative crustal seismic velocity-depth structure that made use of the latest and largest crustal profile database developed to date [Mooney 2013]. A pair of frequency-independent and frequency-dependent *Q* models were used to characterize the crustal damping in each region. A series of simulation scenarios were developed, and two teams produced seismograms for the four crustal regions for earthquakes at focal depths of 5, 10, 20, and 30 km, for distances up to 500 km. The teams then computed PSA for a series of selected oscillator frequencies from 0.5 to 20 Hz and generated a series of analysis tools for comparing the results within a region and between regions.

This study defined the CNA region as the base region and used it to quantify the expected within-region variability due to variability in crustal profile definition. Geographically the largest region, CNA contains a variety of crustal velocity-depth structures that are related to the geological evolution of the crust. This study generalized the 417 available seismic velocity profiles for this region into one representative profile (CNA_{Rep}) and calculated ground motions for earthquakes at the four focal depths mentioned above. A similar process led to the development of representative crustal profiles for the other three regions. The PSA within-region variability was assessed using 18 alternative velocity-depth models for the base region (CNA_{Alt}). The combination of PSA results from each region to those from the CNA_{Alt} suite of profiles was the basis for evaluating systematic differences in regional attenuation for various oscillator frequencies and distance ranges.

The analyses described in this report demonstrate that there are two distinct PSA attenuation groups within CENA:

- GROUP 1: Central North America, Appalachians, Atlantic Coast Plain
- GROUP 2: Mississippi Embayment/Gulf Coast

The CNA and APP regions look very similar for events at all four focal depths considered. Their representative PSA values are very similar and only at larger hypocentral distances do the values show noticeable differences. However, these differences are still with the range of variability of the CNA base region itself (i.e., within the range defined by the alternative models for CNA).

The PSA values for ACP are also very similar to the PSA values of the CNA representative model. However, examination of the transverse component of motion for earthquakes in the focal depth range of 15−20 km shows significant differences between the ACP and CNA regions, whereas the CNA and APP regions are similar in that regard. This difference results from a strong mid-crustal velocity contrast present in the ACP representative model that is lacking in the CNA and APP representative models. This feature of the model results in large PSA response amplitudes on the transverse component over a wide source-receiver azimuth range. It is unclear if this trend is pervasive in the whole ACP region or if the observed effect is mostly due to the simplified 1D models used. (It is unclear if such abrupt velocity contrasts exist in the crust or if they are more progressive in nature.).

The MEM region has attenuation properties significantly different from those of other regions and is assigned its own attenuation group. This conclusion is in agreement with previous analyses that have found that the MEM region has unique attenuation characteristics.

The calculations of PSA presented here show that the biggest effect on the amplitudes of PSA for CENA in the distance range 7.5−500 km is due to the seismic velocity-depth structure of the crust. This is due to the relatively high Q value for most of CENA. One important conclusion that is relevant NGA-East project is that the results are insensitive to whether a frequency-independent or a frequency-dependent Q formulation is used. This makes the conclusion of this report portable to a wide range of simulation methods commonly used in seismology, at least for the range of oscillator frequencies and distances considered in this study.

REFERENCES

Atkinson G.M. (1989). Attenuation of the Lg phase and site response for the Eastern Canada telemetered network. *Seismol. Res. Lett.,* 60(2): 59–69.

Atkinson G.M. (2004). Empirical attenuation of ground-motion spectral amplitudes in southeastern Canada and the northeastern United States, *Bull. Seismol. Soc. Am.,* 94(3): 1079–1095.

Atkinson G.M., Boore D.M. (1995). Ground-motion relations for eastern North America, *Bull. Seismol. Soc. Am.,* 85(1): 17–30.

Atkinson G.M., Mereu R. (1992). The shape of ground motion attenuation curves in southeastern Canada, *Bull. Seismol. Soc. Am.,* 82(5): 2014–2031.

Boatwright J., Seekins L. (2011). Regional spectral analysis of three moderate earthquakes in northeastern North America, *Bull. Seismol. Soc. Am.,* 101(4): 1769–1782.

Baqer S., Mitchell B.J. (1998). Regional variation of Lg coda Q in the continental United States and its relation to crustal structure and evolution, *Pure Appl. Geophys*., 158: 613–638.

Benz, H., Frankel, A., and Boore, D.M. (1997). Regional Lg attenuation for the continental United States, *Bull. Seismol. Soc. Am.,* (3): 606–619.

Bayer K.C. [1983]. Generalized structural lithologic and physiographic provinces in the fold and thrust belts of the United States, U.S. Geological Survey, 3 sheets, scale 1:2,500,000.

Boore D.M. (2012). TSPP - A collection of FORTRAN programs for processing and manipulating time series, Version 4.3, U.S. Geological Survey, *U.S.G.S. Survey Open-File Report 2008-1111*, Washington, D.C.

Bostock M.G. (1999). Seismic imaging of lithospheric discontinuities and continental evolution, *Lithos*, 48: 1–16.

Buffler R.T., Thomas W.A. (1994). Crustal structure and evolution of the southeastern margin of North America and the Gulf of Mexico basin, in *Phanerozoic Evolution of the North American Continent-Ocean Transitions*, R.C. Speed, ed., Boulder, Colorado, Geological Society of America, DNAG Continent-Ocean Transect Volume, pp. 219–264.

Chapman M.C. (2014). Magnitude, recurrence interval and near-source ground motion modeling of the Mineral, Virginia earthquake of August 23, 2011, in *The 2011 Mineral, Virginia, Earthquake and its Significance for Seismic Hazards in Eastern North America*, J.W. Horton, Jr., M.C. Chapman, and R.A. Green, eds: Geological Society of America Special Paper, in press.

Chapman M.C., Godbee R.W. (2012). Modeling geometrical spreading and the relative amplitudes of vertical and horizontal high-frequency ground motions in Eastern North America, *Bull. Seismol. Soc. Am.*, 102(5): 1957–1975.

Chulick G.S. (1997), Comprehensive seismic survey database for developing three-dimensional models of the Earth's crust, *Seismol. Res. Lett.* 68(5): 734–742.

Chulick G.S., Mooney W.D. [2002]. Crustal structure of North America and adjacent oceanic basins; A synthesis, *Bull. Seismol. Soc. Am.,* 92: 2478–2492.

Chun K., West G. (1987). A novel technique for measuring Lg attenuation Results from eastern Canada between 1 to 10 Hz, *Bull. Seismol. Soc. Am.*, 77(2): 398–419.

Cox B.R. (2010). Characterizing earthquake shaking: Ground motion parameters and the acceleration response Spectrum, *Proceedings, Geotechnical Earthquake Engineering for Seismic Design Workshop*, Port-au-Prince, Haiti.

EPRI (1993). Guidelines for determining design basis ground motions. Volume 1: Method and guidelines for estimating earthquake ground motion in Eastern North America, Electric Power Research Institute, *Technical Report*, Palo Alto, CA.

EPRI/USDOE/USNRC (2012) Central and Eastern United States seismic source characterization for nuclear facilities, *U.S. Nuclear Regulatory Commission Report, NUREG-2115; EPRI Report 1021097, 6 Volumes; DOE Report# DOE/NE-0140*.

Erickson D., McNamara D., Benz H. (2004). Frequency-dependent Lg Q within the continental United States, *Bull. Seismol. Soc. Am.,* 94(5): 1630–1643.

Freeman S.A. (2007). Response spectra as a useful design and analysis tool for practicing structural engineers, *J. Earthq. Tech*., 44(1): 25–37.

Gupta I., McLaughlin K. (1987). Attenuation of ground motion in the eastern United States, *Bull. Seismol. Soc. Am.*, 77(2): 366–383.

Hasegawa H. (1985). Attenuation of Lg waves in the Canadian Shield, *Bull. Seismol. Soc. Am.*, 75(6): 1569–1582.Hatcher R.D. Jr. (1989). Tectonic Synthesis of the U.S. Appalachians, in *The Appalachian-Ouachita Orogen in the United States: Boulder, Colorado*, R.D Hatcher Jr., W.A Thomas, and G.W Viele, eds., Geological Society of America, The Geology of North America, F-2: 511–535.

Herrmann R.B. (2013a). Computer programs in seismology: An evolving tool for instruction and research, *Seismol. Res. Lett.*, 84(6): 1081–1088.

Herrmann R.B. (2013b). Computer programs in seismology, *Saint Louis University Earthquake Center*, accessed May 26, 2014, from *http://www.eas.slu.edu/eqc/eqccps.html*.

Hunter, J. D. (2007). Matplotlib: A 2D graphics environment, *Comp. Sci. Eng.*, 9(3): 90–95.

Johnston A.C. (1993). The stable continental interior data base, in The Earthquakes of Stable Continental Regions: an Assessment of Large Earthquake Potential, in: *EPRI Report TR 102261*. Palo Alto, CA.

Kearey P., Brooks M., Hill I. (2002). *An Introduction to Geophysical Exploration*, Chapters 1−5, 3rd ed., Blackwell Publishing.

Kramer S.L. (1996). *Geotechnical Earthquake Engineering*, Prentice Hall: New Jersey.

McNamara D.E., Gee L., Benz H.M., Chapman, M. (2014). Frequency-dependent seismic attenuation in the Eastern United States as Observed from the 2011 central Virginia earthquake and aftershock sequence, *Bull. Seismol. Soc. Am.*, 104(1): 55–72.

Mitchell, B.J. (1995). Anelastic structure and evolution of the continental crust and upper mantle from seismic surface wave attenuation, *Review Geophys*., 33(4): 441–462.

Mooney W.D. (2013). Database of Central and Eastern North American (CENA) Seismic Velocity Structure (Task 2 of USGS-NRC Work Agreement 2011 – 2014), Report submitted to the Nuclear Regulatory Commission, *ADAMS Accession No. ML 14280A412*, Washington, D.C.

Mooney W.D. (1989). Seismic methods for determining earthquake source parameters and lithospheric structure, in *Geophysical Framework of the Continental United States,* L.C. Pakiser and W.D. Mooney, eds., *Geol. Soc. Am. Memoir*, 172: 11–34.

Newmark N.M., Hall W.J. (1982). *Earthquake Spectra and Design*, Earthquake Engineering Research Institute, Oakland, CA, 103 pgs.

Nigam N.C., Jennings P.C. (1969). Calculation of response spectra from strong motion earthquake records, *Bull. Seismol. Soc. Am.*, 59(2): 909–922.

Pakiser L.C., Mooney W.D., eds. (1989). Geophysical framework of the Continental United States, *Geological Society of America Memoir 172*, Boulder, CO, 826 pgs.

SAC Data File Format (2012). Accessed May 26, 2014, from http://www.iris.edu/files/sac-manual/manual/file_format.html.

Scawthorn C., Chen W. (2002). *Earthquake Engineering Handbook*, CRC Press, Technology and Engineering, Boca Raton, FL.

Shi J., Kim W., Richards P. (1996). Variability of crustal attenuation in the northeastern United States from Lg waves, *J. Geophys. Res*., 101(B11): 25231–25242.

Shin T., Herrmann R. (1987). Lg attenuation and source studies using 1982 Miramichi data, *Bull. Seismol. Soc. Am.*, 77(2): 384–397.

Stein S., Wysession M. (2003). *An Introduction to Seismology, Earthquakes and Earth Structure*, Blackwell Publishing.

SLU (2013). Saint Louis University, *http://www.eas.slu.edu/eqc/eqc_mt/MECH.NA/MECHFIG/Plotna.html.*

Swanson M.T. (1986). Preexisting fault control for Mesozoic basin formation in eastern North America, *Geology*, 14: 419–422.

Tange O. (2011). GNU Parallel: The Command-Line Power Tool, *;login:*, 36(1): 42–47.

USGS (2014). Earthquake Hazards 201-Technical Questions and Answers, United States Geological Survey, *http://earthquake.usgs.gov/hazards/about/technical.php* (accessed: February, 2014).

Woodgold C. (1990). Estimation of Q in eastern Canada using coda waves, *Bull. Seismol. Soc. Am.*, 80(2): 411–429.

Zandieh A., Pezeshk, S. (2010). Investigation of geometrical spreading and quality factor functions in the New Madrid seismic zone, *Bull. Seismol. Soc. Am.*, 100(5A): 2185–2195.

Zoback M.L. (1992). Stress field constraints on intraplate seismicity in eastern North America*, J. Geophys. Res*., 97: 11761-11782.

Zhu L. (2012). Frequency-Wavenumber (FK) synthetic seismogram package fk3.2, Department of Earth and Atmospheric Sciences, St. Louis University, available for download at *http://www.eas.slu.edu/People/LZhu/home.html*.

Appendix A References for *Q* Studies

Al-Shukri H., Mitchell B.J. (1990). Three-dimensional attenuation structure in and around the New Madrid seismic zone, *Bull. Seismol. Soc. Am.,* 80(3): 615–632.

Atkinson G.M. (1989). Attenuation of the Lg phase and site response for the Eastern Canada telemetered network. *Seismol. Res. Lett.,* 60(2): 59–69.

Atkinson G.M. (2004). Empirical attenuation of ground-motion spectral amplitudes in southeastern Canada and the northeastern United States, *Bull. Seismol. Soc. Am.,* 94(3): 1079–1095.

Atkinson G.M., Boore D.M. (1995). Ground-motion relations for eastern North America, *Bull. Seismol. Soc. Am.,* 85(1): 17–30.

Atkinson G.M., Mereu R. (1992). The shape of ground motion attenuation curves in southeastern Canada, *Bull. Seismol. Soc. Am.,* 82(5): 2014–2031.

Baqer S., Mitchell B.J. (1998). Regional variation of Lg coda Q in the continental United States and its relation to crustal structure and evolution, *Pure Appl. Geophys*., 158: 613–638.

Benz H., Frankel A., Boore D.M. (1997). Regional Lg attenuation for the continental United States, *Bull. Seismol. Soc. Am.,* 87(3): 606–619.

Boatwright J., Seekins L. (2011). Regional spectral analysis of three moderate earthquakes in northeastern North America, *Bull. Seismol. Soc. Am.,* 101(4): 1769–1782.

Brockman S., Bollinger G. (1992). Q estimates along the Wasatch Front in Utah derived from Sg and Lg wave amplitudes, *Bull. Seismol. Soc. Am.,* 82(1): 135–147.

Chapman M.C., Beale J.N., Catchings R. D. (2008). Q for P Waves in the sediments of the Virginia coastal plain, *Bull. Seismol. Soc. Am.,* 98(4): 2022–2032.

Chun K., West G. (1987). A novel technique for measuring Lg attenuation Results from eastern Canada between 1 to 10 Hz, *Bull. Seismol. Soc. Am.,* 77(2): 398–419.

Dwyer, J. Herrmann R., Nuttli O. (1983). Spatial attenuation of the Lg wave in the central United States, *Bull. Seismol. Soc. Am.,* 73(3): 781–796.

Erickson D., McNamara D., Benz H. (2004). Frequency-dependent Lg Q within the continental United States, *Bull. Seismol. Soc. Am.,* 94(5): 1630–1643.

Ge J., Pujol J., Pezeshk S., Stovall, S. (2009). Determination of shallow shear-wave attenuation in the Mississippi Embayment using vertical seismic profiling data, *Bull. Seismol. Soc. Am.,* 99(3): 1636–1649.

Gupta I., McLaughlin K. (1987). Attenuation of ground motion in the eastern United States, *Bull. Seismol. Soc. Am.,* 77(2): 366–383.

Hasegawa H. (1985). Attenuation of Lg waves in the Canadian Shield, *Bull. Seismol. Soc. Am*., 75(6): 1569–1582.

Langston C.A. (2005). Bulk sediment Qp and Qs in the Mississippi Embayment, Central United States. *Bull. Seismol. Soc. Am.,* 95(6): 2162–2179.

Lawrence J.F., Prieto G.A. (2011). Attenuation tomography of the western United States from ambient seismic noise, *J. Geophys. Res.*, 116(B6): B06302.

Li Q. (2006). Seismic attenuation structure of the Seattle Basin, Washington State, from explosive-source refraction data, *Bull. Seismol. Soc. Am.*, 96(2): 553–571.

Liu Z., Wuenscher M., Herrmann R. (1994). Attenuation of body waves in the central New Madrid seismic zone. *Bull. Seismol. Soc. Am.,* 84(4): 1112–1122.

McNamara D., Frankel A., Wesson R. (2004). Lg Q in the North American Mid-Continent, *geohazards.cr.usgs.gov*, 181(June):1–17.

Phillips W.S., Stead R.J. (2008). Attenuation of Lg in the western US using the US Array. *Geophys. Res. Lett.*, 35(7).

Pulli J.J. (1984). Attenuation of coda waves in New England, *Bull. Seismol. Soc. Am.,* 74(4): 1149–1166.

Saikia C., Kafka A. (1990). Shear velocity and intrinsic Q structure of the shallow crust in southeastern New England from Rg wave dispersion, *J. Geophys. Res*., 95: 8527–8541.

Shi J., Kim W., Richards P. (1996). Variability of crustal attenuation in the northeastern United States from Lg waves, *J. Geophys. Res*., 101(B11): 25231-25242.

Shin T., Herrmann R. (1987). Lg attenuation and source studies using 1982 Miramichi data, *Bull. Seismol. Soc. Am.*, 77(2): 384–397.

Woodgold C. (1990). Estimation of Q in eastern Canada using coda waves, *Bull. Seismol. Soc. Am.*, 80(2): 411-429.

Zandieh A., Pezeshk, S. (2010). Investigation of geometrical spreading and quality factor functions in the New Madrid seismic zone, *Bull. Seismol. Soc. Am.*, 100(5A): 2185–2195.

Zhu L. (2012). Frequency-Wavenumber (FK) synthetic seismogram package fk3.2, Department of Earth and Atmospheric Sciences, St. Louis University, available for download at *http://www.eas.slu.edu/People/LZhu/home.html*.

Appendix B Global Crustal Database

B.1 FORMAT OF THE CRUSTAL SEISMIC VELOCITY STRUCTURE DATABASE, CRITERIA FOR SELECTING DATA, AND USING THE DATABASE

The CENA database is designed to be comprehensive as well as expandable. Hence, it contains material derived from all seismic survey techniques used to determine (or infer) seismic wave velocities and the depth and thicknesses of layers within the Earth's crust. The type of field measurement, quantity and quality of the raw data used in the construction of the database therefore vary greatly according to the survey technique and on the details of the experiment (i.e., on the location of the experiment, on the number of seismometers used or seismograms analyzed, on the method of analysis, etc.). A critical overview of these factors has been presented by Mooney [1989]. Another consideration is the source of the data (journal article, thesis, or abstract), since this will often reflect its completeness. Lastly, the completeness and accuracy of the data may have been influenced by the use of newer, more sophisticated techniques to supplement much of the older data. Nonetheless, such older data has been retained, since it may be still of potential use.

With this in mind, the format of the database requires a standardized set of rules or criteria for handling a variety of problems. These problems also include how to deal with information not currently included in the database (such as gradients) and the sampling frequency of 2D profiles. Each of these factors affecting the data and database are addressed in more detail in the following subsections. The ordering of the subsections is based on the format of the individual seismic entries within the database.

B.1.1 Location

Each entry is located according to latitude and longitude. The criteria used for assigning latitude and longitude are quite complex because they generally depend on the seismic technique used to produce the data. Entries derived from 1D earthquake models are usually located where each model was used for the purpose of study: at the epicenter of a major earthquake, at the geographic center of associated aftershocks, or near the center of a seismic network used to analyze the earthquake.

Two-dimensional (cross-section) profiles from time-term analysis, reflection seismology, and refraction seismology are sampled from figures in the original publication. Each sample is selected according to the following criteria. Ideally, each profile is sampled every 50 km along the profile for continental seismic surveys and approximately every 10–20 km along the profile for oceanic surveys. The selected distance intervals are somewhat arbitrary but do in some manner reflect the cross-over distance for mantle compressional head waves associated with the continental and oceanic crust (~200 km and ~60 km, respectively).

For refraction surveys, several additional criteria are applied. Only one entry is usually extracted from an un-reversed refraction cross section. This is a result of the limitations associated with such surveys: they generally include only apparent velocities and often treat the crust as if it was composed only of flat-laying, uniformly thick layers. These entries are usually located approximately 50 km along the seismic station line from the shot point. The general exception to this rule is if the local crust is extremely thick (in which case the distance from the shot point may be increased to 60–70 km), or thin, as for oceanic crust (in which case the distance from the shot point may be reduced to 20 or 25 km).

Split refraction survey lines, which in some ways are similar to simple reversed refraction lines, are generally done in bodies of water. One entry is selected that is located either at the sonobuoy (if a line of shots passes through the location of a sonobuoy) or at the location of the shot point (if the shot occurs somewhere along a line of sonobuoys).

Reversed refraction surveys are somewhat more complex. For simple reversed refraction surveys (two shot points at opposite ends of a line of seismic stations, generally used in older reversed refraction surveys), two entries are usually taken from the cross section. The rule here is similar to that for unreversed refraction surveys. Each entry is located approximately 50 km in from one of the shot points along the connecting line of seismometers. Note that simple reversed refraction surveys ordinarily lead to crustal models that contain only simple dips in the crustal layers. In the case of multiple shot points, reversed refraction surveys (several shot points along a line of seismic stations, typical of modern refraction surveys), the resultant crustal cross-sections are sampled approximately every 50 km along the cross section. Ideally, the first sample is located at 50 km along the cross section from the first shot-point in the line, and the last sample is located at approximately 50 km short of the last shot point in the line.

Note that the above locations for the various types of refraction surveys apply only to profiles where the seismic waves reach the Moho. The locations are correspondingly shortened for shallow surveys where the rays only penetrate to a certain depth within the crust.

Surface wave-based entries are generally located one-half way between the average source location and the average station location (results from two-station analyses are located one-half way between the two stations).

The locations used for receiver function entries are dependent on the back azimuth to the earthquake source. If the model is constructed from sources located around the compass, then the entry is located at the station/receiver location. If the model is constructed from sources located along a limited range of azimuth, the entry is located much like an un-reversed refraction entry i.e., ~50 km from the station/receiver along the line connecting the receiver location and the average source back azimuth.

Seismic entries extracted from tomographic models of the crust are ideally located at the center of each block into which the modeler has broken the crust. In the situation where the model contains a large sample of blocks, or is smoothed-averaged over the entire seismic wave-sampled volume, only roughly evenly spaced, randomly picked blocks are selected for inclusion as entries in the database.

Exceptions to the above rules are applied to certain data on an individual basis. Latitude and longitude values in the database are given to the nearest one-hundredth of a degree. In reality, the given values are often only good to approximately ±0.05° (and even ±0.1° in some cases), since the location for an entry is usually determined from a large-scale map given in the original published reference.

B1.1.1 Elevation

The elevation of the entry (to the nearest tenth of a kilometer) is included because the depths given for the various layers within each entry are with respect to the Earth's surface. Whenever possible, the elevation is extracted from the source reference for the entry. If the elevation is unknown, it is estimated using the National Geophysical Data Center ETOP05 five minute by five minute topographic database (for data entered approximately before entry number 5000), or the National Geophysical Data Center ETOP02 two minute by two minute topographic database (for more recently added data).

B1.1.2 Reference

The source reference for each entry is coded into the entry as: *yrN.n.* Here *yr* is the last two digits of the publication year, *N* is the surname initial of the first author, and *n* is a number included to cover those cases where the year and the first author's initial are not enough to distinguish the reference.

B1.1.3 Profile Type

A discussion of the various types of seismic surveys, their associated analysis techniques, and their underlying assumptions and sources of error can be found in Mooney [1989]. Given the type of data in the database (seismic wave velocities and layer thicknesses), the best data sources will be the results from refraction seismology and kindred techniques (time-term analysis, tomographic inversion, and earthquake modeling). In most cases, the results from reflection seismology are of limited use here unless the seismic velocities have been determined by other means. However, the results presented in the database can be used to convert nearby two-way travel time reflection results into true depths.

Some crustal models are actually the result of refraction seismology whereby an earthquake plays the role of a man-made explosive shot. Such models are limited by the uncertainty in hypocenter depth, location, and origin time. The entries constructed from such earthquake models are therefore often identified as being derived from refraction results. Until recently, Receiver Functions were identified in the database as earthquake models; they are now entered as a separate category due to the recent upsurge in the use of this technique. They depend on prior information such as a reference velocity; as such they make for good entries as long as this prior data is accurate.

Since wide-angle reflection seismology is essentially a form of refraction seismology, the results from such surveys are normally identified as refraction results.

Note that published results are often the product of a combined methodological analysis of data derived from several techniques that were used in tandem during the experiment. Such results are almost certainly higher quality than those that are derived from a single technique. In such cases where multiple techniques were used to derive the crustal model, the resulting entries have been labeled with what appears to be the principal or most important technique used. In a similar fashion, the results from unusual or new techniques are labeled with what appears to be the most closely related common technique (e.g., receiver functions as earthquake entries).

A list of the one-letter codes used in identifying the survey data type is given below in the “Key to CENA database”.

B.1.1.4 Azimuth

The azimuth for the shot line along which an entry lies is included for anisotropy studies. For fan entries, the angle given is the central angle of the fan. For most earthquake models, the value "999" is used for the azimuth. This is because the seismic stations used in the analysis of the model were generally located in many different directions in all four quadrants with respect to the model location, hence there is no true azimuth. Since the azimuths are usually derived from the large-scale maps that accompany the source publications, the values given in the database are probably generally good to ±5°.

B1.1.5 Geographic Location Code

This is assigned to allow for the selection of the data according to physiographic or geologic province. The code has the format "XXX-xx", where "XXX" identifies the continent or ocean and "xx" is a two-letter code for the geologic province. See below in the “Key to CENA database” for more information.

B1.1.6 Seismic Velocity

The errors associated with measured seismic velocities are usually not given in the references. However, when they are, they are typically less than ±0.05 km/sec (though in some cases, they can be as great as ±0.2 or ±0.3 km/sec [Mooney 1989]. As a rule, this value of ±0.05 km/sec should be applied as a general "goodness-of-fit" or error parameter for seismic velocity values.

B1.1.7 Thickness and Depth

The errors associated with determined layer thicknesses and depths are usually not given in the references. When they are, errors are typically 10% or less for crustal thicknesses and Moho depths [Mooney 1989]. For layers close to the surface, these errors are generally smaller, though in a number of cases they appear to be as large as the errors associated with deeper layers [Mooney 1989]. An additional general source of error also occurs because most layer depths and thicknesses included in the database must be measured from published diagrams. Magnification of digitized images reduces this error, but introduces another (though generally smaller) error due to possible reproduction distortions. Measurements from diagrams are usually estimated to the nearest 0.1 mm. For a layer that has a thickness of 1.0 mm on the diagram, this introduces an additional 10% error; for a layer that has a thickness of 20.0 mm on the diagram, this introduces a 0.5% error. Hence, the measurement uncertainties are much larger for thinner layers than for thick layers. In addition, there is an error when converting from raw millimeter measurements to actual kilometer scale, but this is tiny-0.2% on a verbal scale of 50.0 mm equals 40.0 km, for example. Based on these factors, an estimated error of 10% should be applied to layer thicknesses.

B1.1.8 Age

The age of last tectonic activity in the vicinity of the entry is included.

B1.1.9 Tectonic Province Type

The tectonic "style" in the vicinity of the entry is included.

B1.1.10 Heat

The surface heat flow in mW/m^2 in the vicinity of the entry may be included for heat flow studies. This parameter has not yet been entered into the database, though data has been gathered elsewhere.

B1.1.11 Notes on Type of Layer

The different types of Earth layers included in the database (sedimentary, crystalline, low-velocity, and mantle) are usually identified as such by a one- or two-letter code (see below in the "Key to CENA database") The crustal models presented in many references are sophisticated enough to include velocity gradients. The current version of the database does not include gradients as part of the data. However, gradients are accounted for in the appropriate entries in one of several ways, depending on the type of gradient.

By far, the most common gradient included in crustal models is the linear gradient, where velocity changes at a constant rate with depth. These gradients are usually represented in the corresponding database entry as two constant velocity layers–the upper layer is given the velocity value at the top of the gradient, and the lower layer is given the velocity value at the bottom of the gradient. The thickness of each of these layers is equal to one-half the vertical distance over which the gradient is applicable. In this manner, when the entry is mathematically manipulated (for example, to find the average crustal velocity), the results will usually be the same as if the gradient was included in the analysis as a linear function of the form $v = v_o + gt$, where v_o is the velocity at the top of the gradient, g is the value of the constant gradient (in sec^{-1}), and $v_f = v_o + gT$ is the velocity at the bottom of the gradient where T is the total vertical distance over which the gradient is valid. If there are a series of several gradients in the crustal velocity model, pairs of neighboring representative layers that have the same velocity value are combined into one single layer of that velocity simply by adding the two thicknesses together. This is done to simplify the database entry.

In the case of nonlinear gradients (as typically occur in models displaying iso-velocity lines), the usual representation technique is as follows. The gradient is sampled for depth at regularly spaced velocity intervals (e.g., every 0.1 or 0.2 km/sec). Each of these depths is then treated as if it were the center point of a crustal layer with a uniform velocity equal to the velocity value that corresponds to that depth along the gradient. The boundaries between these artificial layers are set one-half way between each neighboring depth point. The velocities at the top of the gradient and at the bottom of the gradient are each given their own layers in this scheme. The thickness of the top "layer" is set equal to one-half the difference between the depth of the first sampled depth point and the upper depth of the gradient. The thickness of the bottom "layer" is set equal to one-half the difference between the depth of the last sampled depth point and the bottom depth of the gradient. The artificial layers that represent gradients in a given entry include a “g” in their identification code.

Finally, it should be noted that the distinction between "sedimentary rock layers" and "crystalline crust" or "basement" is somewhat arbitrary. For example, in most of the continental U.S., all *Precambrian* rocks are considered "basement." However, along the Gulf and Atlantic Coasts, *pre-Mesozoic* rocks are considered "basement," and, in California, "basement" is pre-Cretaceous rock [Bayer 1983]. An attempt is made to use the source authors' interpretations of rock type; if that is unavailable, the local convention is sometimes used when distinguishing between "sedimentary rock" and "basement" in each entry. A further complication is the occurrence of interlayered sedimentary and volcanic rocks. Hence, we frequently do not separately indicate sedimentary from crystalline rocks. As an alternative, we have FORTRAN code available that allows one to select a “maximum” velocity (*P*- and/or *S*-wave) for sedimentary rock. This is a typical way in which studies of crystalline crust are conducted [Chulick and Mooney 2002].

B2 USING THE DATABASE

The attached CENA compilation is a formatted ASCII file. In addition, the entire database is also available as Matlab format files, EXCEL spreadsheets and ARCGIS shape files. A FORTRAN-based WINDOWS executable application is also included with this report to access and manipulate the database. It allows the user to select subsets of entries according to:

- Latitude and longitude range

- Geographical location
- Survey type
- Tectonic regime

It also allows the user to select specific subsets of data including:

- Crustal thickness.
- Surficial seismic velocity
- Sub-Moho seismic velocity

Finally, it will use the compilation to calculate subsets of derived results, such as:

- Average crustal seismic velocity
- Sedimentary rock thickness
- Average Sedimentary seismic velocity

The application when executed opens a DOS-based window that queries the user as to type of output result. It runs in all forms of Microsoft WINDOWS environments. Thus any PC will fulfill its system requirements.

B3 KEY TO CENA DATABASE:

```
Profile #  Latitude    Vp (km/s) Vs (km/s)  T (km)  D (km)   Nt  Hcc (km)    El (km)  HF (mW)  Geoprov  Lines Type
       Longitude                            Hc (km)    Age      Az      Ref    Geotype
-------------------------------------------------------------------------------------------------------------------
1089    58.13N 5.50 0.00 12.00  0.00    32.00  0.43 90.00 NAC-AL  3 R
    155.00W 6.50 0.00 20.00 12.00    32.00  MCz 999.00  63B.1  ORO
         8.10 0.00  0.00 32.00 m
```

Profile # the record number given this datapoint in the database
Latitude the latitude of the datapoint
Longitude the longitude of the datapoint
V_p the P-wave velocity of a given layer in the 1-D seismic velocity model for the datapoint
Vs the S-wave velocity for same as above ("0.00" indicates no data entry)
T the thickness of the layer described by the given P- and S-wave velocities
D the depth at which the layer described by the given velocities starts
Nt notes on layers: "m" indicates mantle. Other parameters include: "c" crystalline crust, "s" sediments, "g" gradient, "l" low-velocity zone. Combinations may also exist for gradients within the sedimentary (sg), low velocity (lg), crustal (cg) and mantle (mg) layers. A blank space means the layer is not specifically defined in the source reference.
Hcc the crustal thickness at the datapoint without including sediments (crystalline crustal thickness)
Hc the total crustal thickness (including sediments)
El the elevation at the datapoint (if negative then this is the depth of the water).
Age the age of the last thermo-tectonic event at the datapoint (if known)
MCz Mesozoic to Cenozoic mPt Middle Proterozoic

Pz	Paleozoic	ePt	Early Proterozoic
lPt	Late Proterozoic	Ar	Archean

HF heat flow at the datapoint NOTE: units are actually mW/m2

Az the azimuth of the profile from which the 1-D profile was taken (999 indicates multiple directions, 900 indicates unknown)

Geoprov the geologic location of the datapoint (e.g., NAC-BR = North American Continent, Basin and Range; NAO-NA = North Atlantic Ocean, North American Basin; CGM-GU = Caribbean-Gulf of Mexico, Gulf of Mexico Basin) (Complete list available upon request)

Ref the reference in the literature from which the seismic data was taken (e.g., 63B.1 = the year in which the article was published (1963), the initial of the last name of the first author of the article (B), and the number indicating which of the references from "63B" this datapoint was taken (1) (reference list in the WORD document CENA2012-Ref.docx)

Lines (3 shown above) Indicates number of layers in this datapoint entry

Type indicates whether the seismic profile from which the data was taken was reversed refraction (R), unreversed refraction (U), Split (S), Reflection (F), Sonobuoy (B), Tomography (I), Time-Term (T), Earthquake Model (E), Receiver Function (C), waveform model (W), Laboratory Measurement (L), unknown (*) or other (O). (Method of Seismic Survey).

Geotype indicates the geologic province type in which the datapoint is situated (if known)

ORO	orogen	EXC	extended crust
BAS	basin	PLT	platform
SHD	shield		
LIP	large igneous province		

Appendix C *Q*-Factor Models

Table A.1 Q-studies used for extracting the Q-factor model for each of the four regions. Abbreviations for the column "Our Region(s)" are: ACP = Atlantic Coastal Plain, APP = Appalachians, CNA = Central North America, MEM=Mississippi Embayment (Gulf Coastal Region). Others: NMSZ = New Madrid Seismic Zone.

Author/s	**Year**	**Journal**	**Phase**	Signal	**Our Region(s)**	**Comment**	**Geographical Coordinates**		**Spreading**	***Q-f* Relation: $Q_0 = f^{\eta}$**		**Frequency Range**		**Study Distance**
							Lat (°)	**Lon (°)**		**Q_0**	η	**f_{min} (Hz)**	**f_{max} (Hz)**	**d_{max} (km)**
Al-Shukri & Mitchell	1994	*BSSA*	**P**	Teleseismics	MEM	*NMSZ, 3D Study, Upper 5 km layer*	37.00	-89.00	**0.0**	**192**	0.00	10.0	25.0	
Al-Shukri & Mitchell	1994	*BSSA*	**P**	Teleseismics	MEM	*NMSZ, 3D Study, Lower 9 km layer*	37.00	-89.00	**0.0**	**476**	0.00	10.0	25.0	
Atkinson	1989	*SRL*	**Lg**	Teleseismics	CNA, APP	*Canadian Shield*	46.00	-75.00	**-1.0**	**1100**	0.17	0.0	1.0	
Atkinson	1989	*SRL*	**Lg**	Teleseismics	CNA, APP	*Canadian Shield*	46.00	-75.00	**-0.5**	**540**	0.41	0.0	1.0	
Atkinson	2004	*BSSA*	**Lg**	Teleseismics	APP	*Appalachian and Shield*	47.00	-72.00	**-0.5**	**893**	0.32	0.1	20.0	1,000
Atkinson & Boore	1995	*BSSA*	**Lg**	Teleseismics	ACP	*Canadian Shield*	47.00	-70.00	**-0.5**	**670**	0.33	0.5	20.0	
Atkinson & Mereu	1992	*BSSA*	**Lg**	Teleseismics	CNA, APP	*Canadian Shield*	47.00	-70.00	**-0.5**	**670**	0.33	1.0	10.0	
Benz et al.	1997	*BSSA*	**Lg**	Teleseismics		*Basin and Range*	37.50	-116.00	**-0.5**	**235**	0.56	1.0	5.0	
Benz et al.	1997	*BSSA*	**Lg**	Teleseismics		*Basin and Range*	37.50	-116.00	**-0.5**	**575**	1.05	5.0	14.0	800
Benz et al.	1997	*BSSA*	**Lg**	Teleseismics	CNA		36.50	-91.00	**-0.5**	**1291**	0.00	1.5	7.0	900

Author/s	Year	Journal	Phase	Signal	Our Region(s)	Comment	Geographical Coordinates		Spreading	*Q-f* Relation: $Q_0 = f^{\eta}$		Frequency Range		Study Distance
							Lat (°)	Lon (°)		Q_0	η	f_{min} (Hz)	f_{max} (Hz)	d_{max} (km)
Benz et al.	1997	*BSSA*	**Lg**	Teleseismics	APP		44.00	-72.50	**-0.5**	**1052**	0.22	1.5	14.0	900
Benz et al.	1997	*BSSA*	**Lg**	Teleseismics		*South California*	35.00	-117.00	**-0.5**	**187**	0.55	1.0	7.0	800
Boatwright & Seekins	2011	*BSSA*	**Lg**	Teleseismics	APP	*Appalachian*	45.00	-72.50	**-0.5**	**410**	0.50	0.1	20.0	602
Brockman S R & Bollinger G A	1992	*BSSA*	**Lg**	Teleseismics		*Utah, Wasatach Point, West US*	40.00	-112.00	**-0.5**	**94**	0.80	1.0	10.0	
Chapman & Catchings	2008	*BSSA*	**P**	Active	ACP	*Chesapeake Bay, Nearfield perspective*	37.25	-75.75	**0.0**	**80**	0.00	10.0	150.0	
Chun et al.	1987	*BSSA*	**Lg**	Teleseismics	CNA, APP	*Canadian Shield*	46.00	-75.00	**-0.5**	**1100**	0.19	0.6	10.0	
Dwyer et al.	1983	*BSSA*	**Lg**	Teleseismics	MEM	*Mississippi Embayment*	36.50	-89.50	**-0.8**	**1000**	0.40	1.0	10.0	200
Erickson et al.	2004	*BSSA*	**Lg**	Teleseismics		*Basin and Range*	39.00	-115.00	**-0.5**	**200**	0.69	0.8	12.0	
Erickson et al.	2004	*BSSA*	**Lg**	Teleseismics	CNA		37.00	-92.00	**-0.5**	**470**	0.52	1.5	12.0	1,300
Erickson et al.	2004	*BSSA*	**Lg**	Teleseismics		*Northern California*	40.00	-121.50	**-0.5**	**105**	0.67	0.8	12.0	
Erickson et al.	2004	*BSSA*	**Lg**	Teleseismics	APP, ACP	*Appalachian and Shield*	43.00	-74.00	**-0.5**	**650**	0.36	0.8	12.0	800
Erickson et al.	2004	*BSSA*	**Lg**	Teleseismics		*North-West US*	45.00	-119.00	**-0.5**	**152**	0.79	0.8	12.0	
Erickson et al.	2004	*BSSA*	**Lg**	Teleseismics		*Rocky Mountains*	45.50	-112.00	**-0.5**	**166**	0.61	0.8	12.0	
Erickson et al.	2004	*BSSA*	**Lg**	Teleseismics		*South California*	35.00	-118.00	**-0.5**	**152**	0.72	0.8	12.0	
Ge et al.	2009	*BSSA*	**S**	Active	MEM	*Mississippi Embayment, very shallow*	35.00	-89.00	**0.0**	**23**	0.00	15.0	55.0	1,000
Gupta & McLaughlin	1987	*BSSA*	**Lg**	Teleseismics	ACP, APP	*E US*	37.50	-83.00	**-0.5**	**800**	0.32	0.5	7.0	900
Hasegawa	1985	*BSSA*	**Lg**	Teleseismics	CNA, APP	*Canadian Shield*	46.00	-75.00	**-0.5**	**900**	0.20	1.0	10.0	900
Langston et al.	2005	*BSSA*	**P**	Active	MEM	*Mississippi Embayment Sediments*	36.50	-90.00	**-1.0**	**200**	0.00	0.2	4.0	

Author/s	Year	Journal	Phase	Signal	Our Region(s)	Comment	Geographical Coordinates		Spreading	*Q-f* Relation: $Q_0 = f^{\eta}$		Frequency Range		Study Distance
							Lat (°)	**Lon (°)**		**Q_0**	**η**	**f_{min} (Hz)**	**f_{max} (Hz)**	**d_{max} (km)**
Langston et al.	2005	*BSSA*	**S**	Active	MEM	*Mississippi Embayment Sediments*	36.50	-90.00	**-1.0**	**100**	0.00	2.0	12.0	
Li et al.	2006	*BSSA*	**P**	Active		*Seattle Basin, at 4 km depth, North-West US*	48.00	-122.50	**-1.0**	**44**	0.80	1.0	40.0	
Li et al..	2006	*BSSA*	**P**	Active		*Seattle Basin, at 14 km depth, North-West US*	48.00	-122.50	**-1.0**	**77**	1.01	1.0	20.0	
Li et al.	2006	*BSSA*	**P**	Active		*Seattle Basin, at 14 km depth, North-West US*	48.00	-122.50	**-1.0**	**1040**	0.16	20.0	40.0	
McNamara et al.	2004	*BSSA*	**Lg**	Teleseismics		*Western Plains (unpublished, preprint BSSA)*	41.00	-102.00	**-0.5**	**160**	0.65	0.8	12.0	
McNamara et al.	2004	*BSSA*	**Lg**	Teleseismics		*Rocky Mountains (unpublished, preprint BSSA)*	40.00	-107.00	**-0.5**	**181**	0.65	0.8	12.0	
McNamara et al.	2004	*BSSA*	**Lg**	Teleseismics		*Basin and Range (unpublished, preprint BSSA)*	40.00	-112.00	**-0.5**	**380**	0.57	0.8	12.0	
Pulli	1984	*BSSA*	**Lg**	Teleseismics	ACP, APP	*New England*	42.00	-72.00	**-0.5**	**460**	0.40	0.8	10.0	80
Pulli	1984	*BSSA*	**Lg**	Teleseismics	ACP, APP	*New England*	42.00	-72.00	**-0.5**	**460**	0.40	0.8	10.0	400
Shi et al.	1996	*JGR*	**Lg**	Teleseismics	APP	*Adirondack Mountains, Region A*	44.50	-74.50	**-0.5**	**905**	0.40	1.0	15.0	1,394
Shi et al.	1996	*JGR*	**Lg**	Teleseismics	APP	*Erie Ontario Lowland, Region B*	43.00	-76.50	**-0.5**	**721**	0.46	1.0	15.0	1,394
Shi et al.	1996	*JGR*	**Lg**	Teleseismics	APP	*Appalachian Plateau*	41.00	-80.00	**-0.5**	**561**	0.47	1.0	15.0	1,394
Shi et al.	1996	*JGR*	**Lg**	Teleseismics	ACP	*Coastal Basins and Highlands*	40.00	-75.00	**-0.5**	**586**	0.46	1.0	15.0	1,394
Shi et al.	1996	*JGR*	**Lg**	Teleseismics	APP	*Northern New England*	45.00	-70.50	**-0.5**	**705**	0.41	1.0	15.0	1,394
Shin & Hermann	1987	*BSSA*	**Lg**	Teleseismics	CNA, APP	*Canadian Shield*	46.00	-75.00	**-0.5**	**500**	0.65	0.5	7.0	994
Woodgold	1990	*BSSA*	**Lg**	Teleseismics	CNA, APP	*Quebec, Region C*	47.00	-71.80	**-0.5**	**590**	0.45	0.5	20.0	

Author/s	Year	Journal	Phase	Signal	Our Region(s)	Comment	Geographical Coordinates		Spreading	Q-f Relation: $Q_0 = f^{\eta}$		Frequency Range		Study Distance
							Lat (°)	Lon (°)		Q_0	η	f_{min} (Hz)	f_{max} (Hz)	d_{max} (km)
Woodgold	1990	*BSSA*	**Lg**	Teleseismics	APP	*New Brunswick, Region D*	46.70	-66.00	**-0.5**	**450**	0.47	0.5	20.0	
Woodgold	1990	*BSSA*	**Lg**	Teleseismics	CNA, APP	*Canadian Shield, Region A*	47.50	-77.00	**-0.5**	**860**	0.33	0.5	20.0	
Woodgold	1990	*BSSA*	**Lg**	Teleseismics	CNA, APP	*Canadian Shield, Region B*	44.00	-77.50	**-0.5**	**750**	0.40	0.5	20.0	
Zandieh & Pezeshk	2010	*BSSA*	**Lg**	Teleseismics	MEM	*NMSZ, Mississippi Embayment*	36.50	-89.50	**-0.5**	**614**	0.32	1.0	30.0	
Liu et al.	1994	*BSSA*	**S**	Teleseismics	MEM	*NMSZ, Sediments (0.65 km)*	36.30	-89.60	**0.0**	**53**	0.00	9.0	25.0	
Liu et al.	1994	*BSSA*	**P**	Teleseismics	MEM	*NMSZ, Sediments (0.65 km)*	36.30	-89.60	**0.0**	**59**	0.00	5.0	25.0	
Liu et al.	1994	*BSSA*	**S**	Teleseismics	MEM	*NMSZ*	36.30	-89.60	**0.0**	**1020**	0.00	9.0	25.0	
Liu et al.	1994	*BSSA*	**P**	Teleseismics	MEM	*NMSZ*	36.30	-89.60	**0.0**	**1199**	0.00	5.0	25.0	

Appendix D Supplemental Results to Chapter 5

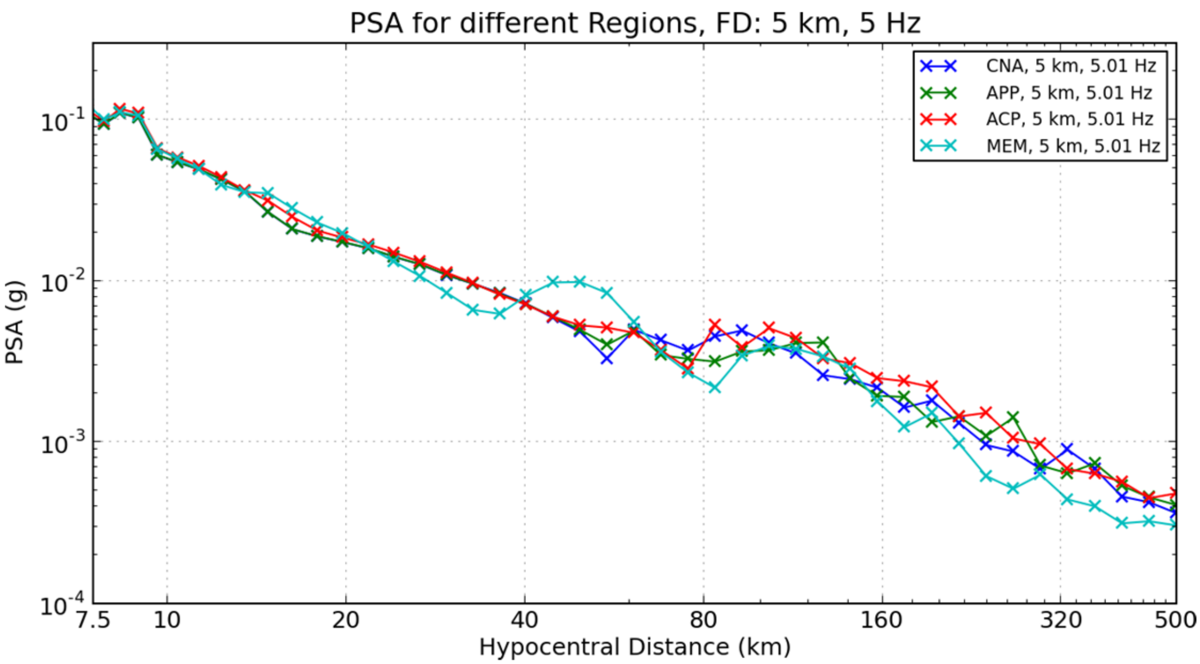

Figure D.1 **Response spectral acceleration at 5 Hz for the ACP the APP, CNA, and MEM regions for an event with a focal depth of 5 km.**

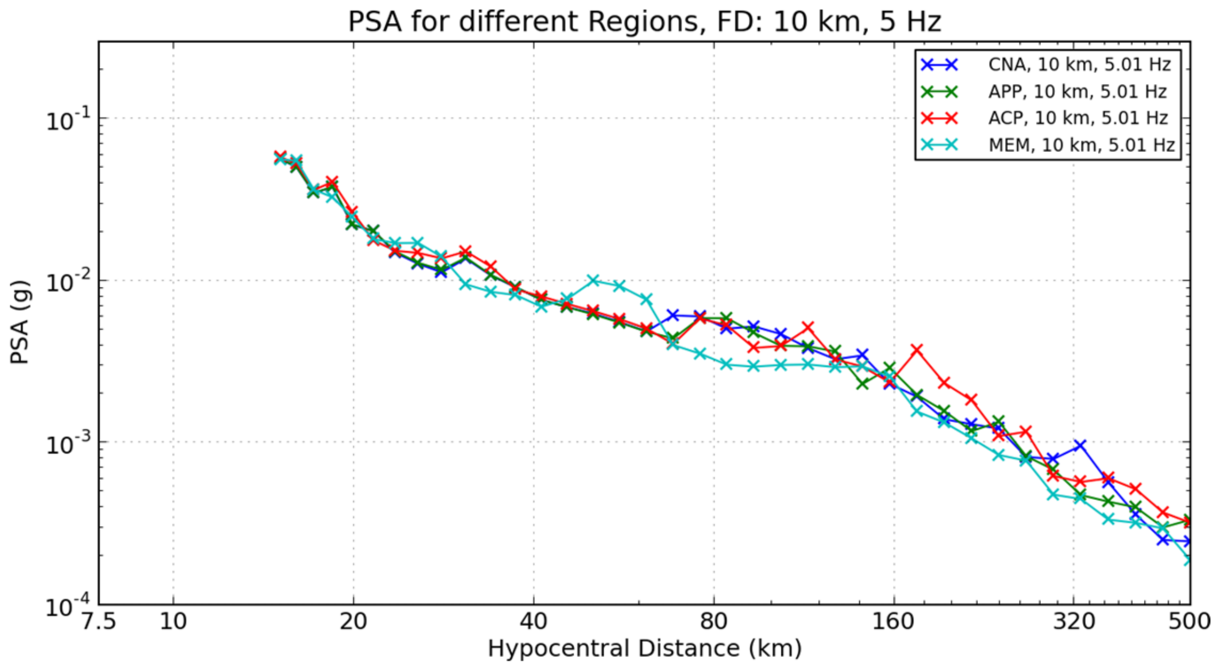

Figure D.2 Response spectral acceleration at 5 Hz for the ACP the APP, CNA, and MEM regions for an event with a focal depth of 10 km.

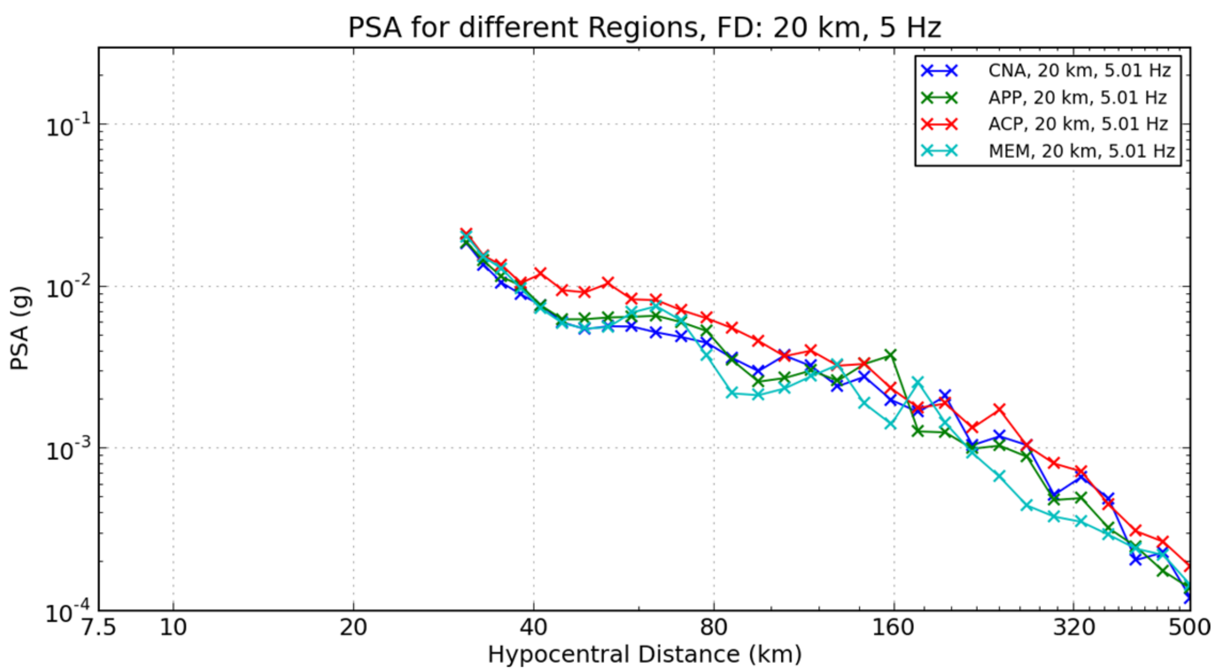

Figure D.3 Response spectral acceleration at 5 Hz for the ACP the APP, CNA, and MEM regions for an event with a focal depth of 20 km.

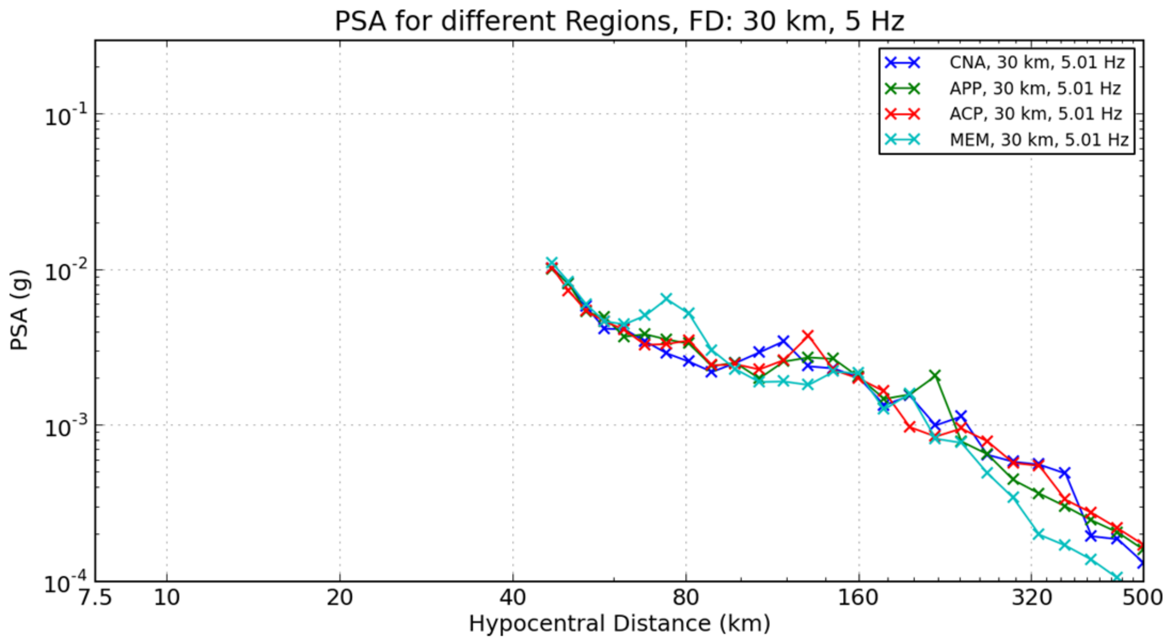

Figure D.4 **Response spectral acceleration at 5 Hz for the ACP the APP, CNA, and the MEM regions for an event with a focal depth of 30 km.**

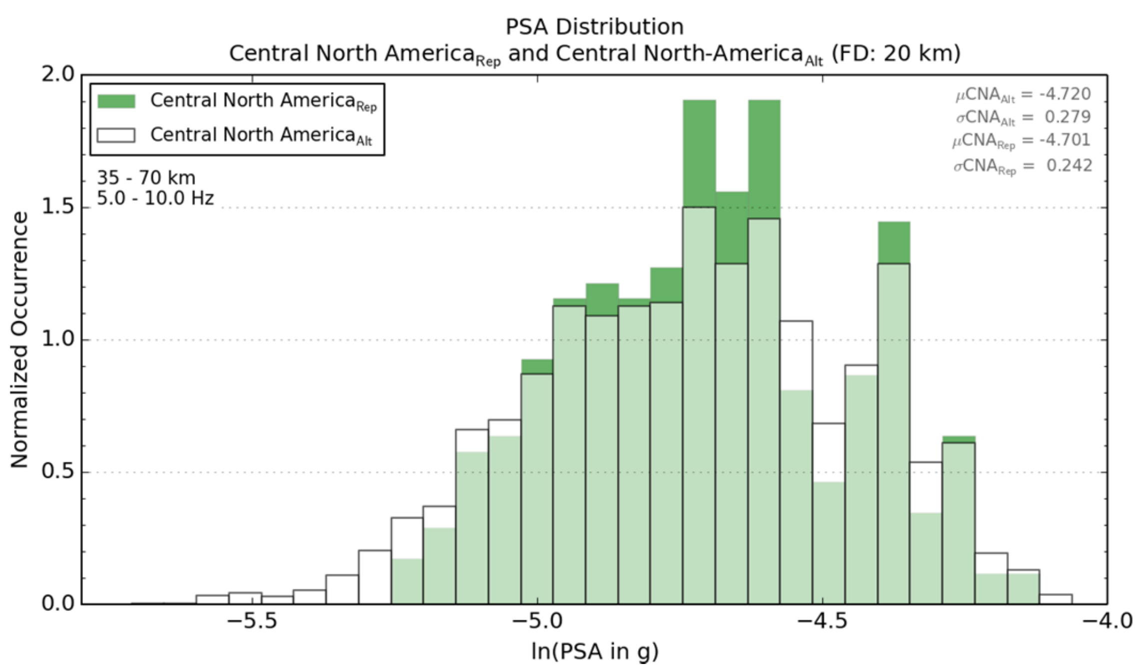

Figure D.5 **The PSA distribution for CNA for both representative and alternative models at a distance of 35–70 km, frequencies 5.0–10 Hz, and focal depth of 20 km.**

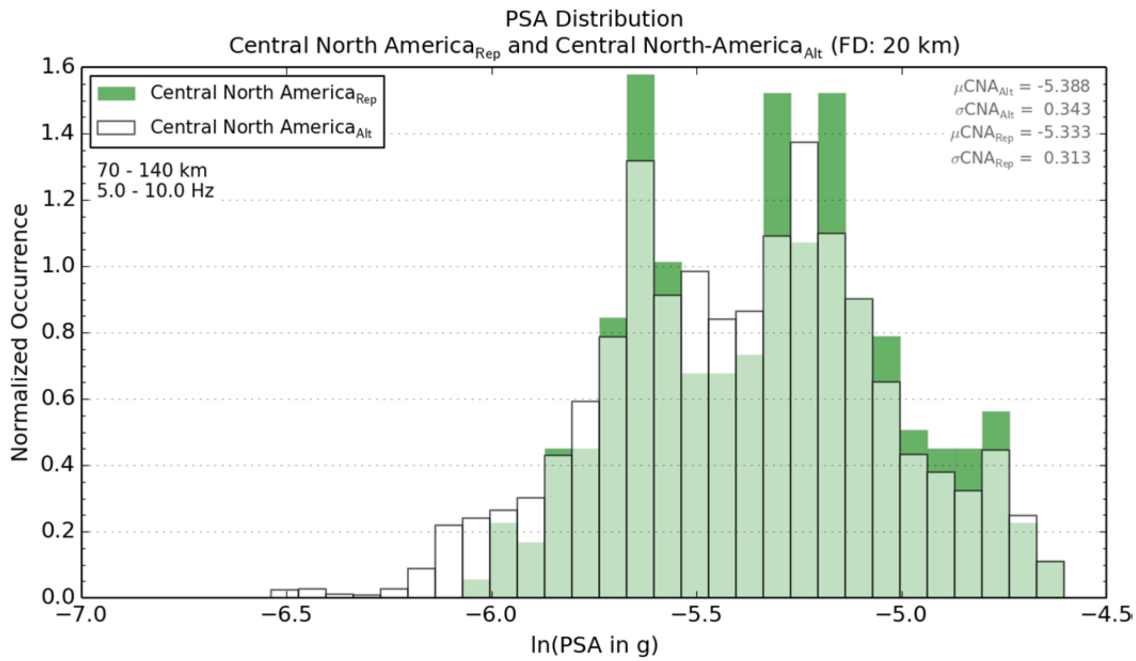

Figure D.6 The PSA distribution for CNA for both representative and alternative models at a distance of 70-140 km, frequencies 5.0–10 Hz, and focal depth of 20 km.

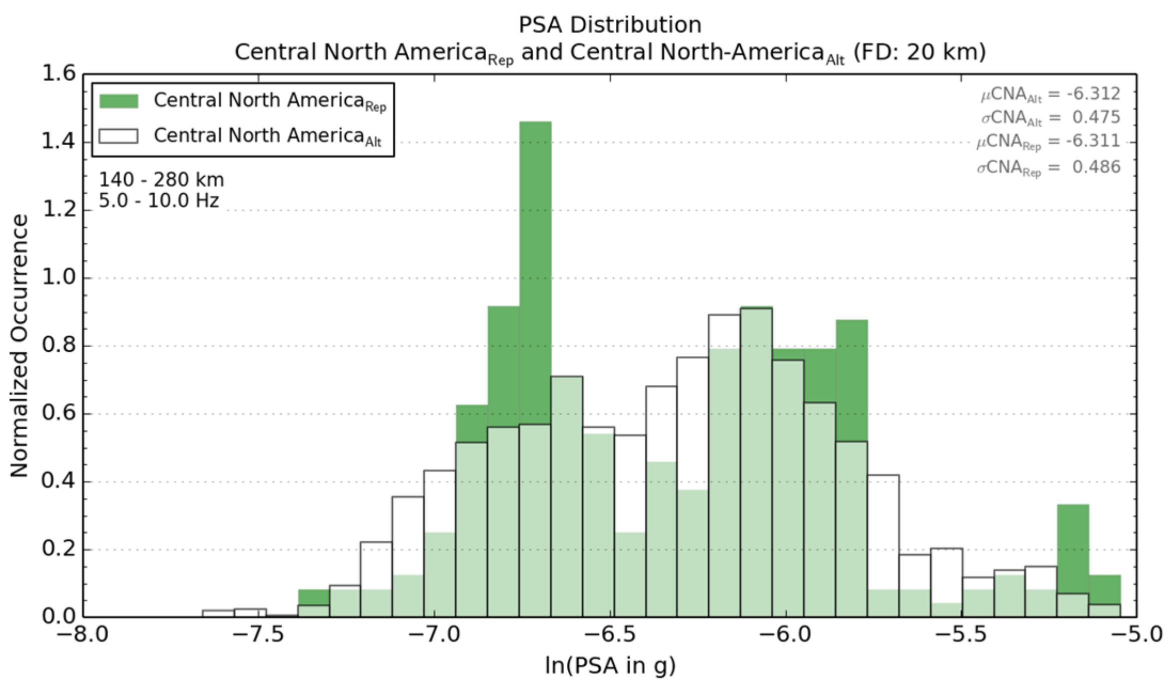

Figure D.7 The PSA distribution for CNA for both representative and alternative models at a distance of 140–280 km, frequencies 5.0–10 Hz, and focal depth of 20 km.

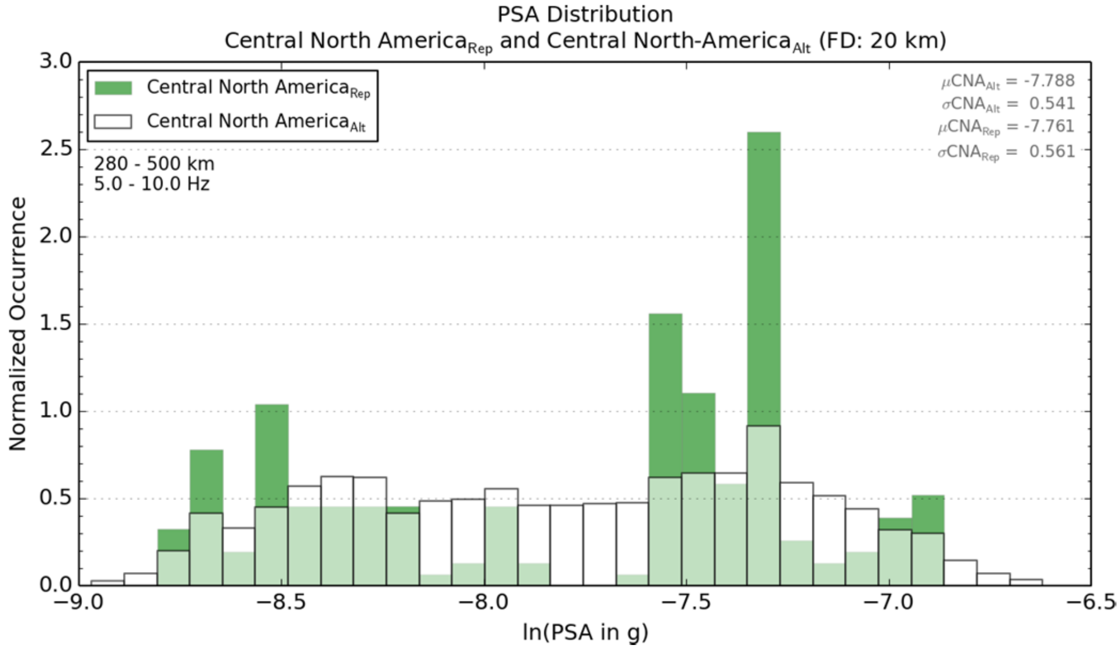

Figure D.8 **The PSA distribution for CNA for both representative and alternative models at a distance of 280–500 km, frequencies 5.0–10 Hz, and focal depth of 20 km.**

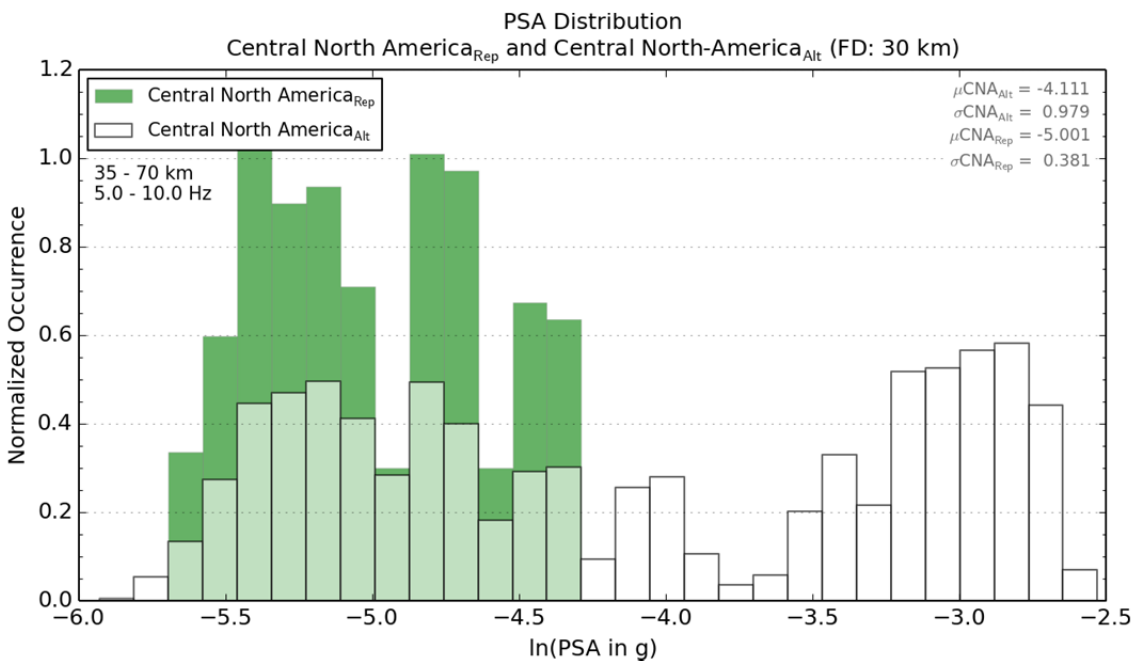

Figure D.9 **The PSA distribution for CNA for both representative and alternative models at a distance of 35–70 km, frequencies 5.0–10 Hz, and focal depth of 30 km.**

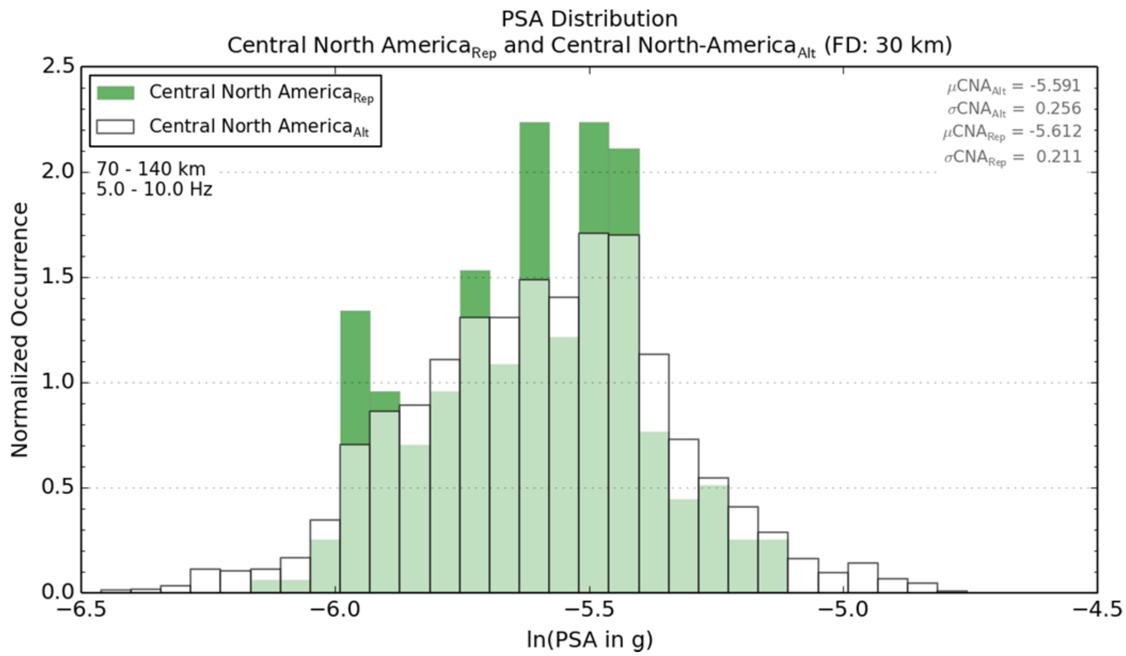

Figure D.10 **The PSA distribution for CNA for both representative and alternative models at a distance of 70–140 km, frequencies 5.0–10 Hz, and focal depth of 30 km.**

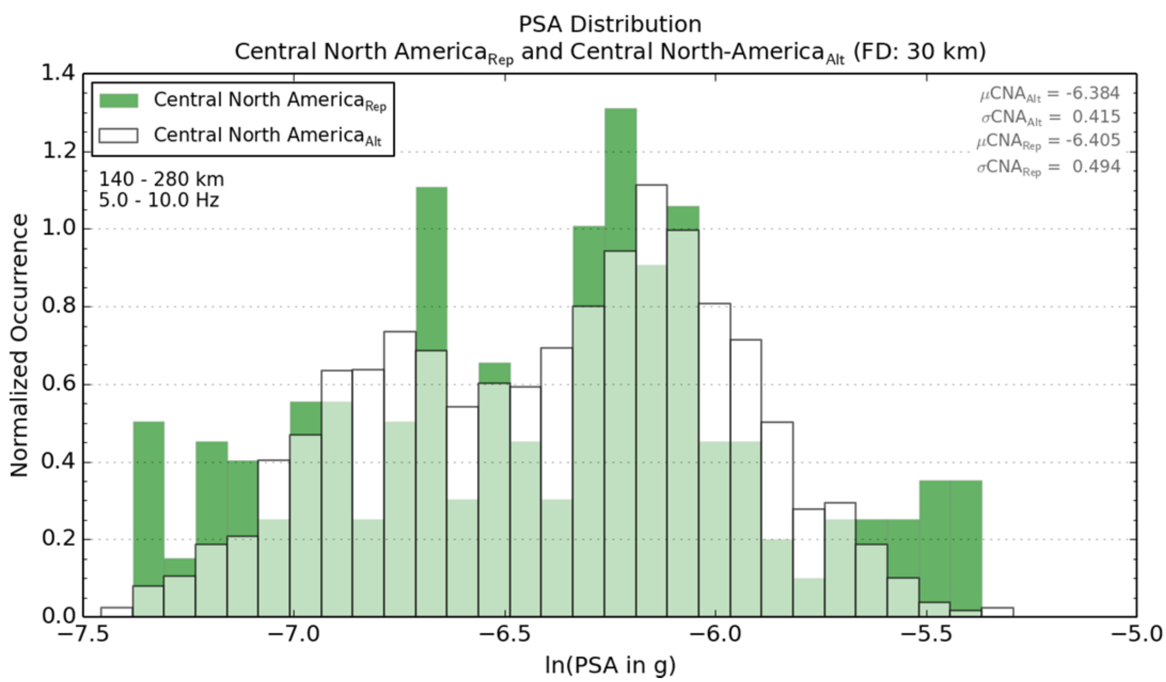

Figure D.11 **The PSA distribution for CNA for both representative and alternative models at a distance of 140–280 km, frequencies 5.0–10 Hz, and focal depth of 30 km.**

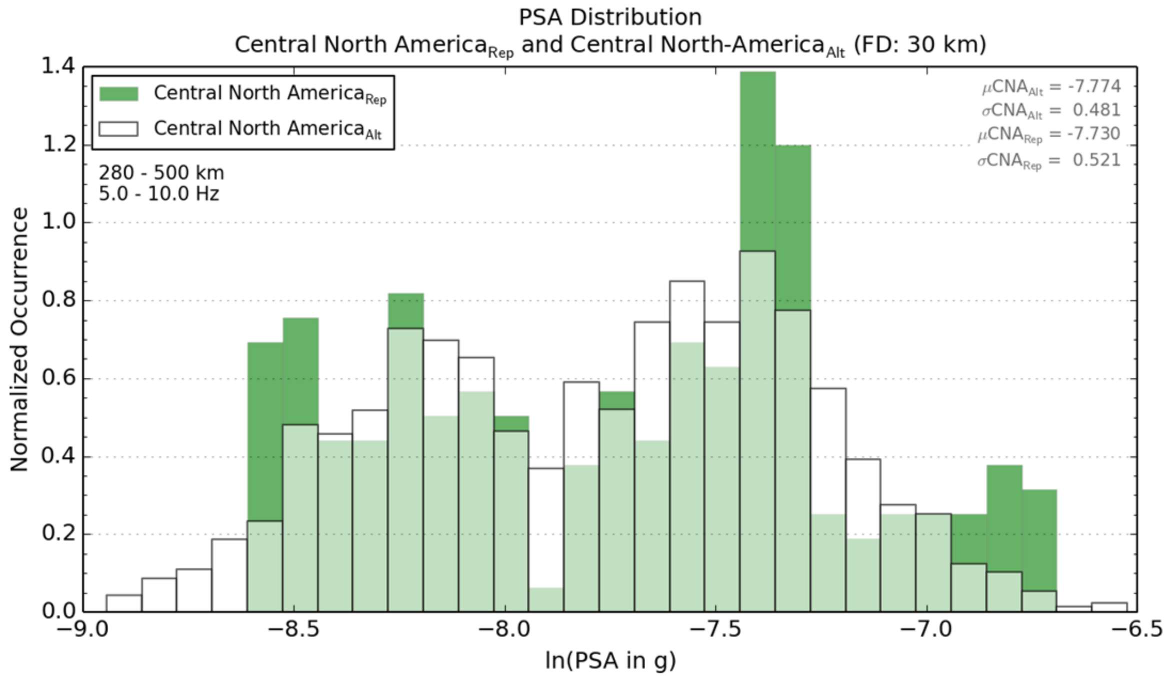

Figure D.12 **The PSA distribution for CNA for both representative and alternative models at a distance of 280–500 km, frequencies 5.0–10 Hz, and focal depth of 30 km.**

Table D.1 **Mean and standard deviation for CNA's ground motions using the representative and the alternative crustal models. These values refer to histograms that present the statistical distribution of PSA-values.**

Region	*F* Depth (km)	Frequencies (Hz)	Distances (km)	ln(PSA)					
				μ CNA_{Rep}	σ CNA_{Alt}	σ CNA_{Rep}	σ CNA_{Alt}	μ CNA_{Rep} - μ CNA_{Alt}	σ CNA_{Rep} - σ CNA_{Alt}
CNA	5	0.5 - 1.0	35 - 70	-5.881	-5.883	0.283	0.288	0.003	-0.005
CNA	5	0.5 - 1.0	70 - 140	-6.269	-6.272	0.258	0.264	0.003	-0.006
CNA	5	0.5 - 1.0	140 - 280	-6.673	-6.678	0.294	0.291	0.005	0.003
CNA	5	0.5 - 1.0	280 - 500	-7.124	-7.098	0.221	0.231	-0.026	-0.010
CNA	5	1.0 - 5.0	35 - 70	-5.755	-5.737	0.368	0.384	-0.018	-0.016
CNA	5	1.0 - 5.0	70 - 140	-6.087	-6.101	0.312	0.365	0.014	-0.053
CNA	5	1.0 - 5.0	140 - 280	-6.714	-6.674	0.340	0.369	-0.039	-0.029
CNA	5	1.0 - 5.0	280 - 500	-7.422	-7.425	0.203	0.220	0.003	-0.017
CNA	5	5.0 - 10.0	35 - 70	-4.925	-4.887	0.311	0.330	-0.038	-0.020
CNA	5	5.0 - 10.0	70 - 140	-5.256	-5.303	0.267	0.344	0.047	-0.077
CNA	5	5.0 - 10.0	140 - 280	-6.277	-6.209	0.471	0.444	-0.068	0.027
CNA	5	5.0 - 10.0	280 - 500	-7.420	-7.422	0.308	0.303	0.002	0.005
CNA	10	0.5 - 1.0	35 - 70	-6.551	-6.555	0.361	0.375	0.004	-0.015
CNA	10	0.5 - 1.0	70 - 140	-6.884	-6.910	0.355	0.373	0.027	-0.018
CNA	10	0.5 - 1.0	140 - 280	-7.513	-7.489	0.359	0.377	-0.023	-0.018
CNA	10	0.5 - 1.0	280 - 500	-8.066	-8.079	0.272	0.242	0.013	0.029
CNA	10	1.0 - 5.0	35 - 70	-5.520	-5.565	0.419	0.463	0.045	-0.045
CNA	10	1.0 - 5.0	70 - 140	-6.097	-6.116	0.507	0.508	0.019	-0.001
CNA	10	1.0 - 5.0	140 - 280	-6.857	-6.862	0.520	0.496	0.005	0.024
CNA	10	1.0 - 5.0	280 - 500	-7.723	-7.775	0.363	0.361	0.052	0.002
CNA	10	5.0 - 10.0	35 - 70	-4.659	-4.682	0.321	0.339	0.023	-0.018
CNA	10	5.0 - 10.0	70 - 140	-5.242	-5.265	0.223	0.278	0.023	-0.055
CNA	10	5.0 - 10.0	140 - 280	-6.202	-6.218	0.436	0.450	0.016	-0.014
CNA	10	5.0 - 10.0	280 - 500	-7.520	-7.570	0.516	0.480	0.050	0.036
CNA	20	0.5 - 1.0	35 - 70	-6.343	-6.339	0.567	0.566	-0.004	0.002

Region	*F* Depth (km)	Frequencies (Hz)	Distances (km)	ln(PSA)					
				μ CNA_{Rep}	σ CNA_{Alt}	σ CNA_{Rep}	σ CNA_{Alt}	μ CNA_{Rep}- μ CNA_{Alt}	σ CNA_{Rep} - σ CNA_{Alt}
CNA	20	0.5 - 1.0	70 - 140	-7.349	-7.335	0.390	0.401	-0.014	-0.011
CNA	20	0.5 - 1.0	140 - 280	-7.871	-7.883	0.504	0.517	0.013	-0.013
CNA	20	0.5 - 1.0	280 - 500	-8.925	-8.917	0.454	0.457	-0.008	-0.004
CNA	20	1.0 - 5.0	35 - 70	-5.547	-5.555	0.508	0.515	0.008	-0.008
CNA	20	1.0 - 5.0	70 - 140	-6.388	-6.394	0.512	0.510	0.006	0.002
CNA	20	1.0 - 5.0	140 - 280	-7.031	-7.069	0.565	0.563	0.038	0.002
CNA	20	1.0 - 5.0	280 - 500	-8.266	-8.283	0.477	0.479	0.017	-0.001
CNA	20	5.0 - 10.0	35 - 70	-4.701	-4.720	0.242	0.279	0.018	-0.037
CNA	20	5.0 - 10.0	70 - 140	-5.333	-5.388	0.313	0.343	0.056	-0.030
CNA	20	5.0 - 10.0	140 - 280	-6.311	-6.312	0.486	0.475	0.002	0.011
CNA	20	5.0 - 10.0	280 - 500	-7.761	-7.788	0.561	0.541	0.026	0.020
CNA	30	0.5 - 1.0	35 - 70	-6.367	-5.903	0.453	0.640	-0.464	-0.187
CNA	30	0.5 - 1.0	70 - 140	-7.345	-7.326	0.391	0.409	-0.020	-0.018
CNA	30	0.5 - 1.0	140 - 280	-7.933	-7.928	0.596	0.572	-0.005	0.023
CNA	30	0.5 - 1.0	280 - 500	-9.050	-9.075	0.479	0.499	0.025	-0.020
CNA	30	1.0 - 5.0	35 - 70	-5.621	-4.934	0.498	0.860	-0.687	-0.362
CNA	30	1.0 - 5.0	70 - 140	-6.553	-6.514	0.428	0.446	-0.038	-0.018
CNA	30	1.0 - 5.0	140 - 280	-7.089	-7.077	0.557	0.537	-0.012	0.020
CNA	30	1.0 - 5.0	280 - 500	-8.331	-8.362	0.546	0.491	0.031	0.055
CNA	30	5.0 - 10.0	35 - 70	-5.001	-4.111	0.381	0.979	-0.890	-0.599
CNA	30	5.0 - 10.0	70 - 140	-5.612	-5.591	0.211	0.256	-0.022	-0.045
CNA	30	5.0 - 10.0	140 - 280	-6.405	-6.384	0.494	0.415	-0.021	0.079
CNA	30	5.0 - 10.0	280 - 500	-7.730	-7.774	0.521	0.481	0.044	0.041

Table D.2 **Mean and standard deviations for the ground motions calculated for ACP representative crustal model. These values refer to histograms of the statistical distribution of PSA-values. Values above the thresholds defined in Chapter 4 are highlighted.**

Region	*F* Depth (km)	Frequencies (Hz)	Distances (km)	$\mu\ ACP_{Rep}$	$\sigma\ ACP_{Rep}$	$\mu\ ACP_{Rep} - \mu\ CNA_{Rep}$	$(\mu\ ACP_{Rep} - \mu\ CNA_{Rep}) / \sigma\ CNA_{Alt}$
ACP	5	0.5 - 1.0	35 - 70	-5.881	0.275	0.000	-0.001
ACP	5	0.5 - 1.0	70 - 140	-6.203	0.245	0.066	0.249
ACP	5	0.5 - 1.0	140 - 280	-6.657	0.224	0.017	0.057
ACP	5	0.5 - 1.0	280 - 500	-7.007	0.225	0.118	0.510
ACP	5	1.0 - 5.0	35 - 70	-5.754	0.408	0.001	0.003
ACP	5	1.0 - 5.0	70 - 140	-5.972	0.302	0.115	0.314
ACP	5	1.0 - 5.0	140 - 280	-6.544	0.337	0.170	0.460
ACP	5	1.0 - 5.0	280 - 500	-7.288	0.236	0.134	0.608
ACP	5	5.0 - 10.0	35 - 70	-4.879	0.321	0.046	0.139
ACP	5	5.0 - 10.0	70 - 140	-5.223	0.276	0.033	0.095
ACP	5	5.0 - 10.0	140 - 280	-6.104	0.398	0.173	0.389
ACP	5	5.0 - 10.0	280 - 500	-7.292	0.317	0.127	0.421
ACP	10	0.5 - 1.0	35 - 70	-6.633	0.392	-0.081	-0.217
ACP	10	0.5 - 1.0	70 - 140	-6.855	0.303	0.029	0.078
ACP	10	0.5 - 1.0	140 - 280	-7.232	0.426	0.281	0.745
ACP	10	0.5 - 1.0	280 - 500	-7.971	0.329	0.095	0.391
ACP	10	1.0 - 5.0	35 - 70	-5.670	0.496	-0.150	-0.324
ACP	10	1.0 - 5.0	70 - 140	-6.087	0.410	0.010	0.020
ACP	10	1.0 - 5.0	140 - 280	-6.687	0.459	0.170	0.343
ACP	10	1.0 - 5.0	280 - 500	-7.694	0.266	0.029	0.081
ACP	10	5.0 - 10.0	35 - 70	-4.741	0.304	-0.082	-0.243
ACP	10	5.0 - 10.0	70 - 140	-5.218	0.240	0.024	0.087
ACP	10	5.0 - 10.0	140 - 280	-6.026	0.503	0.176	0.390
ACP	10	5.0 - 10.0	280 - 500	-7.377	0.318	0.143	0.298
ACP	20	0.5 - 1.0	35 - 70	~~-6.097~~	~~0.609~~	~~0.246~~	~~0.436~~

Region	*F* Depth (km)	Frequencies (Hz)	Distances (km)	μ ACP_{Rep}	σ ACP_{Rep}	μ ACP_{Rep} - μ CNA_{Rep}	(μ ACP_{Rep} - μ CNA_{Rep}) / σ CNA_{Alt}
ACP	20	0.5 - 1.0	70 - 140	~~-7.069~~	~~0.418~~	~~0.280~~	~~0.699~~
ACP	20	0.5 - 1.0	140 - 280	~~-7.547~~	~~0.546~~	~~0.323~~	~~0.625~~
ACP	20	0.5 - 1.0	280 - 500	~~-8.527~~	~~0.374~~	~~0.398~~	~~0.871~~
ACP	20	1.0 - 5.0	35 - 70	~~-5.260~~	~~0.533~~	~~0.287~~	~~0.556~~
ACP	20	1.0 - 5.0	70 - 140	~~-6.052~~	~~0.495~~	~~0.336~~	~~0.658~~
ACP	20	1.0 - 5.0	140 - 280	~~-6.783~~	~~0.523~~	~~0.248~~	~~0.441~~
ACP	20	1.0 - 5.0	280 - 500	~~-7.960~~	~~0.334~~	~~0.306~~	~~0.639~~
ACP	20	5.0 - 10.0	35 - 70	~~-4.297~~	~~0.213~~	~~0.404~~	~~1.451~~
ACP	20	5.0 - 10.0	70 - 140	~~-4.963~~	~~0.368~~	~~0.369~~	~~1.076~~
ACP	20	5.0 - 10.0	140 - 280	~~-6.102~~	~~0.453~~	~~0.209~~	~~0.439~~
ACP	20	5.0 - 10.0	280 - 500	~~-7.567~~	~~0.431~~	~~0.194~~	~~0.358~~
ACP	30	0.5 - 1.0	35 - 70	-6.410	0.435	-0.043	-0.067
ACP	30	0.5 - 1.0	70 - 140	-7.355	0.465	-0.009	-0.023
ACP	30	0.5 - 1.0	140 - 280	-7.898	0.551	0.035	0.061
ACP	30	0.5 - 1.0	280 - 500	-9.077	0.496	-0.028	-0.055
ACP	30	1.0 - 5.0	35 - 70	-5.609	0.524	0.012	0.014
ACP	30	1.0 - 5.0	70 - 140	-6.535	0.446	0.018	0.040
ACP	30	1.0 - 5.0	140 - 280	-7.069	0.570	0.020	0.037
ACP	30	1.0 - 5.0	280 - 500	-8.440	0.416	-0.109	-0.222
ACP	30	5.0 - 10.0	35 - 70	-5.041	0.347	-0.040	-0.040
ACP	30	5.0 - 10.0	70 - 140	-5.592	0.226	0.020	0.079
ACP	30	5.0 - 10.0	140 - 280	-6.303	0.462	0.101	0.244
ACP	30	5.0 - 10.0	280 - 500	-7.754	0.403	-0.024	-0.050

Table D.3 **Mean and standard deviations for the ground motions calculated for the APP representative crustal model. These values refer to histograms of the statistical distribution of PSA-values. No values exceed the thresholds defined in Chapter 4.**

Region	*F* Depth (km)	Frequencies (Hz)	Distances (km)	μ APP_{Rep}	σ APP_{Rep}	μ APP_{Rep} - μ CNA_{Rep}	(μ APP_{Rep} - μ CNA_{Rep}) / σ CNA_{Alt}
APP	5	0.5 - 1.0	35 - 70	-5.884	0.273	-0.003	-0.011
APP	5	0.5 - 1.0	70 - 140	-6.284	0.269	-0.015	-0.056
APP	5	0.5 - 1.0	140 - 280	-6.720	0.232	-0.047	-0.160
APP	5	0.5 - 1.0	280 - 500	-7.119	0.224	0.006	0.024
APP	5	1.0 - 5.0	35 - 70	-5.777	0.379	-0.022	-0.057
APP	5	1.0 - 5.0	70 - 140	-6.142	0.327	-0.055	-0.152
APP	5	1.0 - 5.0	140 - 280	-6.630	0.366	0.084	0.227
APP	5	1.0 - 5.0	280 - 500	-7.378	0.151	0.044	0.199
APP	5	5.0 - 10.0	35 - 70	-4.942	0.343	-0.017	-0.050
APP	5	5.0 - 10.0	70 - 140	-5.257	0.218	-0.001	-0.004
APP	5	5.0 - 10.0	140 - 280	-6.220	0.391	0.057	0.128
APP	5	5.0 - 10.0	280 - 500	-7.434	0.227	-0.014	-0.048
APP	10	0.5 - 1.0	35 - 70	-6.589	0.365	-0.038	-0.100
APP	10	0.5 - 1.0	70 - 140	-6.920	0.316	-0.037	-0.098
APP	10	0.5 - 1.0	140 - 280	-7.430	0.385	0.083	0.219
APP	10	0.5 - 1.0	280 - 500	-8.127	0.201	-0.061	-0.252
APP	10	1.0 - 5.0	35 - 70	-5.596	0.419	-0.077	-0.166
APP	10	1.0 - 5.0	70 - 140	-6.030	0.489	0.067	0.132
APP	10	1.0 - 5.0	140 - 280	-6.816	0.491	0.040	0.081
APP	10	1.0 - 5.0	280 - 500	-7.848	0.276	-0.125	-0.346
APP	10	5.0 - 10.0	35 - 70	-4.705	0.327	-0.046	-0.135
APP	10	5.0 - 10.0	70 - 140	-5.254	0.156	-0.012	-0.044
APP	10	5.0 - 10.0	140 - 280	-6.169	0.453	0.033	0.073
APP	10	5.0 - 10.0	280 - 500	-7.641	0.369	-0.121	-0.252
APP	20	0.5 - 1.0	35 - 70	-6.326	0.579	0.017	0.031
APP	20	0.5 - 1.0	70 - 140	-7.351	0.399	-0.002	-0.005

APP	20	0.5 - 1.0	140 - 280	-7.726	0.559	0.144	0.279
APP	20	0.5 - 1.0	280 - 500	-8.871	0.346	0.054	0.119
APP	20	1.0 - 5.0	35 - 70	-5.505	0.509	0.042	0.082
APP	20	1.0 - 5.0	70 - 140	-6.379	0.544	0.009	0.018
APP	20	1.0 - 5.0	140 - 280	-6.973	0.613	0.059	0.104
APP	20	1.0 - 5.0	280 - 500	-8.269	0.394	-0.003	-0.006
APP	20	5.0 - 10.0	35 - 70	-4.584	0.227	0.117	0.422
APP	20	5.0 - 10.0	70 - 140	-5.367	0.354	-0.034	-0.099
APP	20	5.0 - 10.0	140 - 280	-6.208	0.598	0.103	0.217
APP	20	5.0 - 10.0	280 - 500	-7.862	0.431	-0.101	-0.186
APP	30	0.5 - 1.0	35 - 70	-6.376	0.483	-0.010	-0.015
APP	30	0.5 - 1.0	70 - 140	-7.311	0.441	0.035	0.085
APP	30	0.5 - 1.0	140 - 280	-7.722	0.524	0.211	0.369
APP	30	0.5 - 1.0	280 - 500	-8.979	0.475	0.071	0.142
APP	30	1.0 - 5.0	35 - 70	-5.633	0.514	-0.013	-0.015
APP	30	1.0 - 5.0	70 - 140	-6.570	0.455	-0.017	-0.038
APP	30	1.0 - 5.0	140 - 280	-6.980	0.560	0.109	0.203
APP	30	1.0 - 5.0	280 - 500	-8.366	0.349	-0.034	-0.070
APP	30	5.0 - 10.0	35 - 70	-4.977	0.376	0.024	0.025
APP	30	5.0 - 10.0	70 - 140	-5.622	0.197	-0.010	-0.039
APP	30	5.0 - 10.0	140 - 280	-6.296	0.454	0.108	0.261
APP	30	5.0 - 10.0	280 - 500	-8.011	0.340	-0.281	-0.585

Table D.4 Mean and standard deviations for the ground motions calculated for the MEM representative crustal model. These values refer to histograms of the statistical distribution of PSA-values. Values above the thresholds defined in Chapter 4 are highlighted.

Region	*F* Depth (km)	Frequencies (Hz)	Distances (km)	μ MEM_{Rep}	σ MEM_{Rep}	μ MEM_{Rep} - μ CNA_{Rep}	(μ MEM_{Rep} - μ CNA_{Rep}) / σ CNA_{Alt}
MEM	5	0.5 - 1.0	35 - 70	-5.952	0.305	-0.072	-0.249
MEM	5	0.5 - 1.0	70 - 140	-6.430	0.199	-0.161	-0.610
MEM	5	0.5 - 1.0	140 - 280	-6.769	0.256	-0.096	-0.329
MEM	5	0.5 - 1.0	280 - 500	-7.203	0.224	-0.078	-0.340
MEM	5	1.0 - 5.0	35 - 70	-5.474	0.494	0.281	0.732
MEM	5	1.0 - 5.0	70 - 140	-6.334	0.305	-0.247	-0.676
MEM	5	1.0 - 5.0	140 - 280	-6.906	0.415	-0.192	-0.520
MEM	5	1.0 - 5.0	280 - 500	-7.747	0.227	-0.326	-1.480
MEM	5	5.0 - 10.0	35 - 70	-4.683	0.407	0.242	0.733
MEM	5	5.0 - 10.0	70 - 140	-5.493	0.225	-0.237	-0.689
MEM	5	5.0 - 10.0	140 - 280	-6.440	0.563	-0.163	-0.368
MEM	5	5.0 - 10.0	280 - 500	-7.812	0.259	-0.392	-1.294
MEM	10	0.5 - 1.0	35 - 70	-6.381	0.454	0.171	0.455
MEM	10	0.5 - 1.0	70 - 140	-7.006	0.327	-0.123	-0.329
MEM	10	0.5 - 1.0	140 - 280	-7.542	0.414	-0.029	-0.077
MEM	10	0.5 - 1.0	280 - 500	-8.178	0.207	-0.112	-0.463
MEM	10	1.0 - 5.0	35 - 70	-5.419	0.434	0.100	0.216
MEM	10	1.0 - 5.0	70 - 140	-6.406	0.401	-0.309	-0.609
MEM	10	1.0 - 5.0	140 - 280	-6.985	0.461	-0.129	-0.259
MEM	10	1.0 - 5.0	280 - 500	-8.063	0.343	-0.340	-0.941
MEM	10	5.0 - 10.0	35 - 70	-4.646	0.371	0.013	0.038
MEM	10	5.0 - 10.0	70 - 140	-5.586	0.273	-0.344	-1.238
MEM	10	5.0 - 10.0	140 - 280	-6.429	0.526	-0.227	-0.505
MEM	10	5.0 - 10.0	280 - 500	-7.953	0.310	-0.433	-0.902
MEM	20	0.5 - 1.0	35 - 70	-6.122	0.506	0.221	0.390
MEM	20	0.5 - 1.0	70 - 140	-7.296	0.407	0.053	0.132

Region	*F* Depth (km)	Frequencies (Hz)	Distances (km)	μ MEM_{Rep}	σ MEM_{Rep}	μ MEM_{Rep} - μ CNA_{Rep}	(μ MEM_{Rep} - μ CNA_{Rep}) / σ CNA_{Alt}
MEM	20	0.5 - 1.0	140 - 280	-8.039	0.633	-0.168	-0.325
MEM	20	0.5 - 1.0	280 - 500	-9.052	0.444	-0.127	-0.277
MEM	20	1.0 - 5.0	35 - 70	-5.318	0.399	0.229	0.445
MEM	20	1.0 - 5.0	70 - 140	-6.407	0.563	-0.019	-0.038
MEM	20	1.0 - 5.0	140 - 280	-7.206	0.616	-0.175	-0.311
MEM	20	1.0 - 5.0	280 - 500	-8.535	0.358	-0.269	-0.561
MEM	20	5.0 - 10.0	35 - 70	-4.656	0.223	0.046	0.164
MEM	20	5.0 - 10.0	70 - 140	-5.581	0.255	-0.248	-0.722
MEM	20	5.0 - 10.0	140 - 280	-6.574	0.586	-0.264	-0.554
MEM	20	5.0 - 10.0	280 - 500	-8.068	0.277	-0.307	-0.568
MEM	30	0.5 - 1.0	35 - 70	-6.244	0.443	0.123	0.192
MEM	30	0.5 - 1.0	70 - 140	-7.292	0.453	0.053	0.130
MEM	30	0.5 - 1.0	140 - 280	-8.057	0.680	-0.124	-0.217
MEM	30	0.5 - 1.0	280 - 500	-9.520	0.434	-0.470	-0.943
MEM	30	1.0 - 5.0	35 - 70	-5.432	0.385	0.189	0.220
MEM	30	1.0 - 5.0	70 - 140	-6.445	0.647	0.108	0.241
MEM	30	1.0 - 5.0	140 - 280	-7.174	0.663	-0.085	-0.159
MEM	30	1.0 - 5.0	280 - 500	-8.929	0.418	-0.598	-1.217
MEM	30	5.0 - 10.0	35 - 70	-4.831	0.263	0.171	0.174
MEM	30	5.0 - 10.0	70 - 140	-5.618	0.432	-0.006	-0.023
MEM	30	5.0 - 10.0	140 - 280	-6.530	0.594	-0.125	-0.302
MEM	30	5.0 - 10.0	280 - 500	-8.542	0.469	-0.812	-1.691

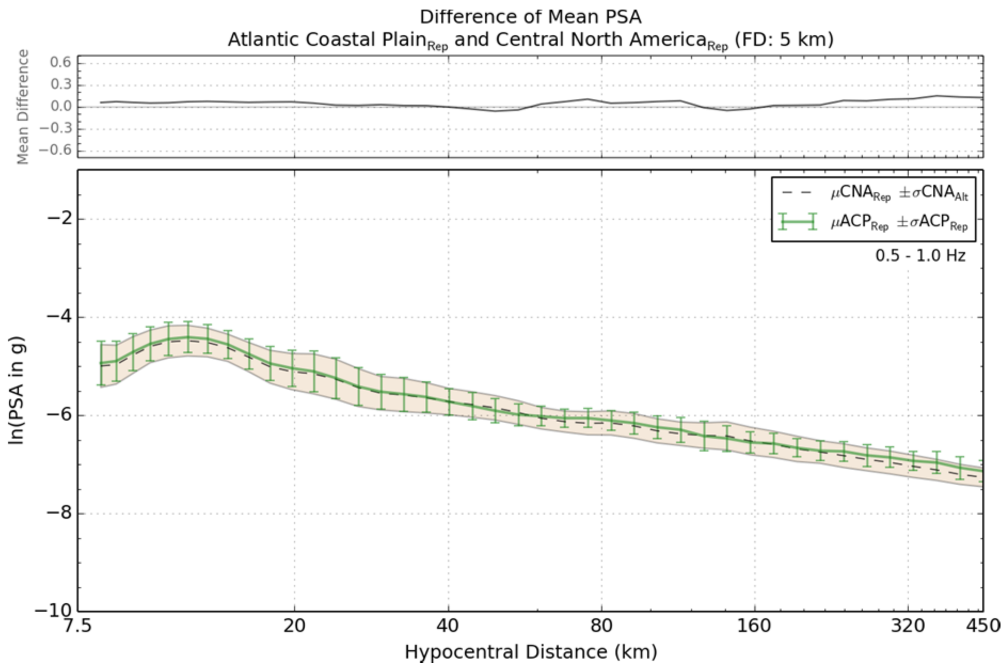

Figure D.13 **Representative mean comparison between the ACP and CNA regions within the standard deviation of CNA$_{Alt}$ at frequency 0.5–1 Hz and focal depth of 5 km.**

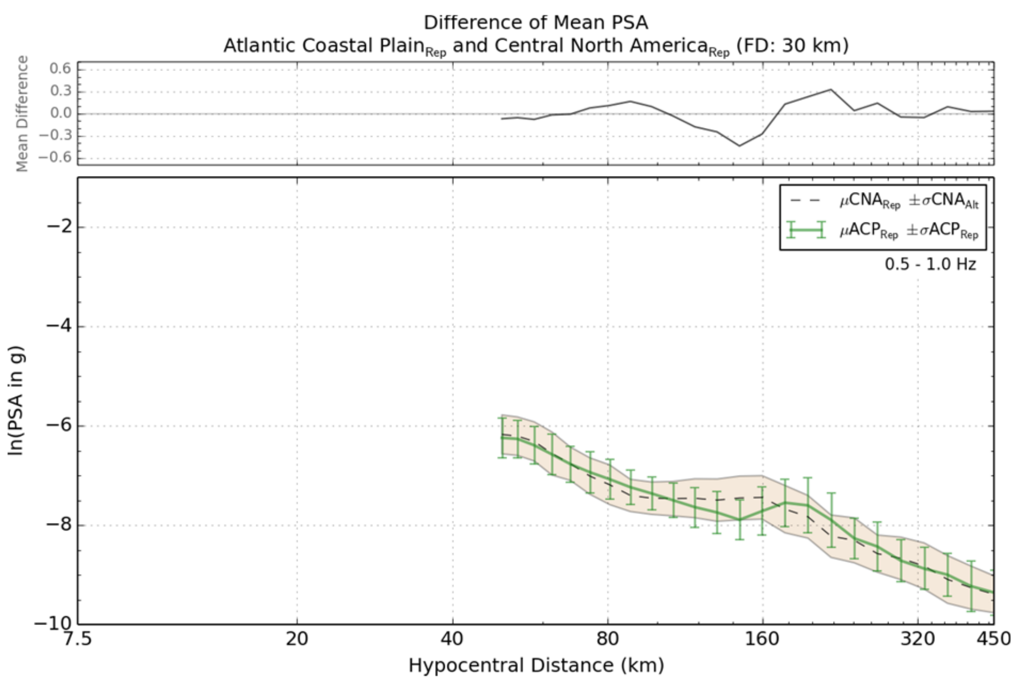

Figure D.14 **Representative mean comparison between the ACP and CNA regions within the standard deviation of CNA$_{Alt}$ at frequency 0.5–1 Hz and focal depth of 30 km.**

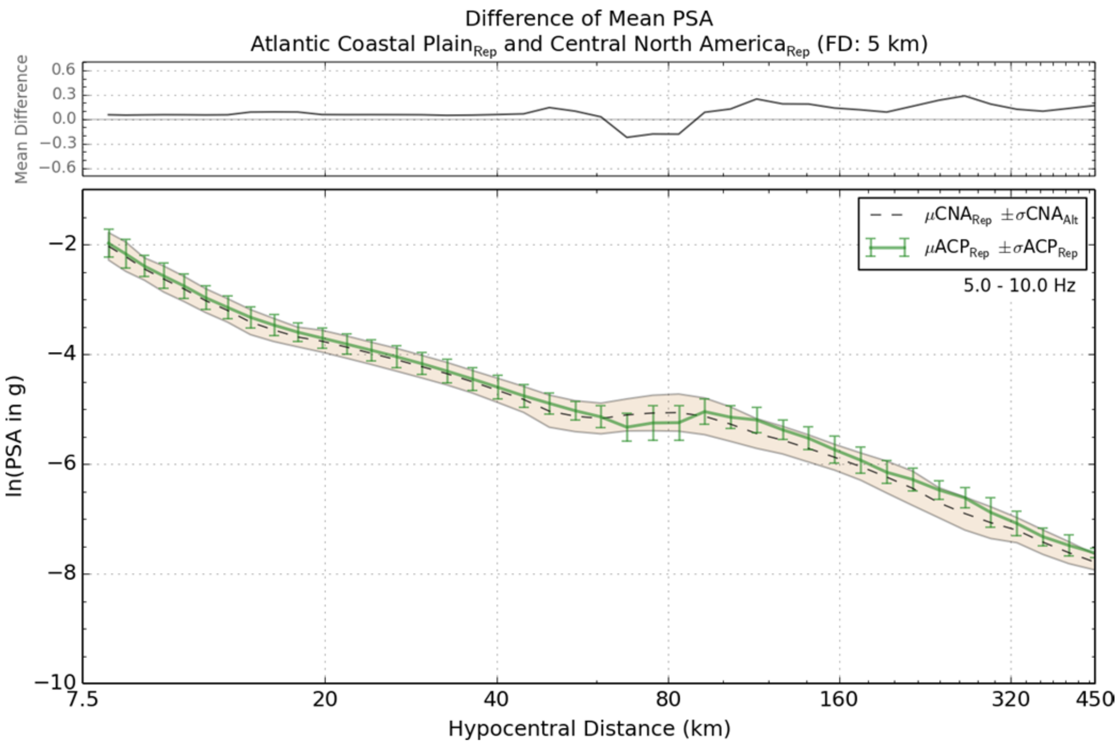

Figure D.15 **Representative mean comparison between the ACP and CNA regions within the standard deviation of CNA$_{Alt}$ at frequency 5.0–10 Hz and focal depth of 5 km.**

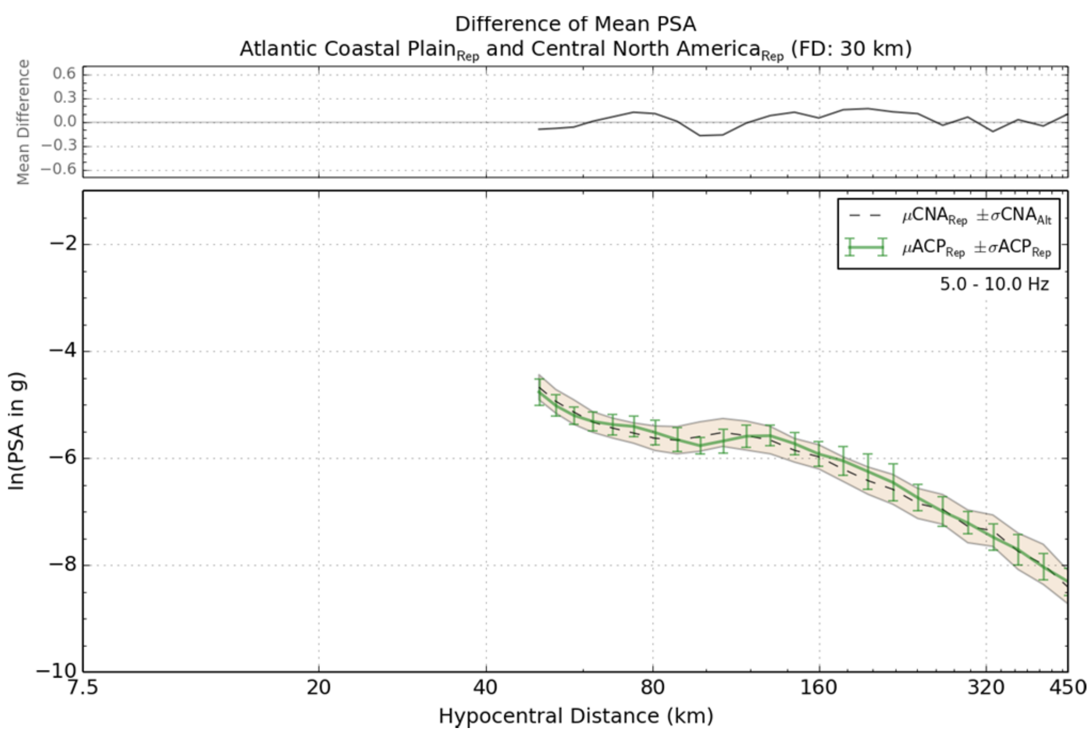

Figure D.16 **Representative mean comparison between the ACP and CNA regions within the standard deviation of CNA$_{Alt}$ at frequency 5.0–10 Hz and focal depth of 30 km.**

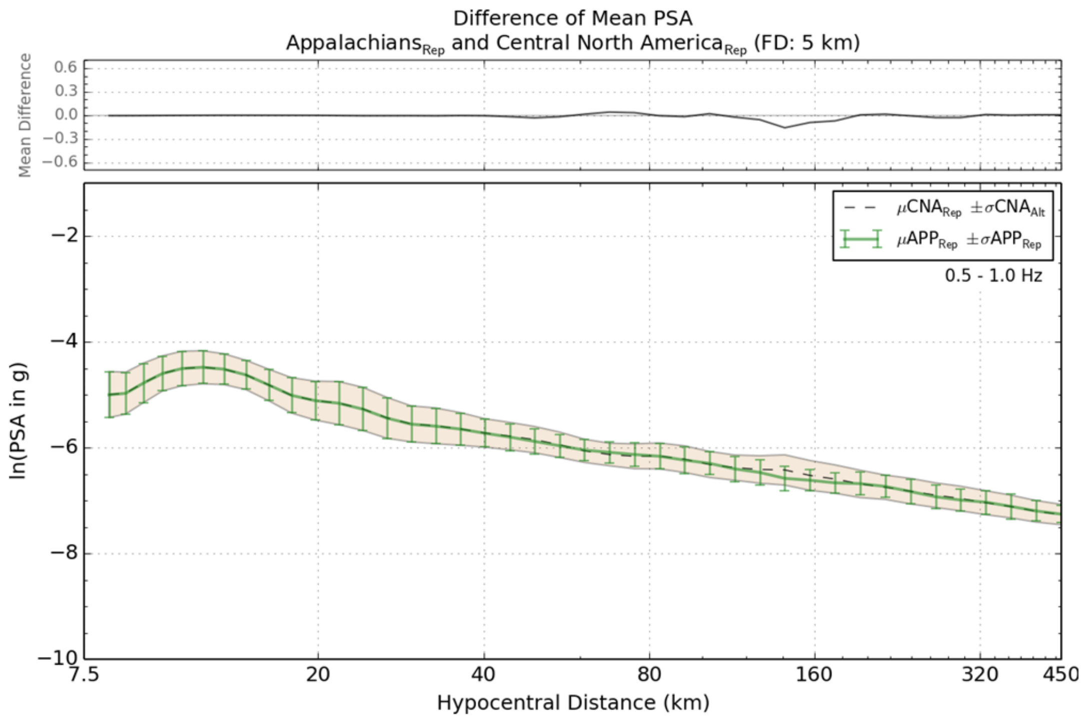

Figure D.17 Representative mean comparison between the APP and CNA regions within the standard deviation of CNA_{Alt} at frequency 0.5–1 Hz and focal depth of 5 km.

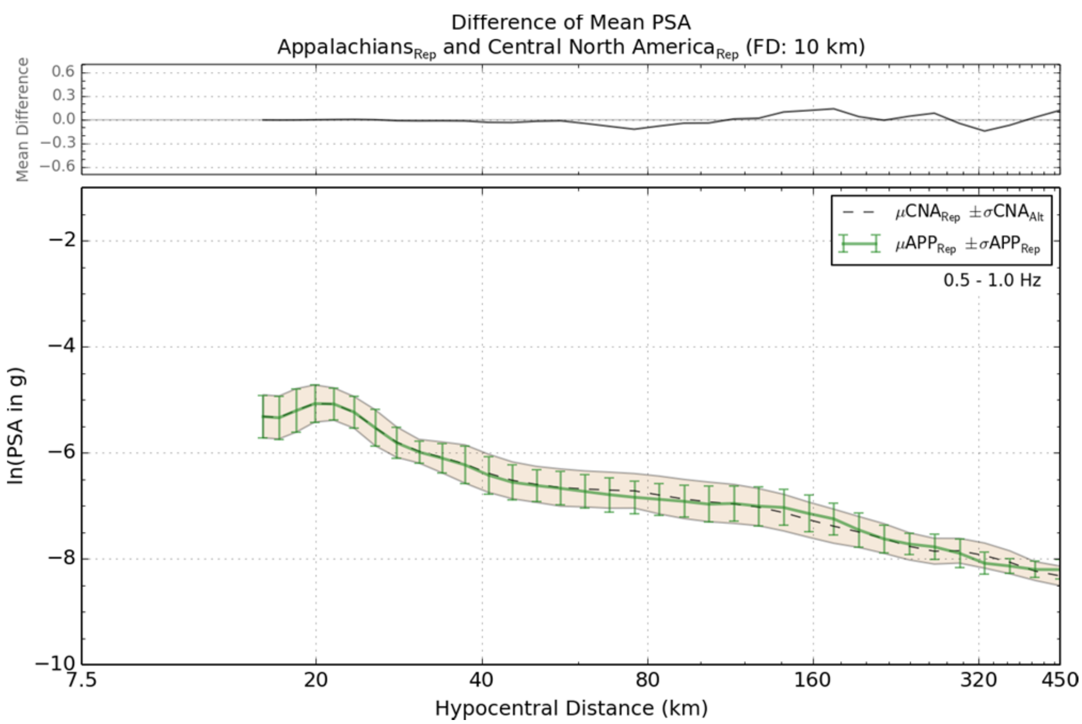

Figure D.18 Representative mean comparison between the ACP and CNA regions within the standard deviation of CNA_{Alt} at frequency 0.5–1 Hz and focal depth of 10 km.

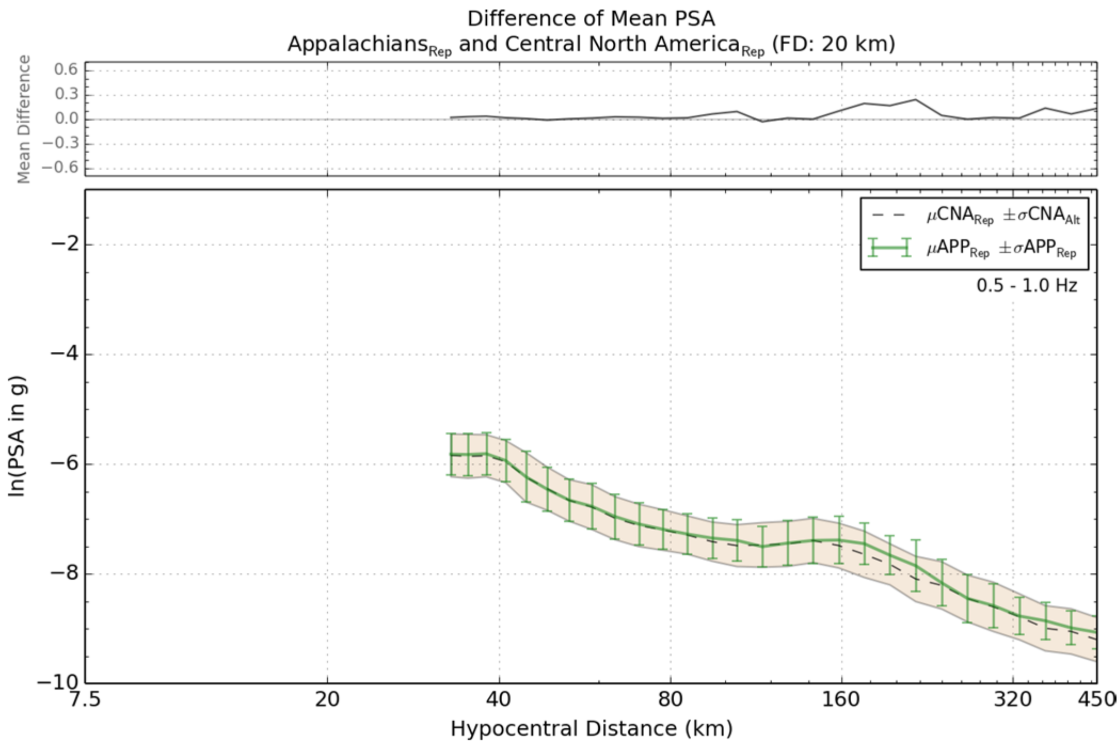

Figure D.19 **Representative mean comparison between the ACP and CNA regions within the standard deviation of CNA$_{Alt}$ at frequency 0.5–1 Hz and focal depth of 20 km.**

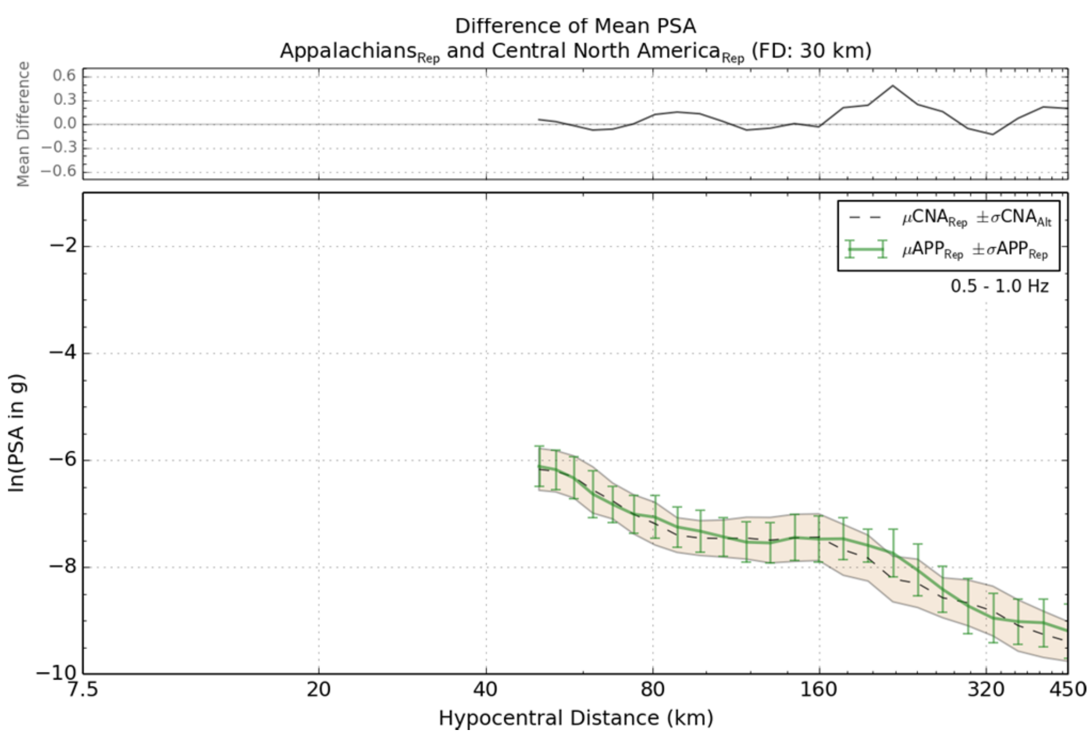

Figure D.20 **Representative mean comparison between the ACP and CNA regions within the standard deviation of CNA$_{Alt}$ at frequency 0.5–1 Hz and focal depth of 30 km.**

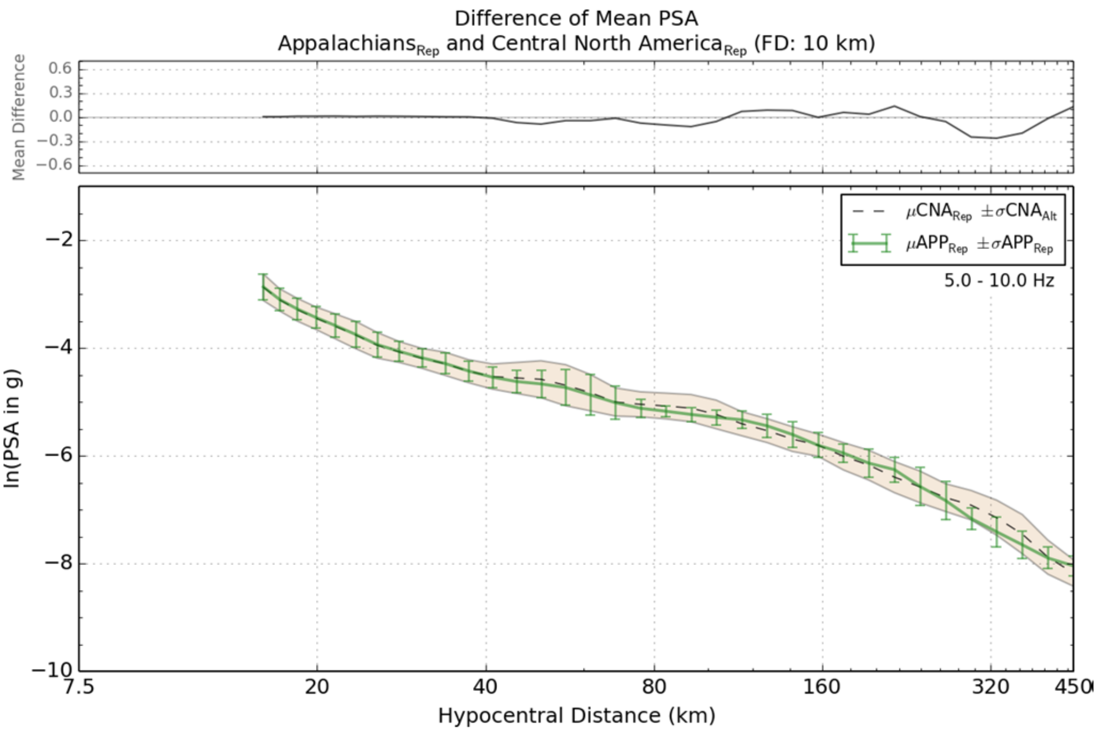

Figure D.21 **Representative mean comparison between the ACP and CNA regions within the standard deviation of CNA$_{Alt}$ at frequency 5.0–10 Hz and focal depth of 10 km.**

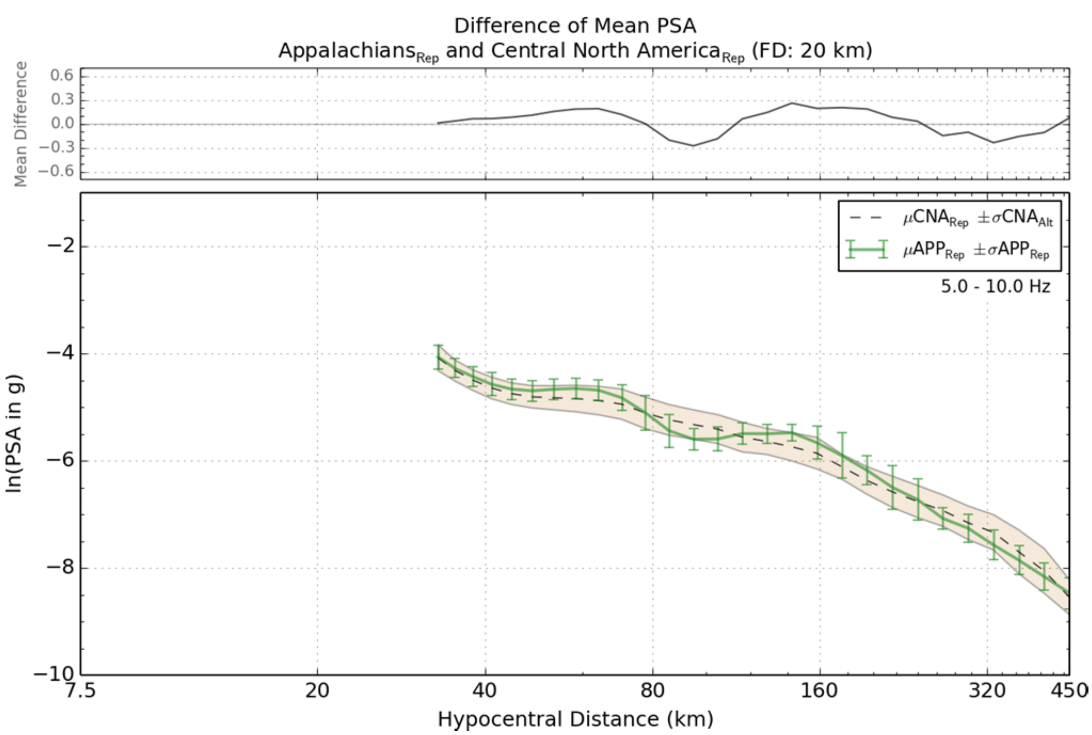

Figure D.22 **Representative mean comparison between the ACP and CNA regions within the standard deviation of CNA$_{Alt}$ at frequency 5.0–10 Hz and focal depth of 20 km.**

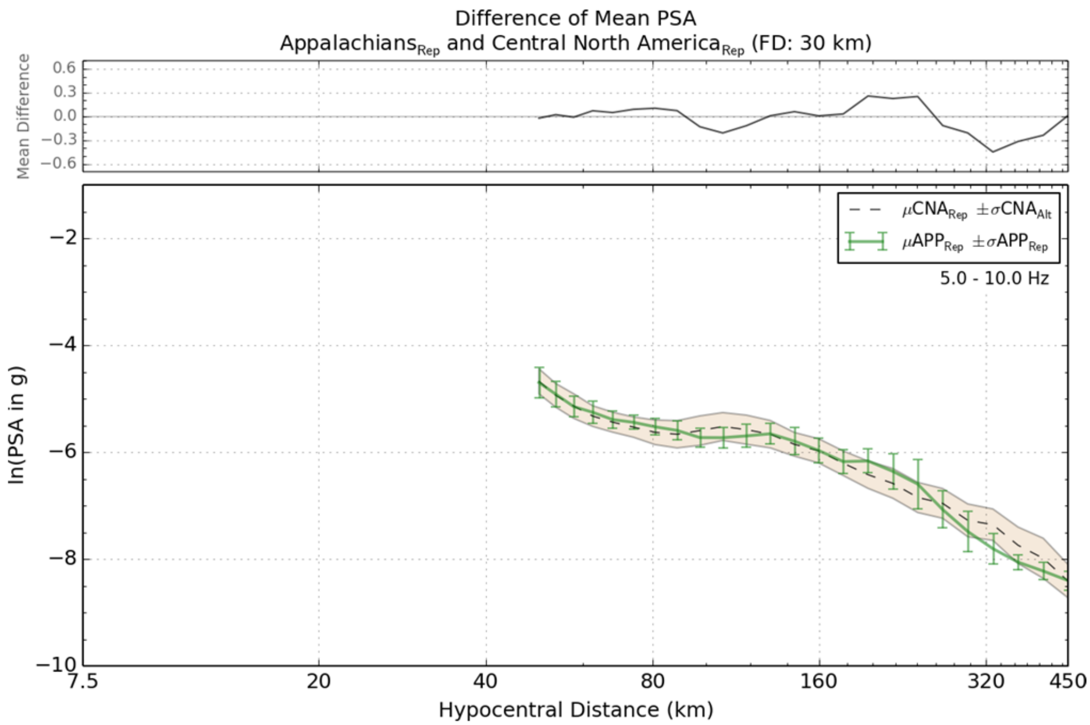

Figure D.23 **Representative mean comparison between the ACP and CNA regions within the standard deviation of CNA$_{Alt}$ at frequency 5.0–10 Hz and focal depth of 30 km.**

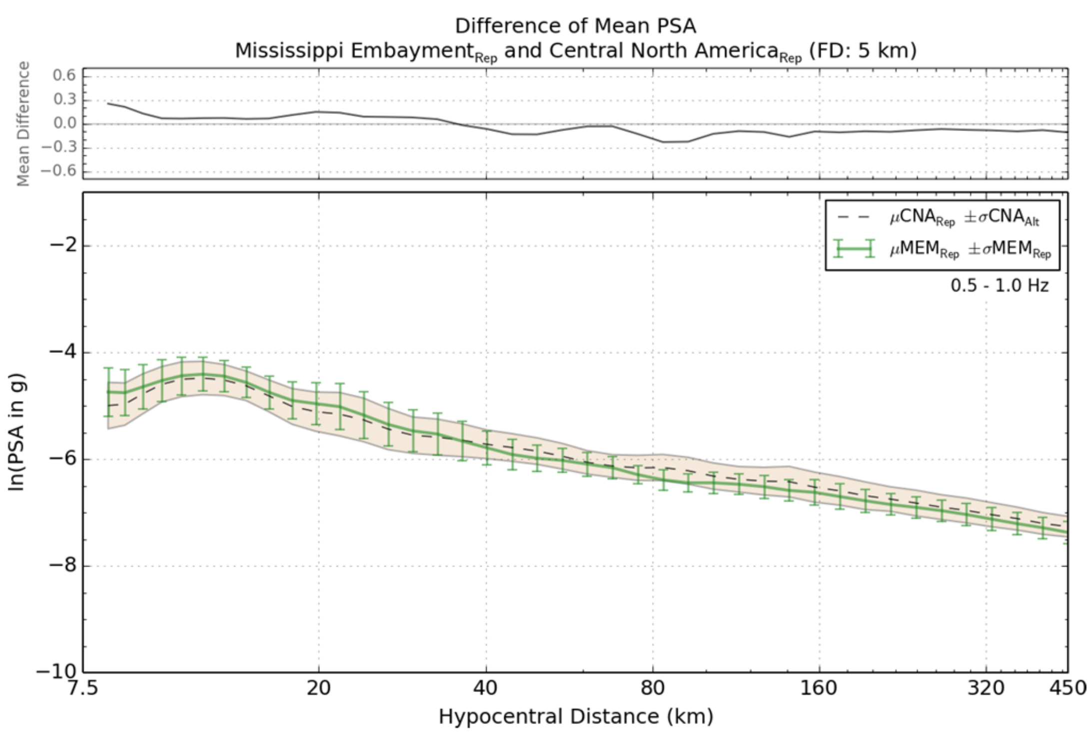

Figure D.24 **Representative mean comparison between the MEM and CNA regions within the standard deviation of CNA$_{Alt}$ at frequency 0.5–1 Hz and focal depth of 5 km.**

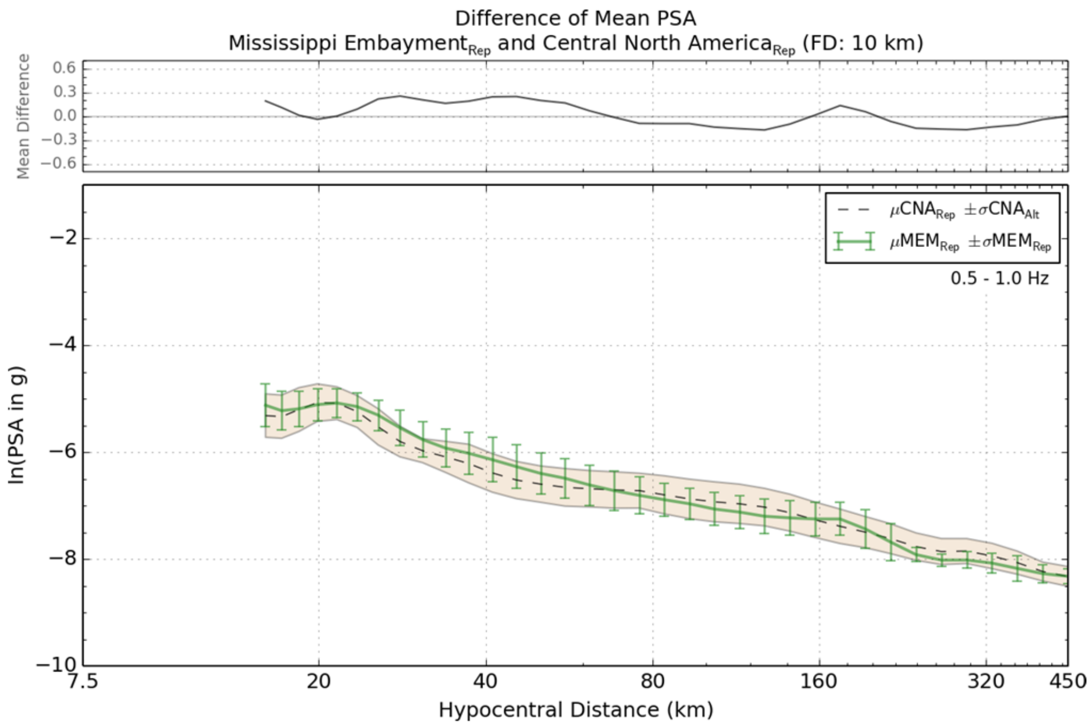

Figure D.25 Representative mean comparison between the MEM and CNA regions within the standard deviation of CNA$_{Alt}$ at frequency 0.5–1 Hz and focal depth of 10 km.

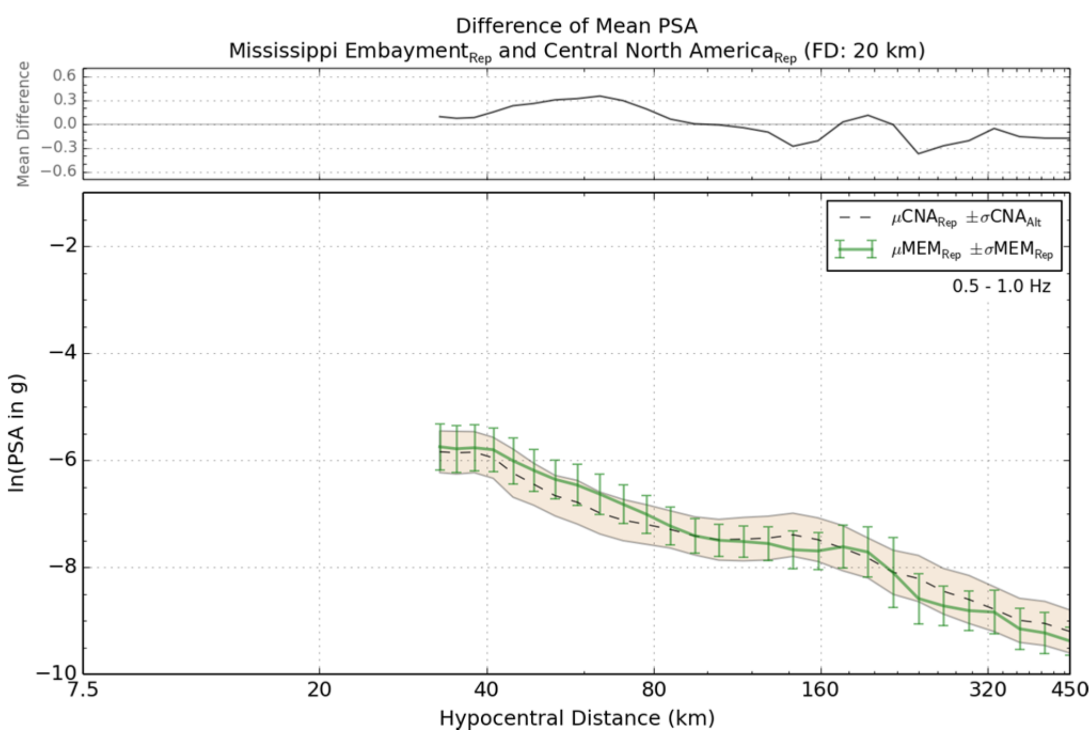

Figure D.26 Representative mean comparison between the AMEM and CNA regions within the standard deviation of CNA$_{Alt}$ at frequency 0.5–1 Hz and focal depth of 20 km.

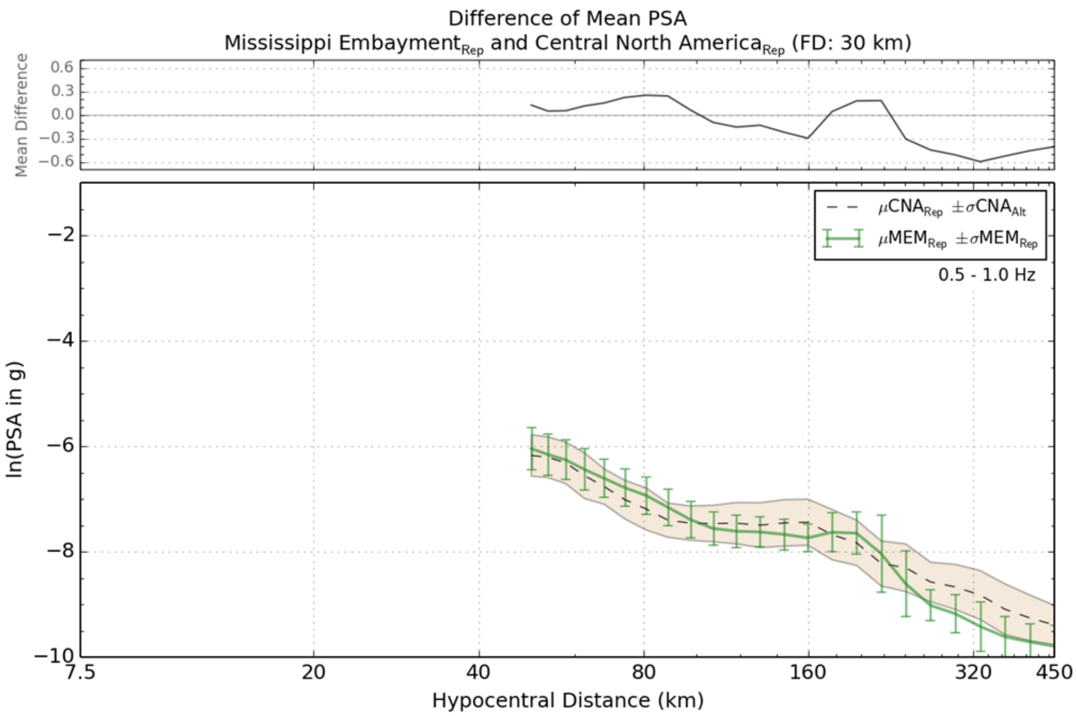

Figure D.27 Representative mean comparison between the MEM and CNA regions within the standard deviation of CNA$_{Alt}$ at frequency 5.0–10 Hz and focal depth of 30 km.

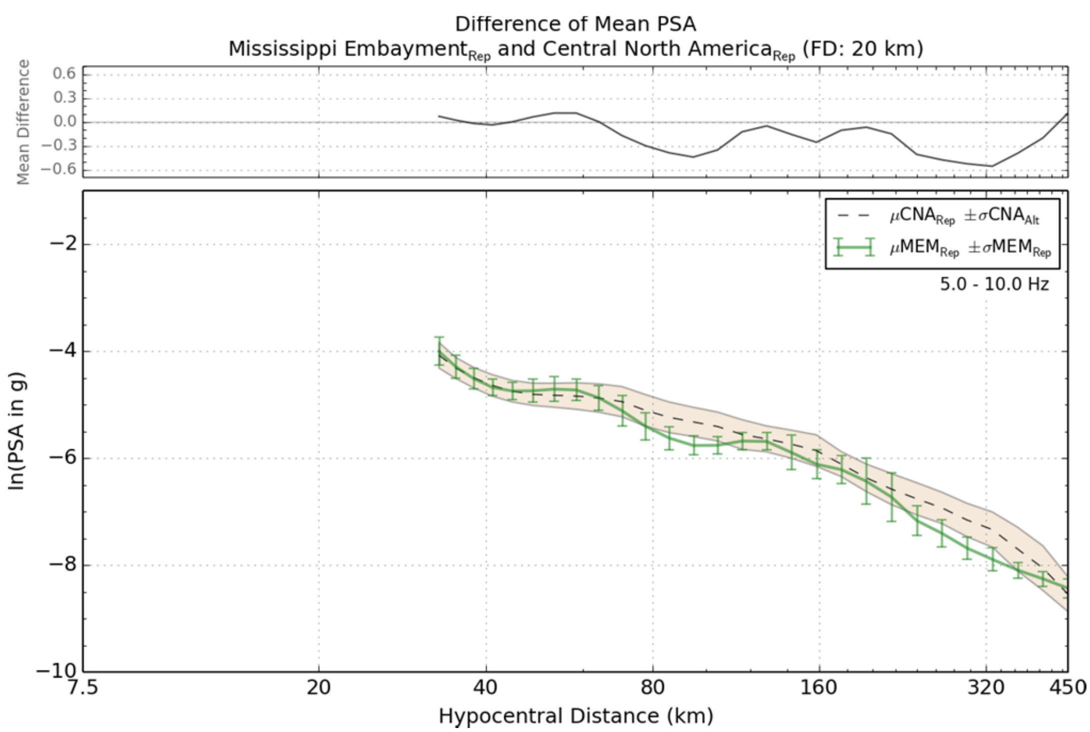

Figure D.28 Representative mean comparison between the MEM and CNA regions within the standard deviation of CNA$_{Alt}$ at frequency 5.0–10 Hz and focal depth of 20 km.

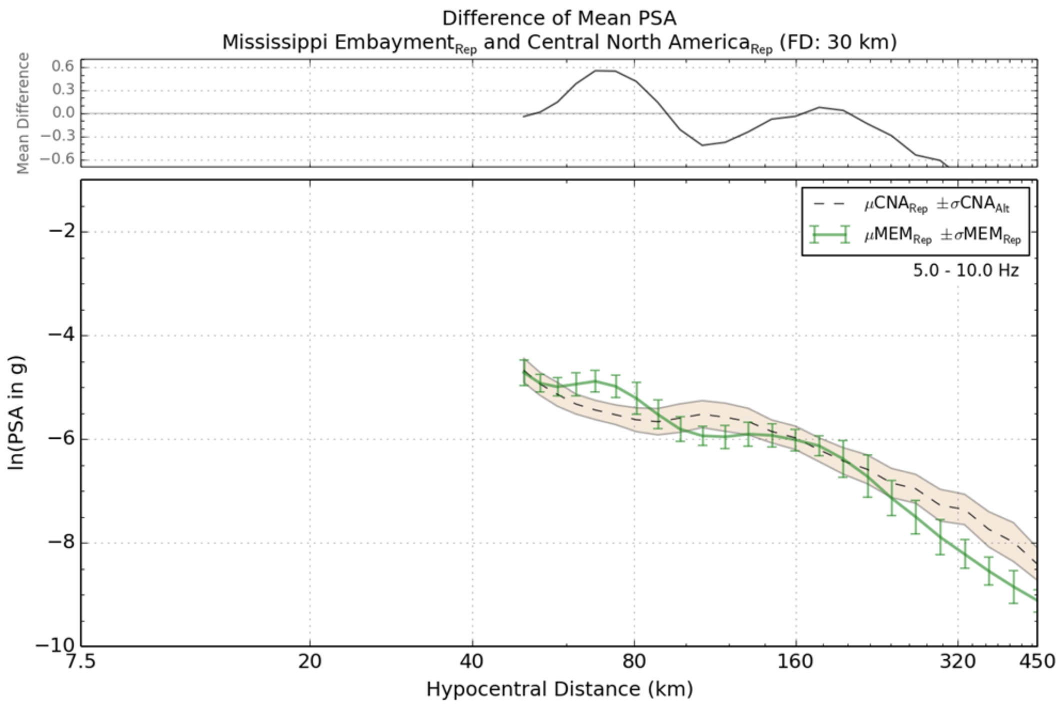

Figure D.29 **Representative mean comparison between the MEM and CNA regions within the standard deviation of CNA$_{Alt}$ at frequency 5.0–10 Hz and focal depth of 30 km.**

PEER REPORTS

PEER reports are available as a free PDF download from http://peer.berkeley.edu/publications/peer_reports_complete.html. Printed hard copies of PEER reports can be ordered directly from our printer by following the instructions at http://peer.berkeley.edu/publications/peer_reports.html. For other related questions about the PEER Report Series, contact the Pacific Earthquake Engineering Research Center, 325 Davis Hall mail code 1792, Berkeley, CA 94720. Tel.: (510) 642-3437; Fax: (510) 665-1655; Email: peer_editor@berkeley.edu

PEER 2014/15 *NGA-East Regionalization Report: Comparison of Four Crustal Regions within Central and Eastern North America using Waveform Modeling and 5%-Damped Pseudo-Spectral Acceleration Response.* Jennifer Dreiling, Marius P. Isken, Walter D. Mooney, Martin C. Chapman, and Richard W. Godbee. October 2014.

PEER 2014/14 *Scaling Relations between Seismic Moment and Rupture Area of Earthquakes in Stable Continental Regions*. Paul Somerville. August 2014.

PEER 2014/13 *PEER Preliminary Notes and Observations on the August 24, 2014, South Napa Earthquake*. Grace S. Kang (Editor), Stephen A. Mahin (Editors). September 2014.

PEER 2014/12 *Reference-Rock Site Conditions for Central and Eastern North America: Part II – Attenuation (Kappa) Definition*. Kenneth W. Campbell, Youssef M.A. Hashash, Byungmin Kim, Albert R. Kottke, Ellen M. Rathje, Walter J. Silva, and Jonathan P. Stewart. August 2014.

PEER 2014/11 *Reference-Rock Site Conditions for Central and Eastern North America: Part I - Velocity Definition.* Youssef M.A. Hashash, Albert R. Kottke, Jonathan P. Stewart, Kenneth W. Campbell, Byungmin Kim, Ellen M. Rathje, Walter J. Silva, Sissy Nikolaou, and Cheryl Moss. August 2014.

PEER 2014/10 *Evaluation of Collapse and Non-Collapse of Parallel Bridges Affected by Liquefaction and Lateral Spreading*. Benjamin Turner, Scott J. Brandenberg, and Jonathan P. Stewart. August 2014.

PEER 2014/09 *PEER Arizona Strong-Motion Database and GMPEs Evaluation*. Tadahiro Kishida, Robert E. Kayen, Olga-Joan Ktenidou, Walter J. Silva, Robert B. Darragh, and Jennie Watson-Lamprey. June 2014.

PEER 2014/08 *Unbonded Pretensioned Bridge Columns with Rocking Detail*. Jeffrey A. Schaefer, Bryan Kennedy, Marc O. Eberhard, John F. Stanton. June 2014.

PEER 2014/07 *Northridge 20 Symposium Summary Report: Impacts, Outcomes, and Next Steps*. May 2014.

PEER 2014/06 *Report of the Tenth Planning Meeting of NEES/E-Defense Collaborative Research on Earthquake Engineering*. December 2013.

PEER 2014/05 *Seismic Velocity Site Characterization of Thirty-One Chilean Seismometer Stations by Spectral Analysis of Surface Wave Dispersion.* Robert Kayen, Brad D. Carkin, Skye Corbet, Camilo Pinilla, Allan Ng, Edward Gorbis, and Christine Truong. April 2014.

PEER 2014/04 *Effect of Vertical Acceleration on Shear Strength of Reinforced Concrete Columns.* Hyerin Lee and Khalid M. Mosalam. April 2014.

PEER 2014/03 *Retest of Thirty-Year-Old Neoprene Isolation Bearings.* James M. Kelly and Niel C. Van Engelen. March 2014.

PEER 2014/02 *Theoretical Development of Hybrid Simulation Applied to Plate Structures.* Ahmed A. Bakhaty, Khalid M. Mosalam, and Sanjay Govindjee. January 2014.

PEER 2014/01 *Performance-Based Seismic Assessment of Skewed Bridges.* Peyman Kaviani, Farzin Zareian, and Ertugrul Taciroglu. January 2014.

PEER 2013/26 *Urban Earthquake Engineering. Proceedings of the U.S.-Iran Seismic Workshop.* December 2013.

PEER 2013/25 *Earthquake Engineering for Resilient Communities: 2013 PEER Internship Program Research Report Collection.* Heidi Tremayne (Editor), Stephen A. Mahin (Editor), Jorge Archbold Monterossa, Matt Brosman, Shelly Dean, Katherine deLaveaga, Curtis Fong, Donovan Holder, Rakeeb Khan, Elizabeth Jachens, David Lam, Daniela Martinez Lopez, Mara Minner, Geffen Oren, Julia Pavicic, Melissa Quinonez, Lorena Rodriguez, Sean Salazar, Kelli Slaven, Vivian Steyert, Jenny Taing, and Salvador Tena. December 2013.

PEER 2013/24 *NGA-West2 Ground Motion Prediction Equations for Vertical Ground Motions.* September 2013.

PEER 2013/23 *Coordinated Planning and Preparedness for Fire Following Major Earthquakes.* Charles Scawthorn. November 2013.

PEER 2013/22 *GEM-PEER Task 3 Project: Selection of a Global Set of Ground Motion Prediction Equations.* Jonathan P. Stewart, John Douglas, Mohammad B. Javanbarg, Carola Di Alessandro, Yousef Bozorgnia, Norman A. Abrahamson, David M. Boore, Kenneth W. Campbell, Elise Delavaud, Mustafa Erdik and Peter J. Stafford. December 2013.

PEER 2013/21 *Seismic Design and Performance of Bridges with Columns on Rocking Foundations.* Grigorios Antonellis and Marios Panagiotou. September 2013.

PEER 2013/20 *Experimental and Analytical Studies on the Seismic Behavior of Conventional and Hybrid Braced Frames.* Jiun-Wei Lai and Stephen A. Mahin. September 2013.

PEER 2013/19 *Toward Resilient Communities: A Performance-Based Engineering Framework for Design and Evaluation of the Built Environment.* Michael William Mieler, Bozidar Stojadinovic, Robert J. Budnitz, Stephen A. Mahin and Mary C. Comerio. September 2013.

PEER 2013/18 *Identification of Site Parameters that Improve Predictions of Site Amplification.* Ellen M. Rathje and Sara Navidi. July 2013.

PEER 2013/17 *Response Spectrum Analysis of Concrete Gravity Dams Including Dam-Water-Foundation Interaction.* Arnkjell Løkke and Anil K. Chopra. July 2013.

PEER 2013/16 *Effect of hoop reinforcement spacing on the cyclic response of large reinforced concrete special moment frame beams.* Marios Panagiotou, Tea Visnjic, Grigorios Antonellis, Panagiotis Galanis, and Jack P. Moehle. June 2013.

PEER 2013/15 *A Probabilistic Framework to Include the Effects of Near-Fault Directivity in Seismic Hazard Assessment.* Shrey Kumar Shahi, Jack W. Baker. October 2013.

PEER 2013/14 *Hanging-Wall Scaling using Finite-Fault Simulations.* Jennifer L. Donahue and Norman A. Abrahamson. September 2013.

PEER 2013/13 *Semi-Empirical Nonlinear Site Amplification and its Application in NEHRP Site Factors.* Jonathan P. Stewart and Emel Seyhan. November 2013.

PEER 2013/12 *Nonlinear Horizontal Site Response for the NGA-West2 Project.* Ronnie Kamai, Norman A. Abramson, Walter J. Silva. May 2013.

PEER 2013/11 *Epistemic Uncertainty for NGA-West2 Models.* Linda Al Atik and Robert R. Youngs. May 2013.

PEER 2013/10 *NGA-West 2 Models for Ground-Motion Directionality.* Shrey K. Shahi and Jack W. Baker. May 2013.

PEER 2013/09 *Final Report of the NGA-West2 Directivity Working Group.* Paul Spudich, Jeffrey R. Bayless, Jack W. Baker, Brian S.J. Chiou, Badie Rowshandel, Shrey Shahi, and Paul Somerville. May 2013.

PEER 2013/08 *NGA-West2 Model for Estimating Average Horizontal Values of Pseudo-Absolute Spectral Accelerations Generated by Crustal Earthquakes.* I. M. Idriss. May 2013.

PEER 2013/07 *Update of the Chiou and Youngs NGA Ground Motion Model for Average Horizontal Component of Peak Ground Motion and Response Spectra.* Brian Chiou and Robert Youngs. May 2013.

PEER 2013/06 *NGA-West2 Campbell-Bozorgnia Ground Motion Model for the Horizontal Components of PGA, PGV, and 5%-Damped Elastic Pseudo-Acceleration Response Spectra for Periods Ranging from 0.01 to 10 sec.* Kenneth W. Campbell and Yousef Bozorgnia. May 2013.

PEER 2013/05 *NGA-West 2 Equations for Predicting Response Spectral Accelerations for Shallow Crustal Earthquakes.* David M. Boore, Jonathan P. Stewart, Emel Seyhan, Gail M. Atkinson. May 2013.

PEER 2013/04 *Update of the AS08 Ground-Motion Prediction Equations Based on the NGA-West2 Data Set.* Norman Abrahamson, Walter Silva, and Ronnie Kamai. May 2013.

PEER 2013/03 *PEER NGA-West2 Database*. Timothy D. Ancheta, Robert B. Darragh, Jonathan P. Stewart, Emel Seyhan, Walter J. Silva, Brian S.J. Chiou, Katie E. Wooddell, Robert W. Graves, Albert R. Kottke, David M. Boore, Tadahiro Kishida, and Jennifer L. Donahue. May 2013.

PEER 2013/02 *Hybrid Simulation of the Seismic Response of Squat Reinforced Concrete Shear Walls.* Catherine A. Whyte and Bozidar Stojadinovic. May 2013.

PEER 2013/01 *Housing Recovery in Chile: A Qualitative Mid-program Review.* Mary C. Comerio. February 2013.

PEER 2012/08 *Guidelines for Estimation of Shear Wave Velocity.* Bernard R. Wair, Jason T. DeJong, and Thomas Shantz. December 2012.

PEER 2012/07 *Earthquake Engineering for Resilient Communities: 2012 PEER Internship Program Research Report Collection.* Heidi Tremayne (Editor), Stephen A. Mahin (Editor), Collin Anderson, Dustin Cook, Michael Erceg, Carlos Esparza, Jose Jimenez, Dorian Krausz, Andrew Lo, Stephanie Lopez, Nicole McCurdy, Paul Shipman, Alexander Strum, Eduardo Vega. December 2012.

PEER 2012/06 *Fragilities for Precarious Rocks at Yucca Mountain.* Matthew D. Purvance, Rasool Anooshehpoor, and James N. Brune. December 2012.

PEER 2012/05 *Development of Simplified Analysis Procedure for Piles in Laterally Spreading Layered Soils.* Christopher R. McGann, Pedro Arduino, and Peter Mackenzie–Helnwein. December 2012.

PEER 2012/04 *Unbonded Pre-Tensioned Columns for Bridges in Seismic Regions.* Phillip M. Davis, Todd M. Janes, Marc O. Eberhard, and John F. Stanton. December 2012.

PEER 2012/03 *Experimental and Analytical Studies on Reinforced Concrete Buildings with Seismically Vulnerable Beam-Column Joints.* Sangjoon Park and Khalid M. Mosalam. October 2012.

PEER 2012/02 *Seismic Performance of Reinforced Concrete Bridges Allowed to Uplift during Multi-Directional Excitation.* Andres Oscar Espinoza and Stephen A. Mahin. July 2012.

PEER 2012/01 *Spectral Damping Scaling Factors for Shallow Crustal Earthquakes in Active Tectonic Regions.* Sanaz Rezaeian, Yousef Bozorgnia, I. M. Idriss, Kenneth Campbell, Norman Abrahamson, and Walter Silva. July 2012.

PEER 2011/10 *Earthquake Engineering for Resilient Communities: 2011 PEER Internship Program Research Report Collection.* Eds. Heidi Faison and Stephen A. Mahin. December 2011.

PEER 2011/09 *Calibration of Semi-Stochastic Procedure for Simulating High-Frequency Ground Motions.* Jonathan P. Stewart, Emel Seyhan, and Robert W. Graves. December 2011.

PEER 2011/08 *Water Supply in regard to Fire Following Earthquake.* Charles Scawthorn. November 2011.

PEER 2011/07 *Seismic Risk Management in Urban Areas. Proceedings of a U.S.-Iran-Turkey Seismic Workshop.* September 2011.

PEER 2011/06 *The Use of Base Isolation Systems to Achieve Complex Seismic Performance Objectives.* Troy A. Morgan and Stephen A. Mahin. July 2011.

PEER 2011/05 *Case Studies of the Seismic Performance of Tall Buildings Designed by Alternative Means.* Task 12 Report for the Tall Buildings Initiative. Jack Moehle, Yousef Bozorgnia, Nirmal Jayaram, Pierson Jones, Mohsen Rahnama, Nilesh Shome, Zeynep Tuna, John Wallace, Tony Yang, and Farzin Zareian. July 2011.

PEER 2011/04 *Recommended Design Practice for Pile Foundations in Laterally Spreading Ground.* Scott A. Ashford, Ross W. Boulanger, and Scott J. Brandenberg. June 2011.

PEER 2011/03 *New Ground Motion Selection Procedures and Selected Motions for the PEER Transportation Research Program.* Jack W. Baker, Ting Lin, Shrey K. Shahi, and Nirmal Jayaram. March 2011.

PEER 2011/02 *A Bayesian Network Methodology for Infrastructure Seismic Risk Assessment and Decision Support.* Michelle T. Bensi, Armen Der Kiureghian, and Daniel Straub. March 2011.

PEER 2011/01 *Demand Fragility Surfaces for Bridges in Liquefied and Laterally Spreading Ground.* Scott J. Brandenberg, Jian Zhang, Pirooz Kashighandi, Yili Huo, and Minxing Zhao. March 2011.

PEER 2010/05 *Guidelines for Performance-Based Seismic Design of Tall Buildings.* Developed by the Tall Buildings Initiative. November 2010.

PEER 2010/04 *Application Guide for the Design of Flexible and Rigid Bus Connections between Substation Equipment Subjected to Earthquakes.* Jean-Bernard Dastous and Armen Der Kiureghian. September 2010.

PEER 2010/03 *Shear Wave Velocity as a Statistical Function of Standard Penetration Test Resistance and Vertical Effective Stress at Caltrans Bridge Sites.* Scott J. Brandenberg, Naresh Bellana, and Thomas Shantz. June 2010.

PEER 2010/02 *Stochastic Modeling and Simulation of Ground Motions for Performance-Based Earthquake Engineering.* Sanaz Rezaeian and Armen Der Kiureghian. June 2010.

PEER 2010/01 *Structural Response and Cost Characterization of Bridge Construction Using Seismic Performance Enhancement Strategies.* Ady Aviram, Božidar Stojadinović, Gustavo J. Parra-Montesinos, and Kevin R. Mackie. March 2010.

PEER 2009/03 *The Integration of Experimental and Simulation Data in the Study of Reinforced Concrete Bridge Systems Including Soil-Foundation-Structure Interaction.* Matthew Dryden and Gregory L. Fenves. November 2009.

PEER 2009/02 *Improving Earthquake Mitigation through Innovations and Applications in Seismic Science, Engineering, Communication, and Response. Proceedings of a U.S.-Iran Seismic Workshop.* October 2009.

PEER 2009/01 *Evaluation of Ground Motion Selection and Modification Methods: Predicting Median Interstory Drift Response of Buildings.* Curt B. Haselton, Ed. June 2009.

PEER 2008/10 *Technical Manual for Strata.* Albert R. Kottke and Ellen M. Rathje. February 2009.

PEER 2008/09 *NGA Model for Average Horizontal Component of Peak Ground Motion and Response Spectra.* Brian S.-J. Chiou and Robert R. Youngs. November 2008.

PEER 2008/08 *Toward Earthquake-Resistant Design of Concentrically Braced Steel Structures.* Patxi Uriz and Stephen A. Mahin. November 2008.

PEER 2008/07 *Using OpenSees for Performance-Based Evaluation of Bridges on Liquefiable Soils.* Stephen L. Kramer, Pedro Arduino, and HyungSuk Shin. November 2008.

PEER 2008/06 *Shaking Table Tests and Numerical Investigation of Self-Centering Reinforced Concrete Bridge Columns.* Hyung IL Jeong, Junichi Sakai, and Stephen A. Mahin. September 2008.

PEER 2008/05 *Performance-Based Earthquake Engineering Design Evaluation Procedure for Bridge Foundations Undergoing Liquefaction-Induced Lateral Ground Displacement.* Christian A. Ledezma and Jonathan D. Bray. August 2008.

PEER 2008/04 *Benchmarking of Nonlinear Geotechnical Ground Response Analysis Procedures.* Jonathan P. Stewart, Annie On-Lei Kwok, Yousseff M. A. Hashash, Neven Matasovic, Robert Pyke, Zhiliang Wang, and Zhaohui Yang. August 2008.

PEER 2008/03 *Guidelines for Nonlinear Analysis of Bridge Structures in California.* Ady Aviram, Kevin R. Mackie, and Božidar Stojadinović. August 2008.

PEER 2008/02 *Treatment of Uncertainties in Seismic-Risk Analysis of Transportation Systems.* Evangelos Stergiou and Anne S. Kiremidjian. July 2008.

PEER 2008/01 *Seismic Performance Objectives for Tall Buildings.* William T. Holmes, Charles Kircher, William Petak, and Nabih Youssef. August 2008.

PEER 2007/12 *An Assessment to Benchmark the Seismic Performance of a Code-Conforming Reinforced Concrete Moment-Frame Building.* Curt Haselton, Christine A. Goulet, Judith Mitrani-Reiser, James L. Beck, Gregory G. Deierlein, Keith A. Porter, Jonathan P. Stewart, and Ertugrul Taciroglu. August 2008.

PEER 2007/11 *Bar Buckling in Reinforced Concrete Bridge Columns.* Wayne A. Brown, Dawn E. Lehman, and John F. Stanton. February 2008.

PEER 2007/10 *Computational Modeling of Progressive Collapse in Reinforced Concrete Frame Structures.* Mohamed M. Talaat and Khalid M. Mosalam. May 2008.

PEER 2007/09 *Integrated Probabilistic Performance-Based Evaluation of Benchmark Reinforced Concrete Bridges.* Kevin R. Mackie, John-Michael Wong, and Božidar Stojadinović. January 2008.

PEER 2007/08 *Assessing Seismic Collapse Safety of Modern Reinforced Concrete Moment-Frame Buildings.* Curt B. Haselton and Gregory G. Deierlein. February 2008.

PEER 2007/07 *Performance Modeling Strategies for Modern Reinforced Concrete Bridge Columns*. Michael P. Berry and Marc O. Eberhard. April 2008.

PEER 2007/06 *Development of Improved Procedures for Seismic Design of Buried and Partially Buried Structures.* Linda Al Atik and Nicholas Sitar. June 2007.

PEER 2007/05 *Uncertainty and Correlation in Seismic Risk Assessment of Transportation Systems.* Renee G. Lee and Anne S. Kiremidjian. July 2007.

PEER 2007/04 *Numerical Models for Analysis and Performance-Based Design of Shallow Foundations Subjected to Seismic Loading.* Sivapalan Gajan, Tara C. Hutchinson, Bruce L. Kutter, Prishati Raychowdhury, José A. Ugalde, and Jonathan P. Stewart. May 2008.

PEER 2007/03 *Beam-Column Element Model Calibrated for Predicting Flexural Response Leading to Global Collapse of RC Frame Buildings.* Curt B. Haselton, Abbie B. Liel, Sarah Taylor Lange, and Gregory G. Deierlein. May 2008.

PEER 2007/02 *Campbell-Bozorgnia NGA Ground Motion Relations for the Geometric Mean Horizontal Component of Peak and Spectral Ground Motion Parameters.* Kenneth W. Campbell and Yousef Bozorgnia. May 2007.

PEER 2007/01 *Boore-Atkinson NGA Ground Motion Relations for the Geometric Mean Horizontal Component of Peak and Spectral Ground Motion Parameters.* David M. Boore and Gail M. Atkinson. May. May 2007.

PEER 2006/12 *Societal Implications of Performance-Based Earthquake Engineering.* Peter J. May. May 2007.

PEER 2006/11 *Probabilistic Seismic Demand Analysis Using Advanced Ground Motion Intensity Measures, Attenuation Relationships, and Near-Fault Effects.* Polsak Tothong and C. Allin Cornell. March 2007.

PEER 2006/10 *Application of the PEER PBEE Methodology to the I-880 Viaduct.* Sashi Kunnath. February 2007.

PEER 2006/09 *Quantifying Economic Losses from Travel Forgone Following a Large Metropolitan Earthquake.* James Moore, Sungbin Cho, Yue Yue Fan, and Stuart Werner. November 2006.

PEER 2006/08 *Vector-Valued Ground Motion Intensity Measures for Probabilistic Seismic Demand Analysis*. Jack W. Baker and C. Allin Cornell. October 2006.

PEER 2006/07 *Analytical Modeling of Reinforced Concrete Walls for Predicting Flexural and Coupled–Shear-Flexural Responses.* Kutay Orakcal, Leonardo M. Massone, and John W. Wallace. October 2006.

PEER 2006/06 *Nonlinear Analysis of a Soil-Drilled Pier System under Static and Dynamic Axial Loading.* Gang Wang and Nicholas Sitar. November 2006.

PEER 2006/05 *Advanced Seismic Assessment Guidelines.* Paolo Bazzurro, C. Allin Cornell, Charles Menun, Maziar Motahari, and Nicolas Luco. September 2006.

PEER 2006/04 *Probabilistic Seismic Evaluation of Reinforced Concrete Structural Components and Systems.* Tae Hyung Lee and Khalid M. Mosalam. August 2006.

PEER 2006/03 *Performance of Lifelines Subjected to Lateral Spreading.* Scott A. Ashford and Teerawut Juirnarongrit. July 2006.

PEER 2006/02 *Pacific Earthquake Engineering Research Center Highway Demonstration Project.* Anne Kiremidjian, James Moore, Yue Yue Fan, Nesrin Basoz, Ozgur Yazali, and Meredith Williams. April 2006.

PEER 2006/01 *Bracing Berkeley. A Guide to Seismic Safety on the UC Berkeley Campus.* Mary C. Comerio, Stephen Tobriner, and Ariane Fehrenkamp. January 2006.

PEER 2005/16 *Seismic Response and Reliability of Electrical Substation Equipment and Systems.* Junho Song, Armen Der Kiureghian, and Jerome L. Sackman. April 2006.

PEER 2005/15 *CPT-Based Probabilistic Assessment of Seismic Soil Liquefaction Initiation.* R. E. S. Moss, R. B. Seed, R. E. Kayen, J. P. Stewart, and A. Der Kiureghian. April 2006.

PEER 2005/14 *Workshop on Modeling of Nonlinear Cyclic Load-Deformation Behavior of Shallow Foundations.* Bruce L. Kutter, Geoffrey Martin, Tara Hutchinson, Chad Harden, Sivapalan Gajan, and Justin Phalen. March 2006.

PEER 2005/13 *Stochastic Characterization and Decision Bases under Time-Dependent Aftershock Risk in Performance-Based Earthquake Engineering.* Gee Liek Yeo and C. Allin Cornell. July 2005.

PEER 2005/12 *PEER Testbed Study on a Laboratory Building: Exercising Seismic Performance Assessment.* Mary C. Comerio, editor. November 2005.

PEER 2005/11 *Van Nuys Hotel Building Testbed Report: Exercising Seismic Performance Assessment.* Helmut Krawinkler, editor. October 2005.

PEER 2005/10 *First NEES/E-Defense Workshop on Collapse Simulation of Reinforced Concrete Building Structures.* September 2005.

PEER 2005/09 *Test Applications of Advanced Seismic Assessment Guidelines.* Joe Maffei, Karl Telleen, Danya Mohr, William Holmes, and Yuki Nakayama. August 2006.

PEER 2005/08 *Damage Accumulation in Lightly Confined Reinforced Concrete Bridge Columns.* R. Tyler Ranf, Jared M. Nelson, Zach Price, Marc O. Eberhard, and John F. Stanton. April 2006.

PEER 2005/07 *Experimental and Analytical Studies on the Seismic Response of Freestanding and Anchored Laboratory Equipment.* Dimitrios Konstantinidis and Nicos Makris. January 2005.

PEER 2005/06 *Global Collapse of Frame Structures under Seismic Excitations.* Luis F. Ibarra and Helmut Krawinkler. September 2005.

PEER 2005//05 *Performance Characterization of Bench- and Shelf-Mounted Equipment.* Samit Ray Chaudhuri and Tara C. Hutchinson. May 2006.

PEER 2005/04 *Numerical Modeling of the Nonlinear Cyclic Response of Shallow Foundations.* Chad Harden, Tara Hutchinson, Geoffrey R. Martin, and Bruce L. Kutter. August 2005.

PEER 2005/03 *A Taxonomy of Building Components for Performance-Based Earthquake Engineering.* Keith A. Porter. September 2005.

PEER 2005/02 *Fragility Basis for California Highway Overpass Bridge Seismic Decision Making*. Kevin R. Mackie and Božidar Stojadinović. June 2005.

PEER 2005/01 *Empirical Characterization of Site Conditions on Strong Ground Motion.* Jonathan P. Stewart, Yoojoong Choi, and Robert W. Graves. June 2005.

PEER 2004/09 *Electrical Substation Equipment Interaction: Experimental Rigid Conductor Studies.* Christopher Stearns and André Filiatrault. February 2005.

PEER 2004/08 *Seismic Qualification and Fragility Testing of Line Break 550-kV Disconnect Switches.* Shakhzod M. Takhirov, Gregory L. Fenves, and Eric Fujisaki. January 2005.

PEER 2004/07 *Ground Motions for Earthquake Simulator Qualification of Electrical Substation Equipment.* Shakhzod M. Takhirov, Gregory L. Fenves, Eric Fujisaki, and Don Clyde. January 2005.

PEER 2004/06 *Performance-Based Regulation and Regulatory Regimes.* Peter J. May and Chris Koski. September 2004.

PEER 2004/05 *Performance-Based Seismic Design Concepts and Implementation: Proceedings of an International Workshop.* Peter Fajfar and Helmut Krawinkler, editors. September 2004.

PEER 2004/04 *Seismic Performance of an Instrumented Tilt-up Wall Building.* James C. Anderson and Vitelmo V. Bertero. July 2004.

PEER 2004/03 *Evaluation and Application of Concrete Tilt-up Assessment Methodologies.* Timothy Graf and James O. Malley. October 2004.

PEER 2004/02 *Analytical Investigations of New Methods for Reducing Residual Displacements of Reinforced Concrete Bridge Columns.* Junichi Sakai and Stephen A. Mahin. August 2004.

PEER 2004/01 *Seismic Performance of Masonry Buildings and Design Implications.* Kerri Anne Taeko Tokoro, James C. Anderson, and Vitelmo V. Bertero. February 2004.

PEER 2003/18 *Performance Models for Flexural Damage in Reinforced Concrete Columns.* Michael Berry and Marc Eberhard. August 2003.

PEER 2003/17 *Predicting Earthquake Damage in Older Reinforced Concrete Beam-Column Joints.* Catherine Pagni and Laura Lowes. October 2004.

PEER 2003/16 *Seismic Demands for Performance-Based Design of Bridges.* Kevin Mackie and Božidar Stojadinović. August 2003.

PEER 2003/15 *Seismic Demands for Nondeteriorating Frame Structures and Their Dependence on Ground Motions.* Ricardo Antonio Medina and Helmut Krawinkler. May 2004.

PEER 2003/14 *Finite Element Reliability and Sensitivity Methods for Performance-Based Earthquake Engineering.* Terje Haukaas and Armen Der Kiureghian. April 2004.

PEER 2003/13 *Effects of Connection Hysteretic Degradation on the Seismic Behavior of Steel Moment-Resisting Frames.* Janise E. Rodgers and Stephen A. Mahin. March 2004.

PEER 2003/12 *Implementation Manual for the Seismic Protection of Laboratory Contents: Format and Case Studies.* William T. Holmes and Mary C. Comerio. October 2003.

PEER 2003/11 *Fifth U.S.-Japan Workshop on Performance-Based Earthquake Engineering Methodology for Reinforced Concrete Building Structures.* February 2004.

PEER 2003/10 *A Beam-Column Joint Model for Simulating the Earthquake Response of Reinforced Concrete Frames.* Laura N. Lowes, Nilanjan Mitra, and Arash Altoontash. February 2004.

PEER 2003/09 *Sequencing Repairs after an Earthquake: An Economic Approach.* Marco Casari and Simon J. Wilkie. April 2004.

PEER 2003/08 *A Technical Framework for Probability-Based Demand and Capacity Factor Design (DCFD) Seismic Formats.* Fatemeh Jalayer and C. Allin Cornell. November 2003.

PEER 2003/07 *Uncertainty Specification and Propagation for Loss Estimation Using FOSM Methods.* Jack W. Baker and C. Allin Cornell. September 2003.

PEER 2003/06 *Performance of Circular Reinforced Concrete Bridge Columns under Bidirectional Earthquake Loading.* Mahmoud M. Hachem, Stephen A. Mahin, and Jack P. Moehle. February 2003.

PEER 2003/05 *Response Assessment for Building-Specific Loss Estimation.* Eduardo Miranda and Shahram Taghavi. September 2003.

PEER 2003/04 *Experimental Assessment of Columns with Short Lap Splices Subjected to Cyclic Loads*. Murat Melek, John W. Wallace, and Joel Conte. April 2003.

PEER 2003/03 *Probabilistic Response Assessment for Building-Specific Loss Estimation.* Eduardo Miranda and Hesameddin Aslani. September 2003.

PEER 2003/02 *Software Framework for Collaborative Development of Nonlinear Dynamic Analysis Program.* Jun Peng and Kincho H. Law. September 2003.

PEER 2003/01 *Shake Table Tests and Analytical Studies on the Gravity Load Collapse of Reinforced Concrete Frames.* Kenneth John Elwood and Jack P. Moehle. November 2003.

PEER 2002/24 *Performance of Beam to Column Bridge Joints Subjected to a Large Velocity Pulse.* Natalie Gibson, André Filiatrault, and Scott A. Ashford. April 2002.

PEER 2002/23 *Effects of Large Velocity Pulses on Reinforced Concrete Bridge Columns.* Greg L. Orozco and Scott A. Ashford. April 2002.

PEER 2002/22 *Characterization of Large Velocity Pulses for Laboratory Testing.* Kenneth E. Cox and Scott A. Ashford. April 2002.

PEER 2002/21 *Fourth U.S.-Japan Workshop on Performance-Based Earthquake Engineering Methodology for Reinforced Concrete Building Structures*. December 2002.

PEER 2002/20 *Barriers to Adoption and Implementation of PBEE Innovations.* Peter J. May. August 2002.

PEER 2002/19 *Economic-Engineered Integrated Models for Earthquakes: Socioeconomic Impacts.* Peter Gordon, James E. Moore II, and Harry W. Richardson. July 2002.

PEER 2002/18 *Assessment of Reinforced Concrete Building Exterior Joints with Substandard Details.* Chris P. Pantelides, Jon Hansen, Justin Nadauld, and Lawrence D. Reaveley. May 2002.

PEER 2002/17 *Structural Characterization and Seismic Response Analysis of a Highway Overcrossing Equipped with Elastomeric Bearings and Fluid Dampers: A Case Study.* Nicos Makris and Jian Zhang. November 2002.

PEER 2002/16 *Estimation of Uncertainty in Geotechnical Properties for Performance-Based Earthquake Engineering.* Allen L. Jones, Steven L. Kramer, and Pedro Arduino. December 2002.

PEER 2002/15 *Seismic Behavior of Bridge Columns Subjected to Various Loading Patterns.* Asadollah Esmaeily-Gh. and Yan Xiao. December 2002.

PEER 2002/14 *Inelastic Seismic Response of Extended Pile Shaft Supported Bridge Structures.* T.C. Hutchinson, R.W. Boulanger, Y.H. Chai, and I.M. Idriss. December 2002.

PEER 2002/13 *Probabilistic Models and Fragility Estimates for Bridge Components and Systems.* Paolo Gardoni, Armen Der Kiureghian, and Khalid M. Mosalam. June 2002.

PEER 2002/12 *Effects of Fault Dip and Slip Rake on Near-Source Ground Motions: Why Chi-Chi Was a Relatively Mild M7.6 Earthquake.* Brad T. Aagaard, John F. Hall, and Thomas H. Heaton. December 2002.

PEER 2002/11 *Analytical and Experimental Study of Fiber-Reinforced Strip Isolators*. James M. Kelly and Shakhzod M. Takhirov. September 2002.

PEER 2002/10 *Centrifuge Modeling of Settlement and Lateral Spreading with Comparisons to Numerical Analyses***.** Sivapalan Gajan and Bruce L. Kutter. January 2003.

PEER 2002/09 *Documentation and Analysis of Field Case Histories of Seismic Compression during the 1994 Northridge, California, Earthquake.* Jonathan P. Stewart, Patrick M. Smith, Daniel H. Whang, and Jonathan D. Bray. October 2002.

PEER 2002/08 *Component Testing, Stability Analysis and Characterization of Buckling-Restrained Unbonded Braces^{TM}*. Cameron Black, Nicos Makris, and Ian Aiken. September 2002.

PEER 2002/07 *Seismic Performance of Pile-Wharf Connections*. Charles W. Roeder, Robert Graff, Jennifer Soderstrom, and Jun Han Yoo. December 2001.

PEER 2002/06 *The Use of Benefit-Cost Analysis for Evaluation of Performance-Based Earthquake Engineering Decisions*. Richard O. Zerbe and Anthony Falit-Baiamonte. September 2001.

PEER 2002/05 *Guidelines, Specifications, and Seismic Performance Characterization of Nonstructural Building Components and Equipment*. André Filiatrault, Constantin Christopoulos, and Christopher Stearns. September 2001.

PEER 2002/04 *Consortium of Organizations for Strong-Motion Observation Systems and the Pacific Earthquake Engineering Research Center Lifelines Program: Invited Workshop on Archiving and Web Dissemination of Geotechnical Data, 4–5 October 2001*. September 2002.

PEER 2002/03 *Investigation of Sensitivity of Building Loss Estimates to Major Uncertain Variables for the Van Nuys Testbed.* Keith A. Porter, James L. Beck, and Rustem V. Shaikhutdinov. August 2002.

PEER 2002/02 *The Third U.S.-Japan Workshop on Performance-Based Earthquake Engineering Methodology for Reinforced Concrete Building Structures*. July 2002.

PEER 2002/01 *Nonstructural Loss Estimation: The UC Berkeley Case Study.* Mary C. Comerio and John C. Stallmeyer. December 2001.

PEER 2001/16 *Statistics of SDF-System Estimate of Roof Displacement for Pushover Analysis of Buildings.* Anil K. Chopra, Rakesh K. Goel, and Chatpan Chintanapakdee. December 2001.

PEER 2001/15 *Damage to Bridges during the 2001 Nisqually Earthquake.* R. Tyler Ranf, Marc O. Eberhard, and Michael P. Berry. November 2001.

PEER 2001/14 *Rocking Response of Equipment Anchored to a Base Foundation.* Nicos Makris and Cameron J. Black. September 2001.

PEER 2001/13 *Modeling Soil Liquefaction Hazards for Performance-Based Earthquake Engineering.* Steven L. Kramer and Ahmed-W. Elgamal. February 2001.

PEER 2001/12 *Development of Geotechnical Capabilities in OpenSees.* Boris Jeremić. September 2001.

PEER 2001/11 *Analytical and Experimental Study of Fiber-Reinforced Elastomeric Isolators.* James M. Kelly and Shakhzod M. Takhirov. September 2001.

PEER 2001/10 *Amplification Factors for Spectral Acceleration in Active Regions.* Jonathan P. Stewart, Andrew H. Liu, Yoojoong Choi, and Mehmet B. Baturay. December 2001.

PEER 2001/09 *Ground Motion Evaluation Procedures for Performance-Based Design.* Jonathan P. Stewart, Shyh-Jeng Chiou, Jonathan D. Bray, Robert W. Graves, Paul G. Somerville, and Norman A. Abrahamson. September 2001.

PEER 2001/08 *Experimental and Computational Evaluation of Reinforced Concrete Bridge Beam-Column Connections for Seismic Performance.* Clay J. Naito, Jack P. Moehle, and Khalid M. Mosalam. November 2001.

PEER 2001/07 *The Rocking Spectrum and the Shortcomings of Design Guidelines.* Nicos Makris and Dimitrios Konstantinidis. August 2001.

PEER 2001/06 *Development of an Electrical Substation Equipment Performance Database for Evaluation of Equipment Fragilities.* Thalia Agnanos. April 1999.

PEER 2001/05 *Stiffness Analysis of Fiber-Reinforced Elastomeric Isolators.* Hsiang-Chuan Tsai and James M. Kelly. May 2001.

PEER 2001/04 *Organizational and Societal Considerations for Performance-Based Earthquake Engineering.* Peter J. May. April 2001.

PEER 2001/03 *A Modal Pushover Analysis Procedure to Estimate Seismic Demands for Buildings: Theory and Preliminary Evaluation.* Anil K. Chopra and Rakesh K. Goel. January 2001.

PEER 2001/02 *Seismic Response Analysis of Highway Overcrossings Including Soil-Structure Interaction.* Jian Zhang and Nicos Makris. March 2001.

PEER 2001/01 *Experimental Study of Large Seismic Steel Beam-to-Column Connections.* Egor P. Popov and Shakhzod M. Takhirov. November 2000.

PEER 2000/10 *The Second U.S.-Japan Workshop on Performance-Based Earthquake Engineering Methodology for Reinforced Concrete Building Structures.* March 2000.

PEER 2000/09 *Structural Engineering Reconnaissance of the August 17, 1999 Earthquake: Kocaeli (Izmit), Turkey.* Halil Sezen, Kenneth J. Elwood, Andrew S. Whittaker, Khalid Mosalam, John J. Wallace, and John F. Stanton. December 2000.

PEER 2000/08 *Behavior of Reinforced Concrete Bridge Columns Having Varying Aspect Ratios and Varying Lengths of Confinement.* Anthony J. Calderone, Dawn E. Lehman, and Jack P. Moehle. January 2001.

PEER 2000/07 *Cover-Plate and Flange-Plate Reinforced Steel Moment-Resisting Connections.* Taejin Kim, Andrew S. Whittaker, Amir S. Gilani, Vitelmo V. Bertero, and Shakhzod M. Takhirov. September 2000.

PEER 2000/06 *Seismic Evaluation and Analysis of 230-kV Disconnect Switches.* Amir S. J. Gilani, Andrew S. Whittaker, Gregory L. Fenves, Chun-Hao Chen, Henry Ho, and Eric Fujisaki. July 2000.

PEER 2000/05 *Performance-Based Evaluation of Exterior Reinforced Concrete Building Joints for Seismic Excitation.* Chandra Clyde, Chris P. Pantelides, and Lawrence D. Reaveley. July 2000.

PEER 2000/04 *An Evaluation of Seismic Energy Demand: An Attenuation Approach.* Chung-Che Chou and Chia-Ming Uang. July 1999.

PEER 2000/03 *Framing Earthquake Retrofitting Decisions: The Case of Hillside Homes in Los Angeles.* Detlof von Winterfeldt, Nels Roselund, and Alicia Kitsuse. March 2000.

PEER 2000/02 *U.S.-Japan Workshop on the Effects of Near-Field Earthquake Shaking.* Andrew Whittaker, ed. July 2000.

PEER 2000/01 *Further Studies on Seismic Interaction in Interconnected Electrical Substation Equipment.* Armen Der Kiureghian, Kee-Jeung Hong, and Jerome L. Sackman. November 1999.

PEER 1999/14 *Seismic Evaluation and Retrofit of 230-kV Porcelain Transformer Bushings.* Amir S. Gilani, Andrew S. Whittaker, Gregory L. Fenves, and Eric Fujisaki. December 1999.

PEER 1999/13 *Building Vulnerability Studies: Modeling and Evaluation of Tilt-up and Steel Reinforced Concrete Buildings.* John W. Wallace, Jonathan P. Stewart, and Andrew S. Whittaker, editors. December 1999.

PEER 1999/12 *Rehabilitation of Nonductile RC Frame Building Using Encasement Plates and Energy-Dissipating Devices.* Mehrdad Sasani, Vitelmo V. Bertero, James C. Anderson. December 1999.

PEER 1999/11 *Performance Evaluation Database for Concrete Bridge Components and Systems under Simulated Seismic Loads.* Yael D. Hose and Frieder Seible. November 1999.

PEER 1999/10 *U.S.-Japan Workshop on Performance-Based Earthquake Engineering Methodology for Reinforced Concrete Building Structures.* December 1999.

PEER 1999/09 *Performance Improvement of Long Period Building Structures Subjected to Severe Pulse-Type Ground Motions*. James C. Anderson, Vitelmo V. Bertero, and Raul Bertero. October 1999.

PEER 1999/08 *Envelopes for Seismic Response Vectors.* Charles Menun and Armen Der Kiureghian. July 1999.

PEER 1999/07 *Documentation of Strengths and Weaknesses of Current Computer Analysis Methods for Seismic Performance of Reinforced Concrete Members.* William F. Cofer. November 1999.

PEER 1999/06 *Rocking Response and Overturning of Anchored Equipment under Seismic Excitations.* Nicos Makris and Jian Zhang. November 1999.

PEER 1999/05 *Seismic Evaluation of 550 kV Porcelain Transformer Bushings.* Amir S. Gilani, Andrew S. Whittaker, Gregory L. Fenves, and Eric Fujisaki. October 1999.

PEER 1999/04 *Adoption and Enforcement of Earthquake Risk-Reduction Measures.* Peter J. May, Raymond J. Burby, T. Jens Feeley, and Robert Wood.

PEER 1999/03 *Task 3 Characterization of Site Response General Site Categories*. Adrian Rodriguez-Marek, Jonathan D. Bray, and Norman Abrahamson. February 1999.

PEER 1999/02 *Capacity-Demand-Diagram Methods for Estimating Seismic Deformation of Inelastic Structures: SDF Systems*. Anil K. Chopra and Rakesh Goel. April 1999.

PEER 1999/01 *Interaction in Interconnected Electrical Substation Equipment Subjected to Earthquake Ground Motions.* Armen Der Kiureghian, Jerome L. Sackman, and Kee-Jeung Hong. February 1999.

PEER 1998/08 *Behavior and Failure Analysis of a Multiple-Frame Highway Bridge in the 1994 Northridge Earthquake.* Gregory L. Fenves and Michael Ellery. December 1998.

PEER 1998/07 *Empirical Evaluation of Inertial Soil-Structure Interaction Effects.* Jonathan P. Stewart, Raymond B. Seed, and Gregory L. Fenves. November 1998.

PEER 1998/06 *Effect of Damping Mechanisms on the Response of Seismic Isolated Structures.* Nicos Makris and Shih-Po Chang. November 1998.

PEER 1998/05 *Rocking Response and Overturning of Equipment under Horizontal Pulse-Type Motions.* Nicos Makris and Yiannis Roussos. October 1998.

PEER 1998/04 *Pacific Earthquake Engineering Research Invitational Workshop Proceedings, May 14–15, 1998: Defining the Links between Planning, Policy Analysis, Economics and Earthquake Engineering.* Mary Comerio and Peter Gordon. September 1998.

PEER 1998/03 *Repair/Upgrade Procedures for Welded Beam to Column Connections.* James C. Anderson and Xiaojing Duan. May 1998.

PEER 1998/02 *Seismic Evaluation of 196 kV Porcelain Transformer Bushings.* Amir S. Gilani, Juan W. Chavez, Gregory L. Fenves, and Andrew S. Whittaker. May 1998.

PEER 1998/01 *Seismic Performance of Well-Confined Concrete Bridge Columns.* Dawn E. Lehman and Jack P. Moehle. December 2000.

ONLINE PEER REPORTS

The following PEER reports are available by Internet only at http://peer.berkeley.edu/publications/peer_reports_complete.html.

PEER 2012/103 *Performance-Based Seismic Demand Assessment of Concentrically Braced Steel Frame Buildings.* Chui-Hsin Chen and Stephen A. Mahin. December 2012.

PEER 2012/102 *Procedure to Restart an Interrupted Hybrid Simulation: Addendum to PEER Report 2010/103.* Vesna Terzic and Bozidar Stojadinovic. October 2012.

PEER 2012/101 *Mechanics of Fiber Reinforced Bearings.* James M. Kelly and Andrea Calabrese. February 2012.

PEER 2011/107 *Nonlinear Site Response and Seismic Compression at Vertical Array Strongly Shaken by 2007 Niigata-ken Chuetsu-oki Earthquake.* Eric Yee, Jonathan P. Stewart, and Kohji Tokimatsu. December 2011.

PEER 2011/106 *Self Compacting Hybrid Fiber Reinforced Concrete Composites for Bridge Columns.* Pardeep Kumar, Gabriel Jen, William Trono, Marios Panagiotou, and Claudia Ostertag. September 2011.

PEER 2011/105 *Stochastic Dynamic Analysis of Bridges Subjected to Spacially Varying Ground Motions.* Katerina Konakli and Armen Der Kiureghian. August 2011.

PEER 2011/104 *Design and Instrumentation of the 2010 E-Defense Four-Story Reinforced Concrete and Post-Tensioned Concrete Buildings.* Takuya Nagae, Kenichi Tahara, Taizo Matsumori, Hitoshi Shiohara, Toshimi Kabeyasawa, Susumu Kono, Minehiro Nishiyama (Japanese Research Team) and John Wallace, Wassim Ghannoum, Jack Moehle, Richard Sause, Wesley Keller, Zeynep Tuna (U.S. Research Team). June 2011.

PEER 2011/103 *In-Situ Monitoring of the Force Output of Fluid Dampers: Experimental Investigation.* Dimitrios Konstantinidis, James M. Kelly, and Nicos Makris. April 2011.

PEER 2011/102 *Ground-motion prediction equations 1964 - 2010.* John Douglas. April 2011.

PEER 2011/101 *Report of the Eighth Planning Meeting of NEES/E-Defense Collaborative Research on Earthquake Engineering.* Convened by the Hyogo Earthquake Engineering Research Center (NIED), NEES Consortium, Inc. February 2011.

PEER 2010/111 *Modeling and Acceptance Criteria for Seismic Design and Analysis of Tall Buildings.* Task 7 Report for the Tall Buildings Initiative - Published jointly by the Applied Technology Council. October 2010.

PEER 2010/110 *Seismic Performance Assessment and Probabilistic Repair Cost Analysis of Precast Concrete Cladding Systems for Multistory Buildlings.* Jeffrey P. Hunt and Božidar Stojadinovic. November 2010.

PEER 2010/109 *Report of the Seventh Joint Planning Meeting of NEES/E-Defense Collaboration on Earthquake Engineering. Held at the E-Defense, Miki, and Shin-Kobe, Japan, September 18–19, 2009.* August 2010.

PEER 2010/108 *Probabilistic Tsunami Hazard in California.* Hong Kie Thio, Paul Somerville, and Jascha Polet, preparers. October 2010.

PEER 2010/107 *Performance and Reliability of Exposed Column Base Plate Connections for Steel Moment-Resisting Frames.* Ady Aviram, Božidar Stojadinovic, and Armen Der Kiureghian. August 2010.

PEER 2010/106 *Verification of Probabilistic Seismic Hazard Analysis Computer Programs.* Patricia Thomas, Ivan Wong, and Norman Abrahamson. May 2010.

PEER 2010/105 *Structural Engineering Reconnaissance of the April 6, 2009, Abruzzo, Italy, Earthquake, and Lessons Learned.* M. Selim Günay and Khalid M. Mosalam. April 2010.

PEER 2010/104 *Simulating the Inelastic Seismic Behavior of Steel Braced Frames, Including the Effects of Low-Cycle Fatigue.* Yuli Huang and Stephen A. Mahin. April 2010.

PEER 2010/103 *Post-Earthquake Traffic Capacity of Modern Bridges in California.* Vesna Terzic and Božidar Stojadinović. March 2010.

PEER 2010/102 *Analysis of Cumulative Absolute Velocity (CAV) and JMA Instrumental Seismic Intensity (I_{JMA}) Using the PEER–NGA Strong Motion Database.* Kenneth W. Campbell and Yousef Bozorgnia. February 2010.

PEER 2010/101 *Rocking Response of Bridges on Shallow Foundations.* Jose A. Ugalde, Bruce L. Kutter, and Boris Jeremic. April 2010.

PEER 2009/109 *Simulation and Performance-Based Earthquake Engineering Assessment of Self-Centering Post-Tensioned Concrete Bridge Systems.* Won K. Lee and Sarah L. Billington. December 2009.

PEER 2009/108 *PEER Lifelines Geotechnical Virtual Data Center.* J. Carl Stepp, Daniel J. Ponti, Loren L. Turner, Jennifer N. Swift, Sean Devlin, Yang Zhu, Jean Benoit, and John Bobbitt. September 2009.

PEER 2009/107 *Experimental and Computational Evaluation of Current and Innovative In-Span Hinge Details in Reinforced Concrete Box-Girder Bridges: Part 2: Post-Test Analysis and Design Recommendations.* Matias A. Hube and Khalid M. Mosalam. December 2009.

PEER 2009/106 *Shear Strength Models of Exterior Beam-Column Joints without Transverse Reinforcement.* Sangjoon Park and Khalid M. Mosalam. November 2009.

PEER 2009/105 *Reduced Uncertainty of Ground Motion Prediction Equations through Bayesian Variance Analysis.* Robb Eric S. Moss. November 2009.

PEER 2009/104 *Advanced Implementation of Hybrid Simulation.* Andreas H. Schellenberg, Stephen A. Mahin, Gregory L. Fenves. November 2009.

PEER 2009/103 *Performance Evaluation of Innovative Steel Braced Frames.* T. Y. Yang, Jack P. Moehle, and Božidar Stojadinovic. August 2009.

PEER 2009/102 *Reinvestigation of Liquefaction and Nonliquefaction Case Histories from the 1976 Tangshan Earthquake.* Robb Eric Moss, Robert E. Kayen, Liyuan Tong, Songyu Liu, Guojun Cai, and Jiaer Wu. August 2009.

PEER 2009/101 *Report of the First Joint Planning Meeting for the Second Phase of NEES/E-Defense Collaborative Research on Earthquake Engineering.* Stephen A. Mahin et al. July 2009.

PEER 2008/104 *Experimental and Analytical Study of the Seismic Performance of Retaining Structures.* Linda Al Atik and Nicholas Sitar. January 2009.

PEER 2008/103 *Experimental and Computational Evaluation of Current and Innovative In-Span Hinge Details in Reinforced Concrete Box-Girder Bridges. Part 1: Experimental Findings and Pre-Test Analysis.* Matias A. Hube and Khalid M. Mosalam. January 2009.

PEER 2008/102 *Modeling of Unreinforced Masonry Infill Walls Considering In-Plane and Out-of-Plane Interaction.* Stephen Kadysiewski and Khalid M. Mosalam. January 2009.

PEER 2008/101 *Seismic Performance Objectives for Tall Buildings.* William T. Holmes, Charles Kircher, William Petak, and Nabih Youssef. August 2008.

PEER 2007/101 *Generalized Hybrid Simulation Framework for Structural Systems Subjected to Seismic Loading.* Tarek Elkhoraibi and Khalid M. Mosalam. July 2007.

PEER 2007/100 *Seismic Evaluation of Reinforced Concrete Buildings Including Effects of Masonry Infill Walls.* Alidad Hashemi and Khalid M. Mosalam. July 2007.

The Pacific Earthquake Engineering Research Center (PEER) is a multi-institutional research and education center with headquarters at the University of California, Berkeley. Investigators from over 20 universities, several consulting companies, and researchers at various state and federal government agencies contribute to research programs focused on performance-based earthquake engineering.

These research programs aim to identify and reduce the risks from major earthquakes to life safety and to the economy by including research in a wide variety of disciplines including structural and geotechnical engineering, geology/seismology, lifelines, transportation, architecture, economics, risk management, and public policy.

PEER is supported by federal, state, local, and regional agencies, together with industry partners.

PEER Core Institutions:
University of California, Berkeley (Lead Institution)
California Institute of Technology
Oregon State University
Stanford University
University of California, Davis
University of California, Irvine
University of California, Los Angeles
University of California, San Diego
University of Southern California
University of Washington

PEER reports can be ordered at http://peer.berkeley.edu/publications/peer_reports.html or by contacting

Pacific Earthquake Engineering Research Center
University of California, Berkeley
325 Davis Hall, mail code 1792
Berkeley, CA 94720-1792
Tel: 510-642-3437
Fax: 510-642-1655
Email: peer_editor@berkeley.edu

ISSN 1547-0587X